The Dissertation Committee for Paul Biju-Duval certifies that this is the approved version of the following dissertation:

DEVELOPMENT OF THREE-DIMENSIONAL FINITE ELEMENT SOFTWARE FOR CURVED PLATE GIRDER AND TUB GIRDER BRIDGES DURING CONSTRUCTION

Committee:

Todd A. Helwig, Co-Supervisor

Eric B. Williamson, Co-Supervisor

Oguzhan Bayrak

Patricia M. Clayton

Michael D. Engelhardt

Chad M. Landis

DEVELOPMENT OF THREE-DIMENSIONAL FINITE ELEMENT SOFTWARE FOR CURVED PLATE GIRDER AND TUB GIRDER BRIDGES DURING CONSTRUCTION

by

Paul Biju-Duval

Dissertation

Presented to the Faculty of the Graduate School of

The University of Texas at Austin

in Partial Fulfillment

of the Requirements

for the Degree of

Doctor of Philosophy

The University of Texas at Austin

December 2017

Dedication

To Raphaël

Acknowledgements

Pursuing a PhD at UT Austin has been an exceptional experience. First of all, I would like to thank Dr. Helwig for the trust he has constantly had in me. Over the last four years, I have felt free to always follow what I thought was most appropriate for the development of the software presented in this dissertation. Although that was not always easy, I have also tried to grasp as much as possible of his deep knowledge in structural stability and steel bridge design. Dr. Williamson's guidance and advice has always been truly beneficial. His rigor in the thinking process is admirable, and I thank him for his constant encouragements. Dr. Bayrak, Dr. Clayton and Dr. Engelhardt are wonderful professors. It has been a true honor to be your student. Thank you also to Dr. Landis for being part of my graduate committee, and to Jason Stith for his suggestions early in the project. Jason kindly left me a few things to improve in his program, which turned out to be the core of my research here at UT.

I will not forget the friends I made during my time in Austin. Colter Roskos is as generous as talented, and I wish him the best for his career. The same applies to Stalin Armijos, who started together as I, as well as Gloriana Arrieta, Kostas Belivanis, Cristobal Bianchi, Lourdes Cueva Chacon, Christian Elguera, Nicolas Emilfork, Magdalena Ganderats, Alicia Garcia, Mario Glikman, Melvin Goh, Guillermo Huaco, Eugenio Iturriaga, Jacqueline Larsen, Francesco Moccia, Eduardo Molina, Magdalena Novoa, Alejandra Reyes, Pedro Serigos, Cesar Silva Santisteban, Drit Sokoli, and so many others. Whether you read those words ten days or ten years from the moment they were written, be sure that you have a friend in Paris, or wherever else I may be.

High up in the list, I would like to thank my brother Thomas Biju-Duval for the moral and financial support, which complemented the already generous sponsoring of this research project by the Texas Department of Transportation. The little escapades to Indonesia, Australia and New Zealand together with his wife Marion Noirot were true moments of happiness.

Finally, to you, Imy, thank you for the sacrifices that moving to Austin has meant. You will do fantastic in your dissertation and Raphael is the cutest little boy I can imagine. Be sure that our next move will be the right move, and that I will support you as much as you have supported me.

DEVELOPMENT OF THREE-DIMENSIONAL FINITE ELEMENT SOFTWARE FOR CURVED PLATE GIRDER AND TUB GIRDER BRIDGES DURING CONSTRUCTION

Paul Biju-Duval, Ph.D.

The University of Texas at Austin, 2017

Supervisors: Todd A. Helwig and Eric B. Williamson

Because of its ability to be easily shaped, steel is an attractive material for curved girders. Plate girder and tub girder bridges, for example, are often the preferred solution for direct connectors in highway networks. This flexibility in fabrication, however, presents challenges for structural engineers because of the difficulties associated with accounting for combined bending and torsion with curved geometry. The potential presence of skewed supports is a further source of complexity. In fact, no commercial structural engineering program currently addresses the evaluation of plate girder and tub girder bridges while modeling them to the full extent of their three-dimensional configuration. Most engineers, for example, use a two-dimensional bridge representation, which is often accurate for typical design of a complete bridge but may also be unconservative in many cases. The few programs that allow a full three-dimensional representation require extensive knowledge of finite element theory as well as significant time to model any complex structure.

This dissertation presents the assumptions, methodology and calculations involved in the programming of a new structural engineering program designed to assess the behavior and stability or curved plate girder and tub girder bridges during erection or deck

placement. It then illustrates the capabilities of the program for various structural systems subjected to a variety of loads, from self-weight to wind and temperature loads. In addition to a linear elastic analysis, multiple types of analysis are offered to the engineer: a geometrically nonlinear analysis provides a more accurate behavior for flexible systems, a linearized buckling analysis yields an upper bound evaluation of the stability of the structure, while a modal dynamic analysis estimates the free vibration modes of that structure.

Table of Contents

List of Figures

Chapter 1: Background

1.0 INTRODUCTION

Horizontally curved bridges are commonly necessary in highway bridges in a variety of applications such as direct connectors between intersecting highways. The curved geometry of the girders can lead to large torsion in the girders. An accurate structural analysis of these girder systems throughout the construction process as well as in the final condition is one of the key aspects for a safe design. This dissertation outlines the development and implementation of UT Bridge V2.2, which is a finite element program capable of modeling straight and horizontally curved girders throughout the erection and deck construction process.

Understanding the unique capabilities of this program necessitates reviewing the commonly used programs used in practice. This introductory chapter provides background information on the analytical methods commonly employed by engineers in the design of horizontally curved bridges. An overview of some of the benefits of steel girders in curved girder applications is also provided along with some of the challenging aspects of the behavior during erection and construction. Finally, a discussion is provided on common limitations on the use of state-of-the-art three-dimensional analysis methods for steel girder systems.

1.1 MODELING CURVED BRIDGES, FROM LINE ANALYSIS TO THREE-DIMENSIONAL ANALYSIS

Advances in technology over the past several decades have resulted in significant improvements in the design, fabrication, and construction of complex bridge systems.

From a design perspective, advances in computational resources have resulted in significant improvements in the level of analyses that can be carried out. The primary method of analyses in structural engineering applies the finite element technique, which has been in use for decades. Numerous programs have been commercialized since the development of the finite element theory in the early 1940s. While the finite element technique can provide an accurate representation of any structural system, there are always necessary modeling assumptions related to the level of detail, boundary conditions, load applications, and a myriad of other aspects of the simulation of the physical system. While improvements in the computational resources have greatly improved the ability to carry out detailed analyses on complex systems, one of the most time-consuming aspects of the analysis is the creation of the model. While nearly any problem can be accurately simulated computationally, one of the most important steps in the modeling phase is the validation of the modeling assumptions.

There are a number of commercial software programs available to structural designers ranging from general purpose finite element programs to specialized design specific programs. In many situations, structural engineers may have relatively little knowledge of the mechanics and assumptions involved in these commercial programs. Thousands of lines of code are typically embedded within a program, and many developers often do not want to share what they consider to proprietary information. As a result, in some situations the finite element program can appear as a bit of a “black box” application to many designers. While simple problems can be modeled with the software to gain confidence in the software capabilities, understanding or gaining confidence in the program for more complex problems can be more difficult. An example of a more complex application would be horizontally curved girders that result in significant torsional moments.

Although curved plate girder or tub girder bridges may be regarded as relatively simple structural systems, they can demonstrate complex behavior that requires a detailed level of understanding regarding how modeling assumptions influence the computed response. For some simple geometries, these girder types can be represented with a simple beam element. This type of one-dimensional analysis has been used for decades for simple, straight bridges to estimate deflected shapes, stresses, as well as shear and moment diagrams. Unlike straight bridges, curved girders are complex systems that have a natural tendency to twist under gravity loads due to the eccentricity of the girder self-weight relative to the line of support. This natural rigid body movement can lead to undesirable behavior and limit bending capacity. Consequently, the rotation restraints that are provided imply that torsional effects must be superimposed with bending effects (Figure 1.1). The most common modeling techniques of these girders makes use of shell elements to simulate the girder cross-section. The theory of shells was developed to study actual shell structures, such as aircraft, pressure vessels, or stadium roofs. Plate girder and tub girder bridges, however, do not conform to the traditional geometry characterizing shell structures. In fact, it may be that beam elements could accurately model the response of these types of structures. Thin-walled beam theory is technically able to analyze curved girders and capture the associated warping stresses. Use of this theory, however, leads to other issues, such as how to apply a load, a boundary condition or a brace on a specific location on the cross-section, or how to study local buckling effects, or the impact of local cross-sectional distortion. In addition, because thin-walled beam elements are still line elements, there is significant post-processing required to render the deflected shape in three dimensions.

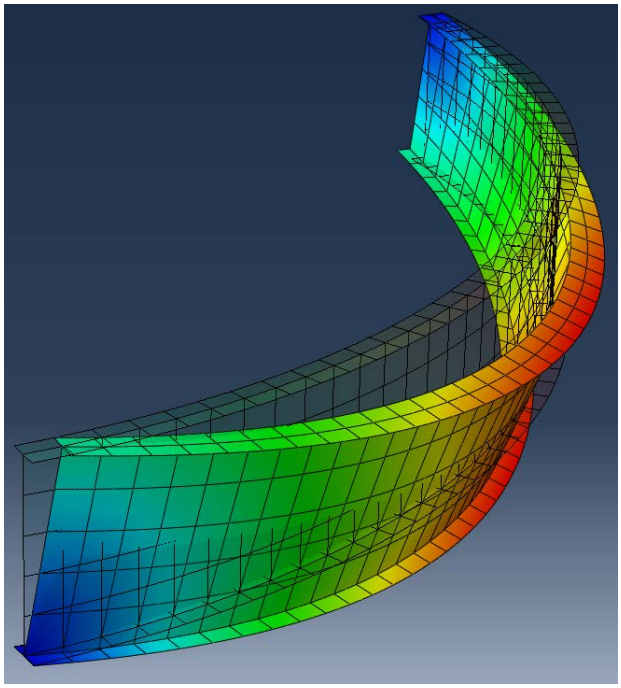

Figure 1.1: Gravity-induced bending and torsion on a horizontally curved simply-supported girder (ABAQUS)

While there are obvious limitations to line girder models, over the years, approximate methods have been developed for analyzing more complex structures. For curved systems with multiple I-girders, the V-load method has proven to be effective at approximating response using a line girder analysis while still accounting for cross-frame forces (Fiechtl, Fenves and Frank 1987). However, the V-load idealization is often inaccurate for skewed configurations and staggered cross-frame patterns, and is therefore limited in its applications. The M/R method is another approximate line girder method to evaluate the torsional effects on curved tub girder bridges, though it too has important limitations (Tung and Fountain 1970).

With the increasing importance of curved bridges to the infrastructure throughout the world, an approximate analysis method accounting for composite action between the concrete deck and the steel superstructure was developed, namely the grid method.

Different versions of the grid method have been proposed, depending on the number of degrees of freedom considered at each node, but they all are two-dimensional analysis methods. The grid method has been widely used over the past several decades, and is reliable for the analysis and design of bridges in their finished state. This analysis method, however, is not reliable for severely curved or skewed bridges during erection and construction, as it does not estimate warping stresses and cross-frame forces accurately. Some improvements have been recently been proposed to enhance the grid method (Sanchez and White 2017).

For complex geometries, cross-frame configurations, or severe curvatures or skews, the three-dimensional finite element method is widely recognized as the most accurate method of estimating deflections, stresses, and other quantities required for a safe and efficient erection and construction (Zureick and Naqib 1999). Plate and tub girders are comprised of flanges and webs welded together, so this level of refinement is beneficial in terms of accuracy. The same applies to web stiffeners, which are also steel plates. With significant progress in computational capabilities over the last twenty years, finite element shell theory, which at first seemed poorly suited for these systems, can be implemented with its potential for accurate analyses fully utilized.

1.2 THE USE OF STEEL FOR CURVED BRIDGES

The two primary materials used for modern bridge structures consist of concrete and steel. For straight, short-span applications (generally less than 150 ft.), prestressed concrete girders often represent an economical solution. Prestressed concrete girders can be precast at plants and shipped to the bridge site. While there have been limited applications to curved and/or spliced prestressed concrete girders (Nickas and Dick 2015),

steel girders have typically been the dominant girder for horizontally curved applications or applications with spans exceeding approximately 150 ft. The advantages of steel in these applications are the ability to achieve curved shapes through a variety of fabrication methods as well as the ability to splice the girders together using bolted connections. In addition, steel has a relatively large strength to weight ratio, resulting in a relatively light superstructure for longer span systems.

The weight of a steel bridge per unit length is often just a fraction of its concrete equivalent. Slender cross-sections are designed to optimize structural efficiency, which may require the use of transverse web stiffeners for shear strength and to prevent local web buckling. Those slender sections, together with the discrete bracing provided during erection and construction and the uncertainty in loads and boundary conditions in the early stages of construction, make the steel girder systems prone to stability issues, particularly during construction.

Direct connectors on highway networks are the primary application for curved steel bridges. Plate girders are the most common structural solution, but tub girders, also called trapezoidal box girders, have also been used extensively because of their greater torsional stiffness, which is commonly 100~1000 times larger than its I-girder equivalent.

1.3 BEHAVIOR OF CURVED BRIDGES DURING ERECTION AND CONSTRUCTION

Bridges are designed to sustain large pedestrian or traffic loads, in addition to wind loads and potential earthquake forces. During erection and construction, loads are limited in magnitude, but their effect may be catastrophic because a bridge has not reached its full stiffness and strength because the concrete deck, which provides lateral bracing to the steel girders, is absent or has not yet stiffened. During erection, self-weight of the steel

superstructure only can be the cause of major serviceability issues. For example, in 2015, an insufficiently braced straight plate girder bridge in Edmonton, Canada suffered lateral-torsional buckling, leading to large displacements (Figure 1.2). Because the girders buckled elastically, lifting them up and replacing the failed cross-frame elements was possible to restore the bridge to its original position. Other common serviceability issues include bridge misalignment and lack-of-fit between components. If deformations are underestimated, then unplanned, sometimes difficult operations may be required to force elements into place, which may itself lead to significant locked-in stresses in the girders and the cross-frames. Other situations include unexpectedly large out-of-plumbness of the girder webs, errors in camber diagrams, excessive support reactions, or the requirement for additional concrete for the deck.

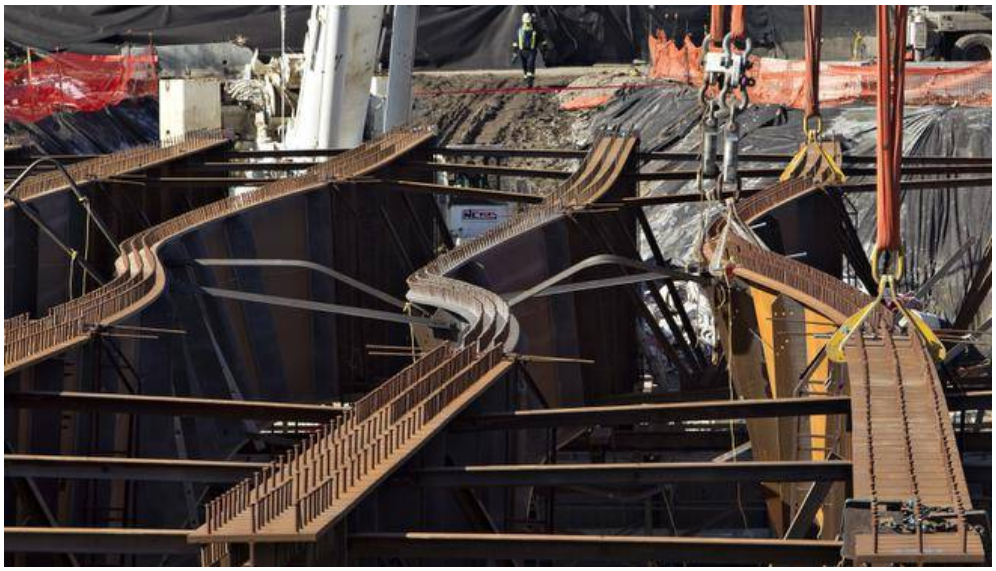

Figure 1.2: Edmonton 102nd Avenue Bridge failure (Source: Edmonton Sun)

While serviceability issues can be costly, structural failures are obviously much worse. In 2002, the Marcy Bridge collapse killed one worker and injured several others.

The Marcy Bridge was a straight tub girder bridge and failed by global lateral buckling during placement of the concrete deck. Failure was attributed to insufficient bracing (Figure 1.3).

Figure 1.3: Marcy Bridge collapse (Corr, McCann and McDonald 2009)

Other collapses have occurred across the United States in recent years. In 2004, a 200-foot long steel girder collapsed onto a highway in Colorado, crushing a passing vehicle and killing its three occupants. The investigation showed the tragic collapse was due to a combination of various factors. The girder was part of a bridge widening project. After being erected, it was braced to the existing concrete deck. Those braces were attached to the existing structure in such a way that very little pullout resistance was provided. Cyclic loading of the braces due to wind loads, lateral vibrations, and thermal expansion resulted

in failure of some bolts. Once a few bolts failed, bracing was insufficient, and the girder collapsed. The contractor had actually planned to stabilize the girder by attaching it to a second girder, connecting one another with cross-frames. Unfortunately, the collapse happened before that second girder erection could take place.

Accurately estimating the stability and deformation of bridges during erection and construction is therefore critical to avoid serviceability or ultimate failures. The selection of the right analysis method is key. While the three-dimensional finite element method is widely considered to be the most accurate, the bridge industry still relies primarily on two-dimensional grid models.

1.4 OBSTACLES FOR ROUTINE USE OF THE THREE-DIMENSIONAL FINITE ELEMENT METHOD

Designing and constructing a bridge on schedule is of primary importance to bridge owners. Time constraints typically necessitate the use of approximate analysis methods unless very complex situations are encountered. The three-dimensional finite element method (FEM), though still approximate, is recognized as being the most accurate analysis approach for characterizing the structural response of bridges under a variety of loading and support conditions. Yet, because time is an important parameter in the design process, FEM is often not implemented, even for complex, curved bridge applications. General finite element software such as ABAQUS or ANSYS require extensive knowledge and training. Moreover, displacements and stresses are the primary output of a finite element analysis program, meaning some of the quantities most valuable to a bridge engineer, namely shear and moment, are not readily available and require considerable post-processing of the stresses. The same applies to cross-frame forces, and to a lesser degree, to support reactions. If various stages of an erection or placement scheme are to be

analyzed, the total time required to model each stage can quickly exceed the duration available to complete this work. Furthermore, as analysis and design is an iterative process, modifying key parameters such as a cross-sectional dimension or a cross-frame arrangement is common. For general purpose finite element applications, such modifications can quickly become time-consuming for large-scale structures.

Software targeted at bridge engineering applications, such as LUSAS and LARSA 4D, still require significant knowledge and training, although the post-processing of the stresses is often automatically performed. Still, the complexity involved in these programs is high, and engineers cannot get access to all the assumptions implemented in the software, sometimes leading to the frustrating impression of working with a "black box".

UT Bridge V2.2, which is the program described in this dissertation, has been developed to fill the gap between the bridge industry and state-of-the-art three-dimensional finite element methods, with the conviction that the most efficient structural analysis programs are developed by structural engineers themselves. The program specifically targets straight or curved plate girder and tub girder bridges during erection and construction. UT Bridge V1.0 was first released in 2010 and the final version of software was V1.6. A number of bugs and limitations were encountered with the first version of the software and the decision was made to develop a major step in the program. The author therefore developed version 2.0, which was released in 2015. Version 2.1 was released in 2016 and Version 2.2 will be released in December 2017.

1.5 RESEARCH PURPOSE

This dissertation has two purposes. First, it aims to build a bridge between basic shell theory and its application to a finite element program, with curved plate girder and

tub girder bridges as the structural systems. Without showing the actual subroutines (except for a select few in the appendices), but moving step-by-step and presenting all the major assumptions going into the code, the dissertation provides insight into the algorithms. Second, as the program is itself a tool, the dissertation illustrates how it might be used for various applications. The program capabilities can target either practicing engineers looking to properly estimate the behavior of the specific bridge they are analyzing, or structural engineering researchers conducting parametric studies on the general behavior of curved bridges. These applications reflect the variety of loads and analysis methods that UT Bridge V2.2 offers, including first-order linear, geometrically nonlinear, linearized buckling, or modal dynamic analyses. The program can be used for straight or curved systems subjected to a variety of loads, including self-weight, point loads, uniform loads, wind loads, and temperature loads.

1.6 ORGANIZATION

Following this introductory chapter, Chapter 2 provides a summary of the research studies recently undertaken in the field of analysis and engineering of curved, skewed, plate-girder and tub-girder bridges. Chapter 3 gives an overview of the program architecture, without giving intricate details of the individual subroutines, but keeping a structure that recalls the algorithmic nature of any finite element program. Chapter 4 describes in detail the assumptions and modeling decisions made throughout the development of the program, from the selection of the finite elements used, to the implementation of the loads and boundary conditions, and so on. Chapter 5 addresses the two general eigenvalue problems addressed by the program, namely the linearized buckling analysis and the modal dynamic analysis, and also provides a description of the

assumptions, method and implementation of the geometrically nonlinear analysis. Chapter 6 contains a series of examples and benchmark problems that illustrate the capabilities of the program for a variety of situations. Finally, Chapter 7 gives a summary of the research, conclusions regarding the major findings, and recommendations for future work.

Chapter 2: Review of Common Bridge Software and Literature on Steel Bridge Girders

This chapter focuses on a review of common software used in the analysis and design of steel bridge systems. The software that is covered includes both commercially developed software as well as structural analysis programs developed through sponsored research studies. The software that is discussed consist of programs that are the most pertinent to the research discussed in this dissertation. In addition to an overview of the various software programs, a discussion of pertinent research is also presented.

2.1 STRUCTURAL ANALYSIS PROGRAMS ADDRESSING CURVED PLATE GIRDER AND TUB GIRDER BRIDGES

This dissertation provides an overview of the development and implementation of UT Bridge V2.2, which is the first structural analysis program that specifically targets straight and curved plate girder and tub girder bridges during erection and construction. Nonetheless, curved steel bridges have been built for decades, and computer programs have played an ever increasing role in their analysis and design. This section provides an overview of commonly used commercial and university developed software that is applicable to steel bridge systems.

2.1.1 COMMERCIAL PROGRAMS

MDX (2009) and DESCUS (2008) are two of the most commonly used programs for curved plate girder and tub girder analysis and design. These programs rely on a two-dimensional grid representation of curved bridge structures and are able to conduct a live load analysis, derive influence surfaces, and check most of the AASHTO *LRFD Bridge*

Design Specifications (2017) requirements. DESCUS was initially developed in the late 1970s and is currently distributed by Opti-Mate, Inc. MDX is a competing software that has also been used for over twenty years. The relatively long duration in the marketplace helps to explain the popularity among bridge engineers. The appeal of the software may also be in the relatively simple input that is necessary with the two-dimensional grid modeling, however this representation of the girder system is not as accurate as a three-dimensional finite element representation.

Another popular software in the bridge industry is LUSAS (2015), which is an acronym for London University Structural Analysis System. LUSAS was originally developed in the 1970s by Paul Lyons as part of his PhD in Civil Engineering at the Imperial College in London, UK, and by other PhD students who later added new capabilities to the program. Part of the motivation behind LUSAS was to study and understand two tragic box girder collapses: the Milford Haven Bridge in Wales in 1970, and the West Gate Bridge in Sydney, Australia, also in 1970. Paul Lyons later optimized the program at Kingston University, and co-founded Finite Element Analysis Limited in 1982 together with David Irving. LUSAS Bridge in particular has become a powerful three-dimensional finite element analysis tool for analyzing steel and concrete bridges.

Computers and Structures Inc. is a company that markets CSi Bridge (2017) which is another commonly used 3D FEA bridge engineering program. Computers and Structures Inc. was originally founded in 1975 by Ashraf Habibullah, a structural engineer from Pakistan who came to the University of California at Berkeley for his graduate studies. Habibullah continued developing programs after his time at Berkeley and founded what is now a multi-national firm that has supplied structural engineering programs to over 160 countries around the world. Besides CSi Bridge, the company markets other widely used programs such as SAP 2000 and ETABS.

LARSA 4D (2016) is another commonly used program that was initially developed in the mid-1980s by Ali Karakaplan from Turkey, who did his graduate studies at Columbia University, New York. The software can model most bridge types and includes a time-dependent staged construction analysis.

While the above software packages specifically target bridge applications, Abaqus (2017) is another program that fits into the categories of a general purpose finite element program that targets civil, mechanical, automotive, and aerospace applications. The company that markets the software was originally founded in 1978 by David Hibbitt (UK), Bengt Karlsson (Sweden) and Paul Sorensen (USA/ Ecuador). Hibbitt and Sorensen hold PhD degrees from Brown University, and Bengt Karlsson has a PhD degree from the University of Illinois at Urbana-Champaign. Abaqus has capabilities to address nonlinear behavior and situations where multiple fields interact. For example, it can conduct a thermo-mechanical analysis. In 2005, Abaqus was acquired by Dassault Systèmes, a French multinational software company. The reason that Abaqus is mentioned in this chapter is that the software was used to validate many of the modeling capabilities of UT Bridge.

2.1.2 UNIVERSITY PROGRAMS

Although it can only model single, straight, plate girder beams and columns, the release of BASP (acronym for Buckling Analysis of Stiffened Plates) represented a breakthrough in the field of structural stability (Akay, Johnson and Will 1977). Developed at the University of Texas at Austin, BASP produces a three-dimensional representation of straight structural elements, with shell elements for the web and beam elements for the flanges, and is able to conduct a linearized buckling analysis to estimate critical buckling

loads. The program originally was created for use on a mainframe computer system and had capabilities of modeling frames; however in the 1980s a smaller subset of the program that targeted individual members (columns and beams) was created for use on a personal computer. The PC-based program was updated in the 1990s. The program was a major tool in formulating or validating many of the provisions on stability bracing in the American Institute of Steel Construction (AISC) Steel Construction Manual (2017). Whether for the development of new moment magnification factors and load-height effect correction factors (Helwig, Frank and Yura 1997) or for studies on beam bracing (Yura 2001), researchers in structural stability have consistently relied on the program accuracy for their parametric studies. BASP is capable of carrying out a 2D analysis on a member comprised of plate elements that are symmetric about the plane of the plate. The software conducts an eigenvalue buckling analysis. The program cannot model tub girders, curved or multi-girder systems.

Another program developed at the University of Texas at Austin is Kurv87 (Hahn 1987). It was developed by Hahn as part of his PhD research on the analysis of curved plate girder bridges. Considering the time it was developed, Kurv87 includes remarkable features. It can model complex, curved geometries, together with a variety of loads, including moving loads. However, Hahn was not able to benefit from the capabilities of general shell elements, which had just been formulated at MIT by Prof. Bathe and his students. The general shell element is a versatile, curved element that can be used for thin and moderately thick shells and is suited both for a linear and a geometrically nonlinear analysis (Bolourchi 1979 and Dvorkin 1984). The limitations on the finite element formulation implemented by Hahn implied that the warping stresses could not be correctly predicted, and Kurv87 was abandoned after a few years, despite a promising start. Also in 1987, Fiechtl, Fenves and Frank, together with the help of Hahn, presented to the Texas

Department of Transportation a report on the use of the V-load method for approximate analysis of curved bridges (Fiechtl, Fenves and Frank 1987). The V-load method proved to be an effective method at a time where engineers could not benefit from the computational capabilities of today's computers.

Because it is capable of analyzing tub girder bridges, UT Bridge V2.2 is also a natural extension of UTrAp, which is yet another program developed at the University of Texas at Austin, this time by Topkaya (2002). Based on a three-dimensional finite element representation using a nine-noded general shell element, UTrAp can better predict the behavior of curved tub girder bridges than traditional two-dimensional grid methods. UTrAp is able to conduct both a linear elastic analysis and a linearized buckling analysis and is an efficient tool for estimating lateral truss forces during deck placement (Topkaya and Williamson 2003). As part of his doctoral research, Topkaya also conducted an extensive field monitoring study during the deck placement of a curved tub girder direct connector in Austin, Texas. Observed measurements were compared against UTrAp (Topkaya, Williamson et al. 2004). Also at the core of Topkaya's doctoral research was the estimation of the shear stud behavior at early concrete ages (Topkaya, Yura et al. 2004). The equations proposed by Topkaya were based on a large number of pushout tests reflecting the stiffness gain in the concrete as a function of time and are the basis for the shear stud stiffness implemented both in UTrAp and UT Bridge V2.2. One limitation of the software is the user-friendliness of the program layout and graphics. With UTrAp, the results displayed are mostly provided via tables, and the loading and bracing options are limited.

In 2006, Chang developed a prototype software named GT-SABRE (for Georgia Tech Structural Analysis and Bridge Evaluation). GT-SABRE is a three-dimensional finite element analysis software, but it does not use shell elements for the steel plates. Instead, it

produces a three-dimensional grid model representation of curved plate girder bridges during erection and construction using a geometrically nonlinear thin-walled beam element (Chang 2006). Advanced options are considered, such as tapered geometries, web distortion, superelevation and cross-frame detailing methods. The program capabilities are outstanding, but it comes at the cost of high complexity, making its routine implementation by the bridge industry unlikely. For the actual bridge that was modeled as a benchmark problem, Chang states: “The steel erection simulation (…) includes more than 400 steps in the finite element modeling. The total number of lines of the input file is more than 10,000”.

In 2010, Stith developed an Excel spreadsheet named UT Lift, aimed at optimizing the location of the crane lifting points on single, curved plate girders (Stith, Helwig et al. 2013). UT Lift is not a structural analysis program properly speaking but has proven to be an effective tools for erectors in ensuring the safety of their lifting methods.

UT Bridge V2.2 is actually the successor of UT Bridge V1.0, which was developed by Stith, Petruzzi, and Kim (Stith 2010). Stith mainly focused on the main processor, while Petruzzi and Kim, respectively, developed the pre-processor and post-processor. Stith developed the program in a remarkably short amount of time as part of his doctoral research at the University of Texas at Austin. His research was part of a TxDOT-funded project on the behavior of curved plate girder bridges during construction. Instead of GT-SABRE, UT Bridge V1.0 produces a three-dimensional shell representation of curved plate girder bridges. UT Bridge V1.0 was released to a wide audience of engineers and generally performs well. Nonetheless, as is common with software, some issues and limitations were identified in the years following its release. Many of the problems were fixed, resulting in subsequent versions of the program, culminating in Version 1.6. However, some of the more complicated issues with the software were not solved. Those issues included the underestimation of deflections for tight curvatures, the excessive stiffening effect of

transverse web stiffeners on the system buckling eigenvalue, and the overestimation of horizontal reactions on curved systems. Other limitations included the restrictive mesh refinement options (in particular, through the web depth), the need for the erection sequence to move from one end of the bridge to the other (for example excluding drop-in segments), and the need for the placement on skewed systems to be parallel (whereas in reality, the contractor has the choice between a parallel and a skewed placement scheme).

The author's original research target was updating UT Bridge V1.6 to fix some of the problematic issues and adding new capabilities. However, because these issues and limitations went deep into the code, and as the process of understanding and editing someone else's code is quite difficult by nature, it was decided to rewrite a new program from the beginning. Therefore, UT Bridge Version 2.0 was released in 2016 and consisted of a new preprocessor, processor, and post-processor as well as new element formulations and other features. Additional aspects of the software were updated and incorporated into Version 2.1 that was released in 2016. The current version that has yet to be released is Version 2.2. In addition to fixing some previous issues and limitations, UT Bridge V2.0-2.2 brings new capabilities, which can be regrouped into different categories. Bracing can now be provided by springs, lateral trusses, K-frames, and X-frames. Loads are not limited to self-weight but include point loads, top flange uniform loads, wind loads, and thermal loads. Boundary conditions, which were limited to default pin and roller supports in UT Bridge V1.0, include the restraint of any translational degree of freedom. Moreover, UT Bridge V2.2 can conduct a modal dynamic analysis or a geometrically nonlinear analysis, in addition to the linearized buckling analysis and linear elastic analysis already offered in UT Bridge V1.0-1.6. Finally, significant new output options can be displayed, such as cross-frame forces, stress components, and load versus displacement charts (for geometrically nonlinear analysis).

UT Bridge V2.2 therefore brings UT Bridge V1.0, UTrAp and BASP into one single program, while adding new modeling and analysis capabilities and producing model renderings that demonstrate extensive structural behavior through displaced shapes and contours.

2.2 RESEARCH ON CURVED PLATE GIRDER BRIDGES

This paragraph briefly lists some landmark or recent research projects undertaken in the field of curved plate girder bridges. As far as analysis methods are concerned, a reference literature review is available in a paper authored by Zureick and Naqib (1999). Further comparison between two-dimensional grid methods and three-dimensional finite element analyses is provided by Chavel, Sanchez et al. (2012).

Although it was conducted almost twenty years ago, the experimental study conducted by Linzell (1999) on a large-scale, curved, plate girder bridge as part of his doctoral studies for the Georgia Institute of Technology remains fundamental, as it was the first of its kind and showed how curved plate girder bridges should be instrumented, as well as limitations of the V-load method on the estimation of their behavior. Motivated by the lack of guidelines on the erection and construction of curved plate girder bridges, Linzell went on studying their behavior, trying to come up with optimized erection methods. Following the case of a curved, five-girder, six-span bridge that experienced misalignment and fit-up issues during erection, a study conducted by Bell and Linzell showed how erecting girders in pairs and using lateral bracing and temporary shoring towers could reduce bridge deformations and avoid those issues (Bell and Linzell 2007). Another study by Linzell and Sharafbayani focused on optimizing the location of temporary shoring during erection and construction to avoid excessive deformations,

recognizing that contractors are not offered any guidelines on the subject (Sharafbayani and Linzell 2012). Different configurations were tested for various erection scenarios. Another study by the same authors was conducted to evaluate the performance of skewed cross-frame configurations, where the cross-frames were rotated by an angle of approximately twenty degrees from the plane orthogonal to the girders (Sharafbayani and Linzell 2014). The performance of this unusual cross-frame layout was compared with the more traditional radial cross-frame layout. The proposed layout turned out to be effective in reducing the rotations and stresses in the girders. Reducing these rotations is important for avoiding construction issues such as fit-up and misalignment problems.

In an effort to minimize the number of cross-frames to be installed on a bridge, Helwig promoted the use of lean-on bracing for straight, skewed plate girder bridges (Herman, Helwig and Zhou 2007). Lean-on bracing is a concept that is commonly used in frames in the building industry. Within a single story, there is no need to brace all bays, which is nice from an architectural point of view in order to preserve space. Lean-on bracing in the bridge industry represents a similar concept. From a stability point of view, not all cross-frames are necessary; many X-frames or K-frames can have their top and bottom chords erected without the diagonals. The process can be highly effective, as cross-frames are the most expensive elements on a bridge and are prone to long-term fatigue issues (Herman, Helwig and Zhou 2007). A decrease in the number of cross-frames also means a faster, less expensive bridge erection and inspection. Lean-on bracing is an option that is directly available in UT Bridge V2.2.

Sanchez, under the direction of White, investigated the influence of bracing systems on the behavior of curved and skewed plate girder bridges (Sanchez 2011). His investigation included a method regarding how two-dimensional grid models could be improved to better estimate cross-frame forces (Sanchez and White 2017). Optimal cross-

frame layouts were also proposed to mitigate the effects associated with skewed supports. Another method proposed by Sanchez to enhance the structural performance of highly skewed bridges was to remove the X-frame top chord. Other findings included the effect of stay-in-place forms on the stability of bridges during erection and construction. The use of stay-in-place forms for bracing stability in the building or bridge industry was investigated by Helwig (Helwig 1994; Egilmez, Helwig and Herman 2016). In his study, Sanchez showed that stay-in-place forms have little influence when sufficient bracing is already provided by cross-frames; however, they do contribute to bridge stability if the cross-frames are insufficient.

Ozgur and White investigated the influence of the cross-frame detailing method on curved and skewed plate girder bridges (Ozgur 2011). Different detailing methods exist, depending on when the girder webs are to be plumb: the no-load fit, the steel dead load fit, and the total load fit. The issues associated with inconsistent detailing were actually first identified by Chavel and Earls (2005) at the University of Pittsburgh. Procedures to determine lack-of-fit forces were proposed, as well as guidelines for selecting a certain detailing method. For curved plate girder bridges, the no-load fit was the one recommended.

As far as the cross-frame stiffness used in finite element models, Wang and Battistini found in their doctoral work at The University of Texas that large errors can result because of the connection flexibility and member eccentricity, which can lead to an underestimation of the bridge deflections during erection and construction as well as an overestimation of the bridge stability (Battistini, Wang et al. 2016). Correction factors based on computational parametric studies and experimental tests were proposed depending on the brace type and cross-sectional properties. UT Bridge V2.2 offers an

option to have those correction factors automatically calculated by the program and included in the analysis.

As far as the process of lifting curved plate girders for bridge erection, Stith conducted a study where he measured the rotations and stresses encountered by actual girders, and compared them with finite element models (Stith, Helwig et al. 2012). The same girders were then monitored during various erection stages and construction of a direct connector in Austin, Texas (Fasl, Stith et al. 2015). This field monitoring provided an effective way to understand plate girder behavior during lifting without the need for costly specimens and experimental setups.

Finally, it is worth mentioning an interesting study on the global lateral buckling capacity of straight plate girder bridges erected using the incremental launching method (Robalino and Sanchez 2017). A slightly conservative equation was proposed to estimate the variation of the global lateral buckling capacity during launching.

2.2 RESEARCH ON CURVED TUB GIRDER BRIDGES

A significant amount of work was conducted over several years at Auburn University under the direction of Yoo. Kim studied the role of different bracing systems on the behavior of straight or curved tub girder bridges during erection and construction, including lateral bracing systems, internal K-frames and X-frames, external cross-frames, and solid diaphragms (2004). Kim showed how the axial force in the bracing systems can be evaluated by closed-form solutions. His equations are actually very close to those previously proposed by Fan and Helwig (1999 and 2002), who were among the first to recognize and estimate the magnitude of the bending and torsionally-induced forces on top lateral bracing and cross-frame systems.

As part of his PhD research at the University of Houston and then at the University of Texas at Austin, Chen conducted research on the effects of thermal loads on curved tub girder bridges (2008). A one-year-long field monitoring study was undertaken, together with experimental and finite element parametric studies. In particular, Chen investigated the effect of the guided bearings orientation on the bridge behavior under thermal loads. Chen showed that actual bridges expand and contract about a stationary point, whose location can be calculated relatively easily under certain assumptions.

Jimenez, under White's direction at the Georgia Institute of Technology, investigated curved and skewed tub girder bridge behavior during construction (Jimenez 2012). Skewed tub girder bridges are structural systems that are rarely covered. Simplified methods were proposed to account for the skewed support lines.

Currently, a study is underway at the University of Texas at Austin by Armijos and Wang to improve tub girder connection details. This research considers using asymmetric top flanges, optimizing the tub top width, and reducing the number of internal K-frames and lateral braces along tub girder bridges (Armijos, Wang et al. 2017).

2.3 GUIDELINES FOR CURVED BRIDGE ANALYSIS, ERECTION AND CONSTRUCTION

White and his former students developed a list of recommendations for the analysis and construction of curved bridges for the National Cooperative Highway Research Program (NCHRP Report No 725). The report, based on the most recent research undertaken at the Georgia Institute of Technology, the University of Texas at Austin, and other schools, discusses the use of one-dimensional, two-dimensional, and three-dimensional methods of analysis. Unless certain modifications are implemented, the first two methods are shown to be inadequate for capturing flange warping stresses and cross-

frame forces, leaving the three-dimensional finite element analysis the only method to accurately estimate bridge behavior. Other aspects, such as cross-frame detailing methods, are also addressed.

Most of the recommendations included in NCHRP Report No. 725 were actually included in the second edition of a document released by The American Association of State Highway Transportation Officials together with the National Steel Bridge Alliance. AASHTO *Guidelines for Steel Girder Bridge Analysis* (2014) provides extensive information for bridge erectors and engineers. It also contains an exhaustive literature review on different aspects of plate girder and tub girder bridge behavior.

As part of a TxDOT-funded project, Helwig, Yura, Herman, Williamson, and Li also developed a series of guidelines for tub girder bridges, which contains relevant information for all tub bridges components, such as lateral bracing, interior K-frames, external K-frames, diaphragms, and so on (Helwig, Yura et al. 2007). The document also mentions UTrAp as one of the tools available for analysis.

2.4 SUMMARY

The use of plate girders and tub girders in straight and horizontally curved bridges have been studied for decades. Significant insight on their behavior has been gained through extensive experimental and numerical studies, but there is still room for improving the erection and construction guidelines and the erection analyses utilized on a daily basis. UT Bridge V2.2 is a program combining the benefits of BASP, UT Bridge V1.0 and UTrAp, while adding new capabilities intended for the accurate analysis of those structures during erection and construction. Because this software targets the behavior during erection and construction, the software is a nice analytical tool to complement other software such

as MDX, LUSAS and LARSA 4D, which generally focus on the behavior of the completed bridge.

The next chapter provides a description of the program architecture, namely the order in which its different subroutines are called.

Chapter 3: UT Bridge V2.2 Architecture

This chapter describes the architecture of UT Bridge V2.2 and its three main components, which coincide with the order in which the different subroutines are called. The subroutines themselves are not described, except for a select few that are available in the appendices. To visually reflect the algorithmic nature of any finite element program, several flowcharts are presented. These flowcharts do not require the knowledge of a specific programming language.

3.1 Overall architecture

Typical of finite element software, UT Bridge V2.2 includes three different components: a pre-processor, a main processor, and a post-processor (Figure 3.1). The function of the individual components is as follows:

Preprocessor: to define a bridge model (geometry, boundary conditions, loads, brace points, erection or placement sequence, etc.),

Processor: to generate a three-dimensional representation of that model and solve for the bridge displacements, stresses and other quantities (cross-frame forces, support reactions, shear and moment diagrams, etc.),

Post-Processor: to display the model and plot displacement diagrams (together with shear and moment diagrams, cross-frame forces, etc.).

In UT Bridge V2.2, the pre-processor and post-processor do not directly communicate with each other. Thus, the bridge model cannot be edited in the post-processor. This arrangement is different from many commercial programs, such as ABAQUS, where the separation is less clearly defined.

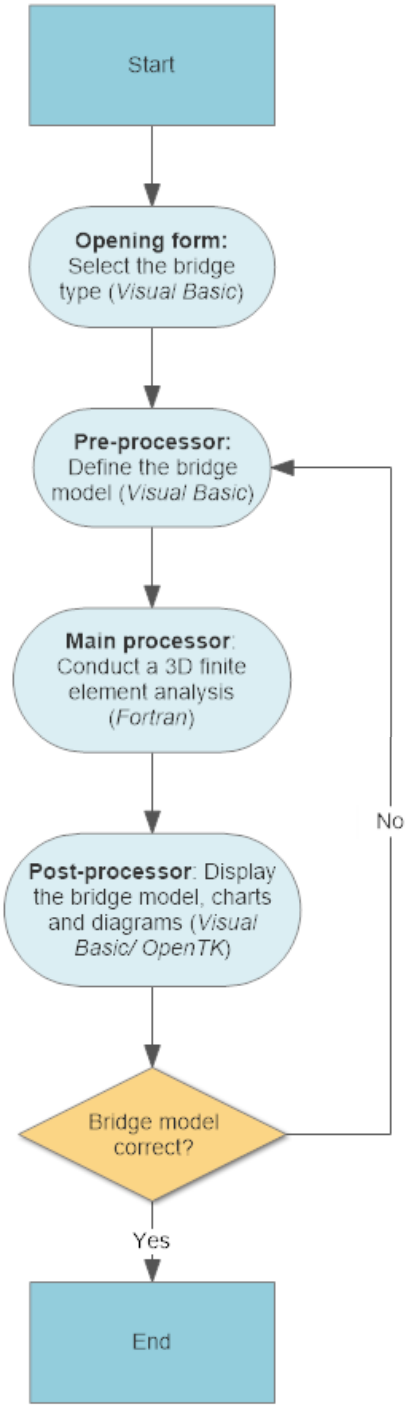

Figure 3.1: Overall program architecture

For a general purpose software such as ABAQUS, this software architecture makes sense as the potential applications are vast, from mechanical to aerospace engineering. An impressive variety of modeling options are available, which means that extensive experience and knowledge of finite element modeling techniques is required to master the use of the program. Instead, UT Bridge V2.2 specifically targets curved plate and tub girder bridges during erection and construction. A succession of forms corresponding to each bridge component can therefore make the bridge definition significantly faster than a general purpose program. Nonetheless, there is a large variety of geometries, loads, support conditions, and bracing configurations that may be encountered in practice, so these forms still need to be designed to accommodate a wide variety of cases. After a bridge model has been defined, a file containing all the relevant information is produced. This input file is read by the main processor, which is the core, or the engine, of the program. The main processor generates a three-dimensional model of the bridge, calculates and assembles the stiffness matrices and load vectors, solves for the displacements and stresses, conducts a linearized buckling analysis, modal dynamic analysis or geometrically nonlinear analysis, and produces all the output files required for the rendering of the model along with its deflected shape and the different charts and diagrams available for output. Finally, the rendering of the structure, its deflected shape and buckling modes or modal dynamic modes, as well as the different charts and diagrams, are displayed by the post-processor.

3.2 ARCHITECTURE OF THE PRE-PROCESSOR

The pre-processor, or modeling wizard, is a succession of forms written in Visual Basic using the Visual Studio integrated development environment. Visual Basic is an object-oriented language that is widely used and allows for relatively easy allocation and

manipulation of data. The first step toward defining a bridge model is to select whether to model a plate girder or a tub girder bridge, as shown in Figure 3.2.

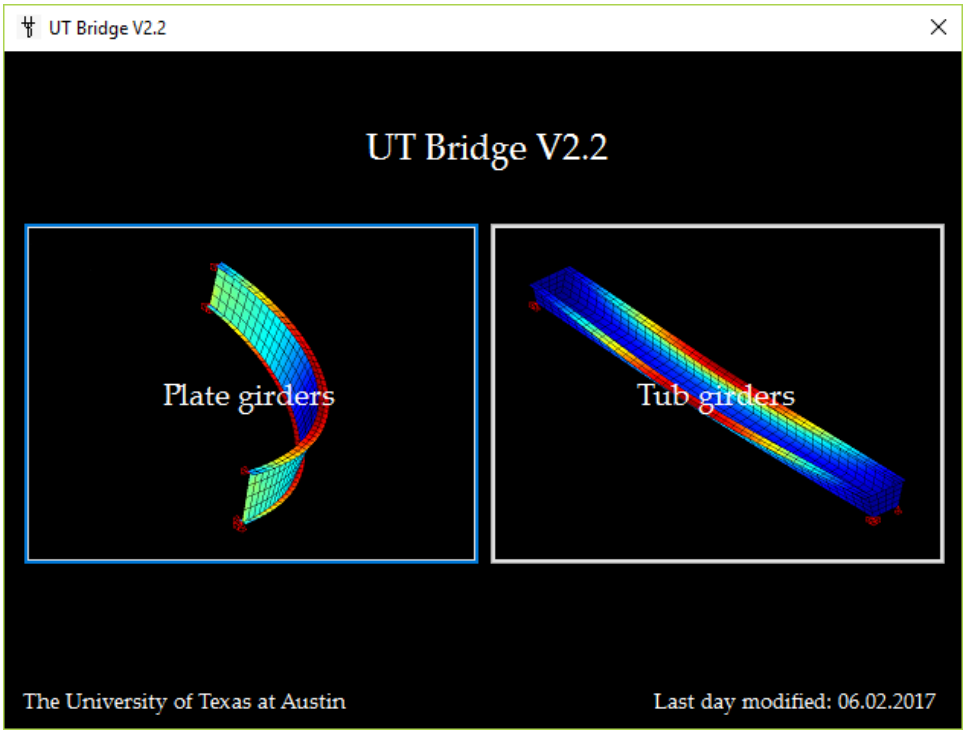

Figure 3.2: Opening form

Once a bridge type is selected, the program prompts the user to select all applicable bridge components, geometric characteristics, and requested analyses. This organization simplifies and expedites the model definition since it ensures only the relevant forms are displayed during the modeling process. The order in which the forms are displayed is also based on these characteristics. However, it is also possible to access a specific form by clicking on the right tab in the main form, which is shown in Figure 3.3. It should be noted that although the pre-processor, main processor, and post-processor have well-defined functions, they are all integrated within one program, which is an advancement over UT

Bridge V1.0-1.6. This new organization allows for optimal definition of the parameters involved in the display of the bridge model by the post-processor.

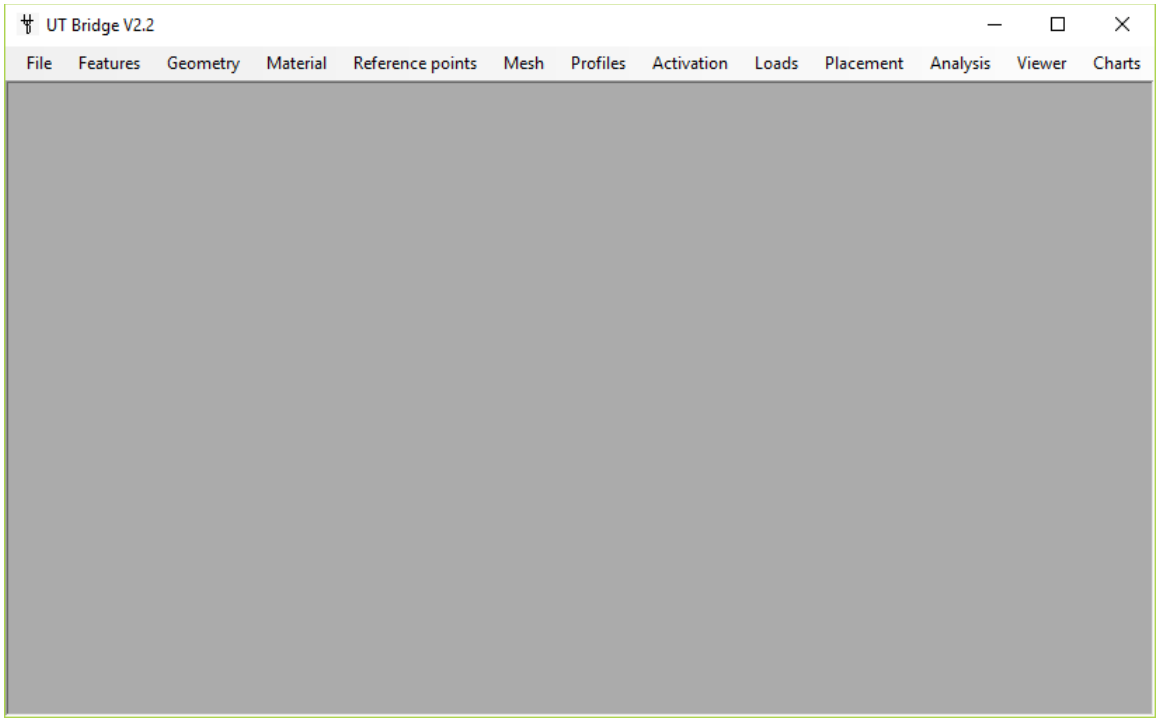

Figure 3.3: Main form of the pre-processor

Modeling of a bridge starts with defining the bridge geometry (girder length, curvature, point of tangency, etc.). Applicable supports, transverse web stiffeners, brace points, splices and transitions are then defined (Figure 3.4). Those points are also referred to as reference points. Nodal points are created at those reference points by the main processor. Because there may be a large number of reference points, a special program embedded within the pre-processor sorts the reference points and makes sure they are well defined. A tolerance is implemented to ensure the reference points are not too close to each other.

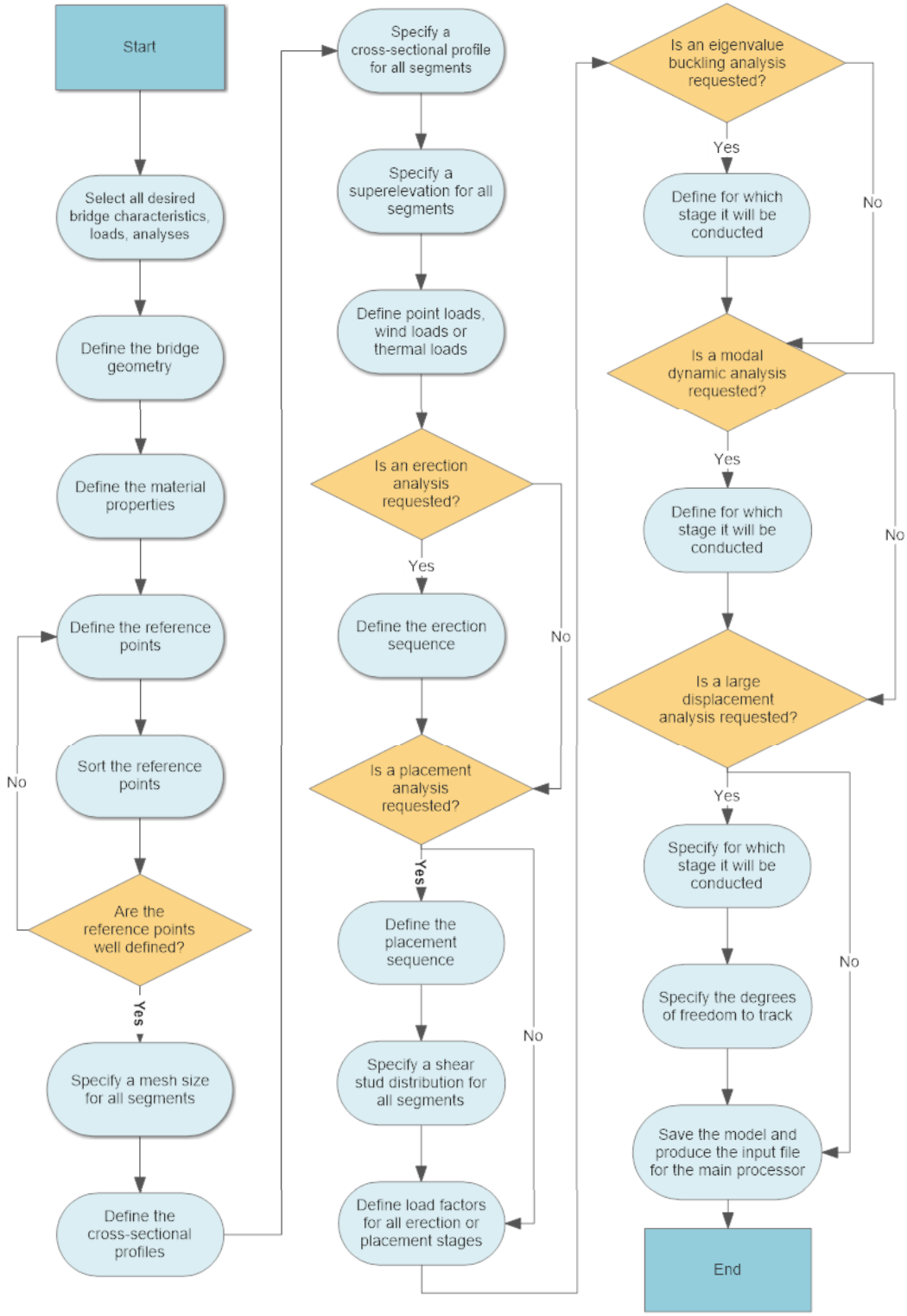

Figure 3.4: Pre-processor architecture

Once reference points are defined, the program prompts the user to specify an approximate mesh size for each segment between the reference points, then to define an erection or placement sequence. This mesh size is approximate as a further algorithm enforces a well-defined number of elements for each segment, as described in Chapter 4. Finally, the user defines the externally applied loads and selects the stage in which they are to be applied. Further, the different special analyses (linearized buckling analysis, geometrically nonlinear analysis, modal dynamic analysis) are also defined.

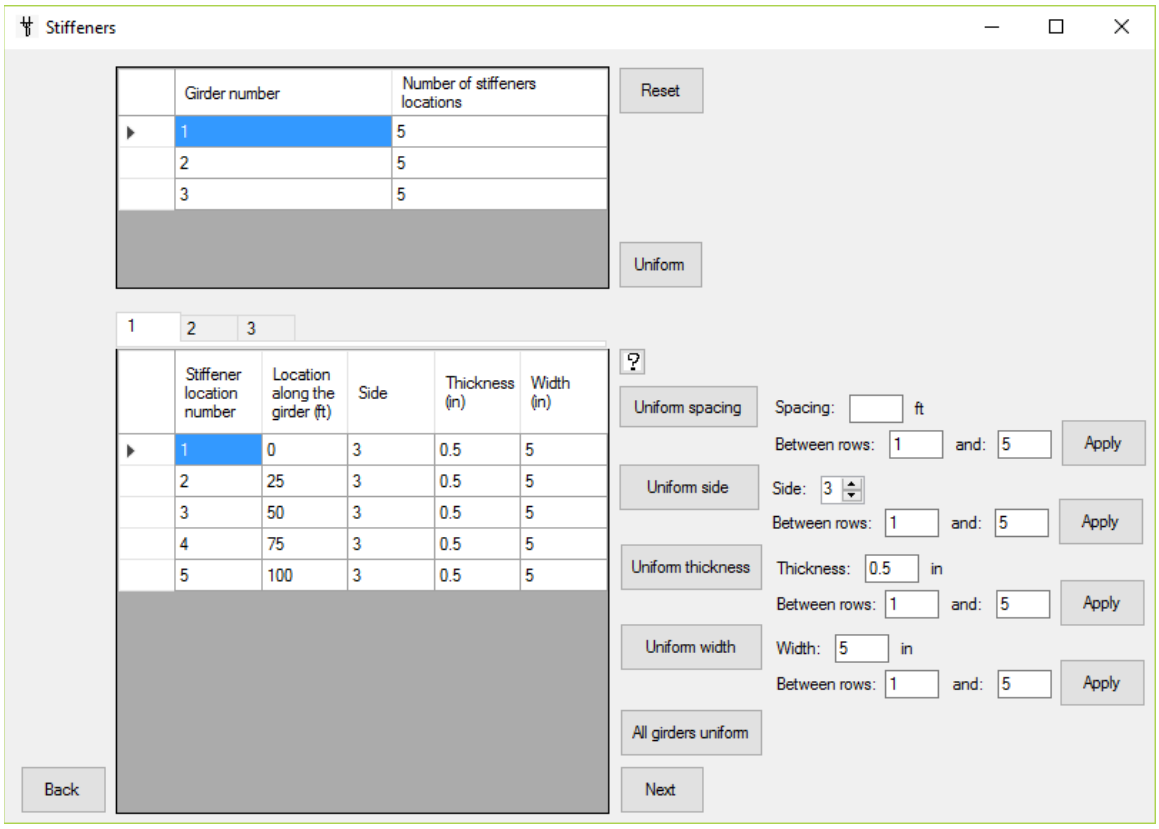

Figure 3.5: Typical form – Definition of the transverse web stiffeners

On most forms, buttons are included to speed up the modeling process. For reference points, such as transverse web stiffeners or brace points, a button enforcing

uniform spacing is provided, while another button can duplicate the reference point arrangement from the first girder to all subsequent girders (Figure 3.5). For cross-frames, buttons are available to quickly accommodate different arrangements, whether parallel, radial, or staggered. Concerning cross-sectional elevation, another button enforces a constant web depth along the bridge being modeled. This assumption is the default configuration in the program, but a user is free to specify any other cross-sectional elevation if this assumption is not valid. For cross-frame activation, meaning the stage during the erection sequence that different cross-frames are supposed to be turned on, a button is included to activate the cross-frames once the corresponding adjacent girders at the brace location are erected. This assumption is the default for the program, but for example, it is also possible to have a girder erected with cross-frames on one side only, or to have only half the cross-frames active in a particular bay.

In general, the goal for the program is to be able to accommodate any kind of geometry, bracing arrangement, and construction sequence, while offering the user default options for an efficient modeling process in the case of simple geometries or cross-frame arrangements. In addition, default values are initially assumed for material properties, support locations, and other typical bridge characteristics in order to provide guidance to the user for selecting input parameters. Help buttons provide further insight on how to fill the forms. Finally, cells can be copied from an Excel spreadsheet directly to the pre-processor and vice versa, which is useful for bridge engineers working on their bridge model directly in Excel.

Nearly half of the code involved in the pre-processor actually deals with error handling. Many errors may occur during the modeling process, whether inadvertently or by misunderstanding parameters used on specific forms. Most errors are handled directly by the pre-processor. In case an error is not detected prior to the generation of the input

file, additional error checking is implemented in the main processor during the reading of input files and in the generation of the three-dimensional analysis model.

3.3 ARCHITECTURE OF THE MAIN PROCESSOR

The main processor consists of a succession of algorithms written in Fortran 90, using the Visual Studio integrated development environment. FORTRAN is a programming language that has been used extensively in engineering applications since the 1960s. Although it may now be considered by some to have become a bit old-fashioned compared to other programming languages such as Java or Python, it nevertheless is an intuitive language that is still frequently used in engineering applications. The compiler selected for UT Bridge V2.2 is the Visual Studio FORTRAN Compiler by Intel. Working with the Intel compiler enables the use of the Intel mathematical library, which is critical to ensuring optimal solvers and eigensolvers are implemented. The main processor reads the input file generated by the pre-processor and then generates all the information required for the finite element analysis of the model (Figure 3.6). This creation of the finite element model occurs before performing the analysis itself.

It should be noted that a log file keeps track of the progress of the main processor during the bridge finite element model generation and analysis. The log file contains useful information, such as the number of nodes, elements and unrestrained degrees of freedom at each stage of the erection or placement sequence. In case a problem occurs during running of the main processor, the log file will help identify where the problem was encountered.

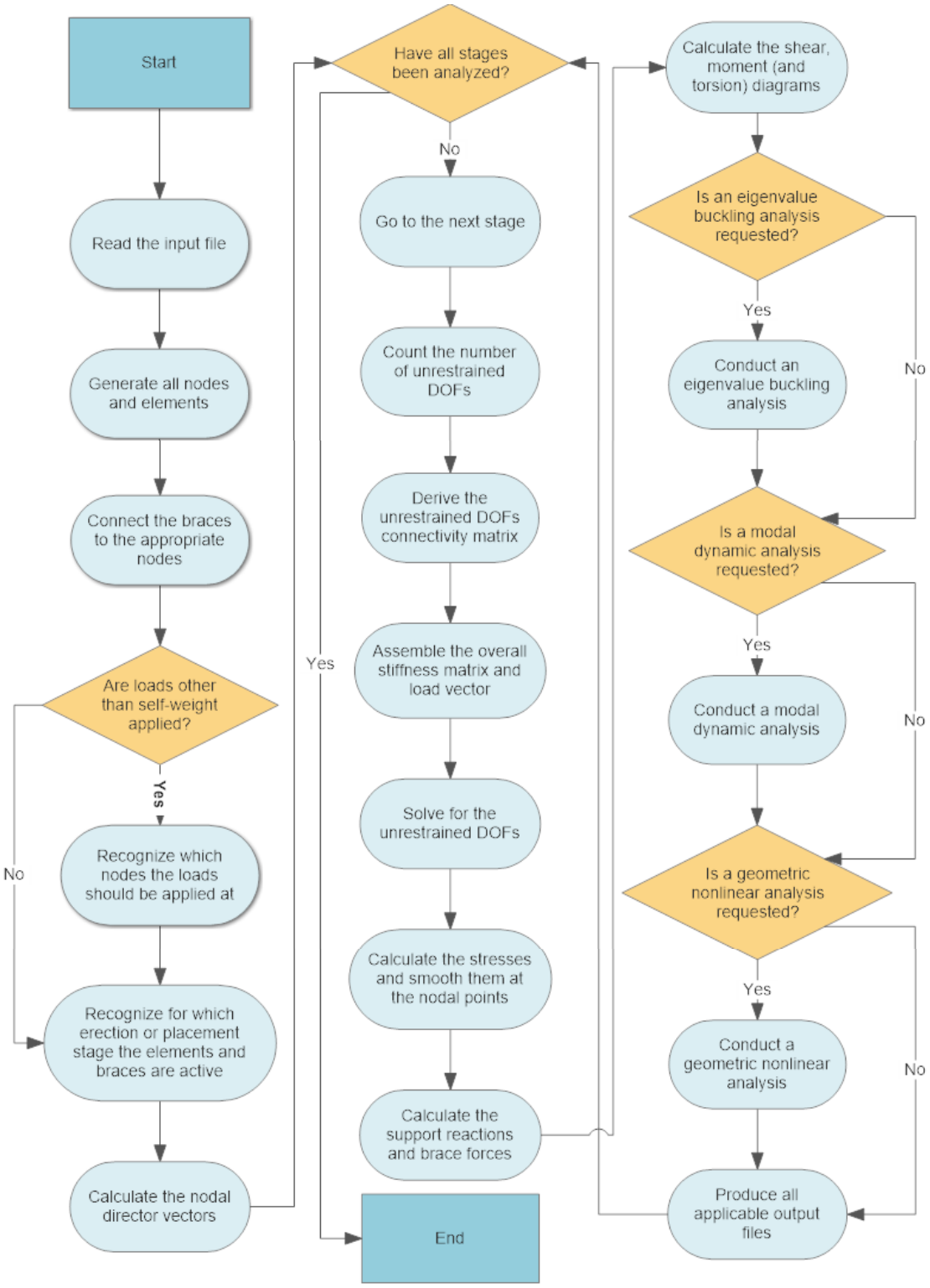

Figure 3.6: Main processor architecture

Many common issues are directly recognized by the main processor, which will issue a warning message describing the problem. Those common issues include the absence of a nodal point where a point load is to be applied, failure to assign a cross-sectional profile to a portion of the bridge, or incorrect specifications of brace points as reference points in the model. When a geometrically nonlinear analysis is required, a separate file also contains the number of iterations that were required for convergence at each load increment.

3.4 ARCHITECTURE OF THE POST-PROCESSOR

The post-processor, or rendering software, is a series of algorithms written in Visual Basic using the Visual Studio integrated development environment, which uses OpenTK. OpenTK is a graphics library that allows the use of many OpenGL functions on a Visual Basic project. OpenGL is an application programming interface for rendering three-dimensional vector graphics and has been widely used for engineering programs but also in the video game industry. An illustration of the rendering offered by the post-processor is presented in Figure 3.7, which shows the Von Mises stress superimposed on top of the deflected shape of a curved girder.

Understanding concepts such as “world” coordinates and screen coordinates is essential for the rendering process. The projection from one coordinate system to another (and vice versa) is the main challenge in rendering objects in space, moving them around, defining zoom buttons, and displaying support reactions and cross-frame forces on top of the model.

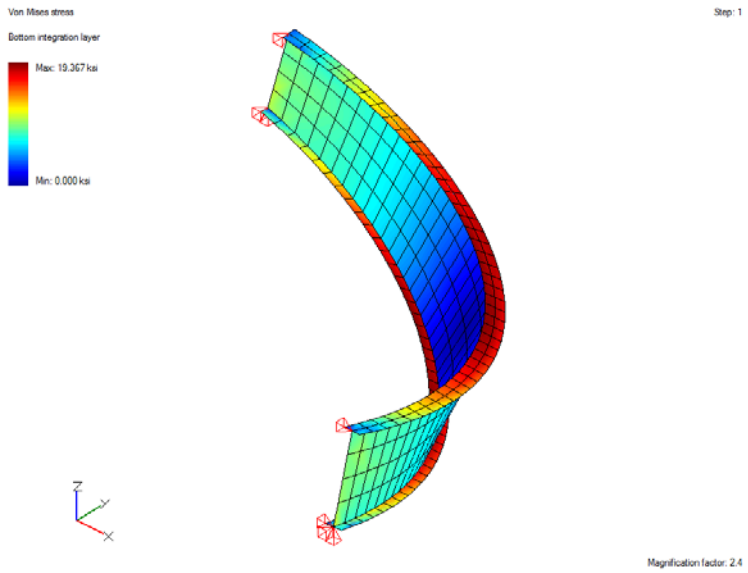

Figure 3.7: Example of a rendering in UT Bridge V2.2

A bridge model is actually projected twice, using two loops (Figure 3.8). The first loop projects the model in wireframe mode (only the edges are projected), while the second loops projects the model in filled mode (only the surfaces within the edges are projected), with a color affected to each active node of the structure. Smoothing of the colors between nodes is automatically performed by the program. Both projections are slightly offset from each other to avoid the undesirable visual effect known as “stitching”. The combination of both projections allows for a visually pleasant rendering.

By default, perspective is turned off during the model display. Nonetheless, a button is available for rendering the model with perspective effects.

The control panel allows users to move the model around, zoom in and out, and switch to any of the requested analyses (Figure 3.9). For printer-friendly renderings, it is also possible to change the default, black-color background color to white.

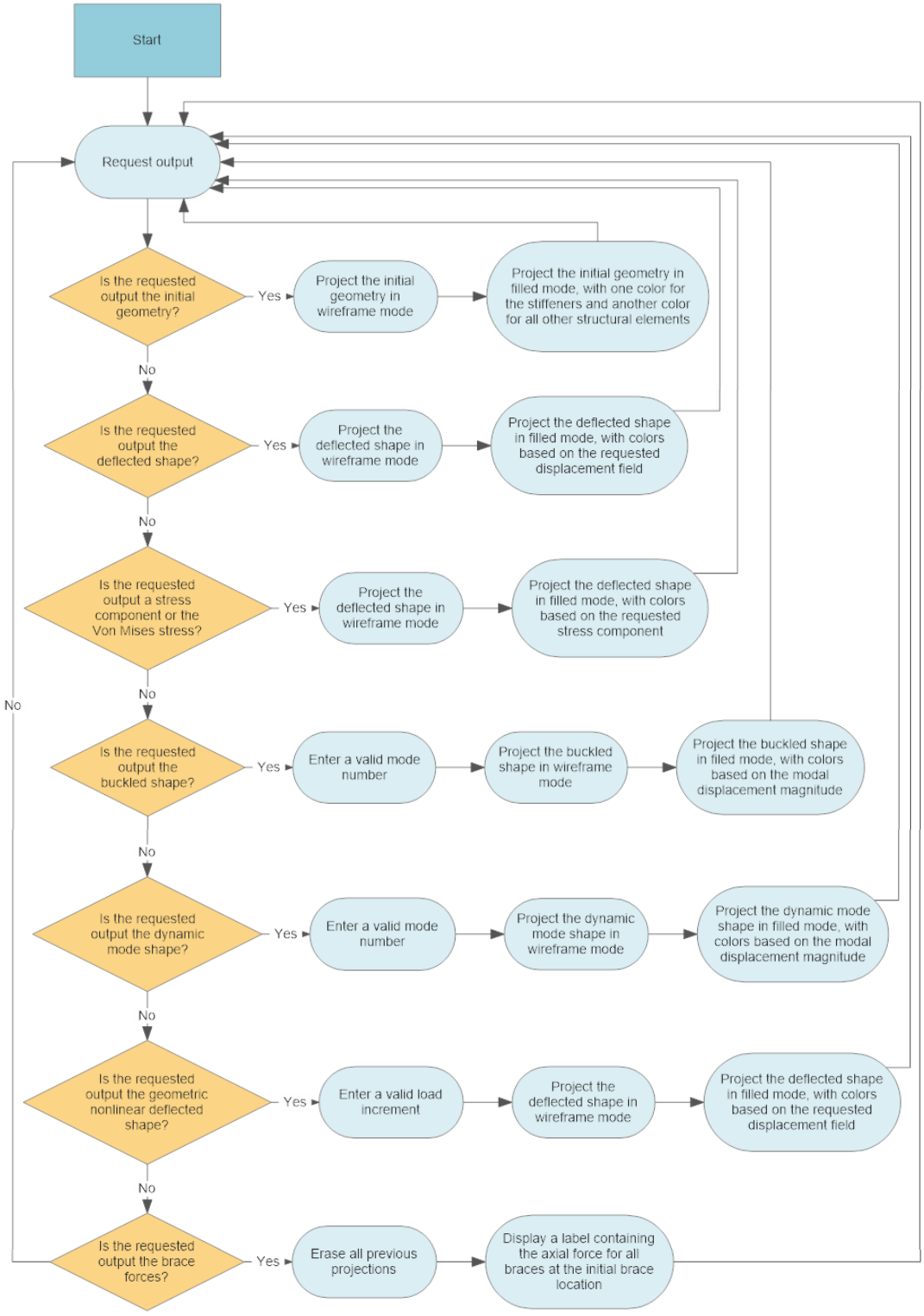

Figure 3.8: Post-processor architecture

Display of the cross-frame forces and support reactions, as well as displacement, stress, shear, torsion, and moment diagrams, is achieved by a single mouse click. The requested diagrams are automatically generated by the post-processor, so no data treatment in Excel is necessary. Finally, the program allows the user to export the bridge rendering to a picture format.

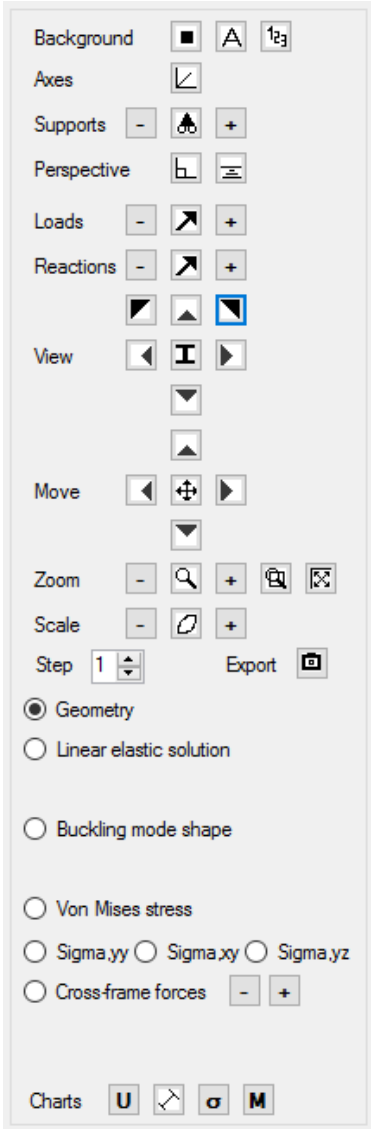

Figure 3.9: Controls available for bridge visualization

Similar to most finite element programs, the color code for contour plots follows a rainbow pattern. A color is a vector of three coordinates: red, green and blue. The conversion from a scalar to a color vector is described below. In the description, the variables “x” and “y” are used to define the scalar and vector. Referring to *x* as the scalar to be displayed, whether a displacement component (*x*-, *y*- or *z*- component), a displacement magnitude, a stress component or the Von Mises stress invariant. The variable *y(r, g, b)* is defined as the vector containing the three color coordinates, respectively the red, green, and blue components.

The scalar *x* is scaled between zero and one based on the maximum and minimum field values encountered for all nodes. A value equal to zero corresponds to the minimum nodal displacement or stress encountered, whereas a value equal to one corresponds to the maximum nodal displacement or stress encountered. The conversion from scalar to vector is shown in Figure 3.10.

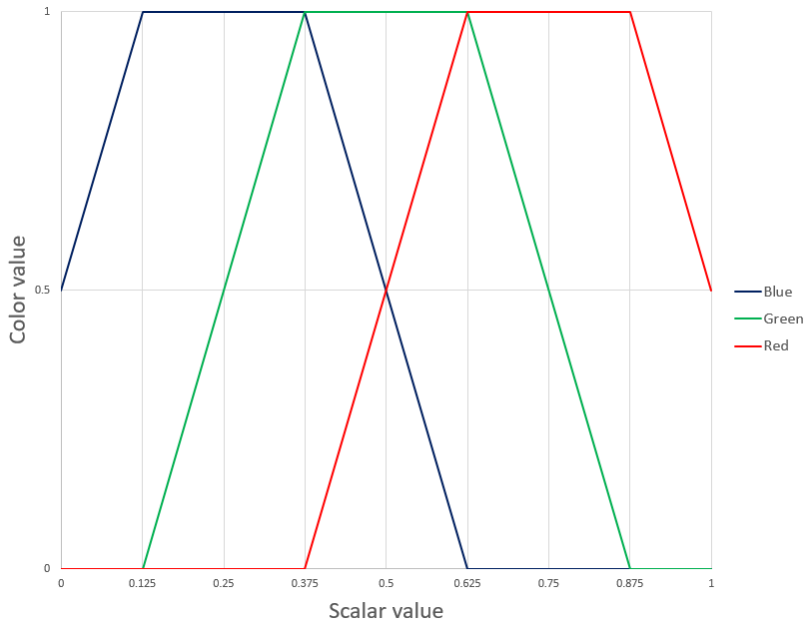

Figure 3.10: Color code

Finally, it is worth mentioning how to increase or decrease the magnitude of the deformations. If X and D are respectively defined as the initial geometry vector and the displacement (or modal displacement) vector, then the deflected shape (or the mode shape) U to be displayed is calculated as:

$$U = X + \alpha \cdot D \qquad \textbf{\textit{Equation 3.1}}$$

where α is the magnification factor.

Reversing the buckled shape or the dynamic mode shape can therefore be achieved with the following simple instruction:

$$\alpha \leftarrow -\alpha \qquad \textbf{\textit{Equation 3.2}}$$

3.5 SUMMARY

UT Bridge V2.2 is an integrated program, including the bridge modeling wizard, finite element analysis, and rendering software merged into a single program. The bridge modeling wizard is user-friendly and allows for a variety of geometric configurations, bracing arrangements, and loading options, while the rendering software is designed to produce pleasant-looking renderings. The finite element analysis is based on as a series of instructions as described in detail in Chapters 4 and 5.

Chapter 4: Finite element formulation and modeling assumptions

This chapter describes the finite element formulation and all modeling assumptions considered for the three-dimensional bridge model generation and the linear elastic analyses included in UT Bridge.

4.1 GEOMETRIC REPRESENTATION

The selection of an appropriate coordinate system is of critical importance for defining complex bridge systems, with multiple cross-frames, support lines, transitions, and other reference points. On a curved bridge plan, the reference points on a specific girder are defined using the local curvilinear coordinate system corresponding to that particular girder. The model definition in the pre-processor works the same way: reference points are defined using curvilinear coordinates, which makes the process of converting a bridge plan to a bridge model user-friendly. However, the assembly of the stiffness matrix requires the nodes to be expressed in a Cartesian coordinate system. Conversion from one coordinate system to another is achieved by the translation (Equation 4.1 and Figure 4.1):

$$\begin{pmatrix} X \\ Y \end{pmatrix}_{global} = \begin{pmatrix} X \\ Y \end{pmatrix}_{local} + T \qquad \textbf{\textit{Equation 4.1}}$$

Where T is a transformation vector that is a function of the girder line, as well as the bridge geometry. For example, for the second girder of a twin girder bridge with initial skew, T is equal to:

$$T = \begin{pmatrix} s \\ s \cdot \tan(\theta) \end{pmatrix} \qquad \textbf{\textit{Equation 4.2}}$$

where s is the girder spacing and θ the skew angle.

For the second girder of a curved, skewed twin-girder system, T is instead equal to:

$$T = (r + s) \cdot \begin{pmatrix} cos\ \alpha \\ \sin \alpha \end{pmatrix} \qquad \textbf{\textit{Equation 4.3}}$$

where r is the radius of curvature of the interior girder, and an expression for α can be determined by trigonometric considerations:

$$\alpha(\theta) = \arctan\left(\frac{\left(-r \cdot cos\ \theta + \sqrt{s^2 + 2rs + r^2 \cdot cos^2\theta}\right) \cdot sin\ \theta}{r + \left(-r \cdot cos\ \theta + \sqrt{s^2 + 2rs + r^2 \cdot cos^2\theta}\right) \cdot cos\ \theta}\right), -\frac{\pi}{2} < \theta < \frac{\pi}{2}$$

Equation 4.4

The equation for α is valid for extreme skew angles, as well as a zero skew angle:

$$\alpha(\theta)_{\theta \to \frac{\pi}{2}} \to \arctan\left(\frac{\sqrt{s^2 + 2rs}}{r}\right)$$

$$\alpha(\theta)_{\theta \to -\frac{\pi}{2}} \to \arctan\left(\frac{-\sqrt{s^2 + 2rs}}{r}\right)$$

$$\alpha(\theta)_{\theta \to 0} \to 0$$

The center of the Cartesian coordinate system selected depends on the bridge geometry (Figure 4.1). For curved systems, the center is located at the bridge center of curvature, which allows for an accurate, efficient definition of the nodal coordinates and

nodal director vectors. For all nodes, with the exception of the support nodes, the unrestrained displacement degrees of freedom correspond to the *x*-, *y*- and *z*-coordinates expressed in the Cartesian coordinate system selected. Conversely, for the support nodes, the direction of the unrestrained degrees of freedom is expressed by default in the local curvilinear coordinate system in order to model radial boundary conditions. However, for curved systems, it is also possible to deviate from purely radial restraints and specify horizontal restraints in any direction.

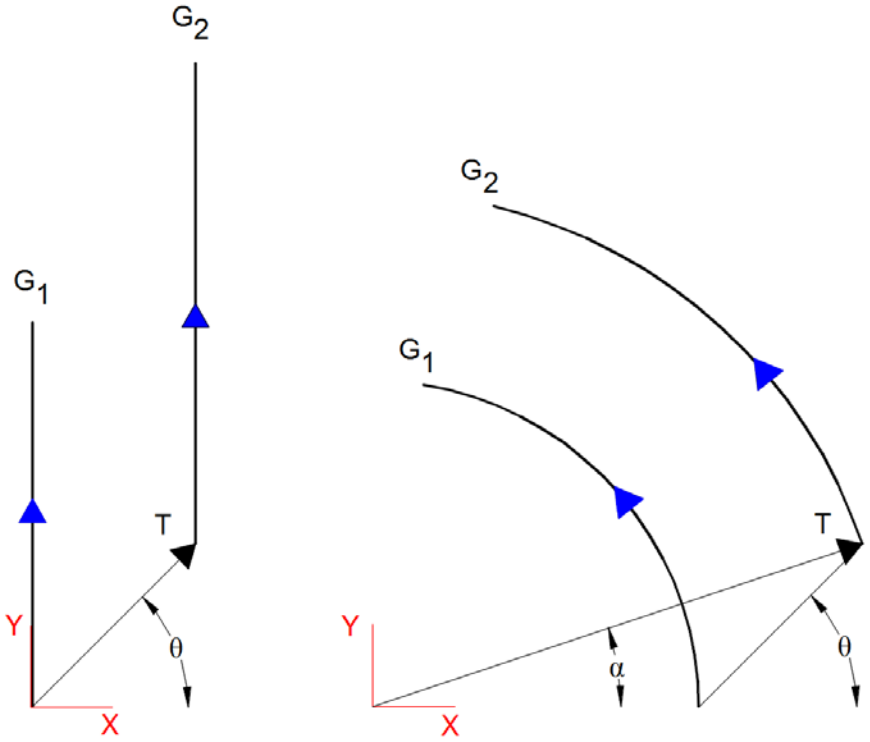

Figure 4.1: Transformation from girder local curvilinear system to global Cartesian coordinate system

4.2 NODE GENERATION

4.2.1 NODE NUMBERING

For straight systems, the nodes are generated in an “extrusion” pattern, from one end of a girder to the other. At each location along a girder, the nodes defining the cross-section are created, and the algorithm used by the program moves one step forward in the longitudinal direction. For curved systems, the nodes are generated in a similar way, using a “sweep” type pattern. It should be noted that there is no unique way to number nodes. For example, one could consider generating all the top flange nodes first, then the webs, then the bottom flanges. As far as obtaining a minimal, optimal bandwidth for the overall stiffness matrix, however, the node numbering is extremely important. The algorithm used by UT Bridge V2.2 leads to an optimal bandwidth, as the nodes at a specified location along the girder are clearly neighbors to one another. Recalling that a girder is specified by its end points and a number of reference points along its length, the node generation algorithm can be summarized in the following lines:

For all girders

    For all segments between the reference points

        Define all the nodes on the cross-section

        Move one step forward in the longitudinal direction

    Loop

Loop

4.2.2 MESHING OPTIONS

An approximate mesh size in the longitudinal direction is specified by the user during bridge modeling in the pre-processor. In most cases, this approximate mesh size will be equally specified for all girder segments. However, UT Bridge V2.2 also allows for mesh refinement anywhere along the bridge. A finer mesh provides more accurate results, but it comes at the expense of additional computation time and memory requirements. The improvement in accuracy may not be worth the additional costs. Further, a coarser mesh may be sufficiently accurate for the case being considered.

The actual mesh size implemented in the longitudinal direction is in many cases slightly different from the approximate mesh size entered by the user. This slight adjustment is to make sure a well-defined number of elements are generated between the reference points. The conversion from the approximate mesh size to the actual mesh size is summarized in the following instructions:

For all girders

For all segments between the reference points

$$Set\ L = Length\ of\ the\ segment$$

$$Actual\ mesh\ size = \frac{L}{2 \cdot \left| \frac{L}{2 \cdot Approximate\ mesh\ size} \right|}$$

Loop

Loop

where $\left| \ \right|$ is the operator for nearest integer.

Regarding meshing in the vertical or transverse directions, UT Bridge V2.2 offers the option between four and eight elements through the web depth (Figure 4.2). For tub girders, the user can also choose between four and eight elements across the bottom flange width (Figure 4.3). Specifying four or eight elements as the only options available was thought to be reasonable to avoid either poorly defined or excessively fine meshes.

For stability problems, based on the results from various parametric studies, eight elements through the web depth has been found to be sufficient for studying local buckling. It is for this reason why the default mesh size of four elements through the web depth can be increased to eight. The default mesh implemented in the program has two elements across the flange width. This value is not modifiable by the user, but this level of refinement has been found to be sufficient for capturing local flange buckling because quadratic elements are used, which allows for stress variation across the width of the flange.

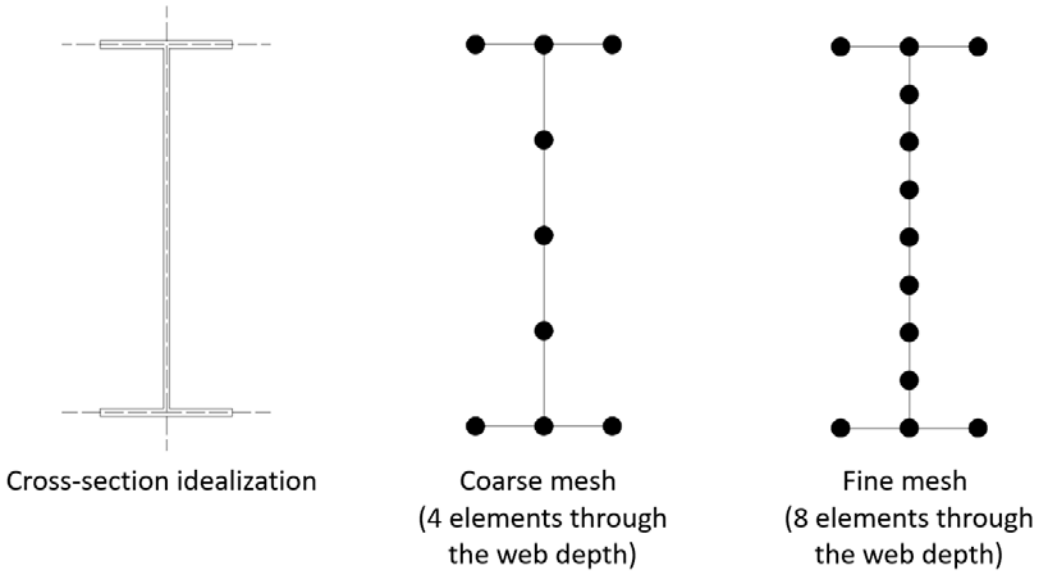

Figure 4.2: Meshing of plate girder cross-sections

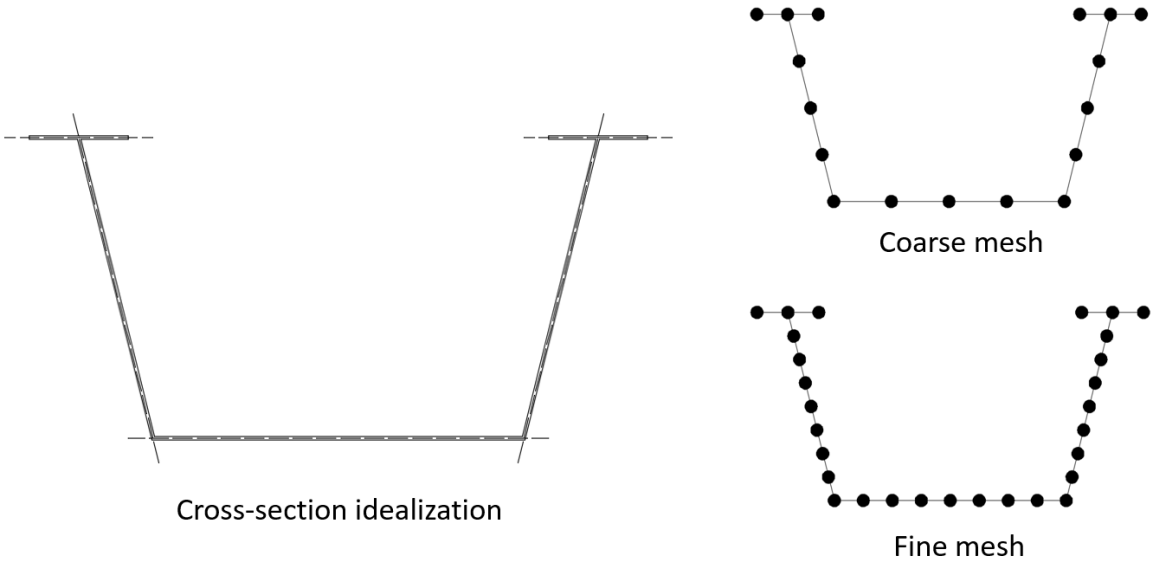

Figure 4.3: Meshing of tub girder cross-sections

4.3 SELECTION AND DESCRIPTION OF THE FINITE ELEMENT

A variety of shell elements have been discussed in the literature. For the purpose of being able to validate the program results against commercial software, analyses initially focused on several benchmark problems having well-known or closed-form solutions. ABAQUS was the commercial software selected for comparison with UT Bridge V2.2. Among the most common elements available, and for simple buckling problems, it was found that the isoparametric quadrilateral general shell element with five degrees of freedom per node and reduced integration, known as the S8R5 element in ABAQUS, provides the most accurate response (Figure 4.4). Another two reasons led to selecting the S8R5 as the validating element. First, being a curved element, the S8R5 is well suited for modeling curved geometries. Second, the S8R5 can model both thin shells and moderately thick shells, which is useful for composite bridges where thin steel plates and a moderately thick concrete deck need to be modeled. While the S8R5 within ABAQUS was selected

for the validation problems, it should be noted that the details on the element formulation are not fully available. Nonetheless, a similar element formulation with five degrees of freedom per node was implemented into UT Bridge V2.2.

The finite element selected for all the girder webs, flanges, and transverse web stiffeners, as well the concrete deck (except for some cases where triangular elements are also required) is therefore an isoparametric eight-noded general shell element, with five degrees of freedom per node. These five degrees of freedom include three displacements and two rotations, where the so-called drilling degree of freedom is not included. The element accounts for both membrane and bending effects. The element was initially developed by Ahmad, Irons and Zienkiewicz (1970) and later improved by Bathe and his students at the Massachusetts Institute of Technology. Dvorkin provides a thoroughly documented description of the element (1984).

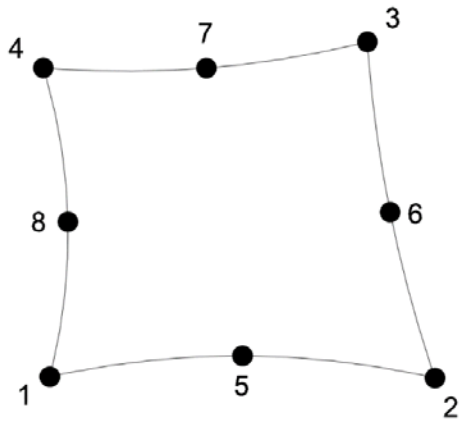

Figure 4.4: Quadrilateral isoparametric eight-noded general shell

The element uses parabolic shape functions described by Bathe (1982) and listed in Appendix B. Unlike the element proposed by Dvorkin (1984), the element implemented in UT Bridge V2.2 does not use mixed interpolation for the out-of-plane shear components.

The use of a mixed interpolation scheme is a way to prevent shear locking, which may occur for very thin shells (Dvorkin 1984). For the bridge models considered in this research, the aspect ratio (longest edge over thickness) of the shells is typically less than 100, and therefore no shear locking phenomenon was ever observed for the wide variety of cases studied.

The element considered uses four integration points per layer, with two layers through the depth of the shell. For bridges under erection and construction, the stresses are relatively low, and plasticity is typically not an issue. Consequently, two layers were considered sufficient. Reduced integration with only four points per layer proved, as expected, to be much faster than full integration containing nine points per layer, both during the stiffness matrix assembly and the stress recovery. Furthermore, a full integration scheme proved to overestimate stresses for severely curved systems. As a result, reduced integration is utilized in UT Bridge V2.2.

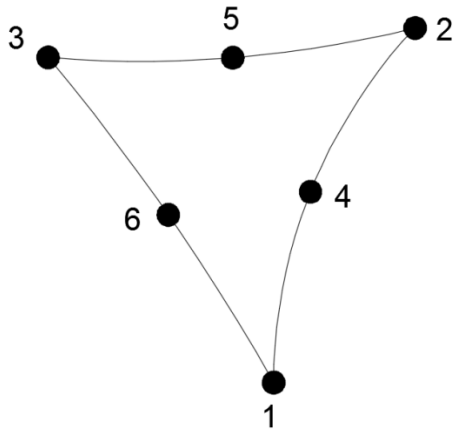

Figure 4.5: Triangular isoparametric six-noded general shell

For some placement analysis problems such as with skewed bridges, triangular elements may also be required to model parts of the concrete deck. The triangular element

selected is an isoparametric six-noded general triangular element with five degrees of freedom per node, which also uses parabolic shape functions (Figure 4.5). Reduced integration is achieved with three integration points per layer and two layers through the shell depth. The isoparametric six-noded triangle is compatible with the isoparametric eight-noded general quadrilateral. Both elements are quite similar in their formulation.

4.4 SHELL KINEMATICS

4.4.1 MERGING OF THE ROTATIONAL DEGREES OF FREEDOM

Understanding shell kinematics is critical for assembling the shell stiffness matrix. The shell kinematics require the definition of a set of three nodal director vectors at each node of the shell. In the case of plate girders, at the web-to-flange intersections or the web-to-stiffener intersections, which are plates that are orthogonal to one another, a decision has to be made on whether to merge one or both rotational degrees of freedom. Typically, shell theory recommends averaging the direction of the nodal director vectors at the intersection of shells having different orientations (Bathe 1982). This is understandable for shells intersecting each other at a small angle. For shells orthogonal to one another, however, no guidance is available, and following this method would make the shell kinematics inconsistent. Therefore, it was decided to merge rotational degrees of freedom, when permitted, in a way that keeps the kinematics of each intersecting shell properly defined. For the case of plate girders, this results in six degrees of freedom, three displacements and three rotations, for nodes located at the intersection of two orthogonal shells. The second nodal tangent director vector, V_2, is indeed the same for a flange and a web element, whereas the first nodal tangent director V_1, is the same for a web and a stiffener element (Figure 4.6).

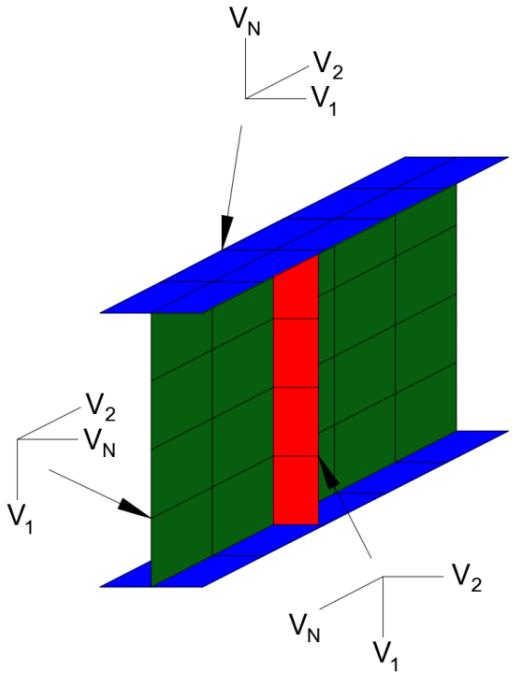

Figure 4.6: Nodal director vectors for plate girders

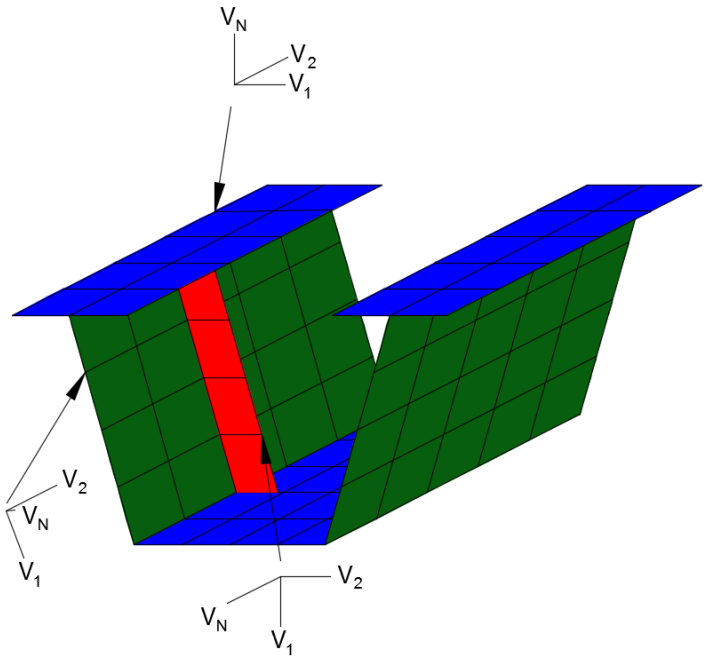

Figure 4.7: Nodal director vectors for tub girders

For the case of tub girders, the webs are inclined with respect to the flanges, so the same process cannot be directly applied, and the rotational degrees of freedom corresponding to the intersecting shells cannot always be "condensed" to only three. For nodes shared between a flange and an inclined web, the definition of six degrees of freedom, namely three displacements and three rotations, is still possible, as the second nodal tangent director vector, V_2, is the same for a flange and an inclined web element. But for nodes belonging both to an inclined web element and a transverse web stiffener element, seven degrees of freedom are necessary (three displacements and four rotations), as neither of the nodal tangent vectors match from one element to another (Figure 4.7).

The fact that seven degrees of freedom are defined at a single node may sound awkward in the field of shell theory, where six degrees of freedom is in most cases the maximum number of degrees of freedom encountered. Nonetheless, one should realize the approach taken is only a numerical procedure intended to keep the kinematics of all intersecting shells properly defined, even though no compatibility equation is enforced between the rotational degrees of freedom. From the different approaches considered, it is the only one that had led to a proper estimation of the deflections, stresses, and buckling eigenvalues.

4.4.2 DEFINITION OF THE NODAL DIRECTOR VECTORS

While there are only two vectors orthogonal to a shell's surface, one being the opposite of the other, the definition of the nodal tangent director vectors is left to the developer. A variety of configurations is possible, provided they define a right-handed coordinate system together with the normal director vector. Bathe proposed a definition that can accommodate most cases (1982). However, as UT Bridge V2.2 exclusively targets

curved steel bridge systems, it was decided to define the tangent director vectors in such a way that would take advantage of the bridge geometry. Thus, the tangent director vectors are calculated in a straightforward and accurate manner using the local curvilinear coordinate system at each node along a modeled bridge. For curved plate girder bridges (Figure 4.6), defining t as the angular coordinate in the global cylindrical coordinate system, the nodal director vectors are therefore defined by:

$$V_1^k = \begin{pmatrix} \cos t \\ \sin t \\ 1 \end{pmatrix}, V_2^k = \begin{pmatrix} -\sin t \\ \cos t \\ 1 \end{pmatrix}, V_N^k = \begin{pmatrix} 0 \\ 0 \\ 1 \end{pmatrix} \qquad \text{For flange elements}$$

$$V_1^k = \begin{pmatrix} 0 \\ 0 \\ -1 \end{pmatrix}, V_2^k = \begin{pmatrix} -\sin t \\ \cos t \\ 1 \end{pmatrix}, V_N^k = \begin{pmatrix} \cos t \\ \sin t \\ 1 \end{pmatrix} \qquad \text{For web elements}$$

$$V_1^k = \begin{pmatrix} 0 \\ 0 \\ -1 \end{pmatrix}, V_2^k = \begin{pmatrix} \cos t \\ \sin t \\ 1 \end{pmatrix}, V_N^k = \begin{pmatrix} \sin t \\ -\cos t \\ 1 \end{pmatrix} \qquad \text{For transverse web stiffener elements}$$

Equation 4.5

For curved tub girders (Figure 4.7), the nodal director vectors are defined by:

$$V_1^k = \begin{pmatrix} \cos t \\ \sin t \\ 1 \end{pmatrix}, V_2^k = \begin{pmatrix} -\sin t \\ \cos t \\ 1 \end{pmatrix}, V_N^k = \begin{pmatrix} 0 \\ 0 \\ 1 \end{pmatrix} \qquad \text{For flange elements}$$

$$V_1^k = \begin{pmatrix} \cos t \cdot \sin \zeta \\ \sin t \cdot \sin \zeta \\ -\cos \zeta \end{pmatrix}, V_2^k = \begin{pmatrix} -\sin t \\ \cos t \\ 1 \end{pmatrix}, V_N^k = \begin{pmatrix} \cos t \cdot \cos \zeta \\ \sin t \cdot \cos \zeta \\ \sin \zeta \end{pmatrix} \qquad \text{For left web elements}$$

$$V_1^k = \begin{pmatrix} -\cos t \cdot \sin \zeta \\ -\sin t \cdot \sin \zeta \\ -\cos \zeta \end{pmatrix}, V_2^k = \begin{pmatrix} -\sin t \\ \cos t \\ 1 \end{pmatrix}, V_N^k = \begin{pmatrix} \cos t \cdot \cos \zeta \\ \sin t \cdot \cos \zeta \\ -\sin \zeta \end{pmatrix} \qquad \text{For right web elements}$$

$$V_1^k = \begin{pmatrix} 0 \\ 0 \\ -1 \end{pmatrix}, V_2^k = \begin{pmatrix} \cos t \\ \sin t \\ 1 \end{pmatrix}, V_N^k = \begin{pmatrix} \sin t \\ -\cos t \\ 1 \end{pmatrix}$$ For transverse web stiffener elements

Equation 4.6

where ζ is the angle between the vertical axis and the inclined web.

For straight systems, considering a value of zero for the angular coordinate and taking the limits of the previous expressions yields the direction of the nodal director vectors.

4.4.3 THE SPECIAL CASE OF FLANGE TRANSITIONS, DAPPED ENDS AND TAPERED SECTIONS

Most steel bridges are not prismatic and have different cross-sections along their length to optimize their design. If there was a well-defined plane passing through the mid-depth of the flanges along the bridge, there would be no need for transition elements, as shells could properly be defined at their mid-depth. However, many steel bridges use constant web depths along their length, with varying flange sizes, which requires the use of transition elements. Other cross-sectional elevations are also possible; the new Tappan Zee Bridge in New York for example uses a constant girder depth instead of a constant web depth.

UT Bridge V2.2 models all flanges at their exact location, with trapezoidal elements for the web when a cross-sectional elevation gradient is observed between two adjacent segments (Figure 4.8). This modeling approach is recommended by White (NCHRP Report No 725, 2012). Because it mimics the stress flow from one flange type to another, the adopted modeling technique is deemed acceptable. At flange transitions, it is necessary to

determine whether or not to average the nodal director vectors. Both options were considered, giving little difference as far as computed displacements and stresses are concerned. For simplicity, the nodal director vectors were not merged to ensure the “exact” kinematics of each intersecting shell. Additionally, this approach also accommodates dapped ends and tapered sections.

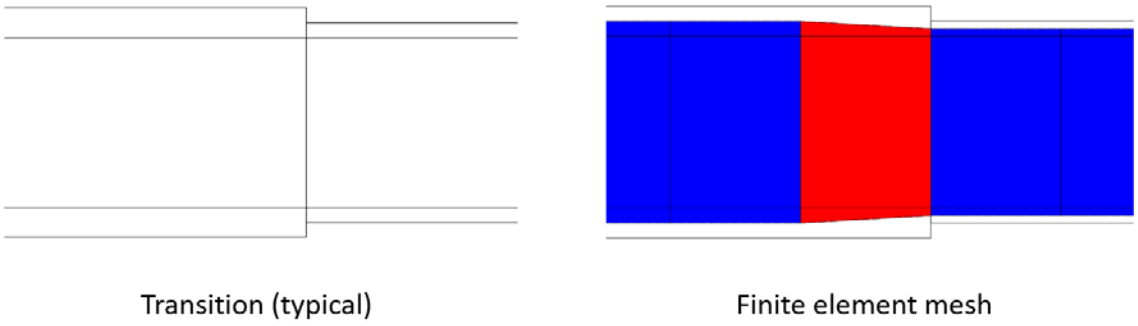

Figure 4.8: Flange transitions

Dapped ends (Figure 4.9) and tapered sections (Figure 4.10) imply the intersection of bottom flange elements at a more severe angle that flange transition elements. Averaging the nodal director vectors at the intersecting nodes led to inaccurate predictions of displacements and was dismissed as an option. For flange transitions, no averaging is performed by the program, and the kinematics of each shell is preserved.

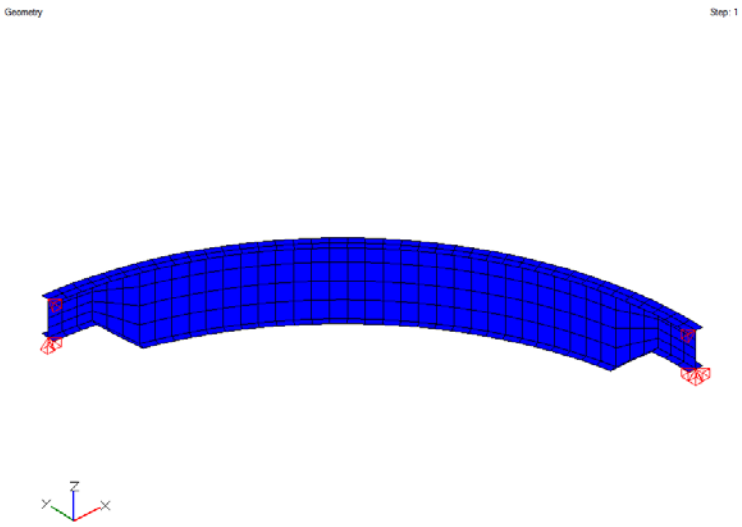

Figure 4.9: Dapped ends on a curved girder

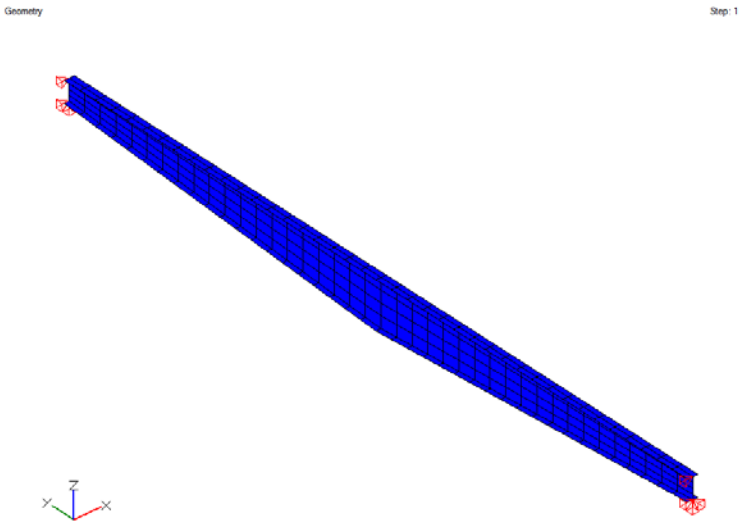

Figure 4.10: Straight tapered girder

4.4.4 CONSTRUCTION OF THE SHELL STIFFNESS MATRIX

The derivation of the shell stiffness matrix is one of the most important steps for an accurate finite element program and therefore deserves a detailed explanation. The mechanics of the general shell element was presented by Bathe and his students (Bolourchi 1979, Dvorkin 1984), and is summarized by Bathe in his reference textbook (1982). Although UT Bridge V1.0 was based on a nine-noded element, which is slightly different from the one selected in UT Bridge V2.2, Stith also recalls some of the steps involved in the stiffness matrix derivation (2010).

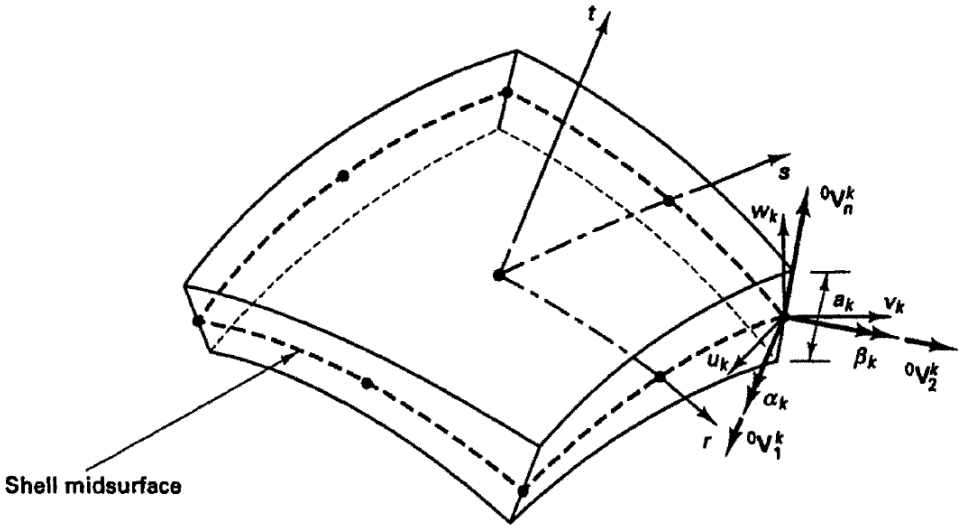

Figure 4.11: Eight-noded shell element (adapted from Bathe 1982)

Likely the most important equation is the one that expresses in Cartesian coordinates the initial position vector $\boldsymbol{X}$ of any point within the shell volume (Figure 4.11):

$$\boldsymbol{X}(r,s,t) = \begin{Bmatrix} x(r,s,t) \\ y(r,s,t) \\ z(r,s,t) \end{Bmatrix} = \sum_{k=1}^{q} h_k(r,s) \cdot \boldsymbol{X_k} + \frac{t}{2} \cdot \sum_{k=1}^{q} a_k \cdot h_k(r,s) \cdot \ {}^0\boldsymbol{V_N^k}$$

Equation 4.7

where:

r, s, t are the shell natural coordinates

$\boldsymbol{X_k}$ is the position vector in Cartesian coordinates of nodal point k

q is the number of nodes within the element (8 for a quadrilateral, 6 for a triangle)

h_k is the shape function evaluated at nodal point k

a_k is the shell thickness evaluated at nodal point k

$\boldsymbol{^0V_N^k}$ is the nodal normal director vector at nodal point k in the shell original configuration.

A similar equation for the position vector in the shell final configuration can be expressed. Subtracting both equations leads to the following expression for the displacement vector $\boldsymbol{U}$ of any point within the shell volume:

$$\boldsymbol{U}(r,s,t) = \sum_{k=1}^{q} h_k(r,s) \cdot \boldsymbol{U_k} + \frac{t}{2} \cdot \sum_{k=1}^{q} a_k \cdot h_k(r,s) \cdot \boldsymbol{V_N^k}$$

Equation 4.8

where $\boldsymbol{U_k}$ is the displacement vector of nodal point k.

Both equations are naturally very similar, as the element considered is isoparametric. In the second equation, $\boldsymbol{V_N^k}$ is the incremental normal director vector at nodal point k from the initial configuration to the final configuration. It can be expressed based on the original nodal tangent director vectors using a third equation:

$$\boldsymbol{V_N^k} = -\boldsymbol{^0V_2^k} \cdot \alpha_k + \boldsymbol{^0V_1^k} \cdot \beta_k \qquad \textbf{\textit{Equation 4.9}}$$

Where α_k and β_k are the rotations corresponding to the first and second rotational degrees of freedom, respectively. More precisely, they are the rotations at nodal point k around the $\mathbf{^0V_1^k}$ and $\mathbf{^0V_2^k}$ vectors respectively.

The three aforementioned equations are the basis for the derivation of the additional equations required to evaluate the strain-displacement matrix $\boldsymbol{B}$. The strain-displacement matrix is a 6×40 matrix for quadrilateral elements or a 6×30 matrix for triangular elements. Columns number 5(k-1)+1 up to 5(k-1)+5, corresponding to the five degrees of freedom at nodal point k, are shown below. Empty positions correspond to a value of 0.

$$\boldsymbol{B} = \begin{bmatrix} \cdots & \partial h_k/\partial x & & & g_{1x}^k G_x^k & g_{2x}^k G_x^k & \cdots \\ \cdots & & \partial h_k/\partial y & & g_{1y}^k G_y^k & g_{2y}^k G_y^k & \cdots \\ \cdots & & & \partial h_k/\partial z & g_{1z}^k G_z^k & g_{2z}^k G_z^k & \cdots \\ \cdots & \partial h_k/\partial y & \partial h_k/\partial x & & g_{1x}^k G_y^k + g_{1y}^k G_x^k & g_{2x}^k G_y^k + g_{2y}^k G_x^k & \cdots \\ \cdots & \partial h_k/\partial z & & \partial h_k/\partial x & g_{1x}^k G_z^k + g_{1z}^k G_x^k & g_{2x}^k G_z^k + g_{2z}^k G_x^k & \cdots \\ \cdots & & \partial h_k/\partial z & \partial h_k/\partial y & g_{1y}^k G_z^k + g_{1z}^k G_y^k & g_{2y}^k G_z^k + g_{2z}^k G_y^k & \cdots \end{bmatrix}$$

Equation 4.10

where:

$$\frac{\partial h_k}{\partial x} = J_{11}^{-1} \cdot \frac{\partial h_k}{\partial r} + J_{12}^{-1} \cdot \frac{\partial h_k}{\partial s} \qquad \frac{\partial h_k}{\partial y} = J_{21}^{-1} \cdot \frac{\partial h_k}{\partial r} + J_{22}^{-1} \cdot \frac{\partial h_k}{\partial s} \qquad \frac{\partial h_k}{\partial z} = J_{31}^{-1} \cdot \frac{\partial h_k}{\partial r} + J_{32}^{-1} \cdot \frac{\partial h_k}{\partial s}$$

Equation 4.11

$$\mathbf{g_1^k} = -\frac{1}{2} a_k \, \mathbf{^0V_2^k} \qquad \mathbf{g_2^k} = +\frac{1}{2} a_k \, \mathbf{^0V_1^k}$$

Equation 4.12

$$G_x^k = t \cdot \frac{\partial h_k}{\partial x} + J_{13}^{-1} \cdot h_k \qquad G_y^k = t \cdot \frac{\partial h_k}{\partial y} + J_{23}^{-1} \cdot h_k \qquad G_z^k = t \cdot \frac{\partial h_k}{\partial z} + J_{33}^{-1} \cdot h_k$$

Equation 4.13

The formulation of the displacement derivatives requires the use of the Jacobian matrix ($\boldsymbol{J}$) to transform them from the shell natural coordinate system to the global Cartesian coordinate system. The Jacobian matrix is defined as:

$$\boldsymbol{J}(r,s,t) = \begin{bmatrix} \frac{\partial x}{\partial r} & \frac{\partial y}{\partial r} & \frac{\partial z}{\partial r} \\ \frac{\partial x}{\partial s} & \frac{\partial y}{\partial s} & \frac{\partial z}{\partial s} \\ \frac{\partial x}{\partial t} & \frac{\partial y}{\partial t} & \frac{\partial z}{\partial t} \end{bmatrix}$$

Equation 4.14

The simplicity of the equation giving the position vector of any point within the shell is easily differentiable to yield the following expression for the first column of the Jacobian matrix:

$$\frac{\partial x}{\partial r}(r,s,t) = \sum_{k=1}^{q} \frac{\partial h_k}{\partial r}(r,s) \cdot \left(x_k(r,s) + \frac{t}{2} \cdot a_k \cdot {}^{0}V_N^k \right)$$

Equation 4.15

$$\frac{\partial x}{\partial s}(r,s,t) = \sum_{k=1}^{q} \frac{\partial h_k}{\partial s}(r,s) \cdot \left(x_k(r,s) + \frac{t}{2} \cdot a_k \cdot {}^{0}V_N^k \right)$$

Equation 4.16

$$\frac{\partial x}{\partial t}(r,s,t) = \frac{1}{2} \cdot \sum_{k=1}^{q} a_k \cdot h_k(r,s) \cdot {}^{0}V_N^k$$

Equation 4.17

The other two columns of the Jacobian matrix are derived in the same way.

Finally, the stress-strain law matrix $\boldsymbol{C_{local}}$ in the shell natural coordinate system is expressed in Equation 4.18, assuming a linear elastic material, where k is the shear correction factor (Bathe 1982). Again, empty coefficients correspond to a value of 0. For bridges under erection and construction, stresses are typically low, so the use of a linear elastic material stress-strain law for steel is acceptable. The case of reinforced concrete is described in a subsequent paragraph.

$$\boldsymbol{C_{local}} = \frac{E}{1-\nu^2}\begin{bmatrix} 1 & \nu & & & & \\ \nu & 1 & & & & \\ & & 0 & & & \\ & & & \frac{1-\nu}{2} & & \\ & & & & k\cdot\frac{1-\nu}{2} & \\ & & & & & k\cdot\frac{1-\nu}{2} \end{bmatrix}$$

Equation 4.18

The third column of the stress-strain matrix is made of zeros only. This relates to the assumption made in the development of the general shell element, which considers that the stress normal to the shell surface is equal to zero. Transforming the stress-strain matrix from the shell natural coordinate system ($\boldsymbol{C_{local}}$) to the Cartesian global coordinate system ($\boldsymbol{C}$) is achieved through the use of a rotation matrix based directly on the Jacobian matrix, which is well documented in Bathe (1982) and is not described here.

Based on the strain-displacement matrix $\boldsymbol{B}$, the shell stiffness matrix can be assembled by integrating the $\boldsymbol{B^T \cdot C \cdot B}$ matrix product over the shell volume:

$$\boldsymbol{K} = \int \boldsymbol{B}^T \cdot \boldsymbol{C} \cdot \boldsymbol{B} \cdot dV \qquad \textit{Equation 4.19}$$

The integration is performed numerically over the Gauss points on both integration layers, using $\alpha_{i,j}$ as weight coefficients:

$$\boldsymbol{K} = \sum_{i,j} \alpha_{i,j} \cdot (\boldsymbol{B}^T \cdot \boldsymbol{C} \cdot \boldsymbol{B})_{i,j} \qquad \textit{Equation 4.20}$$

4.4.5 THE USE OF RADIAL BOUNDARY CONDITIONS

For curved bridges, the local curvilinear coordinate system is selected as the default case when restraining any of the horizontal displacements at a node. This approach allows representing the boundary conditions encountered on curved bridges in a realistic manner. The orientation of the restraints actually plays a significant role in the behavior of a bridge under thermal loads (Chen 2008). Accordingly, the program allows for any support orientation, though only the case of radial supports is presented here. For a shell element containing a corner node that is partially or totally restrained, the stiffness matrix, which is originally assembled in the global coordinate system, must be transformed to the local curvilinear coordinate system. This transformation is achieved by a rotation matrix $\boldsymbol{T}$. An example is given in Figure 4.12, where the radial displacement at nodal point number 4 is to be restrained.

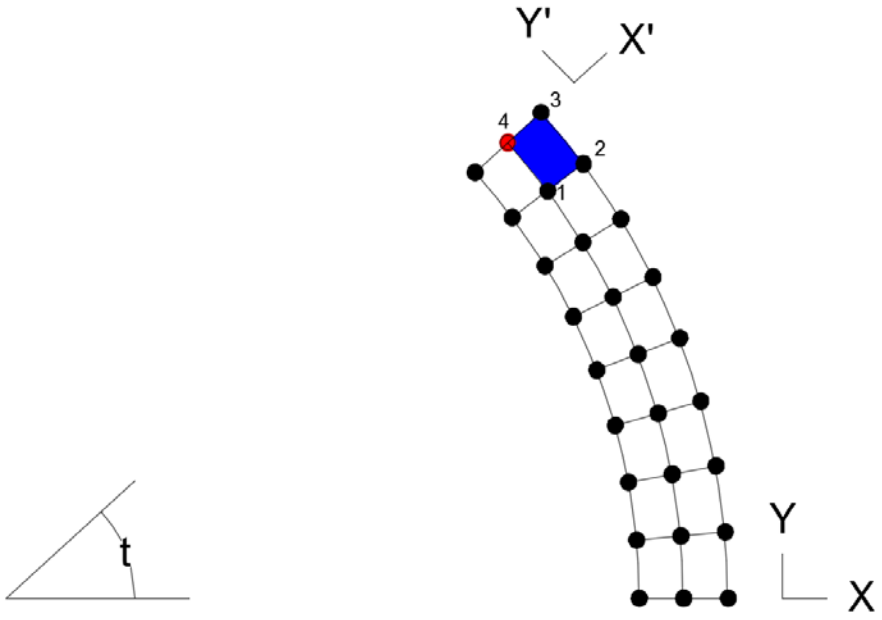

Figure 4.12: Radial boundary conditions (top view) – Example

The displacements in the global Cartesian coordinate system $\begin{Bmatrix} u_4 \\ v_4 \end{Bmatrix}$ are converted to the nodal local curvilinear coordinate system $\begin{Bmatrix} u'_4 \\ v'_4 \end{Bmatrix}$, using:

$$\begin{Bmatrix} u_4 \\ v_4 \end{Bmatrix} = \begin{bmatrix} \cos t & -\sin t \\ \sin t & \cos t \end{bmatrix} \cdot \begin{Bmatrix} u'_4 \\ v'_4 \end{Bmatrix} \qquad \textbf{\textit{Equation 4.21}}$$

As radial boundary conditions are enforced, the shell stiffness matrix is transformed using the following equations:

$$\boldsymbol{K'_{sh}} = \boldsymbol{T}^T_{40x40} \cdot \boldsymbol{K_{sh}} \cdot \boldsymbol{T}_{40x40} \qquad \textbf{\textit{Equation 4.22}}$$

where:

$$\boldsymbol{T}_{40x40} = \begin{bmatrix} \boldsymbol{I}_{5x5} & & & & & & & \\ & \boldsymbol{I}_{5x5} & & & & & & \\ & & \boldsymbol{I}_{5x5} & & & & & \\ & & & \boldsymbol{T}_{5x5} & & & & \\ & & & & \boldsymbol{I}_{5x5} & & & \\ & & & & & \boldsymbol{I}_{5x5} & & \\ & & & & & & \boldsymbol{I}_{5x5} & \\ & & & & & & & \boldsymbol{I}_{5x5} \end{bmatrix} \qquad \textit{Equation 4.23}$$

with $\boldsymbol{I}_{5x5}$ denoting the identity matrix, and $\boldsymbol{T}_{5x5}$ being equal to:

$$\boldsymbol{T}_{5x5} = \begin{bmatrix} \cos t & -\sin t & & & & \\ \sin t & \cos t & & & & \\ & & 1 & & & \\ & & & 1 & & \\ & & & & 1 & \end{bmatrix} \qquad \textit{Equation 4.24}$$

Other cases are treated in a similar way, as the $\boldsymbol{T}_{40x40}$ transformation matrix is simply a function of the node being restrained. For support orientations that differ from the radial orientation, the angular coordinate t needs to be replaced by the actual restraint orientation, and the transformation matrix is assembled similarly.

4.5 MODELING OF THE TRANSVERSE WEB STIFFENERS AND DIAPHRAGMS

Transverse web stiffeners and internal or external diaphragms in tub girders are modeled in a similar way. Each transverse web stiffener is modeled with either four or eight shell elements, depending on the number of elements through the web depth as previously specified by the user. Transverse web stiffeners can be specified on either side of the web. This flexibility is useful for fascia girders, which for aesthetic reasons typically have transverse web stiffeners on one side only, except at the supports where they are

required to prevent web distortion due to large support reactions. The transverse web stiffeners are attached to the web only, and the displacement degrees of freedom corresponding to the intersecting nodes are merged. Merging of the rotational degrees of freedom is described in §4.4.1. For plate girders, merging is considered for the rotational degree of freedom along the longitudinal axis, which results in six degrees of freedom at the node in question. For tub girders, as explained in §4.4.1, merging was considered and found not to be accurate, which results in a number of seven degrees of freedom at the node. It should be noted that in the finite element representation produced by the program, the transverse web stiffeners are not attached to the flanges. Accordingly, this is not quite realistic, as transverse web stiffeners are typically welded to the flanges, at least partially. But as plate girders are often singly-symmetric only, merging the stiffener nodes and the flange nodes would have meant considering a trapezoidal shape for the stiffener. Additional nodes across the flange width could be generated to keep a rectangular shape for the stiffener, but this would substantially increase the complexity of the model. Initially, transverse web stiffeners and flanges were actually connected. When the case of singly-symmetric girders arose, however, the stiffener trapezoidal shape was considered unacceptable, and that connection was not considered further. This absence of connection means that in the finite element bridge model, transverse web stiffeners do provide web distortion restraint, but little flange warping restraint. The effect on the bridge behavior of enforcing (or not) the stiffener-to-flange connection was computationally tested, and the results obtained with both approaches were quite comparable, both for the deflected shape of the structure and the buckling eigenvalue. Enforcing the connection proved to increase the buckling eigenvalue by about five percent for the most severe cases considered.

For tub girders, in addition to transverse web stiffeners, UT Bridge V2.2 offers the option of specifying interior or external diaphragms. Similarly to transverse web stiffeners,

the diaphragms are connected to the webs and the bottom flange only. In this case, however, this modeling approach closely mimics reality, as diaphragms are typically not welded to the top flanges.

4.6 MODELING OF THE BRACES

UT Bridge V2.2 offers a variety of bracing options. For plate girders, these options include X-frames, K-frames, lateral trusses, and springs. For tub girders, they include interior and external K-frames, interior X-frames, struts, lateral trusses, and springs. Interior or external diaphragms also act as braces and are described in the previous section.

All brace types are modeled with three-dimensional linear truss elements, considering axial stiffness only (Figures 4.14, 4.15, 4.16 and 4.17). For plate girder bridges containing K-frames, local instability at the node where both diagonal chords intersect was initially observed. This result is expected because that node has three displacement degrees of freedom only and no stiffness perpendicular to the member axes (unless large deflections are considered). This local instability issue does not affect the overall bridge behavior, and is prevented by implementing a kinematic constraint at the node, which stipulates that the displacement at the node is equal to the average of the neighboring nodal displacements. The constraint, however, impacts the distribution of the forces within the K-frames: the axial forces in both horizontal chords are equal, which is not true in reality.

For all brace types aside from springs, the derivation of the brace stiffness matrix and its assembly into the overall stiffness matrix is described schematically in the following instructions:

For all braces

For all the brace chords

Compute the chord stiffness matrix in the chord local coordinate system

Transform the chord stiffness matrix to the global coordinate system

Assemble the chord stiffness matrix into the brace stiffness matrix

Loop

Assemble the brace stiffness matrix into the overall stiffness matrix

Loop

For X-frames, UT Bridge V2.2 offers the option to consider lean-on bracing, which means that only the top and bottom chords are modeled (Figure 4.13).

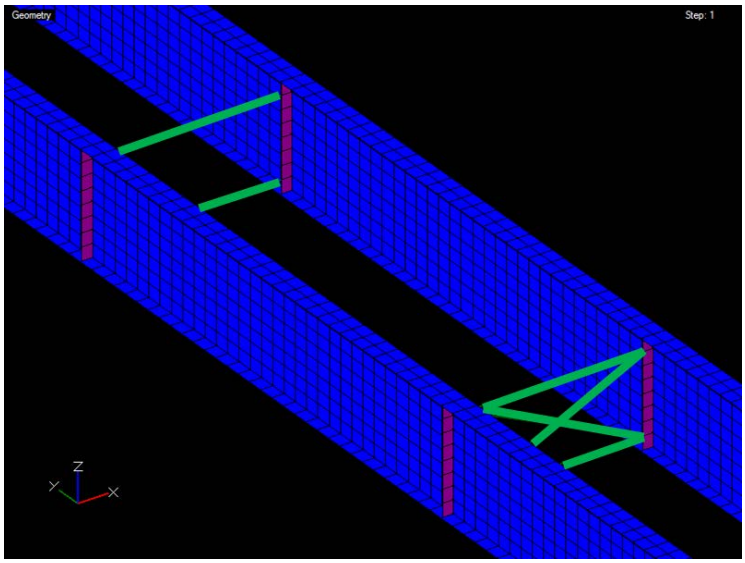

Figure 4.13: Lean-on bracing

In addition, the program offers the option to implement stiffness correction factors to account for connection flexibility (Battistini et al. 2016). The correction factor derived by Battistini and implemented in the program is equal to:

$$R = 1.062 - 0.087\frac{S}{h_b} - 0.159\bar{y} - 0.403t \qquad \text{For X-frames} \qquad \textbf{\textit{Equation 4.25}}$$

$$R = 0.943 - 0.042\frac{S}{h_b} - 0.048\bar{y} - 0.420t \qquad \text{For K-frames} \qquad \textbf{\textit{Equation 4.26}}$$

Where S is the girder spacing, h_b is the depth of the cross-frame, $\bar{y}$ is the member eccentricity, and t is the member thickness.

When this option is selected, the program implements those correction factors by multiplying the cross-sectional area initially specified by the user by the appropriate correction factor, in order to obtain a reduced cross-sectional area.

Connecting the braces to the girders depends on the brace type. X-frames and K-frames (Figures 4.14 and 4.15) are attached to the transverse web stiffeners. More precisely, they are attached to the mid-edge node of the upper and lower elements modeling the transverse web stiffener. This modeling decision is slightly different from a more common approach, where braces are attached to the nodes located at the intersection between flanges and webs. Both methods actually give comparable results, as the lines of action tend align with the flange-to-web nodes. It should be noted, however, that attaching a truss element to a mid-edge node is not directly applicable in ABAQUS, which requires finer meshing in the vertical direction to match equivalent brace locations. A long-term goal for UT Bridge V2.2 could be to specify, if desired, the exact brace location along the

web depth, which could be implemented either by constraint equations or the slight displacement of the transverse web stiffeners' external nodes prior to attaching the brace.

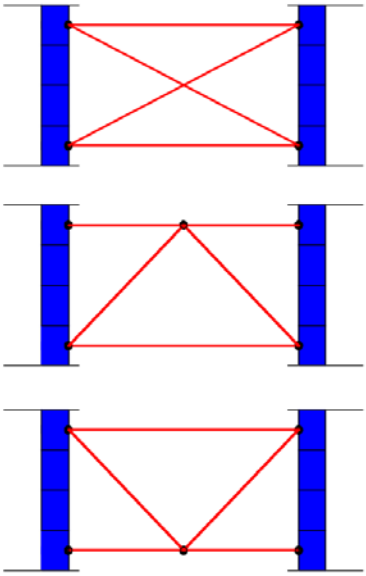

Figure 4.14: Plate girder bracing: X-frame (top), inverted K-frame (middle), regular K-frame (bottom)

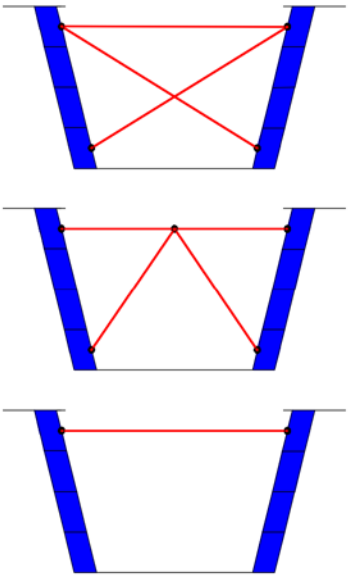

Figure 4.15: Tub girder bracing: X-frame (top), K-frame (middle), strut (bottom)

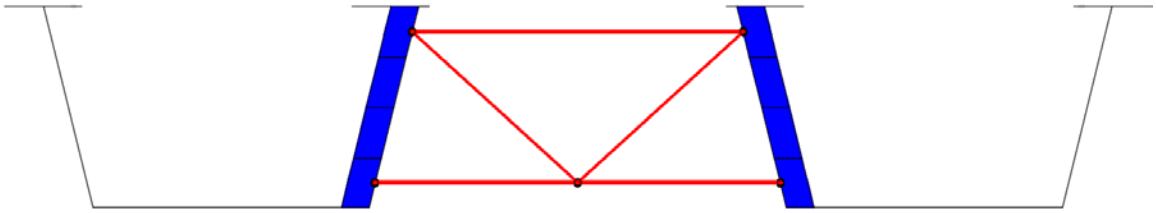

Figure 4.16: Tub girder external bracing (K-frame)

Lateral trusses are attached to the flange edges (Figure 4.17). Again, this modeling decision slightly differs from a more common approach where these braces are connected at the junction between flanges and webs. Both methods yield comparable results. For the case of tub girders, struts are attached to stiffeners and are modeled like interior K-frames (with no diagonals), and external K-frames are attached to external stiffeners (Figure 4.16).

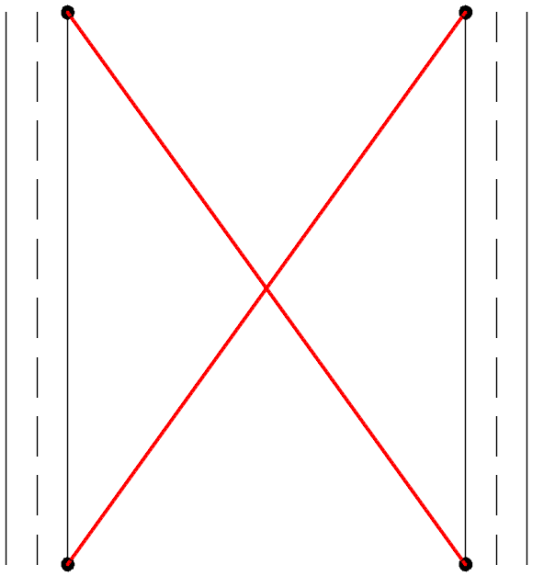

Figure 4.17: Lateral bracing (either between adjacent plate girders or on tub girders)

It should be noted that braces are defined using a no-load fit detailing method. This means that the braces are attached to the girders in their initial, undeformed geometry. Thus, the whole model is assembled before any external load is turned on, including

gravity. The no-load fit detailing method is recommended by White for curved systems, unless they are sharply skewed (NCHRP Report No 725, 2012). For other structural systems, such as straight, skewed bridges, other detailing methods are recommended. Another long-term goal for UT Bridge V2.2 will be the option to consider additional detailing methods.

Finally, UT Bridge V2.2 allows for the definition of translational springs attached from any point on the structure to a fixed point, in any of the three directions. For straight systems, the directions correspond to the global Cartesian coordinate system, whereas for curved geometries, the nodal local curvilinear coordinate system is considered.

For plate girders, the program also accommodates rotational springs in the longitudinal direction. To avoid dealing with rotational degrees of freedom directly, the modeling of a longitudinal rotational spring of stiffness K_T is achieved by the implementation of two equivalent translational lateral springs of stiffness K_H (Figure 4.18), which are attached to the neighboring nodes along the web depth, and whose equivalent stiffness is calculated by:

$$K_H = \frac{K_T}{d^2} \qquad \textbf{\textit{Equation 4.27}}$$

where d is the distance between the neighboring nodes.

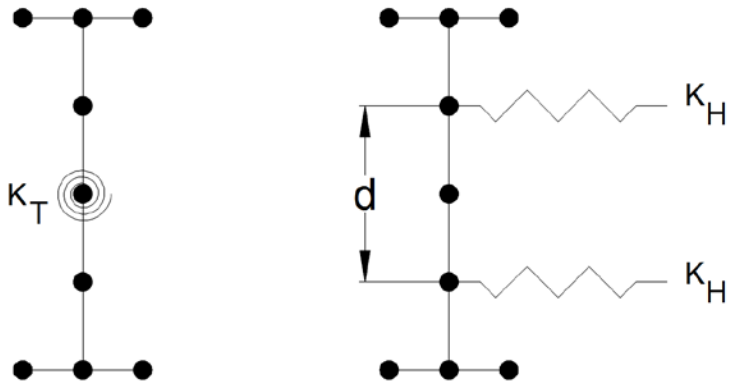

Figure 4.18: Rotational spring and equivalent lateral springs – Case of a rotational spring located at mid-depth of the web

4.7 MODELING OF THE SHEAR STUDS

The shear studs are modeled with three-dimensional spring elements, with K_h and K_v denoting the horizontal and vertical stiffness, respectively. K_h is a function of the concrete nominal strength and is time-dependent to account for stiffening of the concrete deck. Push-out tests conducted by Topkaya (2002) at the University of Texas at Austin are the basis for the time-dependent constitutive model used to define the modulus of elasticity for concrete. The shear stud horizontal stiffness is given by:

$$K_h = n \cdot \frac{A_{sc}}{0.03} \cdot 1.75 \cdot (f_c'(t) \cdot E_c)^{0.3}$$

Equation 4.28

where:

$$f_c'(t) = f_{c,28}' \cdot \frac{t}{4 + 0.85 \cdot t}$$

Equation 4.29

$$E_c = 57{,}000 \cdot \sqrt{f_c'} \qquad \textbf{Equation 4.30}$$

With n being the equivalent number of shear studs at a specific node, based on the number of shear studs per row and the longitudinal mesh size. Other variables used in the preceding equations are defined as follows:

A_{sc} is the shear stud nominal diameter

$f_c'(t)$ is the concrete strength at time t

$f_{c,28}'$ is the 28-day concrete strength

E_c is the concrete modulus of elasticity

t is the number of days that have passed since concrete was cast.

The shear stud vertical stiffness K_v is specified as a large number to ensure the deck and steel superstructure move as a unit in the vertical direction. Overall, the shear stud stiffness matrix is given by:

$$\boldsymbol{K_{shear\ stud}} = \begin{bmatrix} +K_h & & & -K_h & & \\ & +K_h & & & -K_h & \\ & & +K_v & & & -K_v \\ -K_h & & & +K_h & & \\ & -K_h & & & +K_h & \\ & & -K_v & & & +K_v \end{bmatrix} \qquad \textbf{Equation 4.31}$$

For inactive deck portions, as described in Section 4.8.2, a large horizontal stiffness is used to force the flexible uncast deck portions to follow the movement of the steel superstructure.

4.8 MODELING OF THE CONCRETE DECK

This section describes how the concrete deck is meshed, and what stiffness is implemented during the placement analysis.

4.8.1 MESHING OF THE CONCRETE DECK

For bridges with girders having equal reference points and a placement sequence that runs parallel to the girders, meshing of the concrete deck is relatively easy, as only quadrilaterals are required. For all other cases, meshing of the concrete deck likely requires the implementation of triangular elements in addition to the quadrilateral elements. The concrete deck meshing algorithm implemented in the program is designed to keep the number of triangular elements to a minimum.

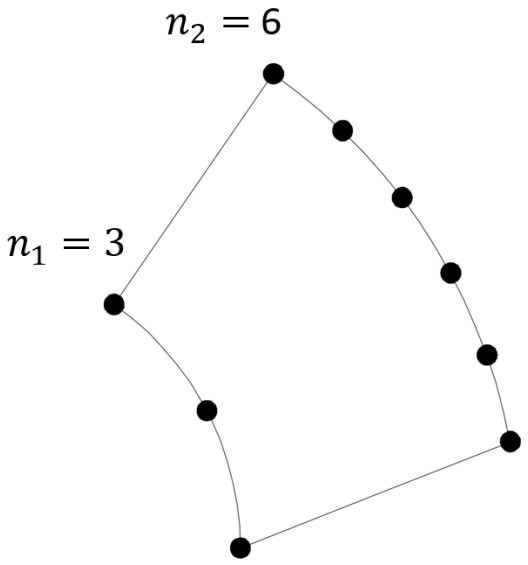

Figure 4.19: Typical deck “panel” defined on a curved bridge between two girders at a specific stage of the placement sequence

For plate girder bridges, meshing of the concrete deck implies meshing of all the concrete deck "panels" defined on each bay for each stage of the placement sequence. For straight bridges, those panels are not necessarily rectangular: in case of a skewed bridge, or when adjacent girders have a different umber of reference points, they are generally trapezoidal. For curved bridges, the deck panels are a fraction of a two-dimensional tore (ring-shaped surface), as shown in Figure 4.19. Accordingly, the number of nodes n_1 and n_2 defined on each girder underneath the panel are different for most cases; therefore, a rectangular mesh cannot be used.

To ensure acceptable aspect ratios, a decision was reached to implement four elements across each bay. This number allows for moving loads in future developments of the program. As far as the left and right overhangs, three elements are retained for plate girder systems, and two for tub girder systems. Three interior lines (called lines 3, 4 and 5) parallel to the girders (called lines 1 and 2) are therefore defined on each panel. For those interior lines, the number of nodes n_3, n_4 and n_5 are set equal to (Figure 4.20):

$$\begin{pmatrix} n_3 \\ n_4 \\ n_5 \end{pmatrix} = \begin{pmatrix} \left|\frac{3n_1 + n_2}{4}\right| \\ \left|\frac{n_1 + n_2}{2}\right| \\ \left|\frac{n_1 + 3n_2}{4}\right| \end{pmatrix}$$

Equation 4.32

Where $\left| \right|$ is the operator for nearest integer.

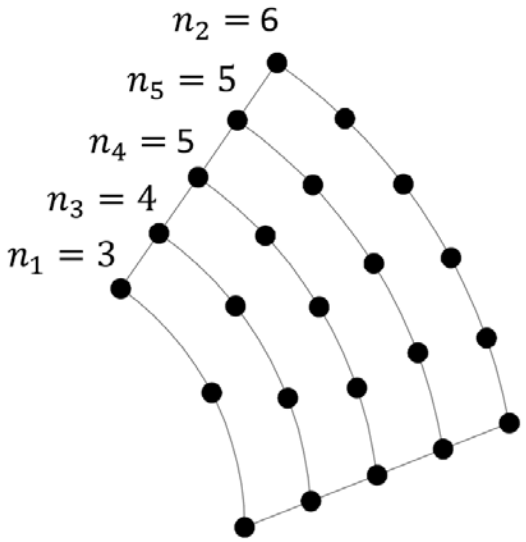

Figure 4.20: Typical deck "panel" meshing (step 1)

Subsequently, the meshing algorithm defines how to connect all nodes on a specific panel. Two cases arise based on whether the left girder has more nodes than the right girder. For example, for the case of a panel where the right girder has more nodes, the number of nodes $f_{13}(i)$ on the first interior line (line 3) to which each node i on the left girder (line 1) should be connected to is specified by:

$$f_{13}(i) = \begin{cases} \left|\frac{n_3}{n_1}\right|, & i = 1 \\ \left|i \cdot \frac{n_3}{n_1}\right| - \sum_{k=1}^{i-1} f(k), & i > 1 \end{cases}$$

Equation 4.33

The use of a quadrilateral or a triangular element is directly dependent on this connectivity (Figure 4.21).

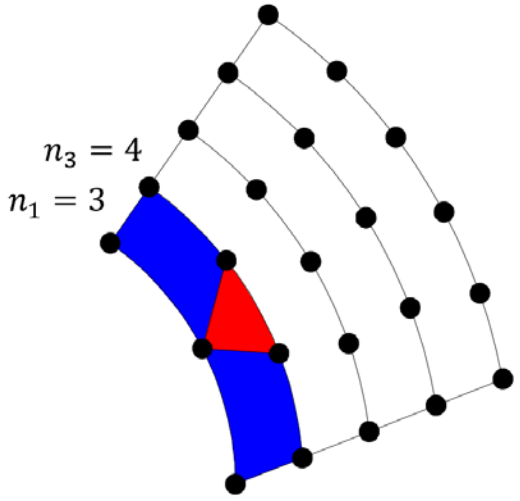

Figure 4.21: Typical deck “panel” meshing (step 2)

The meshing algorithm then moves one line to the right (Figure 4.22), using a similar formula to define the number of nodes $f_{34}(i)$ on the second interior line (line 4) to which each node i on the first interior line (line 3) should be connected to:

$$f_{34}(i) = \begin{cases} \left|\frac{n_4}{n_3}\right|, & i = 1 \\ \left|i \cdot \frac{n_4}{n_3}\right| - \sum_{k=1}^{i-1} f(k), & i > 1 \end{cases}$$

Equation 4.34

The same applies to the last two lines of nodes:

$$f_{45}(i) = \begin{cases} \left|\frac{n_5}{n_4}\right|, & i = 1 \\ \left|i \cdot \frac{n_5}{n_4}\right| - \sum_{k=1}^{i-1} f(k), & i > 1 \end{cases}$$

Equation 4.35

and:

$$f_{52}(i) = \begin{cases} \left|\frac{n_2}{n_5}\right|, & i = 1 \\ \left|i \cdot \frac{n_2}{n_5}\right| - \sum_{k=1}^{i-1} f(k), & i > 1 \end{cases}$$

Equation 4.36

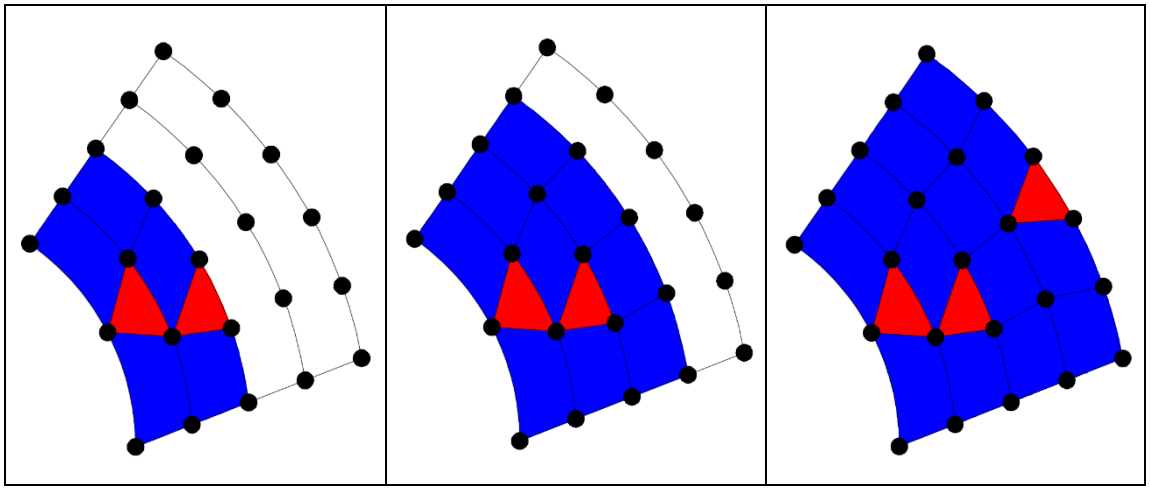

Figure 4.22: Typical deck “panel” meshing (steps 3, 4 and 5)

For plate girders, the concrete deck meshing algorithm can be described in a more algorithmic manner using the following list of instructions. The description is general and does not consider, for example, the generation of the mid-edge nodes also required for the definition of the concrete deck elements. The intent is simply to illustrate the basic sequence of steps needed to implement the algorithm.

For each stage of the placement sequence

For each bay

Recognize the corresponding girder reference points

Count the number of nodes on the girders underneath the panel

Generate new nodes on the panel parallel lines

For each of the first four parallel lines

For each node on those lines

Count how many nodes on the next line to which it should be connected

Loop

Loop

For each of the first four parallel lines

Generate new shell elements in a forward moving manner based on the nodal connectivity previously derived

Loop

Loop

Loop

For tub girder bridges, meshing of the concrete deck between adjacent tubs is achieved in a similar way. Meshing of the deck on an actual twin plate girder bridge and on a tub girder bridge is illustrated in Figure 4.23 and Figure 4.24, respectively.

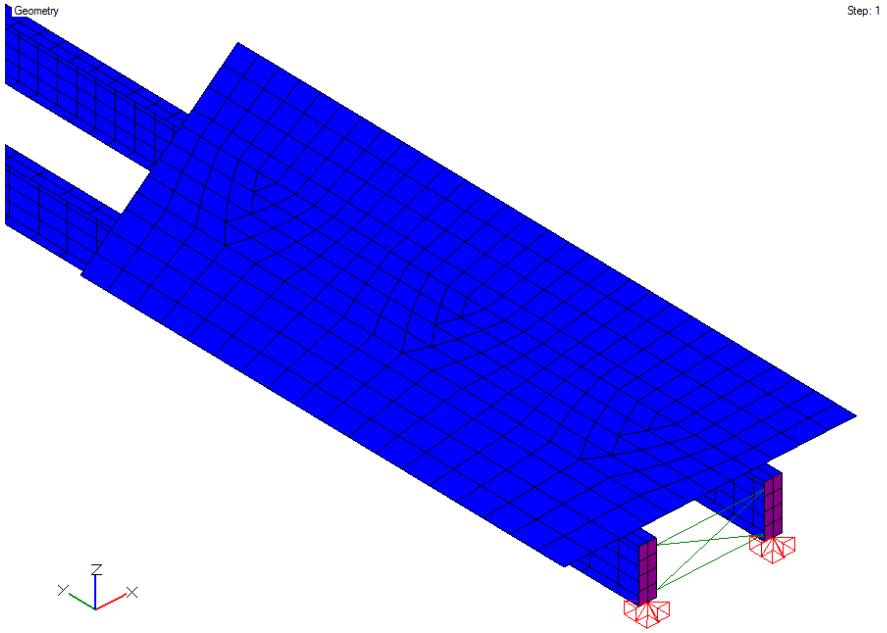

Figure 4.23: Deck meshing on a curved, twin plate girder bridge

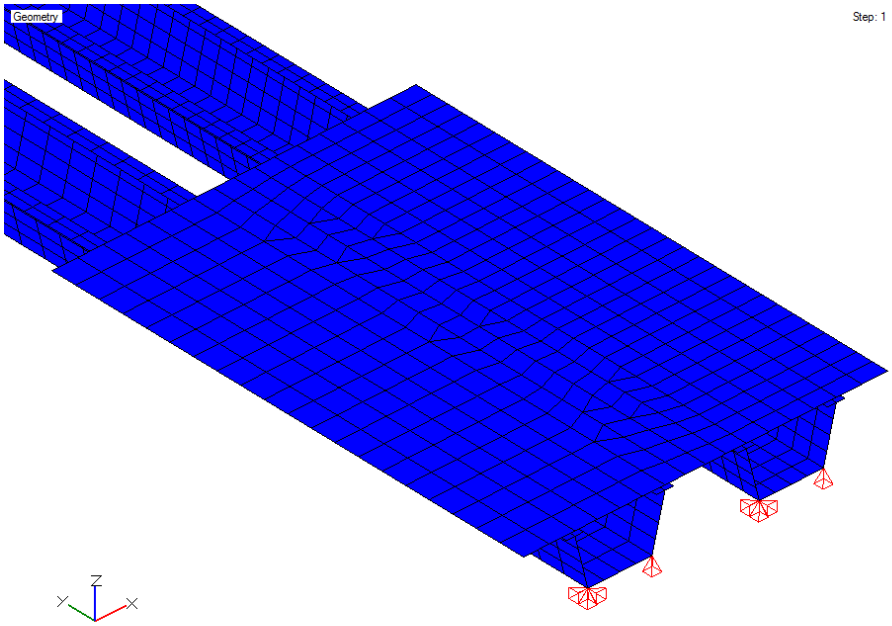

Figure 4.24: Deck meshing on a curved, twin tub girder bridge

4.8.2 STIFFNESS SELECTED FOR THE CONCRETE DECK

There is some uncertainty regarding the specific magnitude that should be used to define the concrete deck. On the construction site, stay-in-place forms are usually provided. These forms are not modeled in UT Bridge V2.2. Regarding the overhangs, brackets are mounted to the girders, and these brackets are not included in the model. The formwork that is installed on the bridge is the only source of stiffness when concrete is first cast and is essentially a fluid. As the formwork is not modeled in the program, the use of a minimum concrete stiffness is necessary to prevent numerical instabilities. That minimum stiffness parameter is left to the decision of the developer. On the one hand, it must be low enough to account for the fact that concrete is basically a fluid when it is being cast. On the other hand, it must be large enough for the structure to be stable. An assumption also needs to be made for uncast segments. If no assumption is made, the shells defined for the uncast portions of the bridge deck will remain in their original position until the placement sequence reaches them. When it does, they will begin to deform, leaving a large, unacceptable discontinuity with the already cast segments. To prevent these discontinuities, it was decided to activate all shells for all stages of the placement sequence, even the uncast portions. This way, the shells corresponding to the uncast portions follow smoothly the deformations of the steel superstructure underneath. The uncast segments are not displayed in the post-processor, and their self-weight is not included. However, they are given a minimum stiffness, which must be low enough to account for the fact that no concrete is cast yet, but large enough to prevent local buckling issues at the intersection with already cast segments. Local buckling at the edge between an already cast segment and a recently cast segment was indeed observed when the stiffness implemented for the uncast segments was too small.

4.9 IMPLEMENTATION OF THE BOUNDARY CONDITIONS

UT Bridge V2.2 allows the definition of boundary conditions either semi-manually, with the specification of pin and roller supports, or fully manually, with the restriction of any desired displacement degree of freedom. For the semi-manual case, the restriction of the appropriate degrees of freedom is described in the following manner. For single-girder systems, a pin support means the restraint of all three displacements at the bottom flange-to-web node, as well as the restraint of the lateral displacement at the top-flange-to-web node (Figure 4.25). A roller support implies the same restraints, except for the longitudinal displacement at the bottom-flange-to-web node, which is kept unrestrained. Torsion is restrained in both cases, but the cross-section is free to warp. For multi-girder systems with at least one active cross-frame on either side of the support, the lateral displacement at the top-flange-to-web node is kept unrestrained so the cross-frame must restrain the lateral and torsional movement (Figure 4.26). The rare case of supports on multi-girder systems with no active cross-frame on either side of the support is treated similarly as the case of single-girder systems.

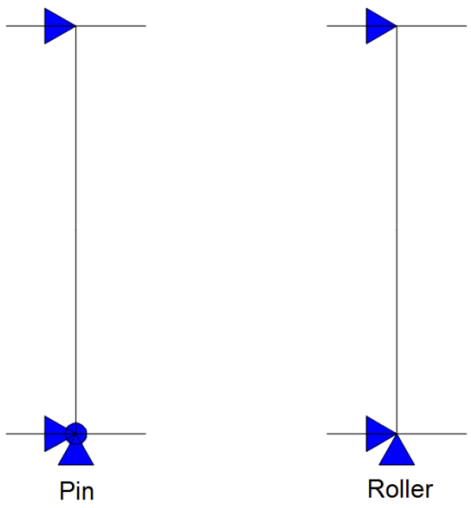

Figure 4.25: Definition of pin and roller supports on single plate girder systems

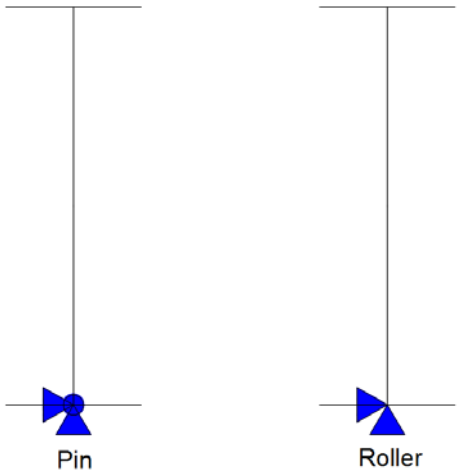

Figure 4.26: Definition of pin and roller supports on multiple plate girder systems (where cross-frames are specified)

For tub girders, the implementation of the pin and roller supports is achieved by restraining appropriate displacements on both sides of the bottom flange (Figure 4.27).

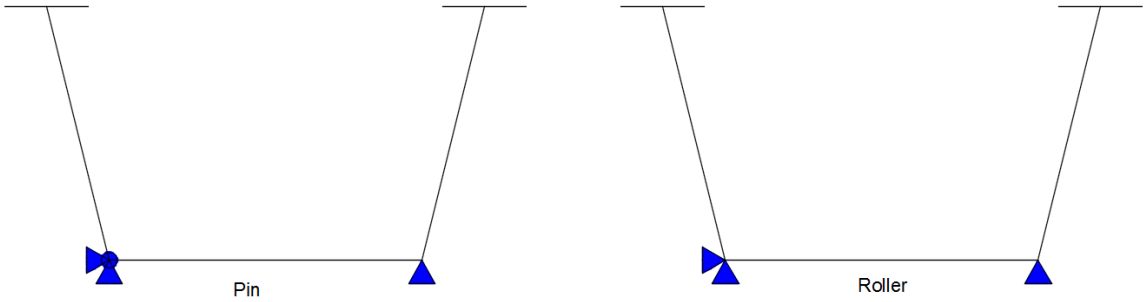

Figure 4.27: Definition of pin and roller supports for tub girder systems

This definition assumes that tub girders sit on two bearings. For many cases, however, tub girders sit on one pot bearing only, whether fixed, free, or guided. Accordingly, UT Bridge V2.2 also allows the use of single bearings only. From a stability standpoint, however, single bearings do not prevent torsional rigid body motion for straight

tubs, which explains why modeling two bearings is the default approach adopted in the program to prevent stability issues.

In the second case, the user can manually select any node, and restrain either the lateral, longitudinal or vertical displacement at that node. For curved geometries, the local curvilinear coordinate system is by default considered instead of the global Cartesian coordinate system, although restraint in any desired orientation is also possible.

UT Bridge V2.2 also allows the use of temporary supports. Shore towers are modeled the same way as roller supports. For plate girder systems, this means restraining the lateral movement at both flange-to-web nodes in addition to restraining the vertical displacement at the bottom-flange-to-web node. Holding cranes, conversely, are simply modeled as upward point loads acting on the top flange and therefore do not provide any lateral or torsional bracing.

4.10 LOADING OPTIONS

From a coding standpoint, the assembly of the stiffness matrix is much more involved than the load vector. While true for linear elastic analyses, this observation is even more pronounced for geometrically nonlinear analyses. This complexity sometimes results in overlooking the load vector, which is as important as the stiffness matrix for proper evaluation of the displacements, stresses, and so on. This paragraph presents the different loading options available in UT Bridge V2.2 and explains their implementation into the code.

4.10.1 SELF-WEIGHT

Self-weight is the primary load acting on a bridge during erection and construction. For shell elements, UT Bridge V2.2 assembles the load vector due to self-weight in a

"consistent" manner (Cook 2001), assigning $-m/12$ to the corner nodes unrestrained vertical displacement degrees of freedom, and $+m/3$ to the mid-edge nodes unrestrained vertical degrees of freedom, where m is the mass of the shell. For all braces, the mass of each chord is equally distributed to the nodal unrestrained vertical degrees of freedom.

For curved systems, it should be recalled that during the assembly of the stiffness matrix, the displacement degrees of freedom at the support nodes are transformed from the global coordinate system to the nodal local curvilinear system (or any other restraint orientation). For consistency with the definition of the unrestrained degrees of freedom, the same operation must be conducted for the load vector due to self-weight when one of the shell nodes corresponds to a support or a temporary support.

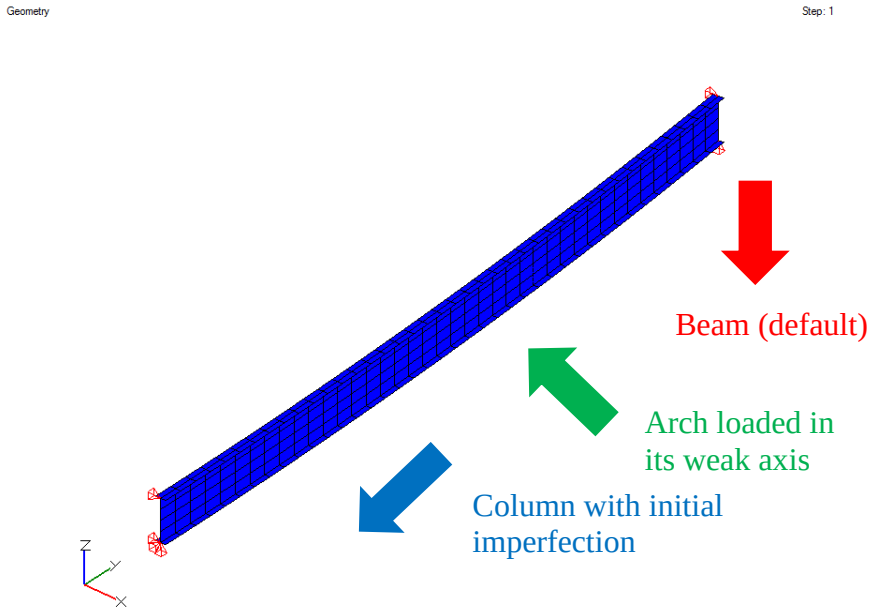

Figure 4.28: Options for gravity direction, in case of single plate girder systems

It should be noted that UT Bridge V2.2 offers the option to change the direction of gravity (Figure 4.28). By default, the program assumes gravity is acting in the vertical direction, which is the correct assumption for bridge models. For single curved plate girders, however, the program is also able to compute the direction of the chord defined between the girder ends and apply gravity in a direction either parallel or orthogonal to that chord. If gravity is applied in a direction parallel to the chord, and if the radius of curvature is sufficiently large, the curved plate girder can be seen as a straight column with an initial imperfection. Otherwise, if gravity is applied in a direction orthogonal to the chord, the curved plate girder can then be seen as an arch loaded with minor axis bending. All three options for gravity direction in case of single plate girder systems are shown in Figure 4.28.

4.10.2 TOP FLANGE UNIFORM LOADS

UT Bridge V2.2 is able to model construction loads as body force loads applied on the top flange. For tub girders, the load can be specified as acting on both top flanges, or on the left or right top flange only. The load vector due to the top flange uniform load is derived in a manner that is “consistent” with the shell interpolation functions, similarly to self-weight.

4.10.3 POINT LOADS

Point loads acting in any direction at any location along a bridge model can be defined by the user. The program internally adds the load to the corresponding unrestrained degree of freedom.

It should be noted that defining point loads in the pre-processor is achieved after the derivation and ordering of the reference points. A common error is to enter a point load

at a location where no node is actually created by the program. In that case, the main processor stops, and an error message describing the cause of the error is displayed to the user. An easy way to avoid this issue is to specifically add extra reference points where the point loads are acting, before having the pre-processor derive and order those reference points. Alternatively, a different approach could be to compute work-equivalent forces and apply them to the nearest nodes. This approach, however, was not considered.

Also, it should be recalled that achieving a uniform moment distribution or a uniform compression through the length of a girder can be achieved by adequately applying point loads at the ends of the girder.

4.10.4 WIND LOADS

Wind loads can be substantial during bridge erection and construction. UT Bridge V2.2 defines wind loads by their direction and magnitude, as well as the girder on which they are acting. The load vector due to wind is assembled by deriving the area of each affected web element, multiplying that area by the wind pressure, and distributing the resulting load in a "consistent" manner, similarly to self-weight and top flange uniform loads. Again, transformation of the load vector due to wind is performed at the support and temporary support nodes. It should also be emphasized that wind is assumed to act on the webs only, not on the flanges.

The definition of wind loads in UT Bridge V2.2 is available only for an erection analysis. Placement of the concrete deck will typically be delayed due to windy conditions.

4.10.5 INITIAL THERMAL LOADS

Thermal effects are typically not considered during bridge erection and construction. For statically indeterminate structures, thermal effects may result in significant reactions at the pin supports. Defining with precision the temperature distribution along a bridge is a complex task, as conduction, convection, and radiation combine depending on the intensity and direction of the solar radiation, the presence or not of formwork and brackets along a bridge, the wind velocity, and many other factors (Chan 2008). For simplicity, UT Bridge V2.2 only considers uniform temperature changes.

The load vector due to uniform temperature changes corresponding to the unrestrained degrees of freedom $\boldsymbol{P_{f0}}$ is assembled using Equation 4.37, where $\boldsymbol{B}$ is the linear strain-displacement matrix, $\boldsymbol{C}$ is the stress-strain matrix, α is the steel coefficient for thermal expansion, and ΔT is the uniform temperature change:

$$\boldsymbol{P_{f0}} = \alpha \cdot \Delta T \cdot \int \boldsymbol{B}^T \cdot \boldsymbol{C} \cdot dV \qquad \textbf{Equation 4.37}$$

or:

$$\boldsymbol{P_{f0}} = \alpha \cdot \Delta T \cdot \sum_{i,j} \alpha_{i,j} \cdot (\boldsymbol{B}^T \cdot \boldsymbol{C})_{i,j} \qquad \textbf{Equation 4.38}$$

For curved systems, transformation of the load vector from global coordinates to nodal local curvilinear coordinates (or any other restraint orientation) is performed when the element contains a node corresponding to a support or a temporary support.

After solving for the displacements and the stresses, and in order to account for the stresses due to the initial thermal loads, the program subtracts from the computed stresses

those directly related to thermal effects. This is the approach typically used to consider the effect of the so-called “fixed-end” forces (Cook 2001). At each shell nodal point, the stress vector is calculated using the following equation:

$$\boldsymbol{\sigma = C \cdot (B \cdot U - \sigma_{th})} \qquad \textit{Equation 4.39}$$

Where $\boldsymbol{U}$ is the displacement vector of the shell nodal points, and $\boldsymbol{\sigma_{th}}$ is the stress vector due the initial thermal loads, which is equal to:

$$\boldsymbol{\sigma_{th} = C \cdot \epsilon_0} \qquad \textit{Equation 4.40}$$

In Equation 4.40, the strain vector due to the initial thermal load is simply equal to:

$$^{T}\boldsymbol{\epsilon_0} = {}^{T}(\alpha \cdot \Delta T \quad \alpha \cdot \Delta T \quad \alpha \cdot \Delta T \quad 0 \quad 0 \quad 0) \qquad \textit{Equation 4.41}$$

For curved systems, it should be noted that this subtraction is performed after transforming the stress vector to the nodal local curvilinear coordinate system.

Prior to computing the support reactions, the program assembles the load vector due to initial thermal loads corresponding to the restrained degrees of freedom $\boldsymbol{P_{r0}}$. This operation is conducted using the same equation previously mentioned, though considering the restrained degrees of freedom only.

Finally, for cases where initial thermal loads are the only external loads acting on the structure being analyzed and a linearized buckling analysis is conducted, the program

assumes constant values for the steel modulus of elasticity and coefficient of thermal expansion. A critical difference in temperature ΔT_{cr} obtained from such a thermal buckling analysis can therefore only be acceptable for small values of ΔT_{cr}. Otherwise, it is well known that material properties, particularly the steel modulus of elasticity, decrease rapidly with increasing temperature.

4.11 SOLVER

The overall stiffness matrix is a sparse, symmetric matrix. UT Bridge V2.2 implements the Intel MKL PARDISO sparse solver (Shenk 2000) for solving the equation:

$$\boldsymbol{K_{ff} \cdot U_f = P_f + P_{f0}} \qquad \textit{Equation 4.42}$$

The Intel MKL PARDISO is a high-performance, user-friendly direct sparse solver widely used for solving large sparse linear systems. The solver takes advantage of the symmetry of the stiffness matrix for computational efficiency. In UT Bridge V2.2, it is used both for the linear elastic analysis and the geometrically nonlinear analysis. A study by Topkaya and Williamson (2008) showed that PARDISO is more efficient than other sparse solvers available on the market.

The use of direct sparse solvers requires the stiffness matrix to be stored in the compressed sparse row format (CSR). UT Bridge V2.2 implements this compressed storage format directly during the definition of the connectivity matrix between all unrestrained degrees of freedom. This organization is a key step in the assembly of the stiffness matrix, as the sparsity index of the stiffness matrix is typically on the order of one

percent or less. This sparsity index indicates that only one percent of the stiffness matrix coefficients, if the stiffness matrix was stored in a traditional format, are not equal to zero.

4.12 STRESS RECOVERY

This section describes the stress recovery process, as well as the stress smoothing at the nodal points.

4.12.1 STRESS EXTRAPOLATION FROM THE INTEGRATION POINTS TO THE NODAL POINTS

After a linear elastic analysis is completed, the stresses are evaluated at each integration point of the shell elements. As mentioned in §4.3, there are eight integration points for quadrilateral shell elements and six integration points for triangular elements. Integration points and nodal points are not coincident. Extrapolation of the stresses from the integration points to the nodal points is performed with the use of extrapolation functions (Figure 4.29). For quadrilateral elements, which represent most of the elements encountered in a bridge model, the extrapolation functions are linear as each layer through the shell thickness contains four integration points only. The extrapolation algorithm is performed for each stress component and is described algorithmically in the following instructions, where $\sigma_{i,j}$ represents the j-th stress component at nodal point i, $\sigma_{Gauss,i,j}$ the j-th stress component at integration point i, and $h_m(k)$ the value of the m-th interpolation function at nodal point k.

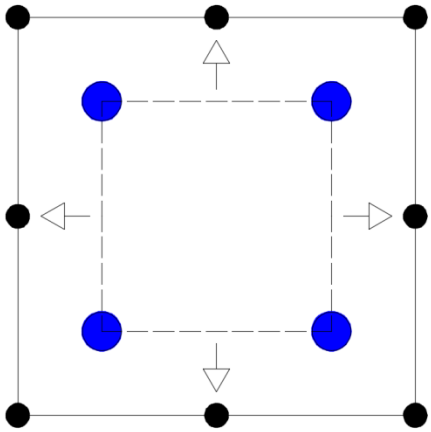

Figure 4.29: Stress extrapolation to the nodal points

For i = 1,2 (For both integration layers through the shell depth)

For k = 1,8 (For all nodal points within the shell)

For l = 1,6 (For all stress components)

For m = 1,4 (Loop over the integration points)

$$\sigma_{(i-1)\cdot 8+k,l} = \sigma_{(i-1)\cdot 8+k,l} + h_m(k) \cdot \sigma_{Gauss,(i-1)\cdot 4+m,l}$$

Loop

Loop

Loop

Loop

The extrapolation for triangular elements is performed in a similar manner, with slightly different extrapolation functions corresponding to a triangular element, which has only three integration points per layer.

4.12.2 NODAL STRESS AVERAGING

For nodes belonging to different elements, the stress vectors obtained from each element are usually not equal, and nodal stress averaging is required for each stress component at each integration layer (Figure 4.30). Nodal stress averaging is performed only between elements of the same type, namely flanges, webs, stiffeners, and diaphragms. For example, stress averaging is not conducted at flange-to-web junctions or at web-to-stiffener junctions, which means that stress discontinuities may occur at those intersections. A separate stress field is obtained for each element type. The post-processor projects the combination of those stress fields.

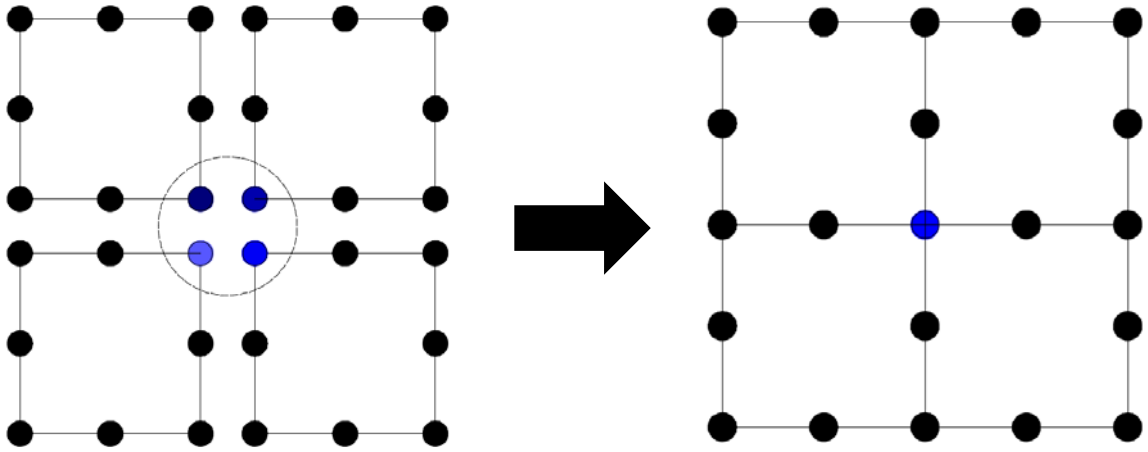

Figure 4.30: Stress averaging

4.13 DERIVATION OF SUPPORT REACTIONS AND CROSS-FRAME FORCES

Computing the support reactions is achieved by assembling the $\boldsymbol{K_{rf}}$ matrix and solving the following equation (Cook 2001):

$$\boldsymbol{P_r = K_{rf} \cdot U_f - P_{r0}}$$ ***Equation 4.43***

The derivation of the cross-frame forces is conducted by evaluating the deformations in each chord:

$$F = EA \cdot \frac{{}^{t}L - {}^{0}L}{{}^{0}L}$$

Equation 4.44

where ${}^{0}L$ and ${}^{t}L$ are the initial and final lengths of the chord.

4.14 DERIVATION OF THE SHEAR, MOMENT AND TORSION DIAGRAMS

UT Bridge V2.2 includes the automatic generation of shear and moment diagrams, which are calculated by the main processor and displayed by the post-processor. For plate girder systems, torsion diagrams are also available. These quantities are calculated discretely at each location along a given modeled bridge by appropriate integration of the stress vector across the section. For curved systems, rotation of the stress vector from global Cartesian coordinates to local curvilinear coordinates is required prior to integration. Finally, these quantities are not calculated at flange transitions in order to prevent local discontinuities in the diagrams.

Derivation of the shear, moment, and torsion quantities at each cross-section along a bridge requires the understanding of the contribution of each stress component to the appropriate quantity.

4.14.1 SHEAR DIAGRAM

Along the length of a bridge, the shear is simply calculated as the integral of the vertical shear stress over the cross-section. Thus, the shear force is computed by:

$$V = \int \sigma_{yz} \cdot dA$$

Equation 4.45

This expression is valid both for plate girders and tub girders and is conducted numerically by multiplying the vertical shear stress at each node on a given cross-section by the respective nodal tributary area, then summing these components. Because there are two integration layers through a shell's thickness, it should be noted that the average value of the vertical shear stress at each integration layer is considered.

$$V = \sum \sigma_{avg,yz} \cdot dA$$

Equation 4.46

4.14.2 MOMENT DIAGRAM

The strong-axis moment is evaluated at each location along a given bridge model by multiplying the average longitudinal normal stress at each node on a particular cross-section by the respective nodal tributary area and the nodal vertical distance to the elastic neutral axis:

$$M = \int \sigma_{yy} \cdot z \cdot dA$$

Equation 4.47

or:

$$M = \sum \sigma_{avg,yy} \cdot z \cdot dA$$

Equation 4.48

The location of the elastic neutral axis is derived for each cross-section using well-known formulas. For plate girders, the elastic neutral axis is located at a distance $\bar{y}$ from the bottom of the cross-section:

$$\bar{y} = \frac{b_{bf} \cdot t_{bf} \cdot \frac{t_{bf}}{2} + h_w \cdot t_w \cdot \left(t_{bf} + \frac{h_w}{2}\right) + b_{tf} \cdot t_{tf} \cdot \left(t_{bf} + h_w + \frac{t_{tf}}{2}\right)}{b_{bf} \cdot t_{bf} + h_w \cdot t_w + b_{tf} \cdot t_{tf}}$$

Equation 4.49

For tub girders, this distance is equal to:

$$\bar{y} = \frac{b_{bf} \cdot t_{bf} \cdot \frac{t_{bf}}{2} + 2 \cdot \frac{h_w}{\cos\zeta} \cdot t_w \cdot \left(t_{bf} + \frac{h_w}{2}\right) + 2 \cdot b_{tf} \cdot t_{tf} \cdot \left(t_{bf} + h_w + \frac{t_{tf}}{2}\right)}{b_{bf} \cdot t_{bf} + 2 \cdot \frac{h_w}{\cos\zeta} \cdot t_w + 2 \cdot b_{tf} \cdot t_{tf}}$$

Equation 4.50

with:

$$\zeta = arctan\left(\frac{\frac{t_w - b_{bf}}{2}}{\frac{t_{bf}}{2} + h_w + \frac{t_{tf}}{2}}\right)$$

Equation 4.51

All the cross-sectional dimensions are presented in Figure 4.31.

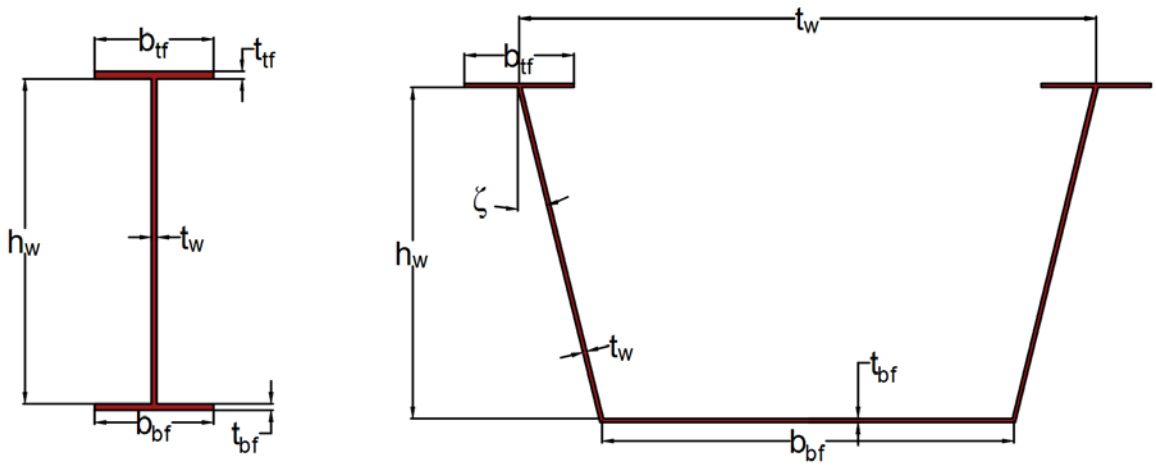

Figure 4.31: Cross-sectional dimensions

4.14.3 TORSION DIAGRAM

For plate girders, UT Bridge V2.2 is also able to calculate the torsion at each location along a bridge. The torsion is evaluated by first considering the shear flow around the cross-section. For all steel plates, namely flanges and webs, a linear variation of the shear flow through the plate depth is assumed. This variation can only be observed if the stress vectors at each integration layer are not averaged prior to the calculation. Thus, to evaluate the variation of the shear flow around a given cross-section, it is necessary to assume at least two integration layers through the shell thickness. The stress components related to the shear flow are σ_{xy} for the flanges and σ_{yz} for the web.

The average shear stress is calculated for each half plate and then multiplied by the respective nodal tributary area. All shear components are then multiplied by the vertical distance to the shear center of the cross-section. Overall, the expression for the torsion is given by:

$$T = \int_{flanges} \sigma_{xy} \cdot z \cdot dA + \int_{web} \sigma_{yz} \cdot z \cdot dA$$

Equation 4.52

or:

$$T = \sum_{flanges} \sigma_{xy} \cdot z \cdot dA + \sum_{web} \sigma_{yz} \cdot z \cdot dA$$

Equation 4.53

where the shear center is located at a distance from the bottom of the cross-section:

$$y_c = \left(t_{bf} + h_w + t_{tf}\right) - \frac{t_{tf}}{2} - \alpha_c \cdot \left(\left(t_{bf} + h_w + t_{tf}\right) - \frac{t_{bf} + t_{tf}}{2}\right)$$

Equation 4.54

with:

$$\alpha_c = \frac{1}{1 + \left(\frac{b_{tf}}{b_{bf}}\right)^3 \cdot \frac{t_{tf}}{t_{bf}}}$$

Equation 4.55

4.15 SUMMARY

This chapter presented all the modeling assumptions considered for linear elastic analyses, including geometric representation of bridges and modeling of braces, loads, and boundary conditions. The chapter also described assembly of the stiffness matrix, methods of equation solving, and construction of the shear, moment, and torsion diagrams. UT Bridge V2.2 is also able to conduct a linearized buckling analysis, a modal dynamic analysis, and a geometrically nonlinear analysis, which are the subject of Chapter 5.

Chapter 5: General eigenvalue problems and geometrically nonlinear analysis

5.1 General eigenvalue problems

The general eigenvalue problem is given in Equation 5.1:

$$\boldsymbol{A} \cdot \boldsymbol{X} + \lambda \cdot \boldsymbol{B} \cdot \boldsymbol{X} = \boldsymbol{0} \qquad \textit{Equation 5.1}$$

where:

$\boldsymbol{A}$ and $\boldsymbol{B}$ are two matrices

$\boldsymbol{X}$ is an eigenvector

λ is an eigenvalue.

Two eigenvalue problems are addressed by UT Bridge V2.2, namely buckling and free vibration.

5.1.1 Linearized buckling analysis

Large unbraced lengths during erection and construction may in some severe cases lead to lateral-torsional buckling. One way to estimate the buckling strength of a structure is to conduct a linearized buckling analysis. In this case, the general eigenvalue equation becomes:

$$\boldsymbol{K} \cdot \boldsymbol{X} + \lambda \cdot \boldsymbol{K_g} \cdot \boldsymbol{X} = \boldsymbol{0} \qquad \textit{Equation 5.2}$$

Where $\boldsymbol{K}$ and $\boldsymbol{K_g}$ are, respectively, the overall stiffness matrix and the overall geometric stiffness matrix. The formulation of both matrices is done primarily using the global Cartesian coordinate system. The only exception is for the unrestrained translational degrees of freedom at the support nodes on curved systems, which are expressed in the nodal local curvilinear coordinate system (by default), or any other local coordinate system depending on the restraint orientation.

The linearized buckling analysis is based on the structural stiffness matrix corresponding to the initial, undeformed configuration, where initial stresses are calculated from a linear elastic analysis. This type of analysis assumes a bifurcation-type structural behavior. Accordingly, pre-buckling displacements are ignored. The computed eigenvalue is therefore an upper bound on the true critical load that a structure can sustain. Although the presence of geometric imperfections prevents a perfect bifurcation-type structural behavior, straight systems without skewed supports are not subjected to significant second-order effects when self-weight is the primary external load. As such, a linearized buckling analysis is applicable. In general, however, other systems are typically subjected to second-order effects to some extent, even when self-weight is the primary external load. These systems include straight, skewed bridges as well as curved bridges where torsional and bending effects combine. The results of a linearized buckling analysis must therefore be considered cautiously. When second-order effects are significant, a geometrically nonlinear analysis yields a better estimate of the structural behavior, but such an analysis comes with significant additional computational cost. This type of analysis is presented in §5.2.

The derivation of the general shell geometric stiffness matrix is described to some extent by Stith (2010). It requires the calculation of the stresses from a linear elastic

analysis and the construction of the nonlinear strain-displacement matrix $\boldsymbol{B_{NL}}$, as described in the following equation:

$$\boldsymbol{K_g} = \int \boldsymbol{B_{NL}^T} \cdot \boldsymbol{S} \cdot \boldsymbol{B_{NL}} \cdot dV$$

Equation 5.3

or:

$$\boldsymbol{K_g} = \sum_{i,j} \alpha_{i,j} \cdot (\boldsymbol{B_{NL}^T} \cdot \boldsymbol{S} \cdot \boldsymbol{B_{NL}})_{i,j}$$

Equation 5.4

Where $\boldsymbol{B_{NL}}$ is a 9×40 matrix for quadrilateral elements or a 9×30 matrix for triangular elements. Columns number 5(k-1)+1 up to 5(k-1)+5, corresponding to the five degrees of freedom at nodal point k, are shown below. All expressions are already described in the derivation of the shell stiffness matrix. Empty positions correspond to a value of 0.

$$\boldsymbol{B_{NL}} = \begin{bmatrix} \cdots & \partial h_k/\partial x & & & g_{1x}^k G_x^k & g_{2x}^k G_x^k & \cdots \\ \cdots & & \partial h_k/\partial x & & g_{1y}^k G_x^k & g_{2y}^k G_x^k & \cdots \\ \cdots & & & \partial h_k/\partial x & g_{1z}^k G_x^k & g_{2z}^k G_x^k & \cdots \\ \cdots & \partial h_k/\partial y & & & g_{1x}^k G_y^k & g_{2x}^k G_y^k & \cdots \\ \cdots & & \partial h_k/\partial y & & g_{1y}^k G_y^k & g_{2y}^k G_y^k & \cdots \\ \cdots & & & \partial h_k/\partial y & g_{1z}^k G_y^k & g_{2z}^k G_y^k & \cdots \\ \cdots & \partial h_k/\partial z & & & g_{1x}^k G_z^k & g_{2x}^k G_z^k & \cdots \\ \cdots & & \partial h_k/\partial z & & g_{1y}^k G_z^k & g_{2y}^k G_z^k & \cdots \\ \cdots & & & \partial h_k/\partial z & g_{1z}^k G_z^k & g_{2z}^k G_z^k & \cdots \end{bmatrix}$$

Equation 5.5

The 9×9 $\boldsymbol{S}$ matrix is based on the stress vector obtained from a linear elastic analysis:

$$\boldsymbol{S} = \begin{bmatrix} \sigma_{xx}\boldsymbol{I_3} & \sigma_{xy}\boldsymbol{I_3} & \sigma_{xz}\boldsymbol{I_3} \\ \sigma_{xy}\boldsymbol{I_3} & \sigma_{yy}\boldsymbol{I_3} & \sigma_{yz}\boldsymbol{I_3} \\ \sigma_{xz}\boldsymbol{I_3} & \sigma_{yz}\boldsymbol{I_3} & \sigma_{zz}\boldsymbol{I_3} \end{bmatrix} \qquad \textit{Equation 5.6}$$

where $\boldsymbol{I_3}$ is the 3×3 identity matrix.

For all braces, the geometric stiffness matrix is an assembly of the geometric stiffness provided by all appropriate chords, where each chord geometric stiffness matrix is defined as:

$$\boldsymbol{K_g} = \frac{F}{L} \cdot \begin{bmatrix} 1 & & & -1 & & \\ & 1 & & & -1 & \\ & & 1 & & & -1 \\ -1 & & & 1 & & \\ & -1 & & & 1 & \\ & & -1 & & & 1 \end{bmatrix}$$

Equation 5.7

Where F is the chord force based on the linear elastic analysis, and L is the initial, undeformed length of the chord (Cook 2001). For a chord in tension, F is positive; for a chord in compression, F is negative.

5.1.2 MODAL DYNAMIC ANALYSIS

In addition to a linearized buckling analysis, UT Bridge V2.2 can conduct a modal dynamic analysis. Although stability issues are the primary concern for bridges during erection and construction, it may also be useful in some cases to evaluate their free vibration modes in order to help understand their structural behavior. Further, this type of analysis may be useful in future versions of the software, where loads will potentially be applied dynamically.

For modal dynamic analysis, the general eigenvalue problem becomes:

$$\boldsymbol{K} \cdot \boldsymbol{X} + \lambda \cdot \boldsymbol{M} \cdot \boldsymbol{X} = \boldsymbol{0} \qquad \textit{Equation 5.8}$$

Where $\boldsymbol{K}$ is the overall stiffness matrix, and $\boldsymbol{M}$ is the overall mass matrix. UT Bridge V2.2 can assemble the mass matrix using either a lumped mass matrix formulation or a consistent mass matrix formulation (Cook 2001). The user selects the mass matrix formulation during the bridge model definition in the pre-processor. The effect of the mass matrix formulation on the free vibration modes is typically very small, as relative differences are within the order of one or two percent.

The lumped mass matrix for general shells is derived by first computing the shell mass m. A fraction of that mass is lumped to each of the shell degrees of freedom. For example, for quadrilateral shells, which represent most of the shells encountered in a bridge model, $m/8$ is lumped to the translational degrees of freedom, and $mh^2/32$ is lumped to the rotational degrees of freedom, where h represents the shell thickness (Bolourchi 1979). This results in a diagonal mass matrix.

By contrast, the consistent mass matrix for general shells, which is not a diagonal matrix, is derived by integrating the interpolation matrix over the shell volume:

$$\boldsymbol{M} = \rho \cdot \int \boldsymbol{N}^T \cdot \boldsymbol{N} \cdot dV \qquad \textit{Equation 5.9}$$

or:

$$\boldsymbol{M} = \rho \cdot \sum_{i,j} \alpha_{i,j} \cdot (\boldsymbol{N}^T \cdot \boldsymbol{N})_{i,j}$$

Equation 5.10

Where $\boldsymbol{N}$ is a 3×40 matrix and ρ is the mass density.

Columns number 5(k-1)+1 up to 5(k-1)+5, corresponding to the five degrees of freedom at nodal point k, are shown below.

$$\boldsymbol{N} = \begin{bmatrix} \cdots & h_k & & & g_{1x}^k & g_{2x}^k & \cdots \\ \cdots & & h_k & & g_{1y}^k & g_{2y}^k & \cdots \\ \cdots & & & h_k & g_{1z}^k & g_{2z}^k & \cdots \end{bmatrix}$$

Equation 5.11

The subroutines implemented for the derivation of both mass matrix formulations are shown in Appendix E.

For all braces, the mass matrix is the assembly of all the individual mass matrices provided by the chords. The chord consistent mass matrix expressed in natural coordinates is equal to the following expression, where m represents the mass of the chord:

$$\boldsymbol{M} = m \cdot \begin{bmatrix} \frac{1}{3} & \frac{1}{6} \\ \frac{1}{6} & \frac{1}{3} \end{bmatrix}$$

Equation 5.12

The chord lumped mass matrix, conversely, is equal to:

$$\boldsymbol{M} = m \cdot \begin{bmatrix} \frac{1}{2} & 0 \\ 0 & \frac{1}{2} \end{bmatrix}$$

Equation 5.13

Transformation of the chord mass matrices from natural to global coordinates is achieved using the same coordinate rotation matrix used for the transformation of the chord stiffness matrix.

5.1.3 THE FEAST EIGENSOLVER

UT Bridge V2.2 tries to take advantage of existing advanced methods for obtaining eigensolutions. It implements FEAST for its eigensolver. FEAST was developed by Polizzi at the University of Massachusetts at Amherst (2009) and differs from the traditional Krylov subspace-iteration-based techniques implemented in the Arnoldi and Lanczos algorithms. These traditional methods are commonly used for general eigenvalue problems in FEA software such as ABAQUS. FEAST implements a density-matrix-based algorithm inspired from quantum mechanics, where the presence of electrons on different orbits may only be assessed using probabilistic functions, leading to the concept of electron density. FEAST is now part of Intel mathematical libraries, which makes its use straightforward compared to other eigensolvers. FEAST is a powerful eigensolver that can capture a large number of eigenvalues to a great level of accuracy, provided the analyst specifies a search interval and estimates the number of eigenvalues within that interval. FEAST has been used in many science and engineering applications such as quantum mechanics, optics, and so on. In the field of bridge dynamics, up to the first ten modes are usually of particular interest, as they capture most of the bridge mass (Ball 2005). In the field of bridge stability,

however, there may be a large number of buckling modes. For flexible structures, buckling modes are well separated. For stiffer structures, a large number of local buckling modes typically occur next to one another, with a few global buckling modes in between.

As the version of FEAST embedded in UT Bridge V2.2 does require the entry of a search interval and a subspace size, an algorithm was implemented to accommodate for most cases, although some computational cost is automatically involved in the loops (Figure 5.1). By default, up to the first 99 modes within an interval are retained, which is useful in cases where the buckling modes are closely spaced.

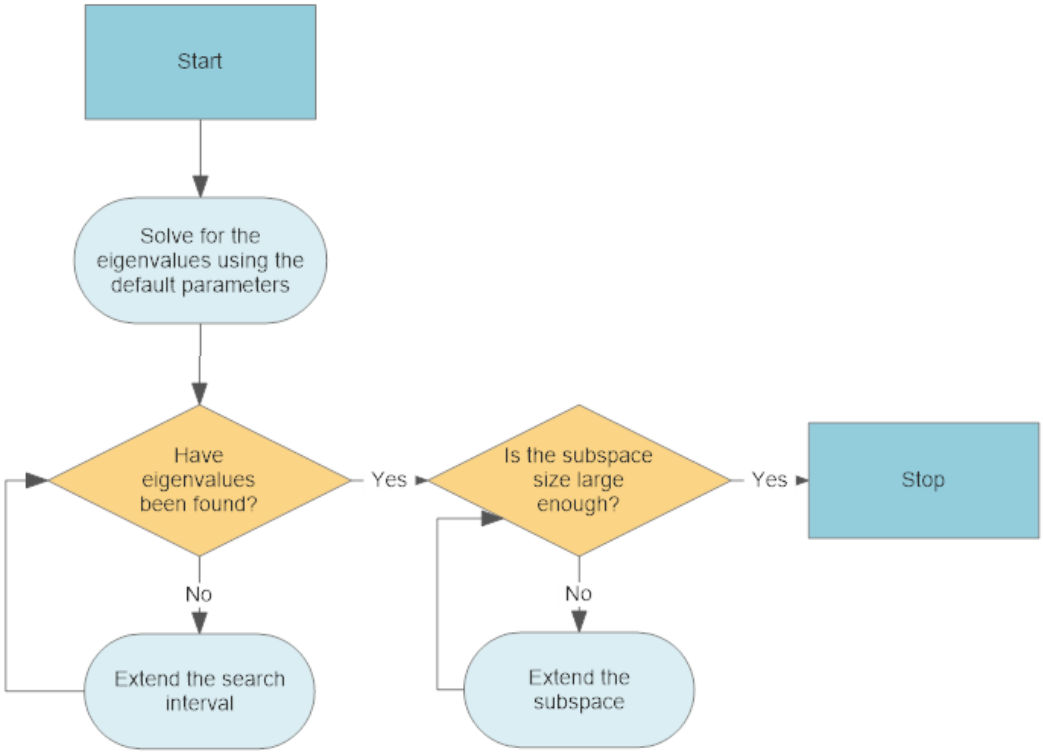

Figure 5.1: Algorithm implemented for the search for eigenvalues and eigenvectors

Another option offered to the analyst is to manually enter a search interval and a subspace size, which can optimize the computational cost when a gross estimate of the

searched eigenvalue can be made and when modes are well sufficiently distinct from one another.

5.2 THE GEOMETRICALLY NONLINEAR ANALYSIS

Steel bridges are flexible systems during erection and construction. A linear elastic analysis may be inaccurate in capturing bridge behavior because second-order effects can become significant. Conducting a geometrically nonlinear analysis, where the equilibrium of the structure is checked in its deformed shape, gives the most accurate estimation of the displacements, cross-frame forces, and other quantities. The increase in accuracy, however, comes with a corresponding increase in computational time and effort needed to obtain a solution. This section describes how geometrically nonlinear analyses are implemented in UT Bridge V2.2.

5.2.1 ASSUMPTIONS

Similarly to what was done for the linear elastic analysis, UT Bridge V2.2 assumes an elastic stress-strain law for steel and concrete. Again, this assumption is reasonable as stresses encountered during erection and construction remain low and well less than those associated with inelastic response. In addition, the program assumes the loads are deformation-independent. As such, the direction of the load does not change as the structure gradually deforms. This assumption is appropriate as all the loads modeled in the program are indeed deformation-independent. Gravity, for example, always acts in the vertical direction. Wind loads act in a specified direction as well. Finally, the program considers large displacements but small strains only. As described by Bathe (1982), this means that displacements and rotations may be large, but that fiber extensions and angle changes between fibers remain small (Figure 5.2).

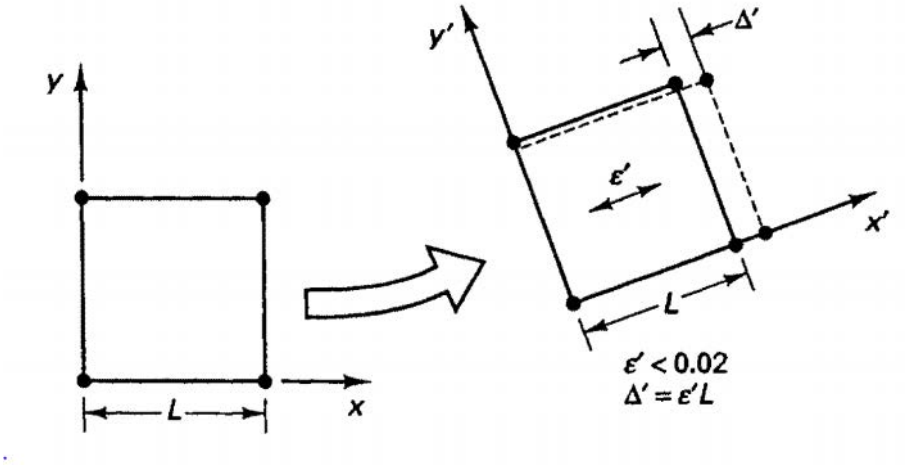

Figure 5.2: Large displacements and large rotations but small strains (adapted from Bathe 1982)

5.2.2 METHOD

The program considers an updated Lagrangian formulation, meaning that all static and kinematic variables are referred to the last computed configuration (Bathe 1982). This formulation differs from the total Lagrangian formulation, where the variables are referred to the initial configuration. There are two benefits of using the updated Lagrangian formulation. First, the shell stresses computed for each load increment are the Cauchy stresses, or "true" stresses. Those stresses have an actual physical meaning, unlike the second Piola-Kirchhoff stresses corresponding to the total Lagrangian formulation (Bathe 1982). Second, after initially trying to use the total Lagrangian formulation, it was found that the computational cost involved in the updated Lagrangian formulation is about fifteen percent lower, due to faster assembly of the tangent stiffness matrix at each load increment.

As far as the evaluation of the tangent stiffness matrix is concerned, a modified Newton-Raphson approach is considered. Accordingly, the overall stiffness matrix is

updated at each load increment, though not at each iteration within that load increment. Updating of the nodal director vectors is also performed at each load increment only. Updating those vectors at each iteration is a reasonable assumption, but it was found that doing so does not bring any additional accuracy to the computed displacements, and it increases the computational cost. It should be noted that the modified Newton-Raphson approach is able to evaluate pre-buckling behavior only. Post-buckling behavior would require the use of an arc-length method of some type (Bathe 1982). For bridges under erection and construction, buckling is the critical limit state, so there is no particular interest in post-buckling behavior.

By default, the program considers 25 equally-spaced load increments. This number was selected through trial and error. The fine discretization is implemented to address severe cases where second-order effects are particularly significant. However, the program also allows the user to manually define the number of load increments. These increments can be fixed, or the program can automatically compute the step length based on the performance of the Newton-Raphson algorithm for the previous load increment, as defined in Equation 5.14:

$$ {}^{t}\Delta\lambda = {}^{t-1}\Delta\lambda \cdot \sqrt{\frac{N_d}{{}^{t-1}N}} $$

Equation 5.14

where:

${}^{t}\Delta\lambda$ is the step length at time *t*

${}^{t-1}\Delta\lambda$ is the step length at time *t*-1

N_d is the desired number of iterations per load increment, specified by the user

${}^{t-1}N$ is the number of iterations achieved to reach convergence at time *t*-1.

Thus, the program updates the step length based on the convergence rate achieved during the previous load increment. If convergence was reached faster than expected, a larger step size is specified. Conversely, for slow convergence rates, the step size is reduced. For the first load increment, an initial step length is selected by the user.

Finally, the convergence criterion selected is based on the relative norm of the residual force vector. At each load increment, the residual force vector is the difference between the vector corresponding to the externally applied loads and the vector of nodal point forces corresponding to the stresses at that load increment (Bathe 1982). Convergence is reached at iteration *i* when:

$$\left\| \frac{{}^{t+\Delta t}R - {}^{t+\Delta t}F^{(i)}}{{}^{t+\Delta t}R} \right\| < \epsilon$$

Equation 5.15

Where ϵ is typically equal to 0.01. This tolerance value was selected by trial and error: a value of 0.1 yields inaccurate solutions, while a value of 0.001 significantly increases the computational cost.

5.2.3 ITERATIVE PROCESS

The geometrically nonlinear analysis involves the updating of the nodal director vectors at each load increment. This step is necessary for proper updating of the tangent stiffness matrix. At each iteration within a specified load increment, the iterative equations are as follows:

$$ {}^{t}_{t}\boldsymbol{K} \cdot \Delta \boldsymbol{U}^{(i)} = \beta^{(i)} \cdot \left({}^{t+\Delta t}\boldsymbol{R} - {}^{t+\Delta t}\boldsymbol{F}^{(i-1)} \right) \qquad \textit{Equation 5.16} $$

where:

${}^{t}_{t}\boldsymbol{K}$ is the tangent stiffness matrix at time t evaluated in the configuration at time t

$\Delta \boldsymbol{U}^{(i)}$ is the vector of incremental displacements at time t and iteration i

${}^{t+\Delta t}\boldsymbol{R}$ is the vector of externally applied loads

${}^{t+\Delta t}\boldsymbol{F}^{(i-1)}$ is the vector of nodal point forces computed from the internal stresses at time $t+\Delta t$ and iteration (i-1).

At each iteration, the incremental displacement at time t is updated using Equation 5.17:

$$ {}^{t}\boldsymbol{U} = {}^{t}\boldsymbol{U} + \Delta \boldsymbol{U}^{(i)} \qquad \textit{Equation 5.17} $$

It should be noted that only a fraction $\beta^{(i)}$ of the out-of-balance load vector is applied to the structure at each iteration. For curved systems, it was indeed found that applying the total out-of-balance load vector would rapidly lead to divergence of the solution. The coefficient β is updated at each iteration within the load increment, depending on the convergence rate of the solution. Typically, β is equal to 0.1 for the first iteration, but then quickly increases to 0.5. It was found that after a few iterations, increasing β to values greater than 1, such as 1.5, further accelerates the convergence rate. The optimization of the β factor is critical to optimizing the speed of convergence.

5.2.4 FORMULATION OF THE TANGENT STIFFNESS MATRIX

The tangent stiffness matrix is derived at the beginning of each load increment, starting from the second load increment. For the first load increment, there is no need to derive the tangent stiffness matrix, and the program simply uses the stiffness matrix assembled for the linear elastic analysis. For all further increments, assembly of the tangent stiffness matrix is performed by adding together the linear and nonlinear stiffness matrices:

$$ {}_{t}^{t}\boldsymbol{K} = {}_{t}^{t}\boldsymbol{K_L} + {}_{t}^{t}\boldsymbol{K_{NL}} \qquad \textit{Equation 5.18} $$

where:

$$ {}_{t}^{t}\boldsymbol{K_L} = \int {}_{t}^{t}\boldsymbol{B_L^T} \cdot \boldsymbol{C} \cdot {}_{t}^{t}\boldsymbol{B_L} \cdot dV $$

Equation 5.19

and:

$$ {}_{t}^{t}\boldsymbol{K_{NL}} = \int {}_{t}^{t}\boldsymbol{B_{NL}^T} \cdot {}_{t}^{t}\boldsymbol{S} \cdot {}_{t}^{t}\boldsymbol{B_{NL}} \cdot dV $$

Equation 5.20

Numerical integration is performed using the same integration points as for the linear elastic analysis. The linear and non-linear strain-displacement matrices are 6×40 matrices. Columns number 5(*k*-1)+1 up to 5(*k*-1)+5, corresponding to the five degrees of freedom at nodal point *k,* are shown below in Equation 5.21:

$$
{}^{t}_{t}\boldsymbol{B_L} = \begin{bmatrix}
\cdots & \partial h_k/\partial x & & & g^k_{1x}G^k_x & g^k_{2x}G^k_x & \cdots \\
\cdots & & \partial h_k/\partial y & & g^k_{1y}G^k_y & g^k_{2y}G^k_y & \cdots \\
\cdots & & & \partial h_k/\partial z & g^k_{1z}G^k_z & g^k_{2z}G^k_z & \cdots \\
\cdots & \partial h_k/\partial y & \partial h_k/\partial x & & g^k_{1x}G^k_y + g^k_{1y}G^k_x & g^k_{2x}G^k_y + g^k_{2y}G^k_x & \cdots \\
\cdots & \partial h_k/\partial z & & \partial h_k/\partial x & g^k_{1x}G^k_z + g^k_{1z}G^k_x & g^k_{2x}G^k_z + g^k_{2z}G^k_x & \cdots \\
\cdots & & \partial h_k/\partial z & \partial h_k/\partial y & g^k_{1y}G^k_z + g^k_{1z}G^k_y & g^k_{2y}G^k_z + g^k_{2z}G^k_y & \cdots
\end{bmatrix}
$$

Equation 5.21

and:

$$
{}^{t}_{t}\boldsymbol{B_{NL}} = \begin{bmatrix}
\cdots & \partial h_k/\partial x & & & g^k_{1x}G^k_x & g^k_{2x}G^k_x & \cdots \\
\cdots & & \partial h_k/\partial x & & g^k_{1y}G^k_x & g^k_{2y}G^k_x & \cdots \\
\cdots & & & \partial h_k/\partial x & g^k_{1z}G^k_x & g^k_{2z}G^k_x & \cdots \\
\cdots & \partial h_k/\partial y & & & g^k_{1x}G^k_y & g^k_{2x}G^k_y & \cdots \\
\cdots & & \partial h_k/\partial y & & g^k_{1y}G^k_y & g^k_{2y}G^k_y & \cdots \\
\cdots & & & \partial h_k/\partial y & g^k_{1z}G^k_y & g^k_{2z}G^k_y & \cdots \\
\cdots & \partial h_k/\partial z & & & g^k_{1x}G^k_z & g^k_{2x}G^k_z & \cdots \\
\cdots & & \partial h_k/\partial z & & g^k_{1y}G^k_z & g^k_{2y}G^k_z & \cdots \\
\cdots & & & \partial h_k/\partial z & g^k_{1z}G^k_z & g^k_{2z}G^k_z & \cdots
\end{bmatrix}
$$

Equation 5.22

The linear strain-displacement matrix is similar to the one used for the linear elastic analysis, while the nonlinear strain-displacement analysis is similar to the one used for the linearized buckling analysis. A major difference though is that both strain-displacement matrices are evaluated using the shell spatial configuration at time t, instead of the initial, undeformed configuration. In addition, while the stress-strain matrix $\boldsymbol{C}$ is constant through the deformation, the Cauchy stress matrix ${}^{t}_{t}\boldsymbol{S}$ is updated at each load increment by first calculating the incremental Green-Lagrange strain vector $\boldsymbol{\varepsilon}$ from time t-Δt to time t:

$$\boldsymbol{\varepsilon} = {}_{t}^{t}\boldsymbol{B}_{\boldsymbol{L}} \cdot \hat{\boldsymbol{u}} \qquad \textit{Equation 5.23}$$

where $\hat{\boldsymbol{u}}$ is the incremental displacement vector from time t-Δt to time t.

The incremental Cauchy stress vector $\boldsymbol{\tau}$ from time t-Δt to time t is calculated as:

$$\boldsymbol{\tau} = \boldsymbol{C} \cdot \boldsymbol{\varepsilon} \qquad \textit{Equation 5.24}$$

The Cauchy stress vector at time t is then derived:

$${}_{t}^{t}\hat{\boldsymbol{S}} = {}_{t-\Delta t}^{t-\Delta t}\hat{\boldsymbol{S}} + \boldsymbol{\tau} \qquad \textit{Equation 5.25}$$

Finally, the Cauchy stress matrix at time t is assembled from the Cauchy stress vector:

$$\boldsymbol{{}_{t}^{t}S} = \begin{bmatrix} {}_{t}^{t}\hat{S}_1 & & & {}_{t}^{t}\hat{S}_4 & & & {}_{t}^{t}\hat{S}_5 & & \\ & {}_{t}^{t}\hat{S}_1 & & & {}_{t}^{t}\hat{S}_4 & & & {}_{t}^{t}\hat{S}_5 & \\ & & {}_{t}^{t}\hat{S}_1 & & & {}_{t}^{t}\hat{S}_4 & & & {}_{t}^{t}\hat{S}_5 \\ {}_{t}^{t}\hat{S}_4 & & & {}_{t}^{t}\hat{S}_2 & & & {}_{t}^{t}\hat{S}_6 & & \\ & {}_{t}^{t}\hat{S}_4 & & & {}_{t}^{t}\hat{S}_2 & & & {}_{t}^{t}\hat{S}_6 & \\ & & {}_{t}^{t}\hat{S}_4 & & & {}_{t}^{t}\hat{S}_2 & & & {}_{t}^{t}\hat{S}_6 \\ {}_{t}^{t}\hat{S}_5 & & & {}_{t}^{t}\hat{S}_6 & & & {}_{t}^{t}\hat{S}_3 & & \\ & {}_{t}^{t}\hat{S}_5 & & & {}_{t}^{t}\hat{S}_6 & & & {}_{t}^{t}\hat{S}_3 & \\ & & {}_{t}^{t}\hat{S}_5 & & & {}_{t}^{t}\hat{S}_6 & & & {}_{t}^{t}\hat{S}_3 \end{bmatrix}$$

Equation 5.26

This operation is conducted for all shells at each integration point, which means that the tangent stiffness matrix assembly is computationally intensive. In addition, for

curved systems, transformation of the tangent stiffness matrix from the global coordinate system to the nodal local curvilinear system (or any other local coordinate system, depending on the restraint orientation) is required at the supports for all horizontal displacements degrees of freedom.

For all braces, the tangent stiffness matrix is assembled using the same formulation for the chord linear and nonlinear tangent stiffness matrices, expressed using natural coordinates (Bathe 1982):

$$ {}^{t}_{t}\boldsymbol{K_L} = \frac{EA}{L_0} \cdot \begin{bmatrix} 1 & -1 \\ -1 & 1 \end{bmatrix} $$

Equation 5.27

where L_0 is the initial length of the chord.

And:

$$ {}^{t}_{t}\boldsymbol{K_{NL}} = \frac{{}^{t}P}{L_0} \cdot \begin{bmatrix} 1 & -1 \\ -1 & 1 \end{bmatrix} $$

Equation 5.28

Where the axial force in the chord is expressed in the following equation, using ${}^{t}L$ to denote the chord length at time t (Bathe 1982):

$$ {}^{t}P = EA \cdot \frac{{}^{t}L - L_0}{L_0} $$

Equation 5.29

5.2.5 FORMULATION OF THE STRESS-EQUIVALENT NODAL POINT VECTOR

The nodal point vector equivalent to the shell stresses at time t and iteration i is updated using the following equation (Bathe 1982):

$$ {}^{t}_{t}\boldsymbol{F}^{(i)} = {}^{t}_{t}\boldsymbol{F}^{(i-1)} + {}^{t}_{t}\boldsymbol{B}_{L} \cdot \boldsymbol{\tau}^{(i)} \qquad \textit{Equation 5.30} $$

Where ${}^{t}_{t}\boldsymbol{B}_{L}$ is the linear strain-displacement matrix, already described in the previous paragraph, and $\boldsymbol{\tau}^{(i)}$ is the incremental Cauchy stress vector from iteration i-1 to iteration i, derived in the following manner:

$$ \boldsymbol{\tau}^{(i)} = \boldsymbol{\tau}^{(i)} + \boldsymbol{C} \cdot {}^{t}_{t}\boldsymbol{B}_{L} \cdot \Delta \boldsymbol{U}^{(i)} \qquad \textit{Equation 5.31} $$

where $\Delta U^{(i)}$ is the incremental displacement vector from iteration i-1 to iteration i.

Again, for curved systems, transformation of the nodal point vector equivalent to the stresses is required at the support nodes.

5.2.6 UPDATE OF THE NODAL DIRECTOR VECTORS

The formulation of the tangent stiffness matrix and the nodal point vector equivalent to the stresses requires the nodal director vectors to be updated at each load increment. The normal director vector at each shell node is updated using a formula similar to the one encountered during the linear elastic analysis:

$$ {}^{t+\Delta t}\boldsymbol{V}_{N}^{k} = {}^{t}\boldsymbol{V}_{N}^{k} - {}^{t}\boldsymbol{V}_{2}^{k} \cdot \alpha_{k} + {}^{t}\boldsymbol{V}_{1}^{k} \cdot \beta_{k} \qquad \textit{Equation 5.32} $$

where α_k and β_k are the incremental rotations at nodal point k from time t to time $t+\Delta t$.

The update of the tangent director vectors differs according to whether the bridge is straight or curved. For straight systems, flange and web elements are updated using the formula:

$$^{t+\Delta t}\boldsymbol{V}_{\boldsymbol{1}}^{\boldsymbol{k}} = \boldsymbol{e}_{\boldsymbol{2}} \times {}^{t+\Delta t}\boldsymbol{V}_{\boldsymbol{N}}^{\boldsymbol{k}} \qquad \textbf{\textit{Equation 5.33}}$$

Transverse web stiffeners are initially orthogonal to the *y*-axis, so updating the first nodal tangent director vector is performed differently:

$$^{t+\Delta t}\boldsymbol{V}_{\boldsymbol{1}}^{\boldsymbol{k}} = \boldsymbol{e}_{\boldsymbol{1}} \times {}^{t+\Delta t}\boldsymbol{V}_{\boldsymbol{N}}^{\boldsymbol{k}} \qquad \textbf{\textit{Equation 5.34}}$$

The second nodal tangent director vector is then obtained using:

$$^{t+\Delta t}\boldsymbol{V}_{\boldsymbol{2}}^{\boldsymbol{k}} = {}^{t+\Delta t}\boldsymbol{V}_{\boldsymbol{N}}^{\boldsymbol{k}} \times {}^{t+\Delta t}\boldsymbol{V}_{\boldsymbol{1}}^{\boldsymbol{k}} \qquad \textbf{\textit{Equation 5.35}}$$

For curved systems, the same formulas cannot be applied to flange elements because the normal director vectors for these elements are uniformly oriented upward. Consequently, Equation 5.33 would give a uniform distribution for the first tangent vector. Instead, it was decided to use compatibility equations at the flange-to-web nodes. Update of the tangent director vectors is therefore achieved in the following order. First, the program updates the vectors for all webs and stiffeners:

$$^{t+\Delta t}\boldsymbol{V}_{\boldsymbol{1}}^{\boldsymbol{k}} = \boldsymbol{e}_{\boldsymbol{2}} \times {}^{t+\Delta t}\boldsymbol{V}_{\boldsymbol{N}}^{\boldsymbol{k}} \quad \text{for web elements} \qquad \textbf{\textit{Equation 5.36}}$$

$$^{t+\Delta t}\boldsymbol{V}_{\boldsymbol{1}}^{\boldsymbol{k}} = -\boldsymbol{e}_{\boldsymbol{3}}$$ for transverse web stiffener elements ***Equation 5.37***

and:

$$^{t+\Delta t}\boldsymbol{V}_{\boldsymbol{2}}^{\boldsymbol{k}} = {}^{t+\Delta t}\boldsymbol{V}_{\boldsymbol{N}}^{\boldsymbol{k}} \times {}^{t+\Delta t}\boldsymbol{V}_{\boldsymbol{1}}^{\boldsymbol{k}}$$ ***Equation 5.38***

Then, using compatibility between the flange and the web, the program updates the tangent director vectors for all flange elements:

$$^{t+\Delta t}\boldsymbol{V}_{\boldsymbol{1,flange}}^{\boldsymbol{k}} = {}^{t+\Delta t}\boldsymbol{V}_{\boldsymbol{N,web}}^{\boldsymbol{k}}$$ ***Equation 5.39***

and:

$$^{t+\Delta t}\boldsymbol{V}_{\boldsymbol{2,flange}}^{\boldsymbol{k}} = {}^{t+\Delta t}\boldsymbol{V}_{\boldsymbol{2,web}}^{\boldsymbol{k}}$$ ***Equation 5.40***

The previous equation can also be regarded as a way to preserve the merging of the second rotational degree of freedom at flange-to-web nodes. Finally, at the flange tips, the program assumes the same tangent director vectors as for the flange-to-web nodes. This approximation is valid for situations where lateral-torsional buckling or local web buckling prevails, as the flange as a whole describes a rigid-body type of rotation. Conversely, it is an incorrect assumption where local flange buckling controls, as the rotations over the flange are non-uniform. Local flange buckling typically controls for structures having considerable stiffness, which is unlikely for partially-erected, flexible structures prone to lateral-torsional or global lateral buckling. As such, the assumption employed for the flange tips is reasonable.

5.2.7 IMPLEMENTATION

Overall, the subroutine performing the geometrically nonlinear analysis can be briefly described in the following flowchart (Figure 5.3):

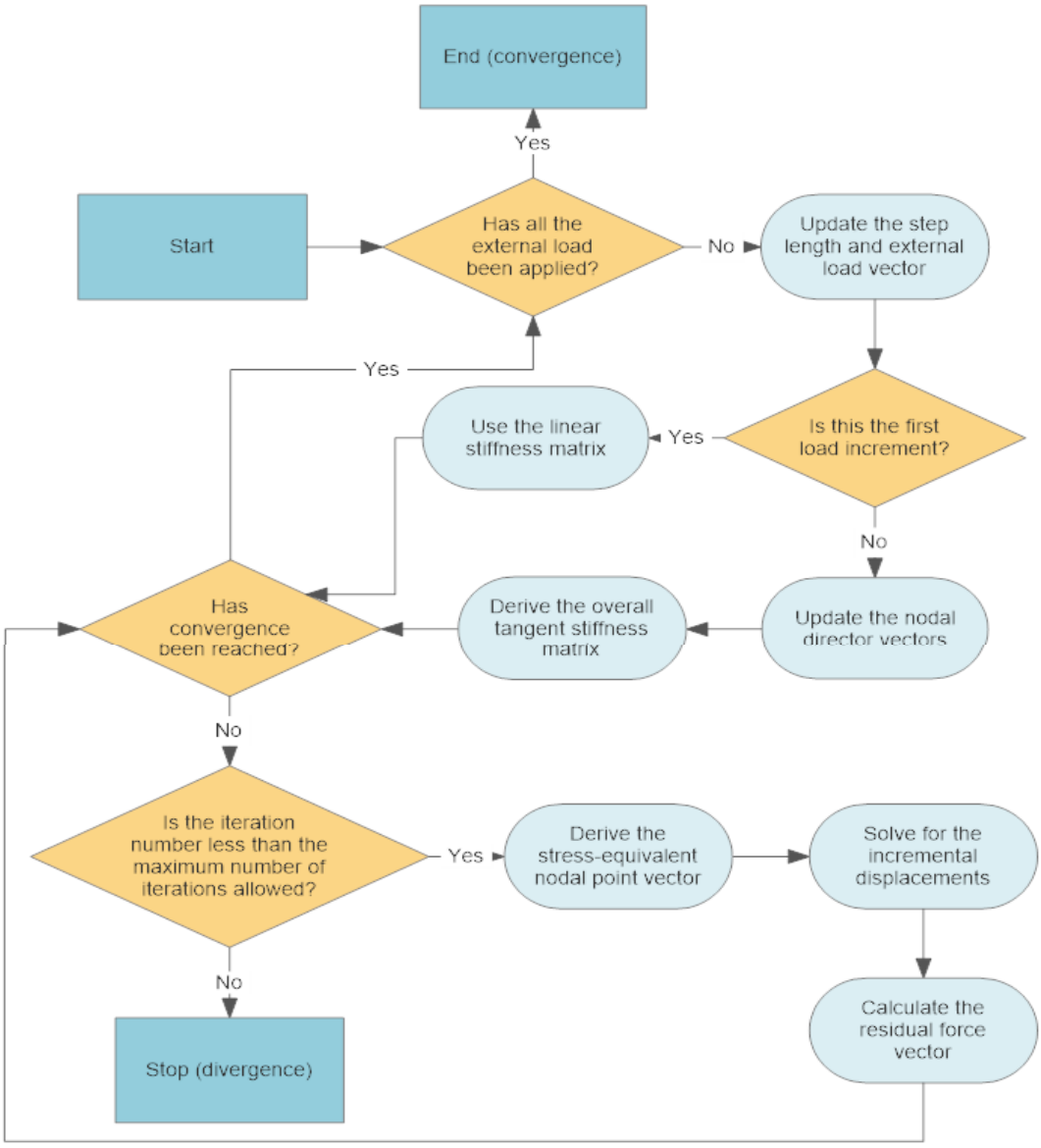

Figure 5.3: Geometrically nonlinear analysis flowchart

5.3 SUMMARY

This chapter described how the linearized buckling analyses, modal dynamic analyses, and geometrically nonlinear analyses are conducted by UT Bridge V2.2 and how some key modeling decisions were implemented into the code. In the next chapter, applications are presented to show the variety of situations the program can model.

Chapter 6: Applications

This chapter presents a series of examples that illustrate the capabilities of UT Bridge V2.2.

6.1 PLATE GIRDER STABILITY

In this first application, a 60-ft. long W30×90 is modeled with four elements through the web depth. The cross-sectional dimensions are 10.4-in. × 0.61-in. for the flanges and 28.89-in. × 0.47-in. for the web. The longitudinal mesh size implemented is equal to one foot. This model has approximately 8,120 unrestrained degrees of freedom.

6.1.1 BEAM BUCKLING, MOMENT DISTRIBUTION FACTOR AND LOAD HEIGHT EFFECT

The beam is simply-supported. Twist is restrained at the ends, but the flanges are free to warp. The beam is subjected to its self-weight only. The deflection and bending moment at mid-span given by beam theory are respectively equal to:

$$\Delta_{max} = \frac{5}{384} \cdot \frac{wL^4}{EI} = \frac{5}{384} \cdot \frac{0.00745 \cdot (60 \cdot 12)^4}{29{,}000 \cdot 3{,}705^4} = 0.24\ in$$

Equation 6.1

$$M_{max} = \frac{wL^2}{8} = \frac{0.0894 \cdot 60^2}{8} = 40.2\ k \cdot ft = 483\ k \cdot in$$

Equation 6.2

UT Bridge V2.2 gives a deflection of 0.25 in. and a bending moment of 483 k·in. (Figure 6.1), which is very close to the theoretical solution.

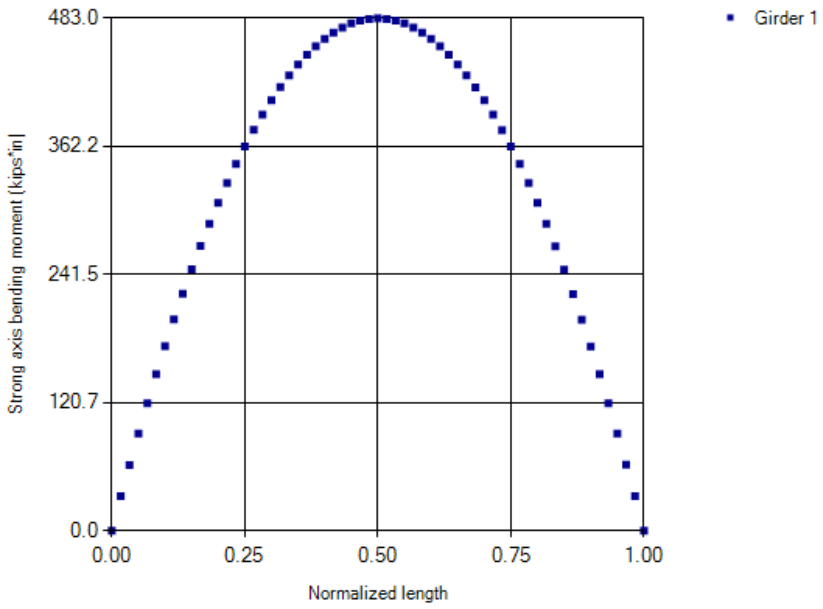

Figure 6.1: Moment diagram (self-weight)

According to Timoshenko's equation (Timoshenko and Gere 1963), the critical moment for the onset of lateral torsional buckling is equal to:

$$M_{cr} = C_b \cdot \frac{\pi}{L_b} \cdot \sqrt{EI_y GJ + E^2 \left(\frac{\pi}{L_b}\right)^2 I_y C_w}$$

Equation 6.3

$$M_{cr} = 1.14 \cdot \frac{\pi}{60 \cdot 12} \cdot \sqrt{29{,}000 \cdot 114 \cdot 11{,}154 \cdot 2.57 + 29000^2 \left(\frac{\pi}{60 \cdot 12}\right)^2 114 \cdot 24{,}881}$$

$$M_{cr} = 1{,}866\ k \cdot in$$

A linearized buckling analysis in UT Bridge V2.2 (Figure 6.2) gives a first eigenvalue equal to:

$$\lambda = 3.73$$

which means that the critical moment obtained from the program is equal to:

$$M_{cr} = 3.73 \cdot 483 = 1{,}802\ k \cdot in$$

which is 3.4% less than the value obtained from the Timoshenko equation.

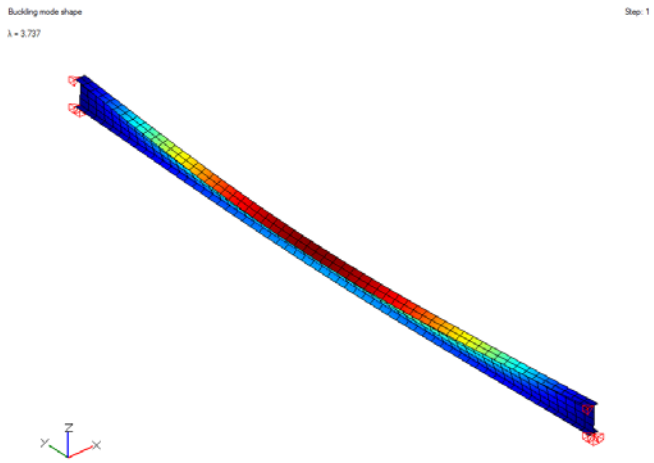

Figure 6.2: Beam buckling (self-weight)

If the self-weight is turned off and a point load is applied at mid-span at the centroid of the section, the first eigenvalue computed by the program is equal to:

$$\lambda = 12.06$$

and the moment at mid-span obtained from the program is equal:

$$M_{max} = 180\ k \cdot in$$

which means the moment distribution factor is equal to:

$$C_b = \frac{12.06 \cdot 180}{\frac{1{,}866}{1.14}} = 1.33$$

A value of 1.32 is provided in the AISC Steel Construction Manual (2017), which is fairly close.

If the load is applied at the top-flange-to-web junction, the first eigenvalue computed by the program becomes equal to:

$$\lambda = 8.83$$

This result means that the load-height correction factor is equal to:

$$\alpha = \frac{8.83}{12.06} = 0.73$$

The AISC Steel Construction Manual (2017) proposes the following equation for the correction factor:

$$\alpha = 1.4^{\frac{2y}{h}} = 1.4^{-1} = 0.73 \qquad \textbf{\textit{Equation 6.4}}$$

which is the exact same value obtained from the program.

6.1.2 IDEAL STIFFNESS

A lateral spring acting as a brace is added at mid-span at the top-flange-to-web junction. A transverse web stiffener is also added at mid-span on each side of the web to prevent web distortion. A uniform moment is applied to the beam by the use of point loads at the beam ends. The ideal stiffness β_i, defined as the minimum stiffness that leads to buckling of the structure between the brace points (Yura 2001), is calculated by trial and error and is equal to (Figure 6.3):

$$\beta_i = 0.72\ k/in$$

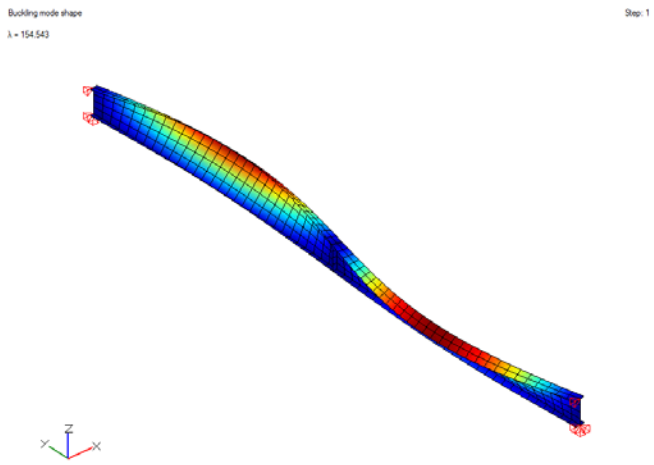

Figure 6.3: Beam lateral-torsional buckling (ideal brace stiffness at mid-span)

If instead, lateral springs are added at the beam third points (Figure 6.4), the computed ideal stiffness is equal to:

$$\beta_i = 3.58\ k/in$$

Finally, if lateral springs are added at the beam quarter points (Figure 6.5), the computed ideal stiffness is equal to:

$$\beta_i = 9.59\ k/in$$

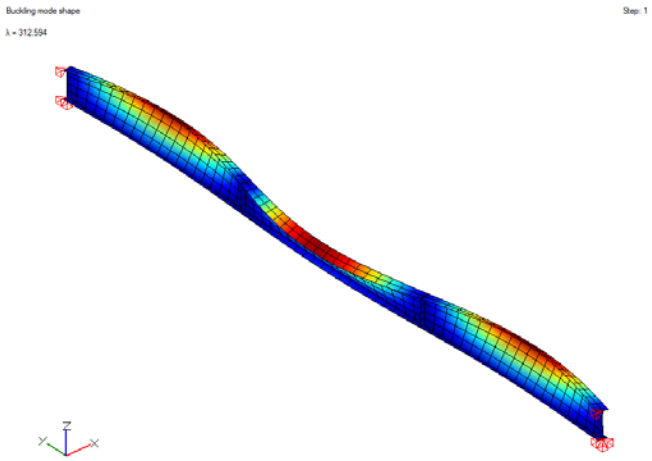

Figure 6.4: Beam lateral-torsional buckling (ideal brace stiffness at third points)

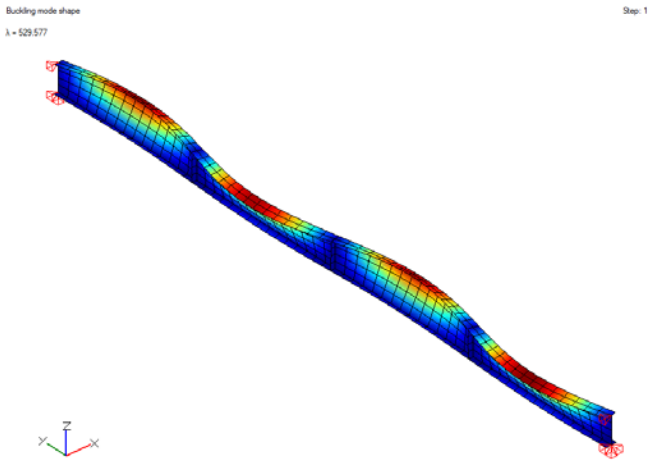

Figure 6.5: Beam lateral-torsional buckling (ideal brace stiffness at quarter points)

Those results are quite close to Winter's equation for the ideal lateral brace stiffness (Yura 2001), given by:

$$\beta_i = \frac{N_i \cdot P_f}{L_b}$$

Equation 6.5

where:

$$P_f = EI_{yc} \cdot \left(\frac{\pi}{L_b}\right)^2$$

Equation 6.6

and:

$N_i = 2$	If 1 brace is provided
$N_i = 3$	If 2 braces are provided
$N_i = 3.41$	If 3 braces are provided

yielding:

$$\beta_{i,1\ brace} = 0.70\ k/in$$
$$\beta_{i,2\ braces} = 3.55\ k/in$$
$$\beta_{i,3\ braces} = 9.57\ k/in$$

The maximum relative difference for those three expressions is indeed equal to 2.6%.

6.1.3 COLUMN BUCKLING, LATERAL AND TORSIONAL BRACING

The model is now subjected to uniform compression by applying point loads at the ends. The critical buckling load calculated by the program (Figure 6.6) is equal to:

$$P_{cr} = 63.3\ k$$

which is nearly identical (0.3% difference) to the Euler buckling load given by:

$$P_E = EI_y \cdot \left(\frac{\pi}{L_b}\right)^2 = 63.1\ k$$

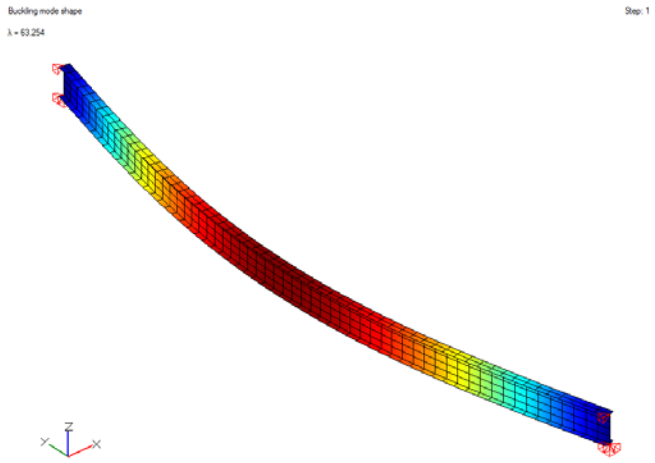

Figure 6.6: Column lateral buckling

If lateral bracing is provided at the third points at the top-flange-to-web junction and the bottom-flange-to-web junction, the unbraced length is only one third of its original value, and the critical load computed by the program (Figure 6.7) is equal to:

$$P_{cr} = 557.7\ k$$

For this case, the Euler buckling load is computed to be:

$$P_E = EI_y \cdot \left(\frac{\pi}{L_b}\right)^2 = 29{,}000 \cdot 114 \cdot \left(\frac{\pi}{240}\right)^2 = 568.3\ k$$

Which corresponds to a 1.9% difference between the computed value and the theoretical one.

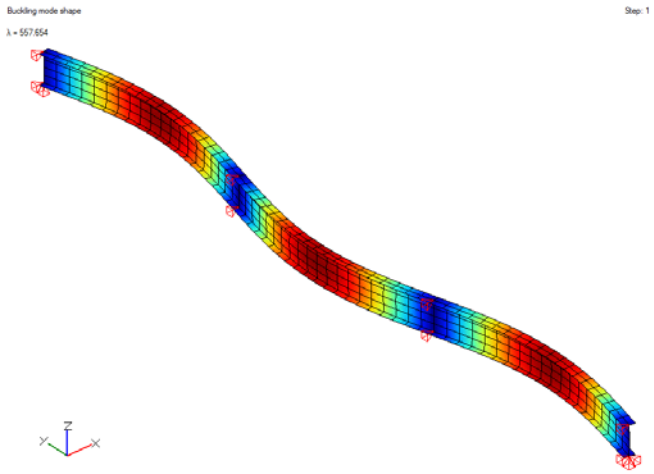

Figure 6.7: Column lateral buckling (lateral bracing at third points)

If instead, lateral movement is restrained at the flange centroid, torsional buckling controls (Figure 6.8), and the critical load computed by the program is equal to:

$$P_{cr} = 287.4\ k$$

Note that in this case, transverse web stiffeners were attached at the ends, otherwise distortion of the web at the ends reduces the critical load. This result can be compared with the column torsional capacity, derived by Timoshenko in the following expression:

$$P_T = \frac{P_{ey}\frac{d^2}{4} + GJ}{r_x^2 + r_y^2}$$

Equation 6.7

where:

$$P_{ey} = EI_y \cdot \left(\frac{\pi}{L_b}\right)^2$$

Using this formula, one obtains a critical load of:

$$P_T = \frac{63.1\frac{29.5^2}{4} + 11{,}115 \cdot 2.57}{11.9^2 + 2.1^2} = 291.9\ k$$

which is 1.5 percent larger than the value produced by UT Bridge V2.2.

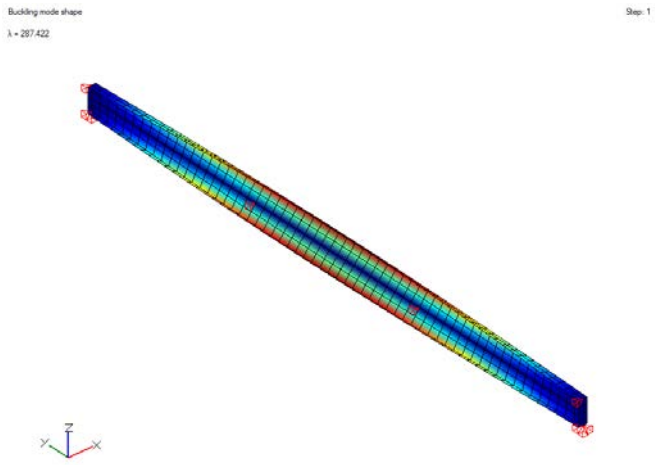

Figure 6.8: Column torsional buckling (lateral bracing at third points)

6.1.4 SENSITIVITY TO INITIAL IMPERFECTIONS

Shell structures in general are sensitive to initial imperfections, as they are primarily design to work in compression (Arbocz and Babcock 1980). An initial imperfection generally implies a reduction in the buckling capacity of a shell structure. In this example, in addition to gravity, a lateral notional load of 0.1 kip is applied at mid-span, at the top-flange-to-web junction. The magnitude of this point load represents only 1.8% of the beam self-weight (which is equal to 5.42 kips). Because plate girders are flexible in minor-axis bending, this small load still results in significant torsional effects. Torsional deformations contribute significantly to second-order effects. Figures 6.9 and 6.10 show how a geometrically nonlinear analysis is able to capture these second-order effects, leading to an overall amplification of the deformation of approximately 21.2%.

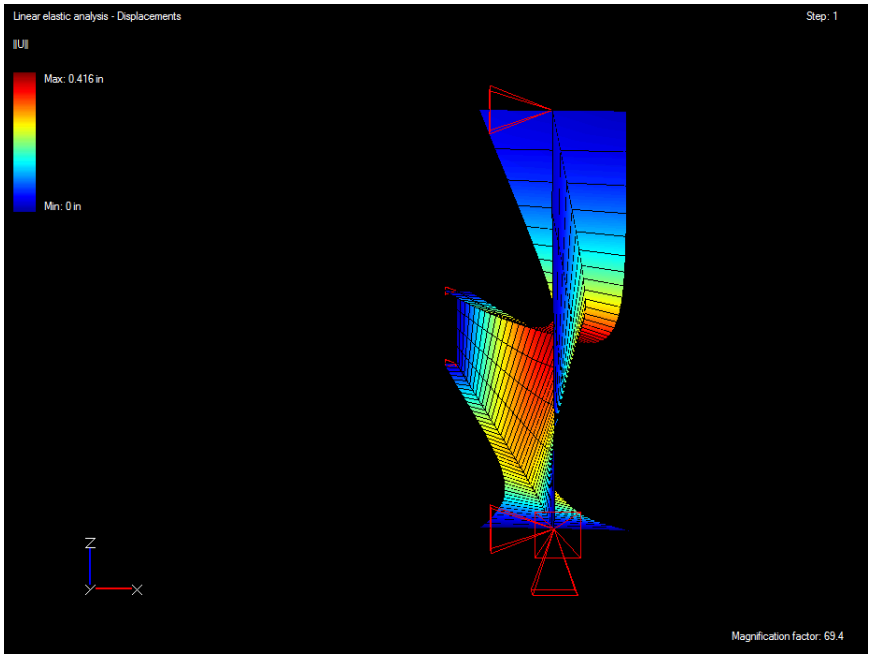

Figure 6.9: Deflected shape (linear elastic analysis, self-weight plus notional lateral load)

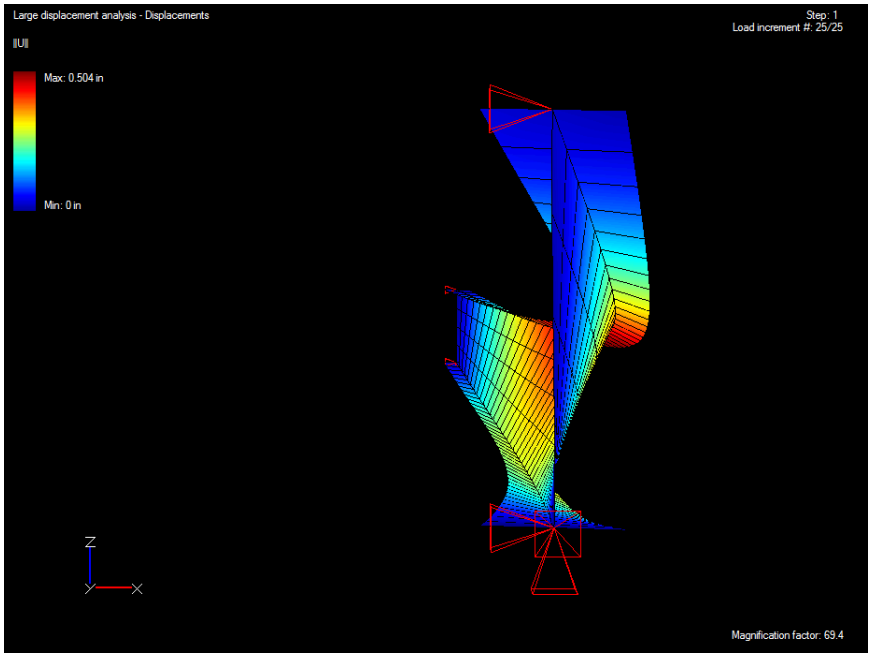

Figure 6.10: Deflected shape (geometrically nonlinear analysis, self-weight plus notional lateral load)

6.1.5 UNIFORM TEMPERATURE CHANGE AND THERMAL BUCKLING

For the case of a uniform temperature change of 20°C with no other loads acting, the calculated deflection at the end of the beam (Figure 6.11) is equal to:

$$\Delta = 0.144\ in$$

This value is identical to the theoretical solution of:

$$\Delta = \alpha \cdot \Delta T \cdot L = (10 \cdot 10^{-6}) \cdot 20 \cdot (60 \cdot 12) = 0.144\ in \qquad \textbf{\textit{Equation 6.8}}$$

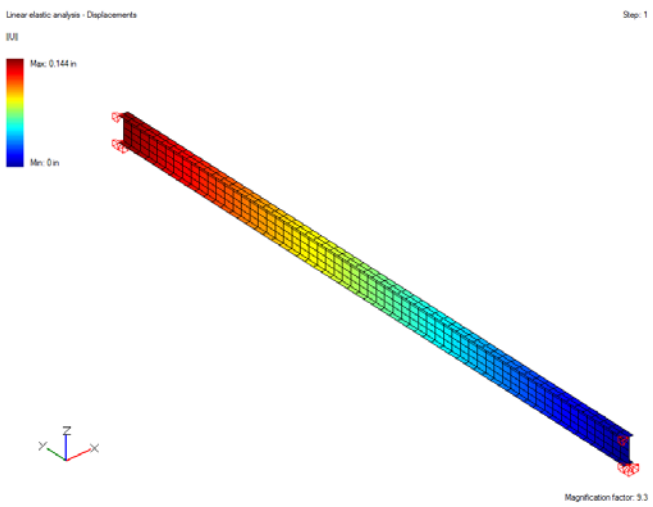

Figure 6.11: Deflected shape (uniform temperature change)

As the beam is free to deform, the stresses and support reactions computed by the program are equal to zero (Figure 6.12).

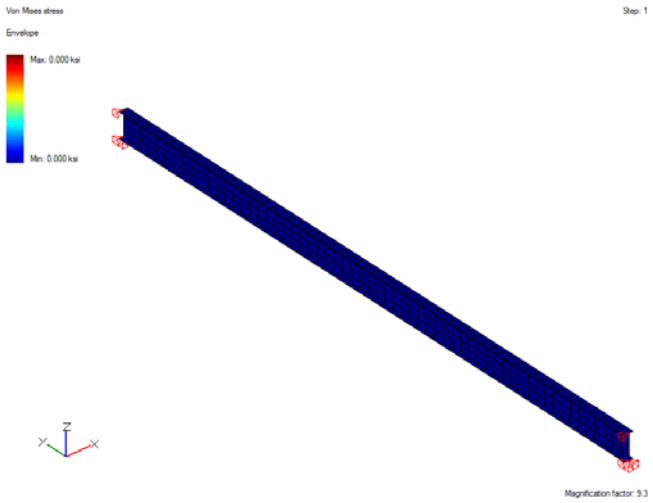

Figure 6.12: Von Mises stress invariant distribution (uniform temperature change)

6.1.6 GLOBAL BUCKLING

A second girder is modeled next to the first one. If the spacing between the girders is sufficiently small, global buckling controls. Here, a spacing of four feet is specified. Cross-frames with a cross-sectional area equal to 4.75 in^2 are attached at the quarter points on stiffeners that are 5-in. wide and 0.5-in. thick. A uniform moment distribution is created by applying point loads at the ends of the girders. The first buckling mode calculated by the program (Figure 6.13) is a global buckling mode, where:

$$\lambda = 272.13$$

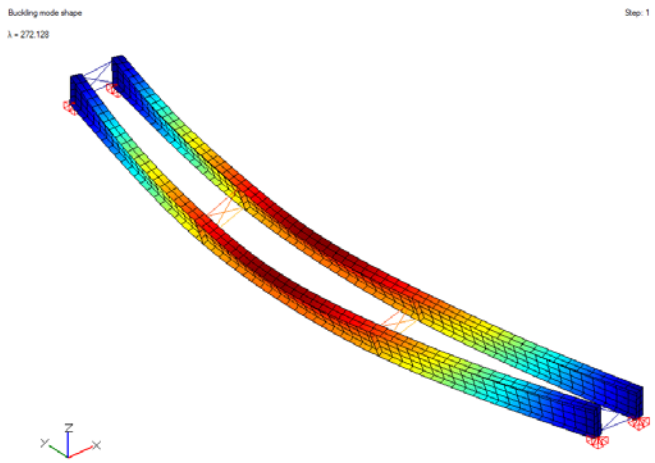

Figure 6.13: Twin girder system – global buckling

The critical moment obtained by the program is therefore equal to:

$$M_{cr} = \lambda \cdot M = 272.13 \cdot (1 \cdot 29.5) = 8{,}028\ k \cdot in = 669\ k \cdot ft$$

The system global buckling capacity equation proposed by Yura, Helwig et al. (2008) is the following:

$$M_{cr} = \frac{1}{2} \cdot \frac{\pi^2 SE}{L_g^2} \cdot \sqrt{I_y I_x}$$

Equation 6.9

where S is the girder spacing and L_g is the length of the bridge, yielding:

$$M_{cr} = \frac{1}{2} \cdot \frac{\pi^2 \cdot (4 \cdot 12) \cdot 29{,}000}{(60 \cdot 12)^2} \cdot \sqrt{114 \cdot 3705} = 8{,}626\ k \cdot in = 719\ k \cdot ft$$

In this case, the program gives a conservative estimate of the buckling capacity (9.3% relative difference). The flexibility of the X-frames connection to the girders, as well as the little warping restraint provided by the stiffeners (cf. Chapter 4) are believed to be responsible for this discrepancy.

6.1.7 EFFECT OF SKEW ON GLOBAL BUCKLING

The equation derived by Yura, Helwig et al. (2008) is valid for non-skewed systems only. A parametric study is conducted to evaluate the influence of the skew angle α on the buckling behavior of the twin-girder system described above. Two cross-frame arrangements are considered, parallel and staggered. For a parallel cross-frame arrangement, the lateral and torsional restraint provided at each brace point is equal to the cosine of that restraint without skew (Figures 6.14 and 6.15). For large skews, as the lateral restraint approaches zero, the parametric study shows that the buckling capacity of the twin-girder system tends to the buckling capacity of a single girder only, with an unbraced

length equal to the distance between the supports. The proposed equation is therefore the following:

$$\lambda_{twin-girder}(\alpha) = \lambda_{single\ girder} + \left(\lambda_{twin-girder,\alpha=0} - \lambda_{single\ girder}\right) \cdot \sin\alpha$$

Equation 6.10

Figure 6.18 shows that the proposed formula tends to under-predict the capacity computed by the software, at least for skew angles equal to less than 60 degrees.

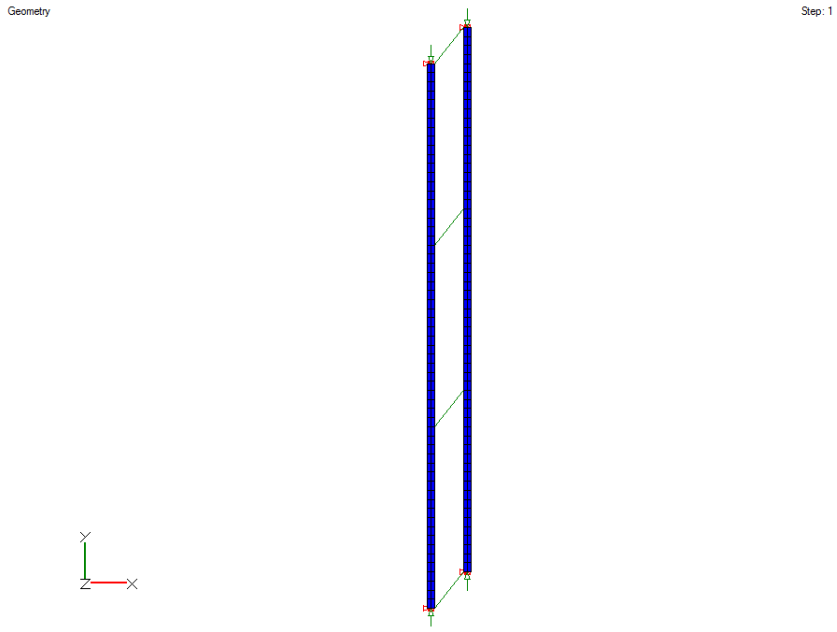

Figure 6.14: Twin girder system – Parallel cross-frame arrangement – 45-degree skew – Initial geometry

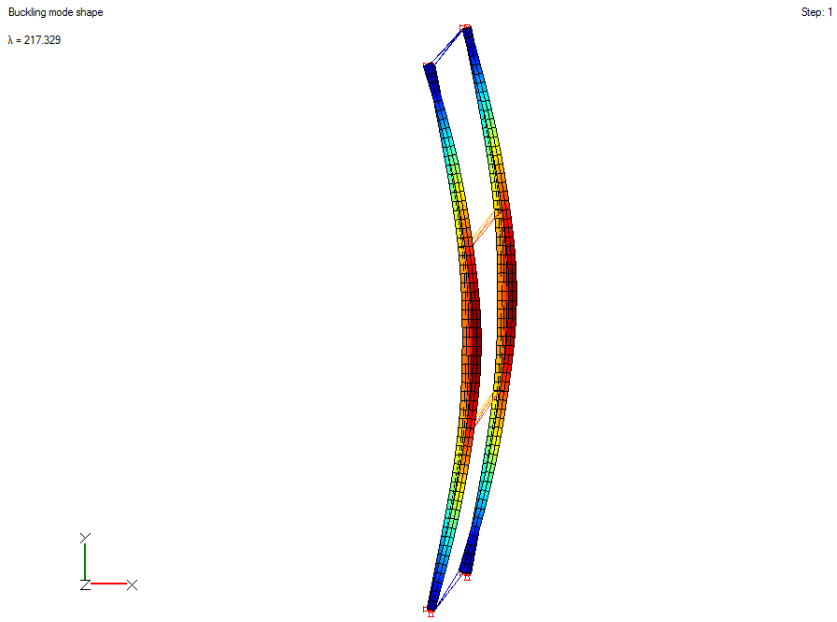

Figure 6.15: Twin girder system – Parallel cross-frame arrangement – 45-degree skew – buckled shape (λ = 217.33)

For a staggered cross-frame arrangement, the critical unbraced length, which is initially equal to the cross-frame spacing, gradually increases, until a cross-frame needs to be removed. The twin-girder system capacity therefore approaches that of a single girder system with an unbraced length equal to double the initial cross-frame spacing (Figures 6.16 and 6.17). For even larger skew angles, which in this case means extreme skew angles, only one intermediate cross-frame can be installed between the girders. As the skew angle keeps increasing, the critical unbraced length increases too, and the twin-girder system buckling capacity tends to that of a single girder system, with an unbraced length equal to three times the initial cross-frame spacing.

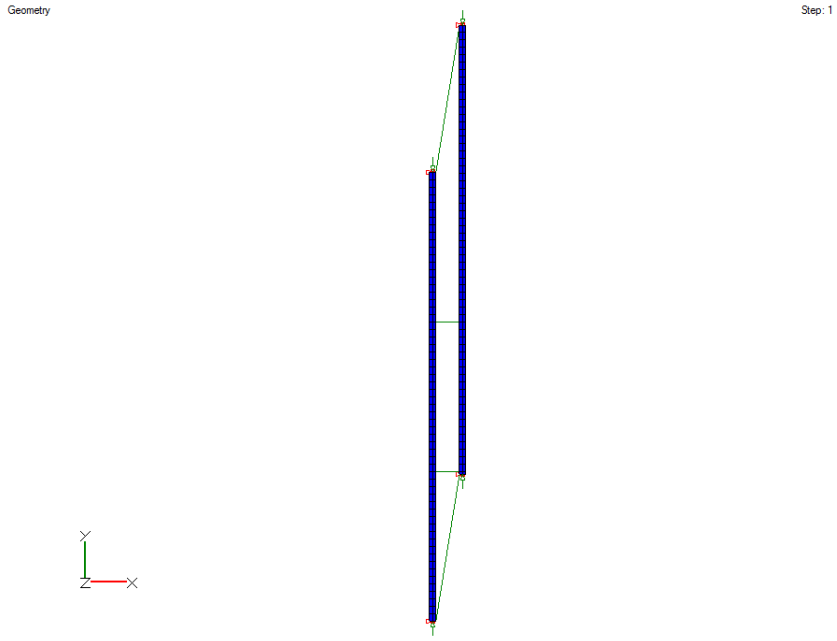

Figure 6.16: Twin girder system – Staggered cross-frame arrangement – 78.5-degree skew – initial geometry

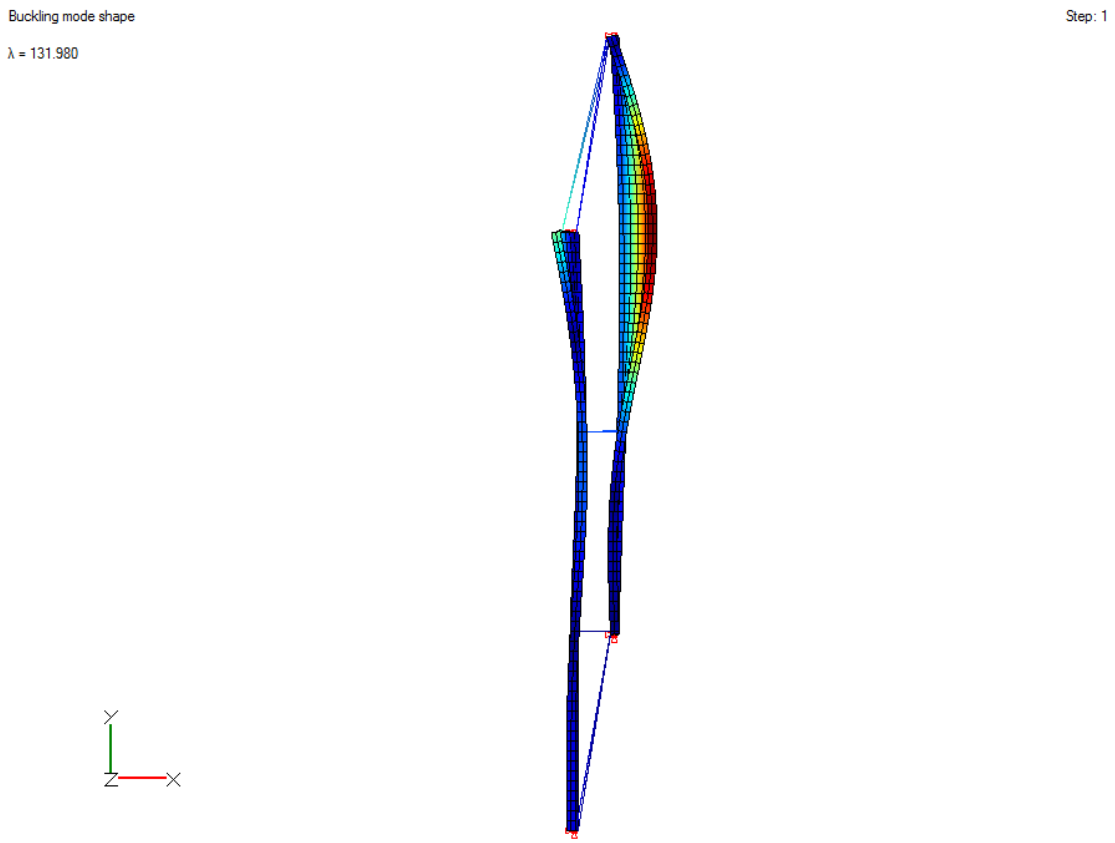

Figure 6.17: Twin girder system – Staggered cross-frame arrangement – 78.5-degree skew – buckled shape (λ = 131.98)

Figure 6.18 shows that a staggered cross-frame arrangement provides a little more stability to the twin-girder system than a parallel cross-frame arrangement, so a higher degree interpolation is considered. For the first portion of the curve, which means for a skew angle that is such that all cross-frames are kept on the structure, and for this cross-frame arrangement, the proposed equation is the following:

$$\lambda_{twin-girder}(\alpha) = \frac{\lambda_{single\ girder,L_b=2L_{b,initial}} - \lambda_{twin-girder,\alpha=0}}{\left(\arctan\left(\frac{L_{b,initial}}{s}\right)\right)^{2.5}} \cdot \alpha^{2.5} + \lambda_{twin-girder,\alpha=0}$$

Equation 6.11

where s is the girder spacing, and $L_{b,initial}$ is the original cross-frame spacing.

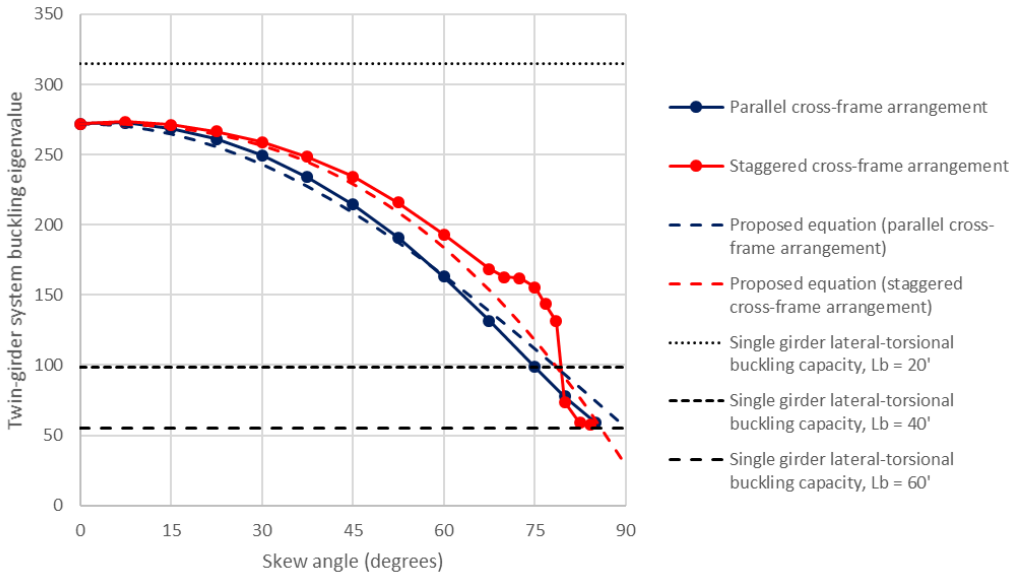

Figure 6.18: Effect of the skew angle on the twin-girder system buckling capacity

It should be noted that cross-frames on skewed systems are often mounted on bent plates, which are flexible and hence reduce the torsional restraint provided by the cross-frames to the girders. A study on split pipe stiffeners was conducted by Quadrato (2010), which showed how efficient this connection detail can be to restrain warping of the cross-section. UT Bridge V2.2 does not account for the additional flexibility (or reduced restraint) provided by the bent plate, nor does it model pipe stiffeners as such. Modeling pipe stiffeners is an area of improvement for the program.

6.2 CURVED PLATE GIRDER BRIDGE

In this second example, a curved plate girder bridge is modeled. The bridge geometry is adapted from Davidson and Yoo (1996). It consists of a three-girder single-span bridge, with a radius of curvature of 300’ for the exterior girder (Figure 6.19).

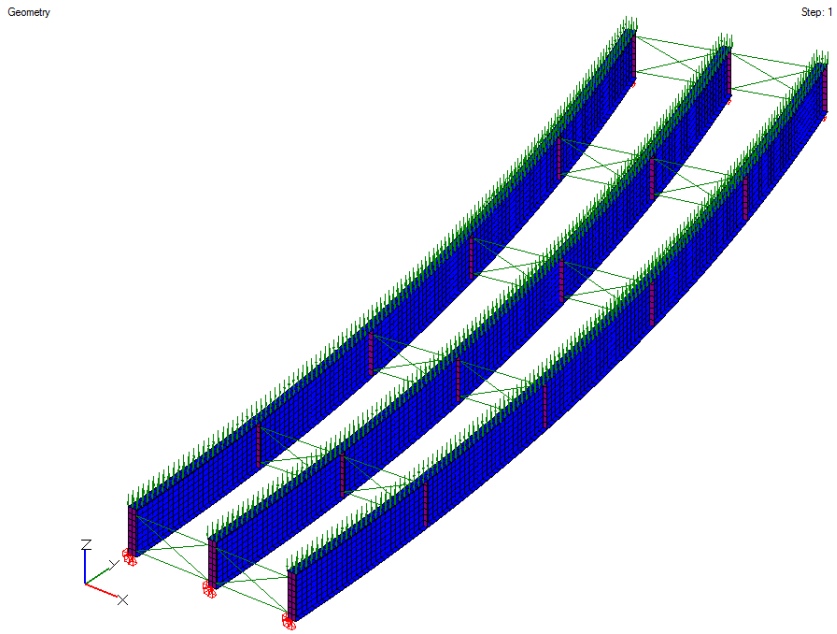

Figure 6.19: Geometry

Girder spacing is assumed to be equal to 9-ft. Cross-sectional dimensions are 12-in.×1-in. for the flanges, and 58-in.×0.5-in. for the web. A radial cross-frame arrangement is considered, resulting in an unbraced length of 18.8-ft. for the interior girder, and 20-ft. for the exterior girder. X-frames are mounted on 5-in.×0.5-in. stiffeners. As per Davidson and Yoo (1996), a uniform load is applied to the top flange equal to 1.034 k/ft^2 for the interior and exterior girders, and 1.247 k/ft^2 for the intermediate girder. This load models the self-weight of the steel superstructure in addition to an 8-in. thick concrete deck. Standard pin and roller supports are considered at both ends. The approximate longitudinal

mesh size is specified as 9 in., and eight elements through the web depth are considered to achieve fine accuracy associated with potential local web buckling modes. Overall, this model results in 15,831 nodes, 4,968 shell elements, and 80,976 unrestrained degrees of freedom.

6.2.1 MOMENT, SHEAR, TORSION AND LATERAL FLANGE MOMENT DIAGRAMS

Under the externally load applied, bending and torsion combine. The maximum calculated deflection by the program is equal to 5.7 in. (Figure 6.20).

The principal axis bending moment, shear, torsion, and lateral flange bending moments are shown in Figures 6.21-6.25. These diagrams are produced automatically by UT Bridge V2.2. Thus, no additional post-processing of the displacements or stresses is necessary. In addition, there is no need to copy and paste data to Excel to plot the diagrams.

The shear diagram, which is cut at the ends as numerical divergence was sometimes observed on other models, is consistent with the support reactions displayed by the program. For example, for the exterior girder, extrapolating the shear diagram up to the support leads to a shear at the support equal to 79.57 kips, which is essentially the same as the value of 78.56 kips calculated directly by the program.

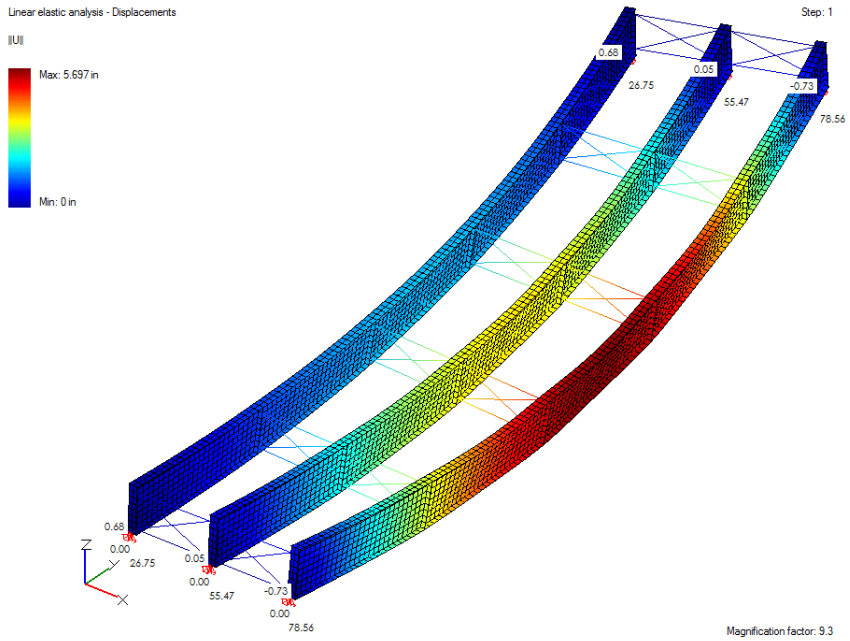

Figure 6.20: Deflected shape and support reactions (fine mesh)

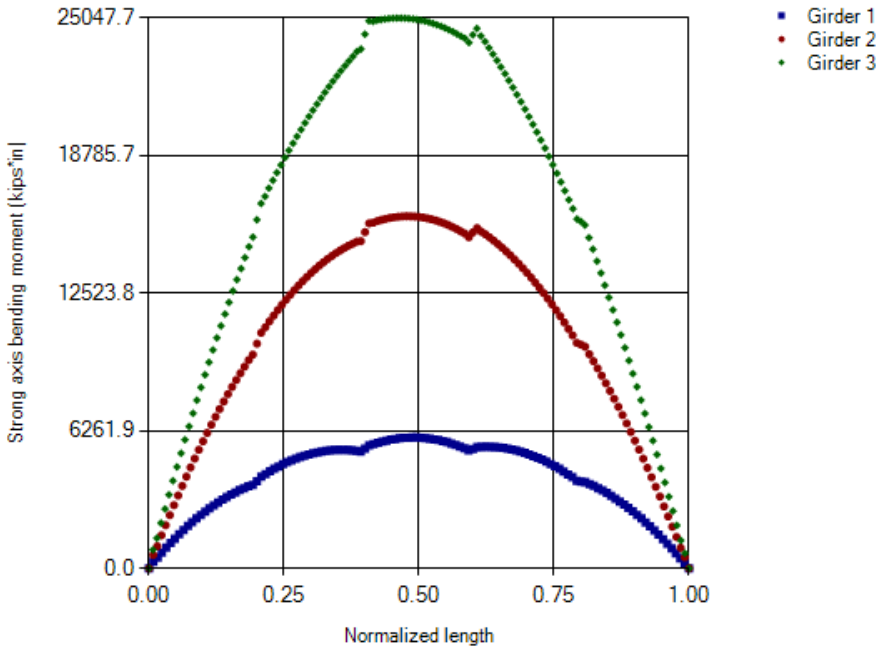

Figure 6.21: Principal axis moment diagram

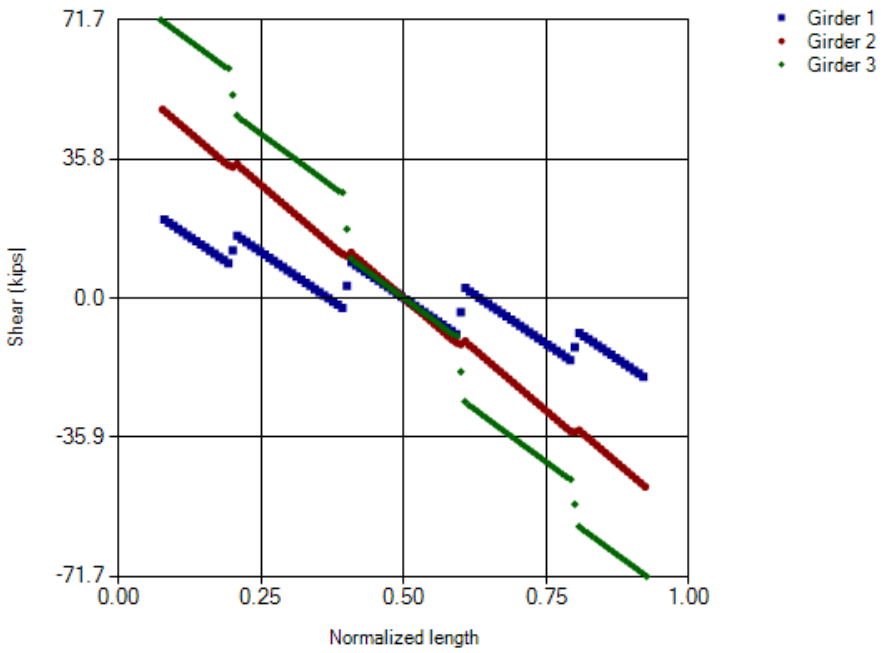

Figure 6.22: Shear diagram

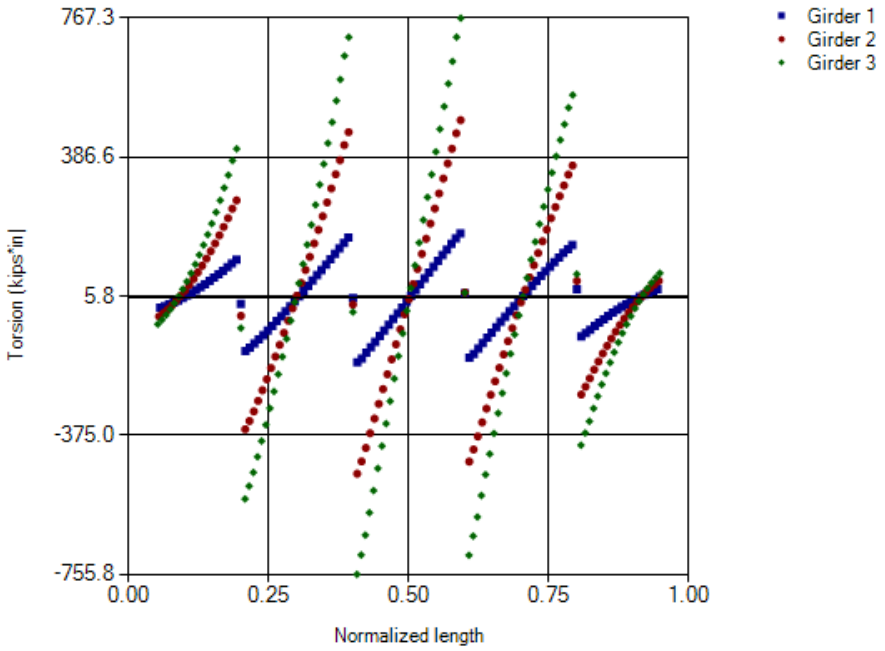

Figure 6.23: Torsion diagram

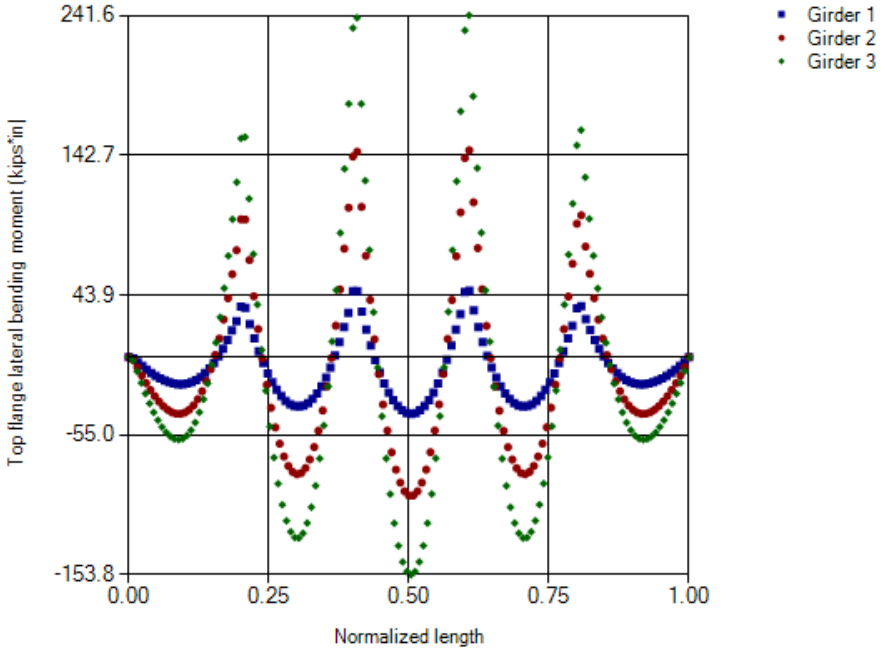

Figure 6.24: Top flange lateral bending moment diagram

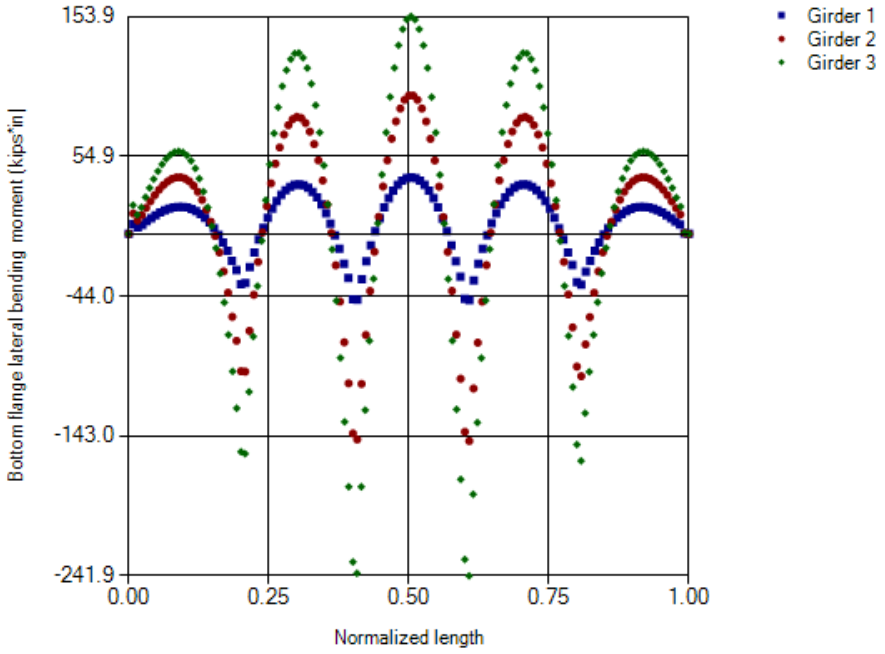

Figure 6.25: Bottom flange lateral bending moment diagram

The top flange and bottom flange lateral bending moment, also called bi-moments, are directly related to the magnitude of the flange warping stresses. The ratio of the flange warping stresses to the flange bending stresses is important to the design of curved plate girder bridges. Figures 6.26 and 6.27 show the magnitude of the σ_{yy} stress at the top flange interior and exterior edge, respectively. More precisely, the maximum absolute value of the σ_{yy} stress at both integration layers is displayed. Again, these diagrams are generated automatically by the program.

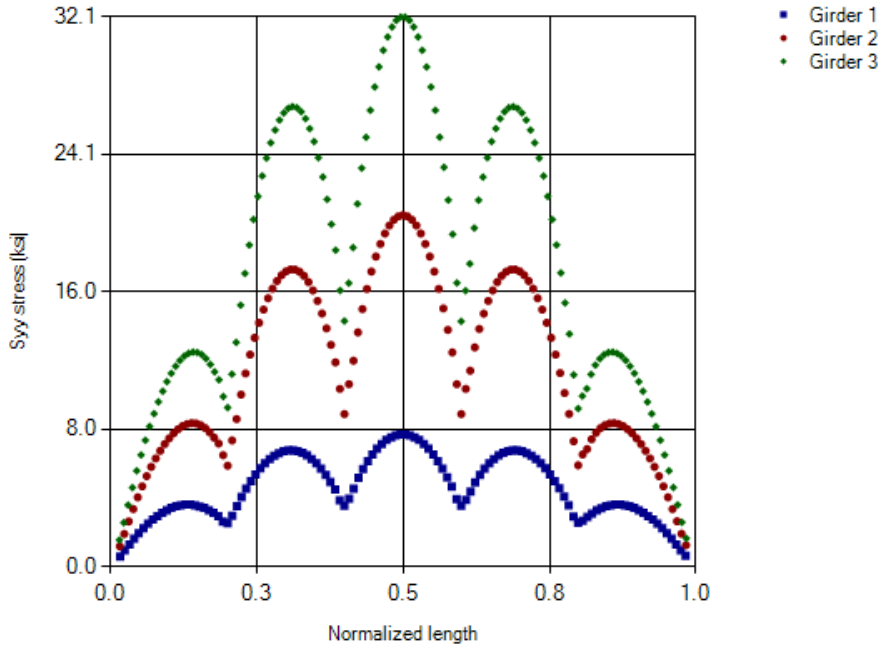

Figure 6.26: Top flange σ_{yy} stress (inside edge)

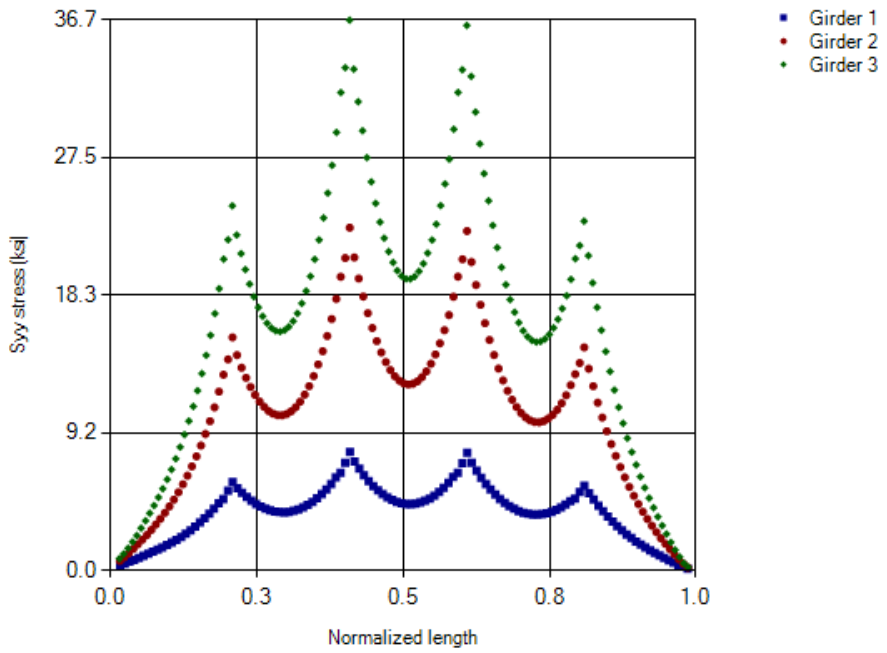

Figure 6.27: Top flange σ_{yy} stress (outside edge)

As expected, the flange warping bi-moments are equal to zero when the σ_{yy} stress value is equal at both edges of the top flange. It should be noted that the σ_{yy} stress value adds the contribution from both the principal axis bending stresses and the warping stresses.

6.2.2 EFFECT OF CURVATURE ON WARPING STRESS TO BENDING STRESS RATIO

The subtended angle of the bridge, *L/R*, where *L* is the length of the bridge and *R* its radius of curvature, is modified to assess the influence of its value on the warping-stress-to-bending-stress ratio. The selected values for the radius of curvature of the exterior girder are: 200-ft., 500-ft., 700-ft., 1000-ft., and 2000-ft. The length of the first two girders are adjusted to keep the same *L/R* ratio for all three girders. Davidson and Yoo (1996) showed that the relationship is linear. UT Bridge V2.2 shows a similar trend line (Figure 6.28).

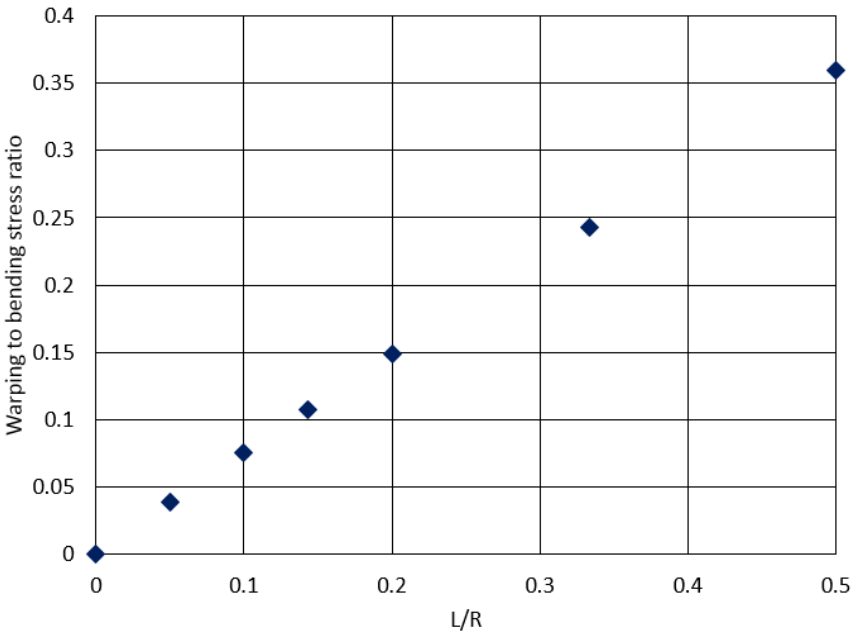

Figure 6.28: Effect of curvature on the warping to bending stress ratio

6.2.3 BUCKLING MODES

A linearized buckling analysis is conducted. Several closely-spaced buckling modes are encountered by the program. The first mode shows buckling of the third girder between intermediate brace points (Figure 6.29). The second mode is the global buckling mode (Figure 6.30), while the third and fourth modes are local web buckling modes (Figures 6.31 and 6.32). A large number of higher-order local web buckling modes can be found after the fourth mode.

As second-order effects are significant for curved bridges, a better understanding of the bridge behavior can be obtained with a geometrically nonlinear analysis.

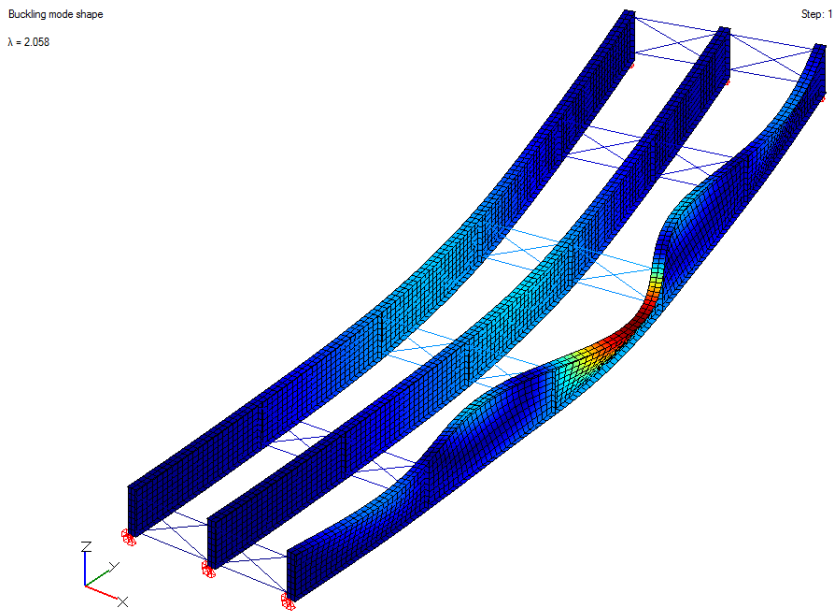

Figure 6.29: First buckling mode (λ = 2.058)

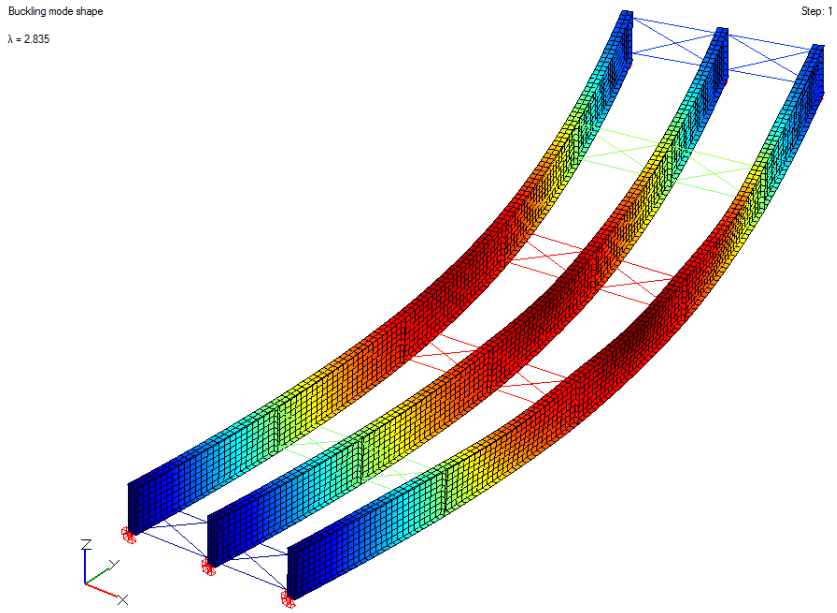

Figure 6.30: Second buckling mode (λ = 2.835)

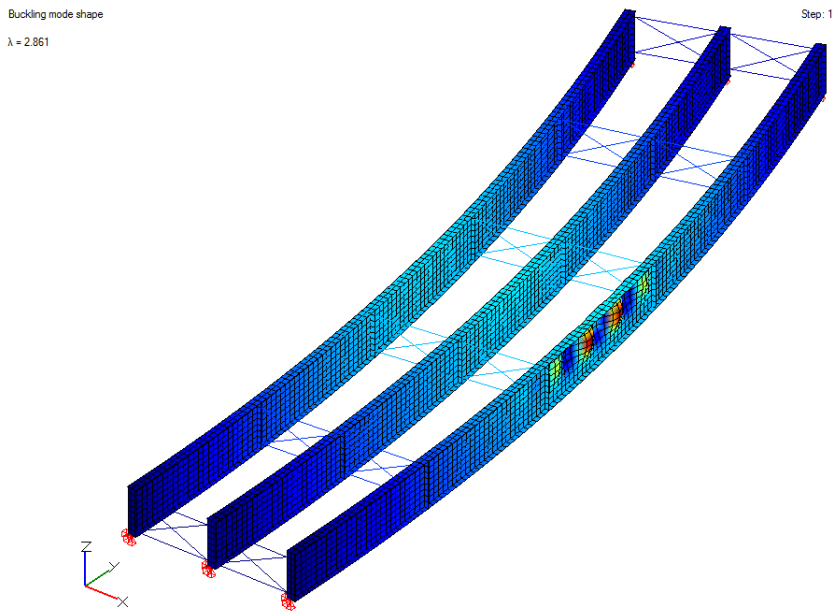

Figure 6.31: Third buckling mode (λ = 2.861)

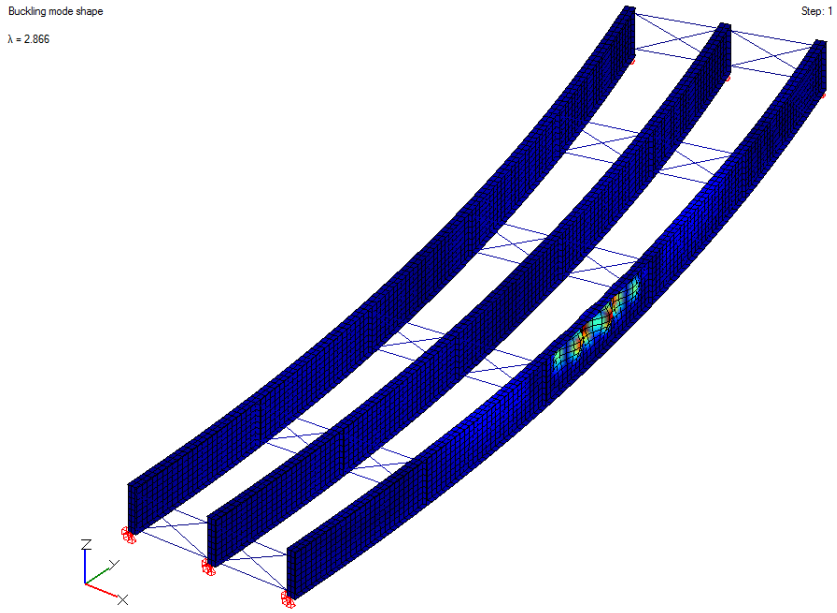

Figure 6.32: Fourth buckling mode (λ = 2.866)

6.2.4 GEOMETRICALLY NONLINEAR ANALYSIS AND CROSS-FRAME FORCES

A geometrically nonlinear analysis is conducted. A coarse mesh is specified, consisting of four elements through the web depth and an approximate longitudinal mesh size of 2-ft. This mesh density is selected to accelerate convergence. An amplification of 60.7% in the maximum displacement (Figure 6.34) is observed relative to the linear elastic analysis (Figure 6.33).

The deflected shape obtained from a geometrically nonlinear analysis (Figure 6.34) and the first buckling mode shape (Figure 6.29) are somewhat similar, as the top flange between cross-frames 3 and 4 on the exterior girder exhibits large lateral deflections. In general, however, the deflected shapes are not consistent, which shows that a linearized buckling analysis is not quite appropriate for curved, flexible systems. The deflected shape is actually a combination of the first and the second buckling shapes.

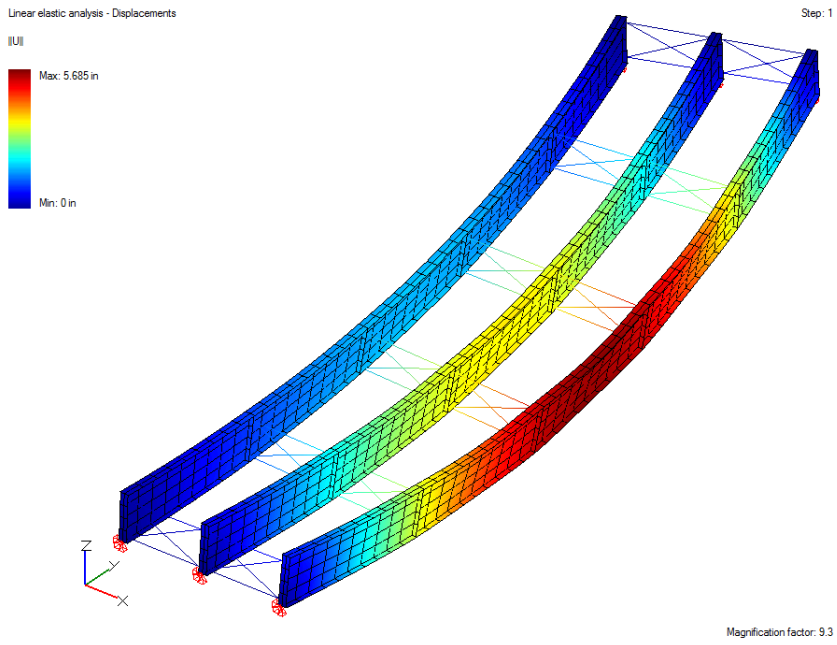

Figure 6.33: Deflected shape (coarse mesh, linear elastic analysis)

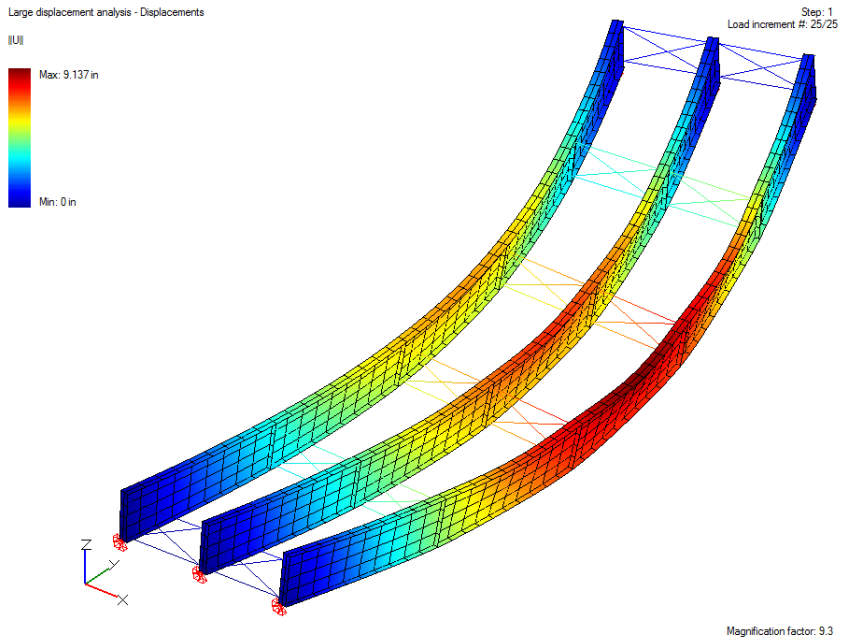

Figure 6.34: Deflected shape (coarse mesh, geometrically nonlinear analysis)

The load versus displacement curves for the displacement in the *x*-direction of the top-flange-to-web node (DOF 1) and the bottom-flange-to-web node (DOF 2) at mid-span of the exterior girder are shown in Figure 6.35. The tangent stiffness for the top-flange-to-web node *x*-displacement degree of freedom (DOF 1) at the end of the deformation is only about 6.6% of its initial value. A gradual loss of stiffness is observed. The eigenvalue corresponding to the first buckling mode of 2.2 is therefore quite unconservative: at 100% of the applied loads, the structure has already lost 93.4% of its stiffness, at least for that degree of freedom. Also, Figure 6.35 shows the behavior of the bottom flange through the deformation. It initially deflects toward the center of curvature of the bridge, but as deformation takes place, the bridge deflects and rotates laterally as a unit causing the bottom flange to deflect in the other direction.

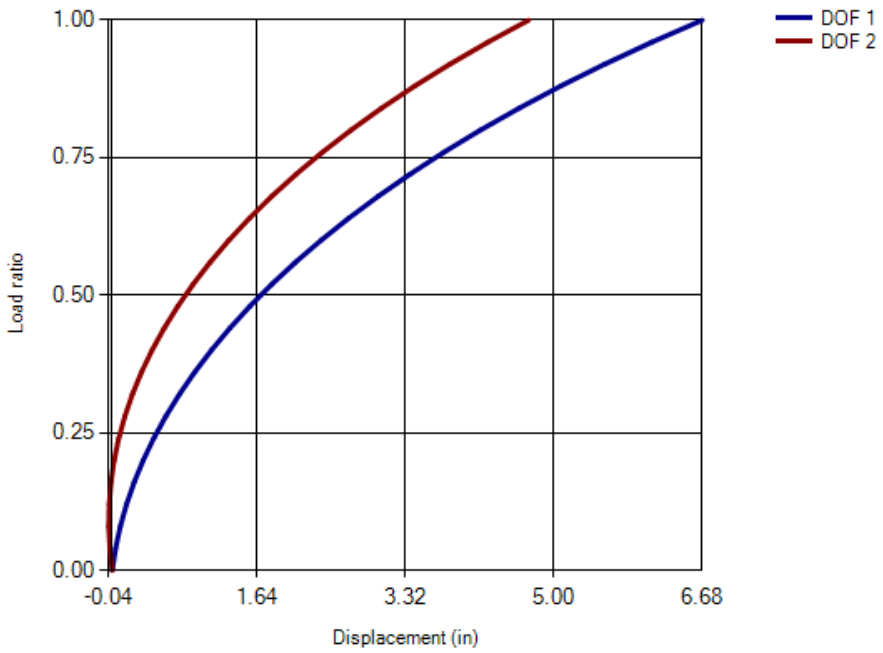

Figure 6.35: Load versus displacement curve (geometrically nonlinear analysis)

Behavior of the top and bottom flanges is important in evaluating the cross-frame forces. A large discrepancy can be observed between the forces obtained from a linear elastic analysis (Figures 6.36 and 6.38) and those obtained from a geometrically nonlinear analysis (Figure 6.37 and 6.39). For example, on the right bay, at the third cross-frame from the left support, a linear elastic analysis overestimates the tension forces and underestimates the compression forces. A linear elastic analysis is therefore not appropriate for evaluating cross-frame forces for curved, flexible systems. Because of this observation, a parametric study is conducted to evaluate the influence of curvature on the cross-frame forces obtained from both a linear elastic analysis and a geometrically nonlinear analysis.

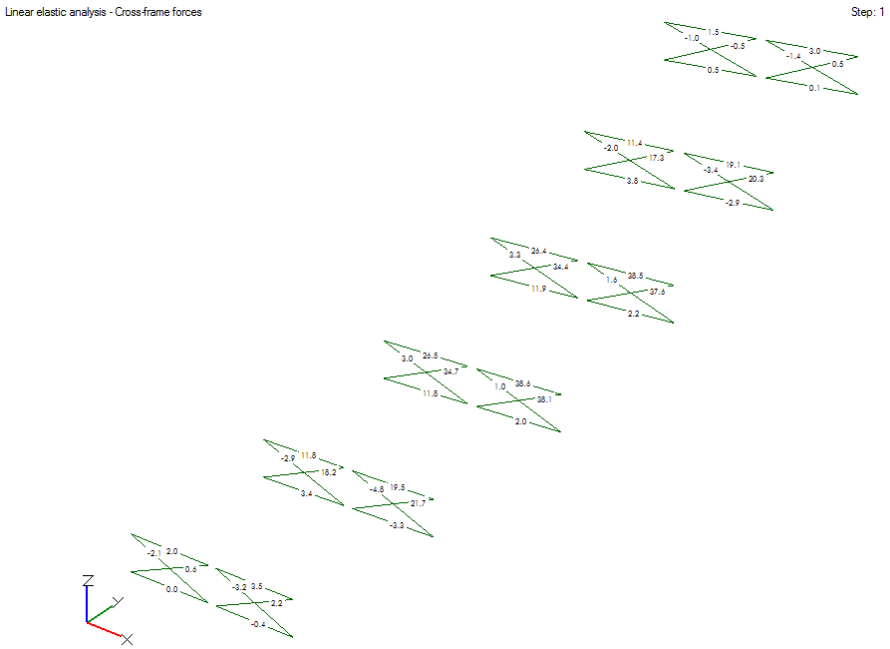

Figure 6.36: Cross-frame forces (linear elastic analysis)

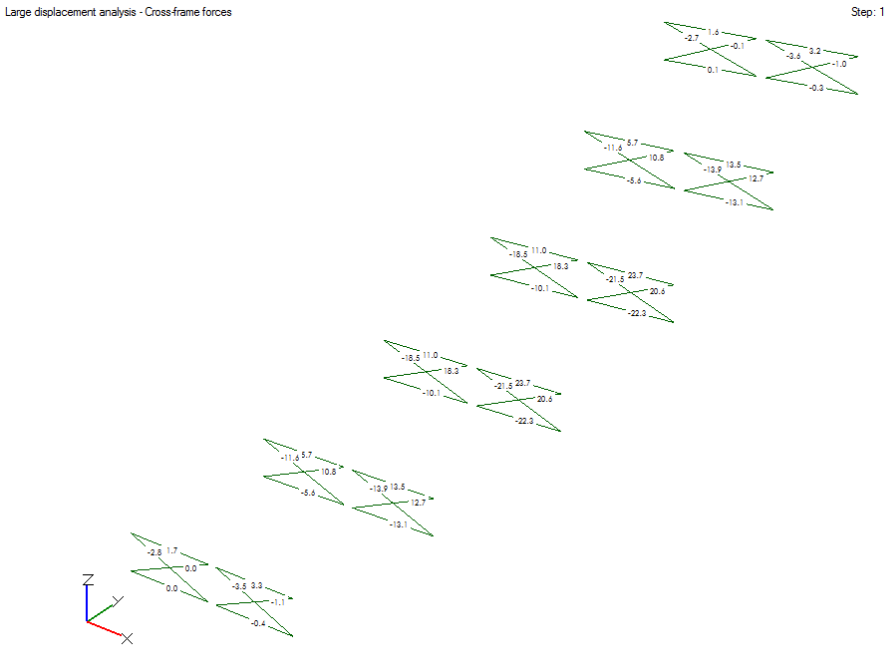

Figure 6.37: Cross-frame forces (geometrically nonlinear analysis)

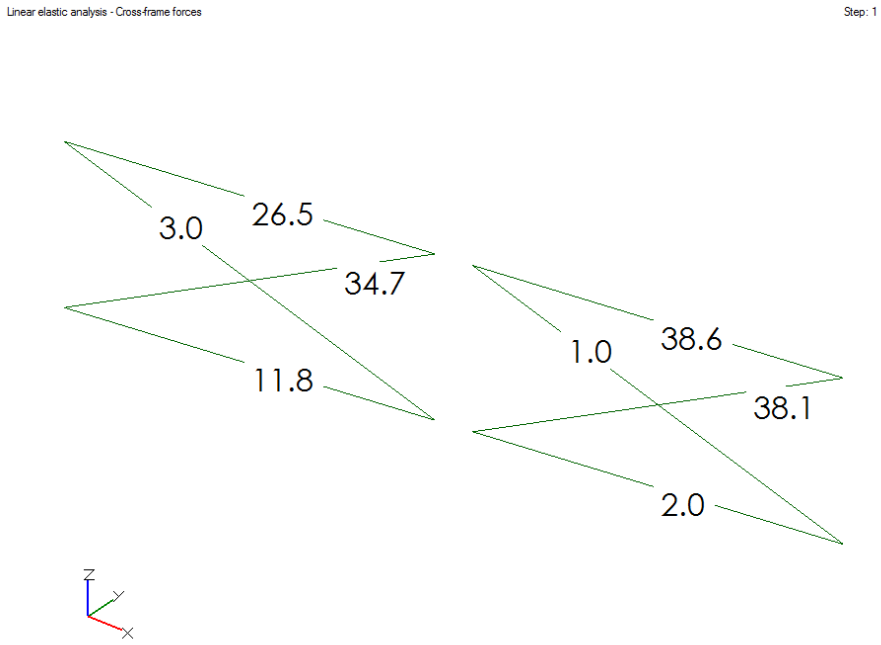

Figure 6.38: Axial forces in the third cross-frame of each bay (linear elastic analysis)

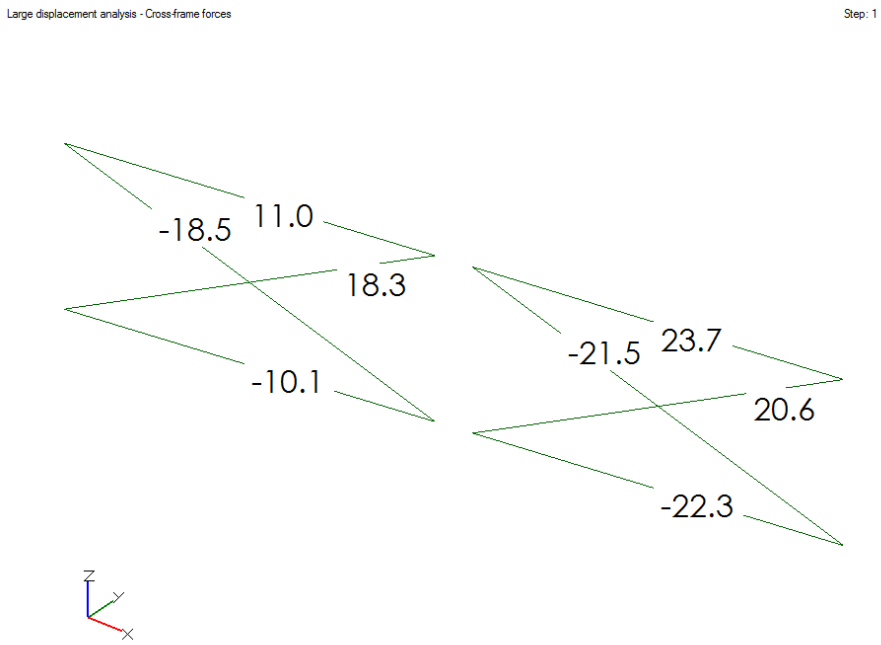

Figure 6.39: Axial forces in the third cross-frame of each bay (geometrically nonlinear analysis

6.2.5 EFFECT OF CURVATURE ON CROSS-FRAME FORCES AND DEFLECTION MAGNIFICATION

The effect of curvature on cross-frame forces is analyzed in a parametric study. The radii of curvature selected for the exterior girder are equal to those previously selected in Section 6.2.2. A straight bridge is also analyzed to model a bridge approaching an infinite radius of curvature. The third cross-frame from the left support in the right bay is considered for further study. This particular cross-frame is critical in maintaining structural stability, as the first buckling mode, as well as the deflected shape from the geometrically nonlinear analysis, have shown. Results are presented in Figure 6.40, which shows that cross-frame forces are typically low for mildly curved systems. For severely curved systems, cross-frame forces increase significantly. Self-weight of the steel structure and weight of the wet concrete may be the only loads acting on the structure, but cross-frames carry substantial amounts of load to resist torsion, which makes them primary structural members. In addition, Figure 6.40 shows how a linear elastic analysis does not capture cross-frame forces accurately for large curvatures. For this particular cross-frame, compression forces are underestimated, which can be problematic when assessing the potential for buckling, and tension forces are overestimated. Finally, Figure 6.40 shows how a geometrically nonlinear analysis gives a symmetrical distribution of cross-frame forces, with the axial forces in the diagonals opposite to one another. The same applies to the axial forces in the top and bottom chords. The axial forces in the diagonals increase linearly with the curvature.

Finally, the influence of curvature on the maximum deflection experienced by the bridge is presented in Figure 6.41. As expected, curvature amplifies the maximum deflection. A linear elastic analysis is unable to accurately capture the behavior of severely curved bridges. For mildly curved bridges, however, a linear elastic analysis is sufficient.

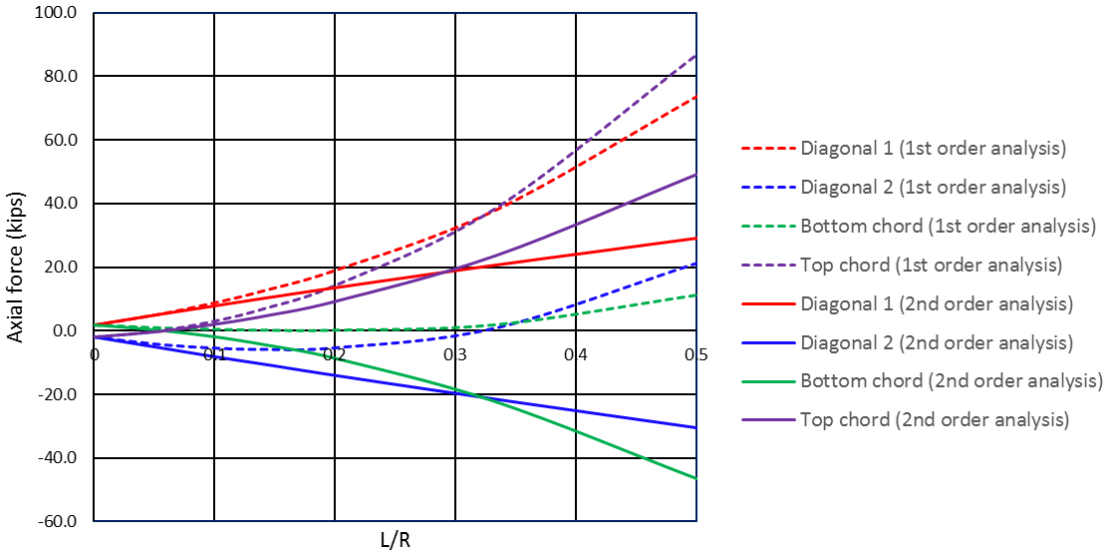

Figure 6.40: Effect of curvature on cross-frame forces

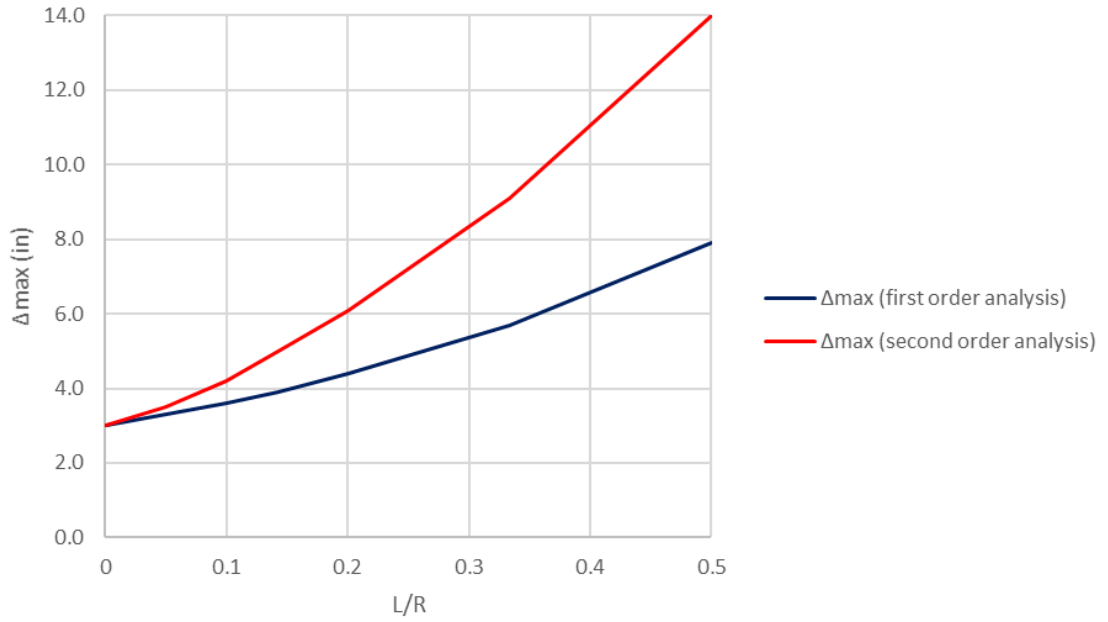

Figure 6.41: Effect of curvature on the maximum deflection

6.3 STRENGTHENING OF THE MARCY BRIDGE

The Marcy Bridge collapse in 2002 is well-documented (Corr et al. 2009, Yura and Widianto 2005). The pedestrian bridge consisted of a simply-supported straight tub girder, and it failed by global lateral buckling during casting of the concrete deck. In this example, UT Bridge V2.2 is used to model the bridge, assess its stability during casting, and evaluate bracing options that could have prevented the structure from collapsing.

The bridge is simply-supported and spans a length L of 170.6 ft. The span is divided into 27 uniformly spaced panels. Diaphragms are provided at the ends, and K-frames at every three panel points to prevent distortion of the cross-section. For the other panels, only struts are installed. No lateral bracing is considered. The bridge is not prismatic, as three cross-sectional profiles are selected along its length (Popp 2004). The bridge model is shown in Figure 6.42 and contains 33,000 unrestrained degrees of freedom. Loads applied include self-weight of the steel superstructure, plus an additional uniformly distributed load of 1.65 k/ft acting on top of the steel superstructure (0.825 k/ft on each top flange) to represent the self-weight of the concrete (Popp 2004). A parametric study is conducted, varying the extent x/L over which the uniformly distributed load is applied. A linearized buckling analysis shows that the bridge fails by global lateral buckling when the uniformly distributed load reaches an extent of approximately 60 ft. (Figure 6.45). Under actual conditions, the bridge collapsed when the pour reached approximately the mid-span (Popp 2004). The linearized buckling analysis is therefore slightly conservative, but this can be explained by the fact that the model does not account for the bracing that is provided by the permanent metal deck forms. Global buckling of the bridge when the uniformly distributed load is applied up to the 12th panel is shown in Figure 6.43. It should be noted that buckling occurs at relatively low stress levels, as the critical stress in the longitudinal direction for this particular load case is equal to 13.8 ksi (Figure 6.44).

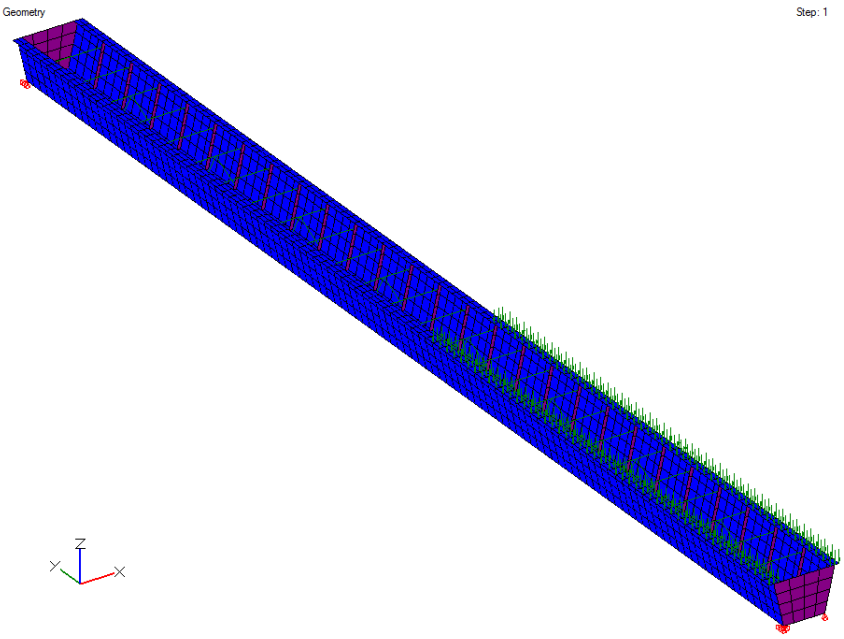

Figure 6.42: Marcy Bridge model (uniformly distributed load applied up to the 12th panel)

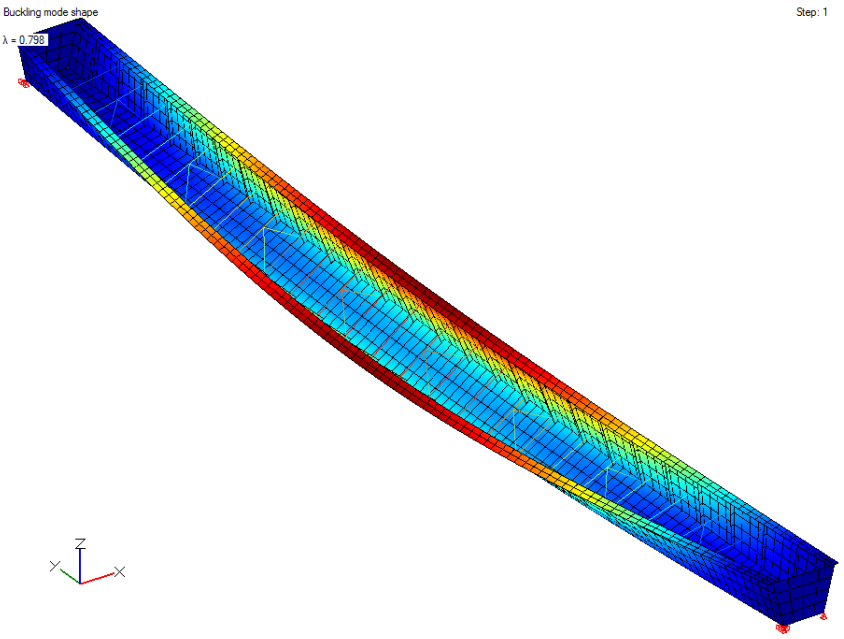

Figure 6.43: Marcy Bridge global lateral buckling – Uniformly distributed load applied up to the 12th panel ($\lambda = 0.798$)

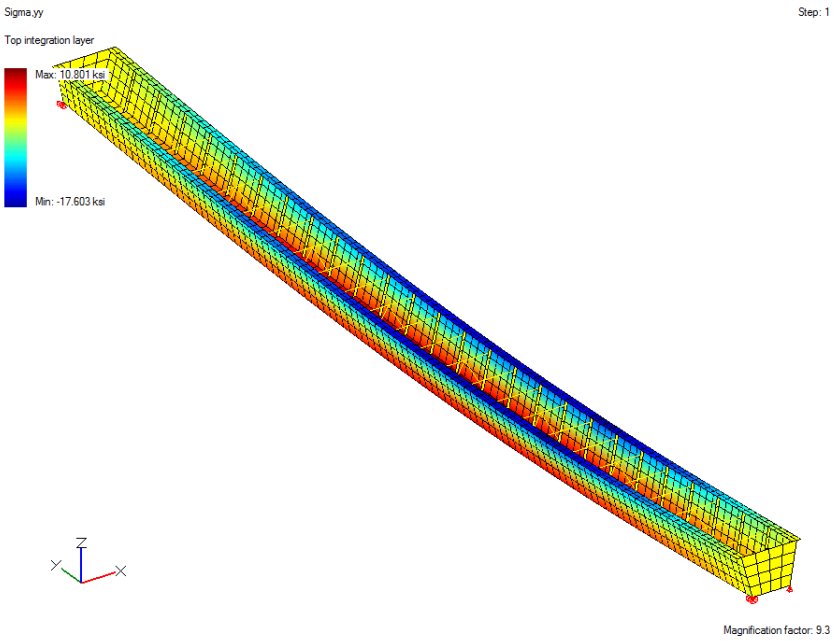

Figure 6.44: Marcy Bridge principal axis bending stress distribution – Uniformly distributed load applied up to the 12th panel

A linearized buckling analysis therefore shows that the Marcy Bridge collapsed due to insufficient bracing. Retrospectively, it can be meaningful to study the influence of lateral bracing, first by adding one lateral truss on each end of the bridge (SD ×1). The cross-sectional area is taken equal to 2.11 in^2, which is equal to the cross-sectional area selected for the internal K-frames and the struts.

A linearized buckling analysis is conducted again, showing how the lateral truss dramatically increases structural stability (Figure 6.45). However, the parametric study also shows that one lateral truss on each end is not quite sufficient, so the number of lateral trusses is increased from one to two (SD ×2), three (SD ×3), and four (SD ×4) on each end. Global lateral buckling of the bridge with four lateral trusses on each end and self-weight of the steel superstructure only is shown in Figures 6.46 and 6.47.

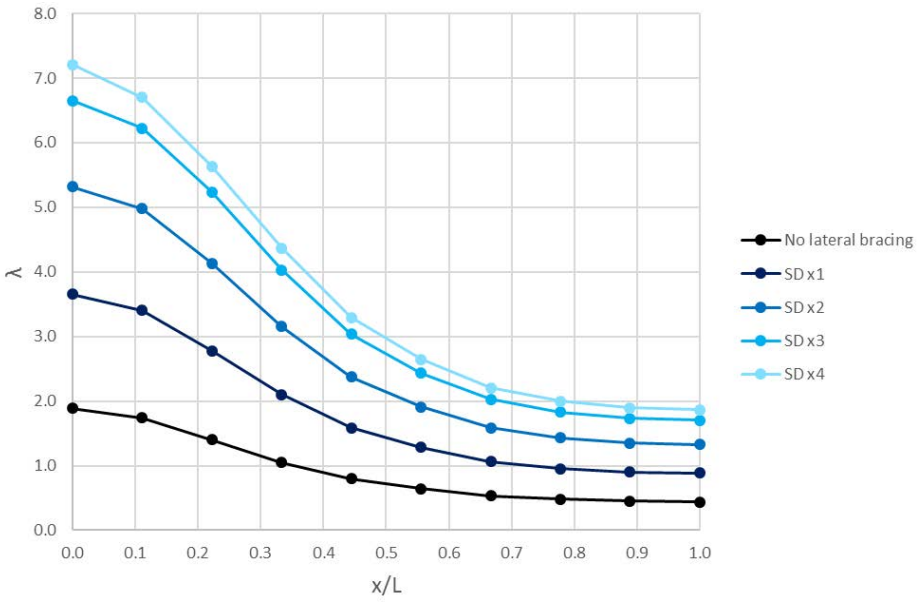

Figure 6.45: Influence of lateral bracing and length of the pour on the global buckling mode

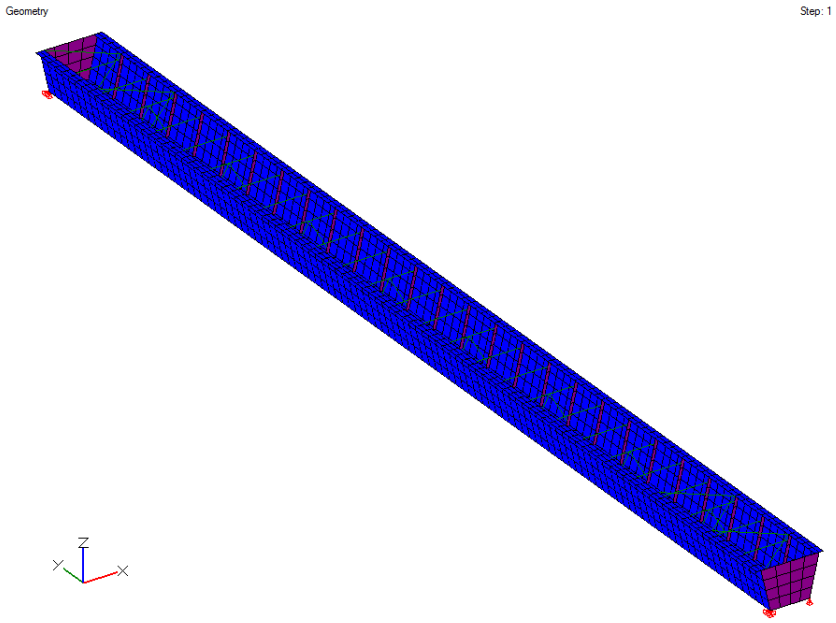

Figure 6.46: Bridge model with four lateral trusses at each end – Initial geometry

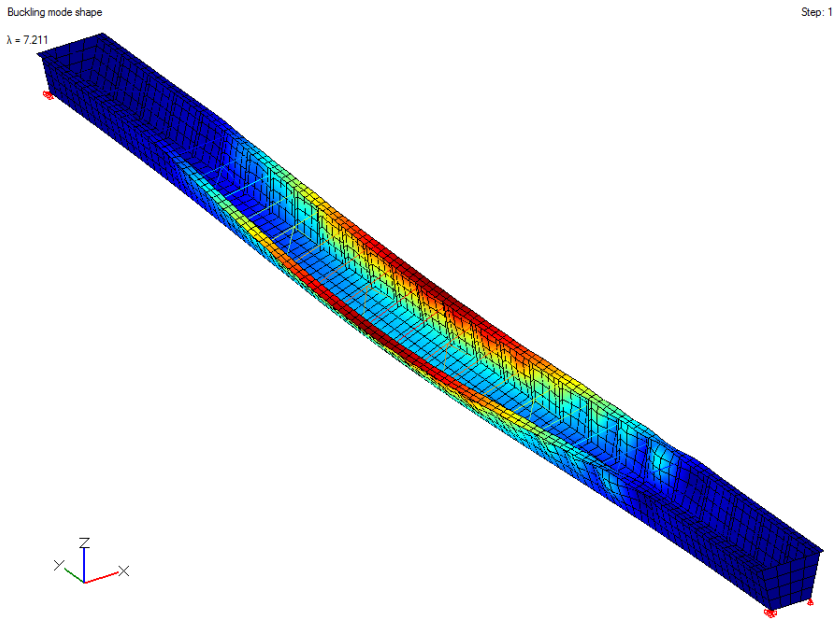

Figure 6.47: Bridge model with four lateral trusses at each end – Self-weight only – Global lateral buckling mode ($\lambda = 7.211$)

As warping deformation is maximal at the bridge ends, the benefit of adding lateral trusses gradually decreases. Providing three lateral trusses at each end proves to be a quick solution that would have prevented global buckling of the bridge. It should be noted, however, that although global lateral buckling controlled the behavior of the Marcy Bridge, other buckling modes may also occur. In some cases, when the unbraced length is sufficiently small, local buckling modes may control over global lateral buckling. For example, local web buckling controls when four lateral trusses are installed at each end and self-weight of the steel superstructure is the only applied load (Figure 6.48).

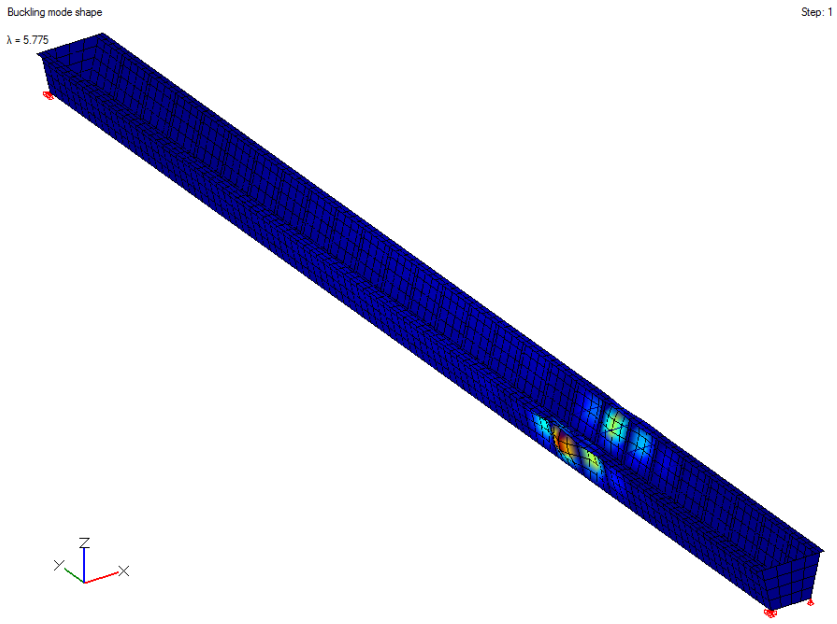

Figure 6.48: Bridge model with four lateral trusses at each end – Self-weight only – Local web buckling mode (λ = 5.775)

Finally, a study is conducted to evaluate the influence of wind loads on the bridge behavior. All lateral trusses are removed, and a horizontal pressure of 6.25 psf is applied to the left web. This magnitude corresponds to a wind velocity of 35 mph. Wind direction is taken orthogonal to the bridge to maximize the wind effects, although the program also allows for any direction. Vertical load is taken as self-weight of the bridge. Even though deck placement is usually conducted during clement weather conditions, it may be interesting to evaluate whether wind has any impact on bridge stability. The maximum lateral deflection calculated is equal to 2.0 in. (Figure 6.49). Although the bridge exhibits little lateral stiffness, the global lateral buckling mode is reached for an eigenvalue of 1.867 (Figure 6.50), which is just 1% less than without the wind load acting. As global lateral buckling is due to buckling of the top flanges, and as the wind load does not induce additional compression in the top flanges, wind load has little influence on the bridge

stability estimated by a linearized buckling analysis. In reality though, the lateral deflection induced by the wind load acts as a geometric imperfection, reducing the bridge stability.

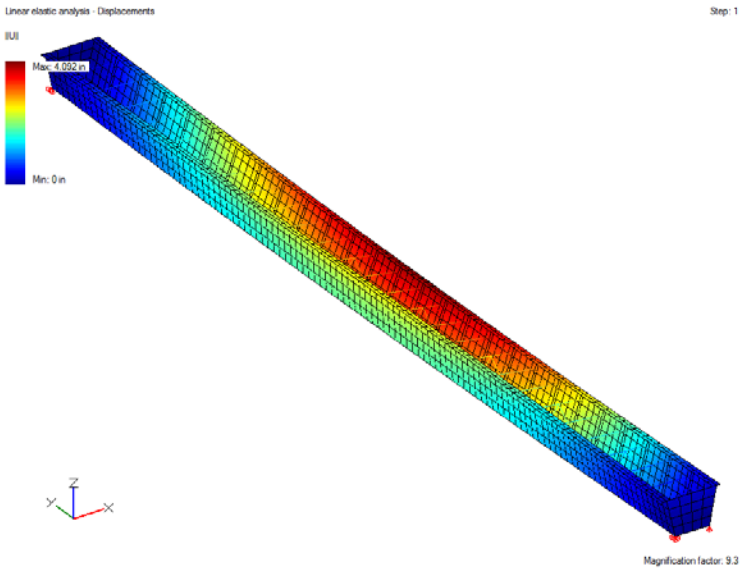

Figure 6.49: Marcy Bridge – Deflected shape – Self-weight plus wind load

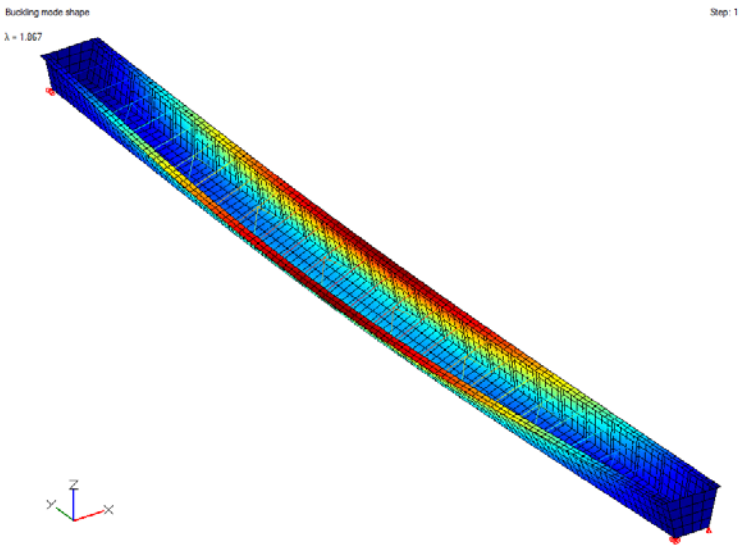

Figure 6.50: Marcy Bridge global lateral buckling – Self-weight plus wind load (λ = 1.867)

6.4 ANALYSIS OF A THREE-SPAN CONTINUOUS TWIN TUB GIRDER BRIDGE

In this last example, a fairly typical curved, three-span continuous twin tub girder bridge is analyzed during erection and placement of the concrete deck. The bridge is adapted from Kim (2004). The centerline radius of curvature and total length are respectively equal to 700 ft. and 530 ft. (Figure 6.51). Solid diaphragms of thickness equal to 0.5-in. are modeled at the support locations.

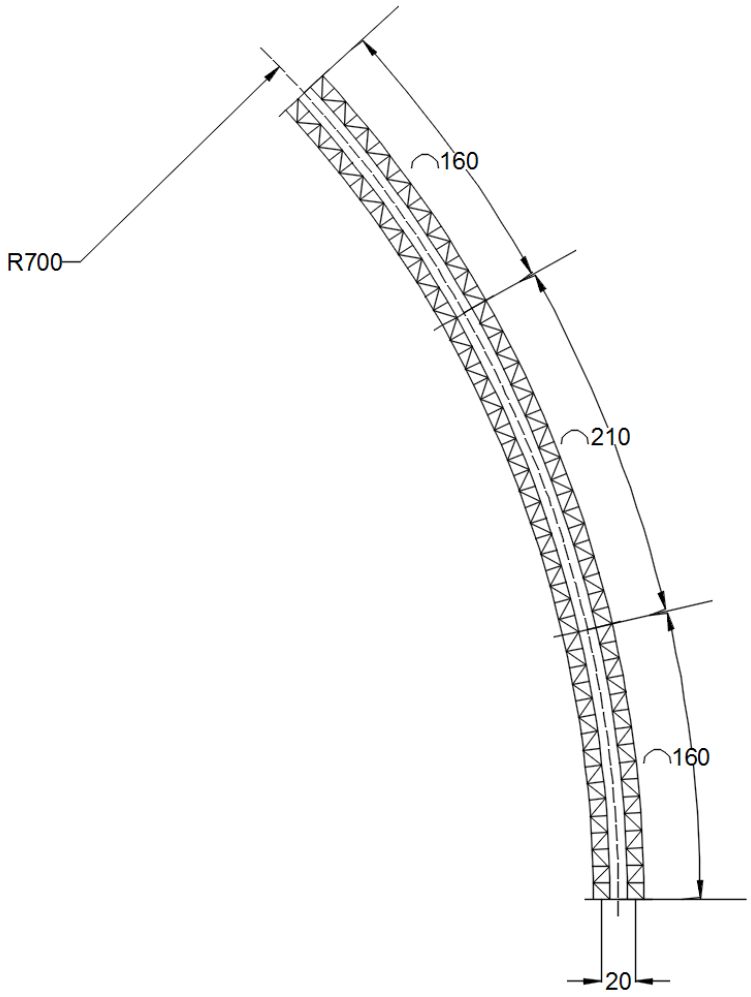

Figure 6.51: Twin tub girder bridge planar dimensions

Intermediate internal cross-frames (X-frames) are modeled at every panel. They are attached on 6-in.×0.5-in. connecting plates. The panels are uniformly distributed at a 10-ft. spacing. A single diagonal type lateral bracing system is considered. All lateral trusses, struts, and cross-frame diagonals have a cross-sectional area taken equal to 2.11 in^2. Spacing of the tub centerlines is equal to 20-ft. The bridge is not uniform but instead consists of three different cross-sections (Figures 6.52 and Table 1).

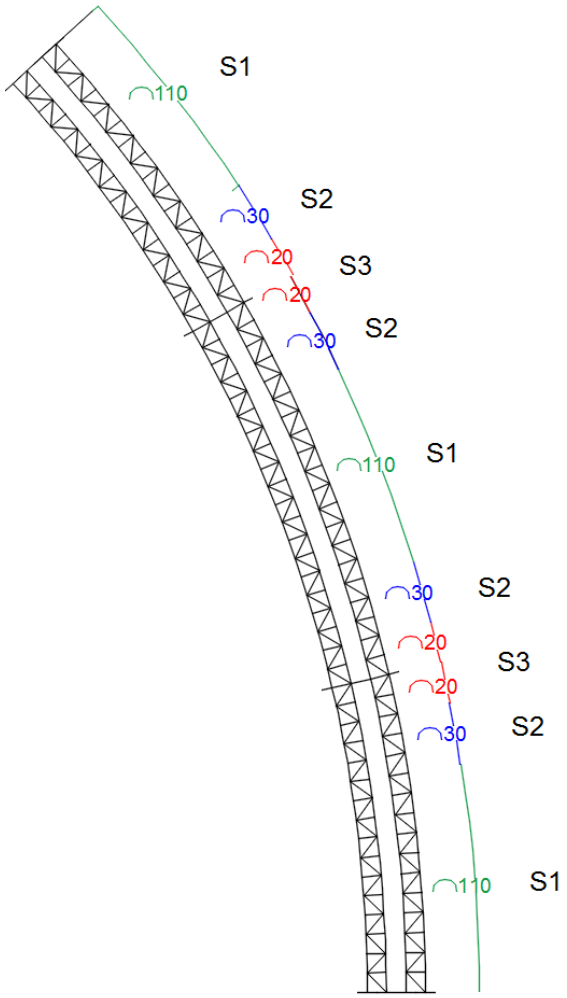

Figure 6.52: Twin tub girder cross-sectional dimensions (1/2)

Table 1: Twin tub girder cross-sectional dimensions (2/2)

Section	b_{tf} (in)	t_{tf} (in)	h_w (in)	t_w (in)	b_{bf} (in)	t_{bf} (in)	tw (in)
S1	16	1.25	78	0.56	81	0.75	117
S2	16	1.75	78	0.56	81	1.25	117
S3	16	3.25	78	0.56	81	1.75	117

The boundary conditions implemented are described in Figure 6.53. The lateral restraints at the guided supports are radial. Boundary conditions are applied only at the bottom flange middle node. Thus, there is only one bearing pad per support. This differs from the default assumption of two bearing pads per support. As described in Chapter 4, that default assumption is implemented to prevent potential instability issues.

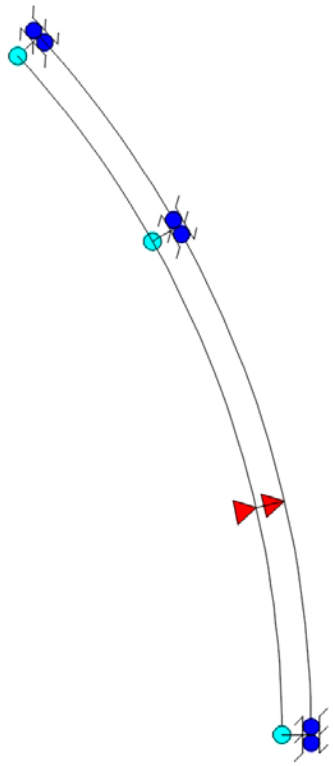

Figure 6.53: Twin tub girder boundary conditions

6.4.1 ERECTION ANALYSIS

An erection sequence consisting of three stages is considered, where the bridge is erected from both sides first, and then a drop-in segment corresponding to the remaining portion of the bridge is erected. A linear elastic analysis is conducted on the partially erected bridge to evaluate its behavior. In particular, the displacements and rotations at the free ends are of primary importance for fit-up of the different parts. The deflected shape for all three stages is shown in Figures 6.54 to 6.56. Rotations are not shown by the post-processor but can be directly calculated from the displacements at different nodes of the cross-section.

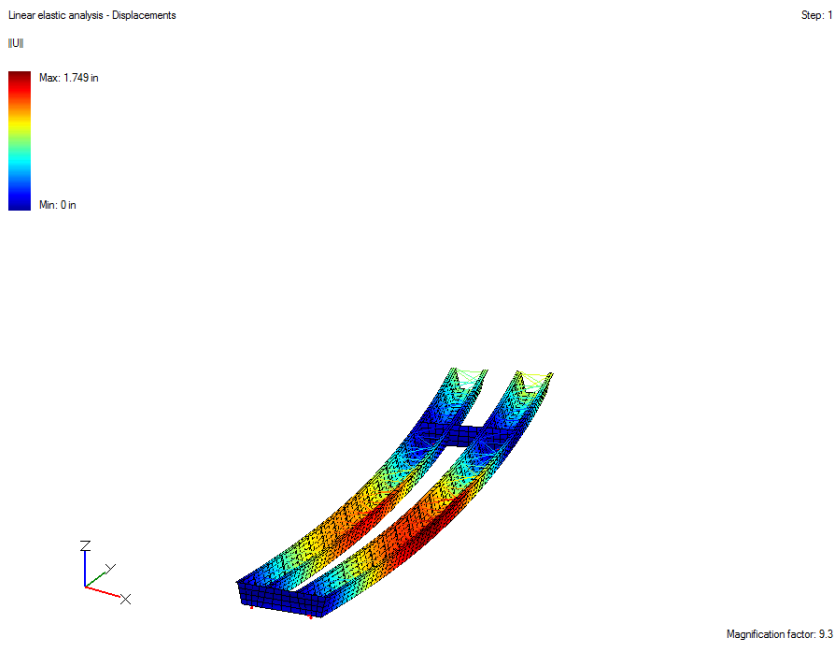

Figure 6.54: Deflected shape (erection stage 1)

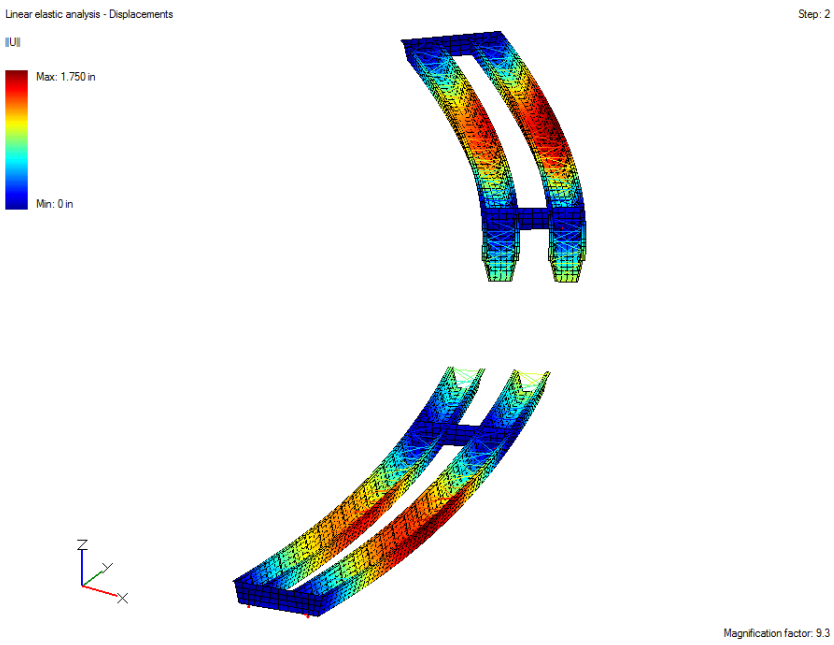

Figure 6.55: Deflected shape (erection stage 2)

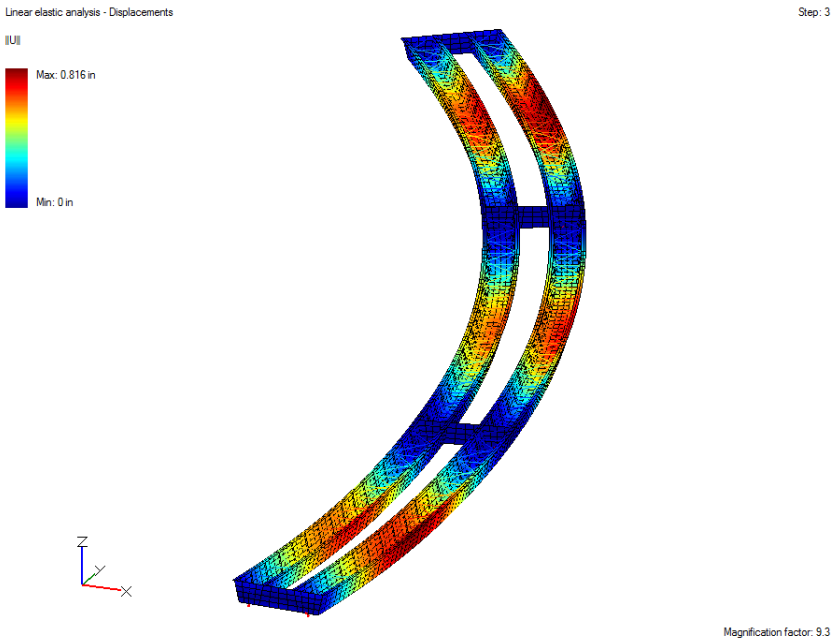

Figure 6.56: Deflected shape (erection stage 3)

Because there is only one fixed support per girder, a longitudinal spring (acting in the tangential direction) is provided at the bottom flange middle node of both tubs to prevent rigid body movement during stage 2. It is then deactivated for stage 3.

The program can also be used to check stresses during erection. For example, Figures 6.57 and 6.58 show the σ_{yy} and σ_{yz} stresses for stage 1. The σ_{yy} stresses include the bending and warping-induced stresses, while and σ_{yz} stresses correspond to the uniform torsion or twisting of the cross-section. These stresses can be displayed for either the top or bottom integration layer of the shells. The program can also display the envelope of the values calculated at both layers.

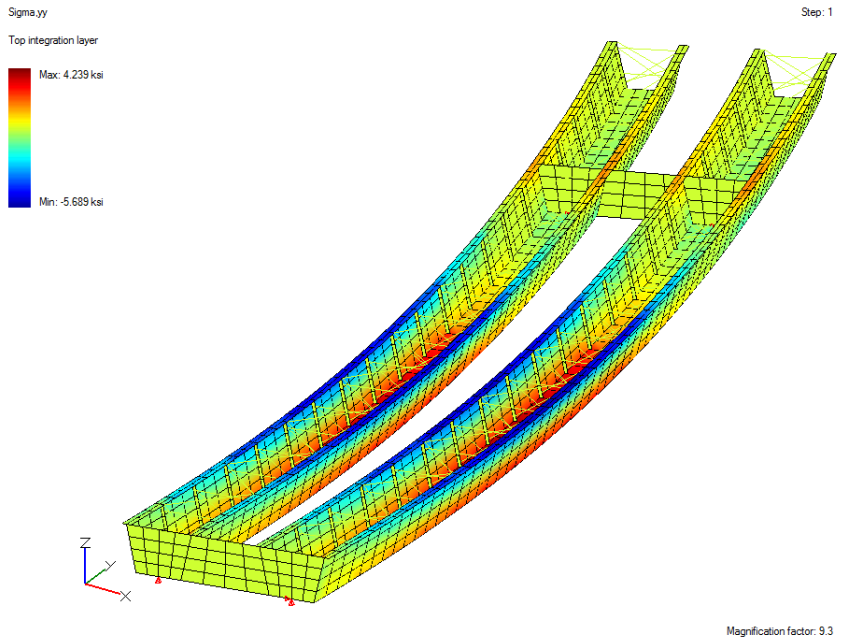

Figure 6.57: σ_{yy} stresses (erection stage 1)

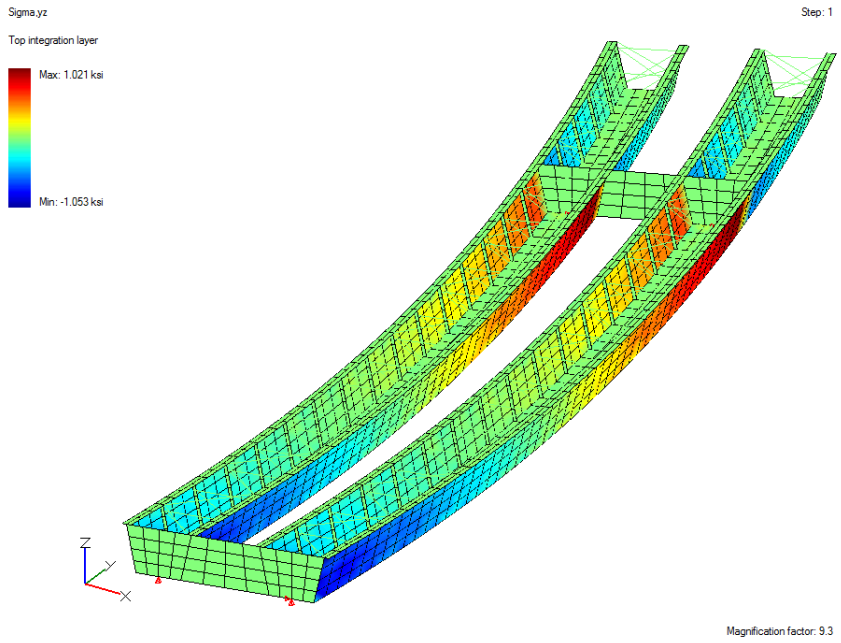

Figure 6.58: σ_{yz} stresses (erection stage 1)

In addition, the program can also automatically derive the shear and moment diagrams for all three stages. For example, Figures 6.59 and 6.60 show the shear and moment diagrams, respectively, for the final erection stage.

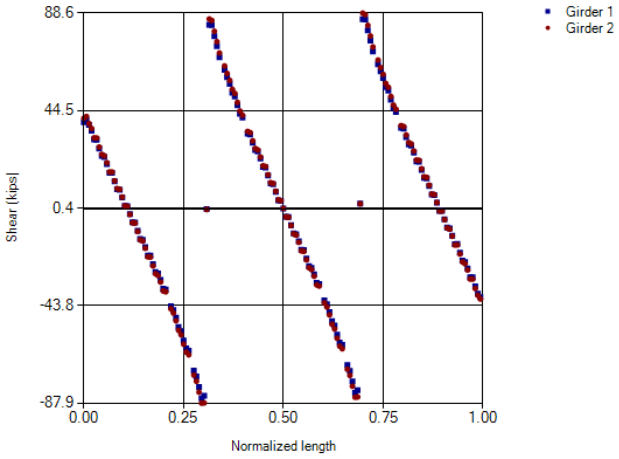

Figure 6.59: Shear diagram (erection stage 3)

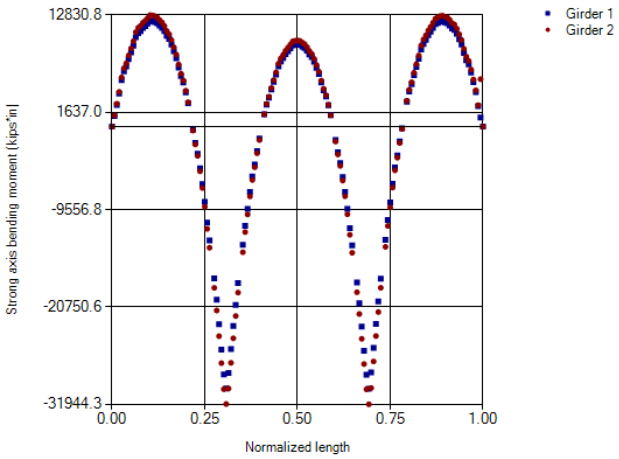

Figure 6.60: Moment diagram (erection stage 3)

Finally, the erector may be interested in evaluating the free vibration modes of the partially erected structure, which are shown for stages 1 and 3 in Figures 6.61 and 6.62, respectively. For curved systems, the exterior girder is longer, so from a dynamic period standpoint, free vibration of the exterior girder usually controls.

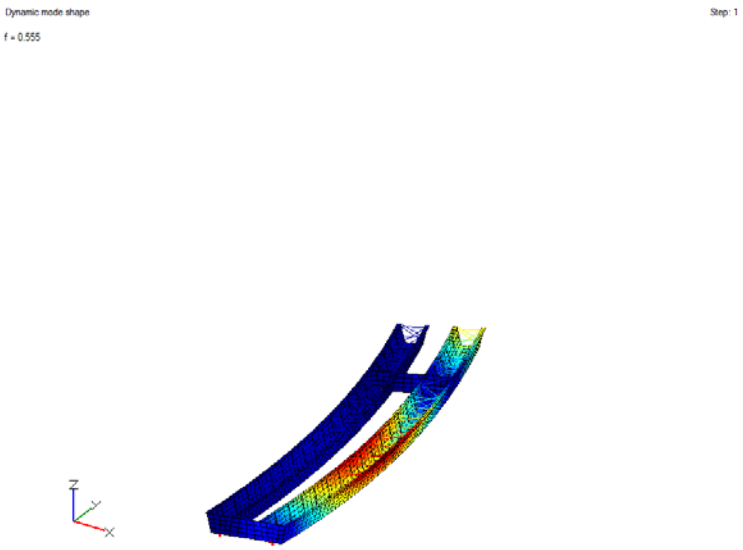

Figure 6.61: First dynamic mode (erection stage 1)

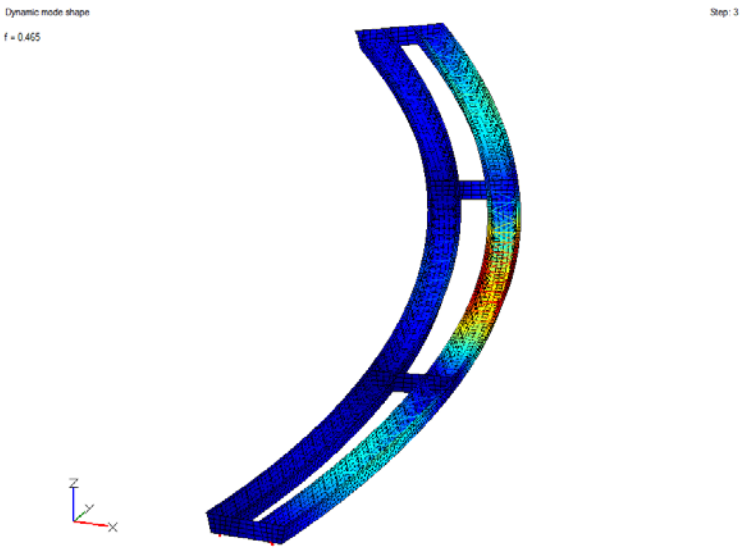

Figure 6.62: First dynamic mode (erection stage 3)

6.4.2 EFFECT OF THE EXTERNAL DIAPHRAGMS ON THE DIFFERENTIAL DEFLECTIONS

To ensure a relatively constant deck thickness over the width of the bridge, which is itself a key factor for durability, it is important to control deformations between adjacent tubs. External bracing consisting of either K-frames or diaphragms are typically provided at regular locations along curved bridges. In this section, the influence of external diaphragms on the differential deflections is studied and summarized. Three cases are considered. In the first case, no external diaphragm is provided. The second case corresponds to the structure studied previously and has four external diaphragms, namely one at each support. In the third case, additional diaphragms are provided at mid-span, resulting in seven diaphragms. The diaphragms are modeled as plates resisting adjacent movements through shear deformations only. Figures 6.63 and 6.64 show the effect of the external diaphragms on the vertical deflection of the top-flange-to-web nodes of both tubs at two different locations: at mid-span between the first and second supports (Figure 6.63),

and at mid-span between the second and third supports (Figure 6.64). When no external diaphragms are provided, the tubs deflect independently from each other, resulting in large differential deflections. Providing four external diaphragms stabilizes these differential deflections. As expected, the best alignment is achieved when seven diaphragms are used.

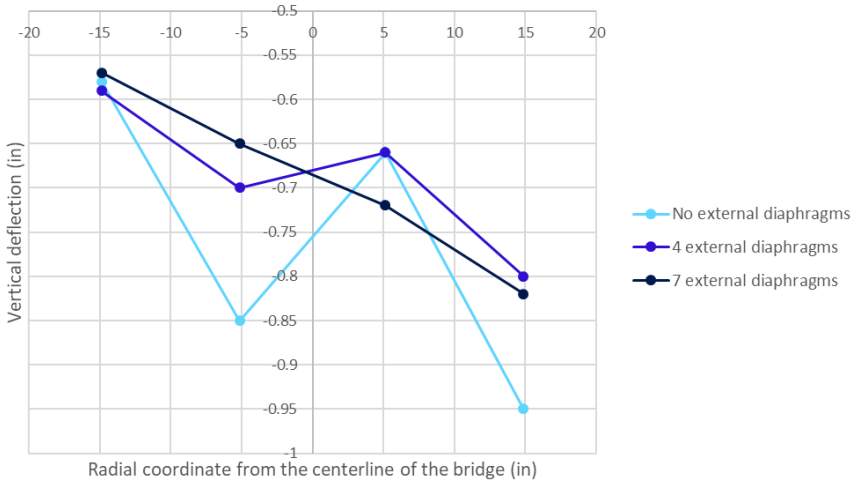

Figure 6.63: Effect on the external diaphragms on the differential deflection at mid-span between the first and second support lines

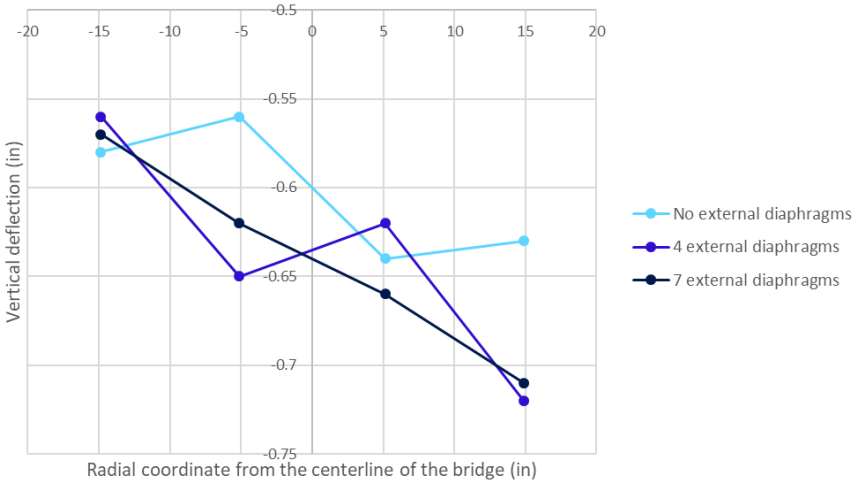

Figure 6.64: Effect on the external diaphragms on the differential deflection at mid-span between the second and third support lines

6.4.3 EFFECT OF THE GUIDED BEARINGS ORIENTATION ON THE BRIDGE BEHAVIOR UNDER THERMAL EXPANSION

Thus far, only radial boundary conditions have been enforced in the model. It may be interesting, however, to study the effect of the guided bearing orientation on the bridge behavior. A similar study was conducted on a different bridge model using a different analysis software by Chen (2008). In UT Bridge V2.2, this study is achieved by specifying a differential angle from the perfectly radial condition. Five cases are considered. The first case uses the default radial orientation. In the second case, a positive angle of 15 degrees from the perfectly radial orientation is considered on the second tub guided bearings (Figure 6.65). In the third case, this angle is increased to 30 degrees. The fourth case uses a chorded layout, where the point of fixity is the second girder fixed support (Figure 6.66). Finally, the fifth case is quite different, as the fixed support is moved to the first abutment on both girders, and a chorded layout with respect to that fixed point is considered.

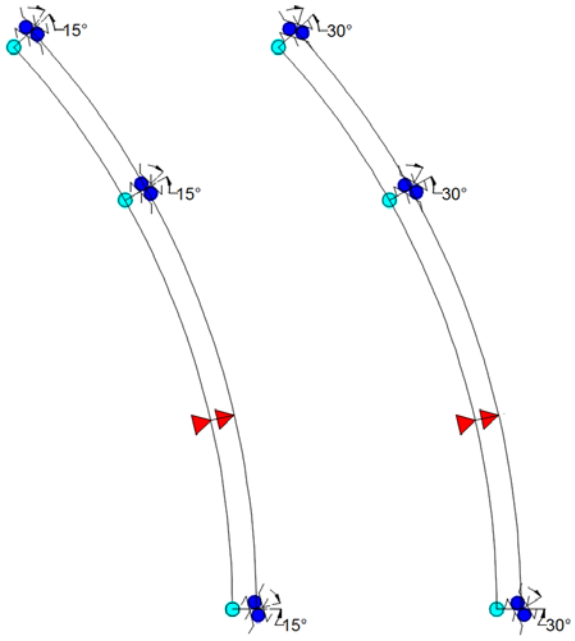

Figure 6.65: Misalignment from the perfectly radial boundary conditions

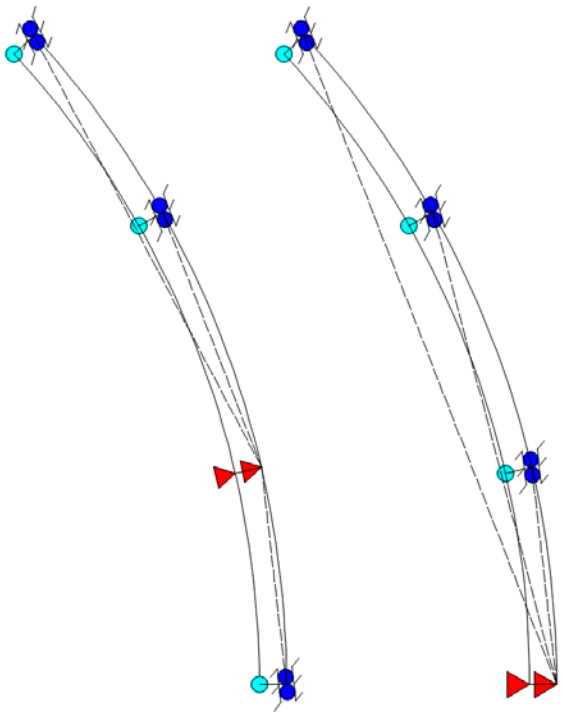

Figure 6.66: Chorded layout with respect to the 2nd support (left) and to the 1st support (right)

The five different models are subjected to a uniform thermal expansion of 30 degrees Celsius. Among other parameters, the effect of the guided bearing orientation on the "breathing" of the bridge, namely the maximum deflection experienced by the bridge under the temperature load, is shown in Figures 6.67 and 6.68. Having the fixed support at the abutment yields the maximal deflection for all cases. Interestingly, increasing the misalignment from a perfectly radial layout has a significant impact on the breathing.

The effect of the guided bearing orientation on the lateral guide horizontal reaction is shown in Figures 6.69 and 6.70. Misalignment from the radial layout results in increased lateral reactions. The chorded layout and the radial yield significantly different lateral reactions.

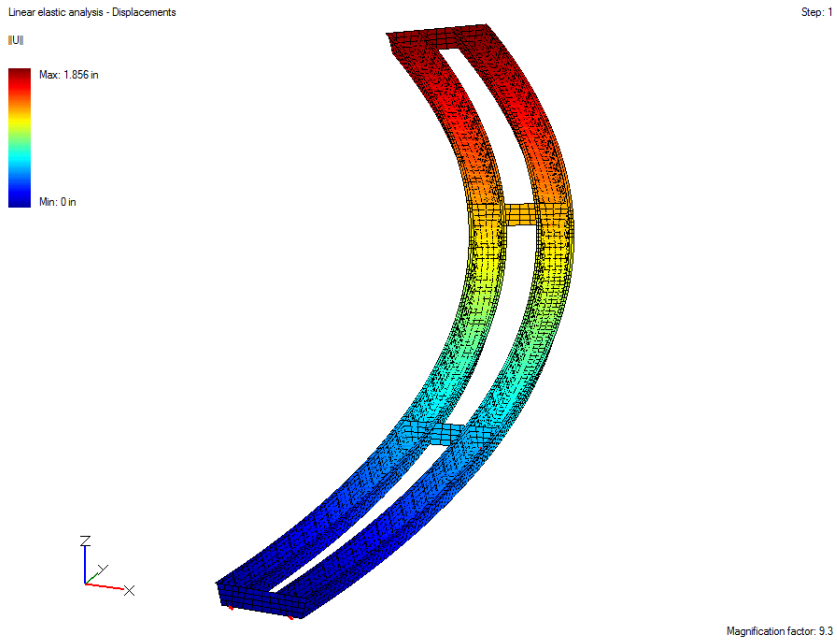

Figure 6.67: Bridge deflected shape under 30°C thermal expansion (chorded layout with respect to the 1st support)

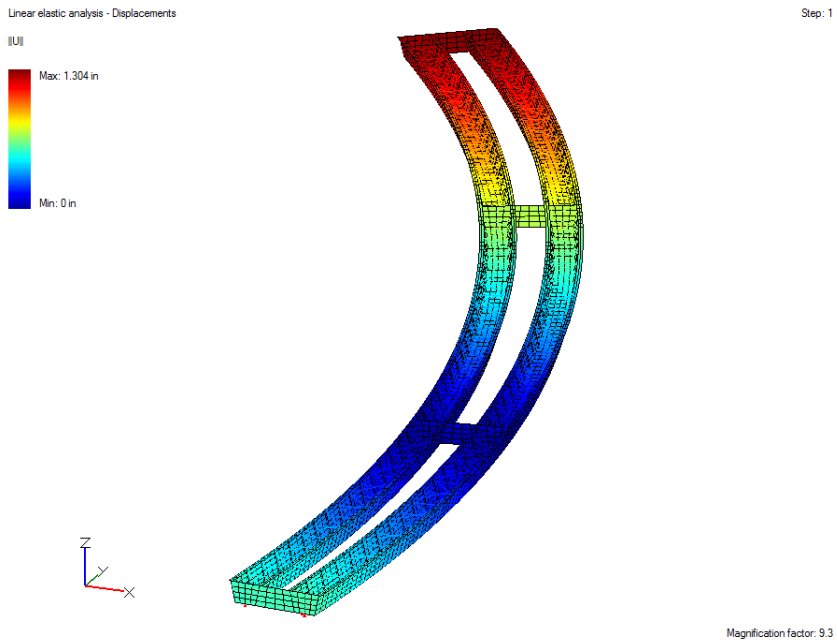

Figure 6.68: Bridge deflected shape under 30°C thermal expansion (chorded layout with respect to the 2nd support)

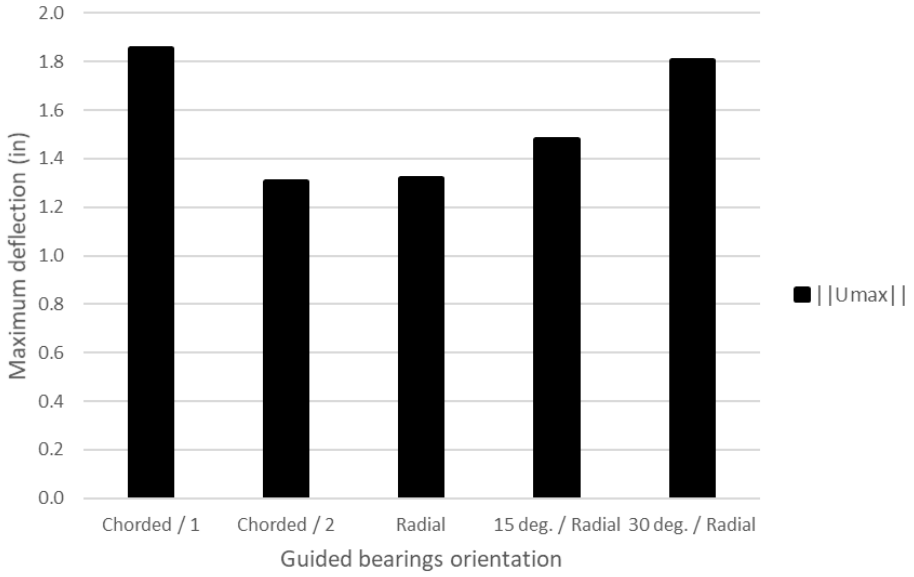

Figure 6.69: Effect of the guided bearings orientation on the bridge maximal deflection

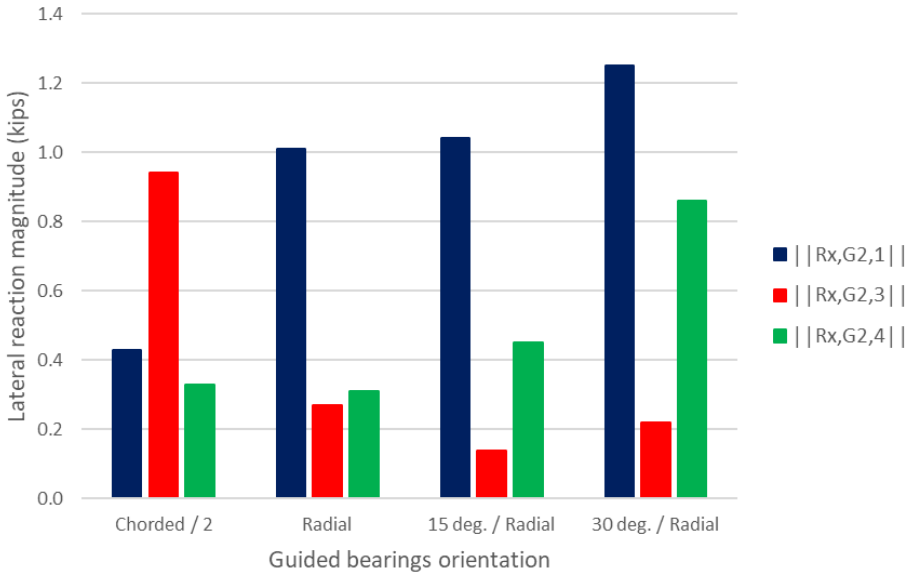

Figure 6.70: Effect of the guided bearings orientation on the lateral guide horizontal reactions (for each of the four guided bearing orientations experimented, the blue, red and green colors correspond respectively to the lateral reaction at the first, third and fourth support on the second tub girder)

6.4.4 PLACEMENT ANALYSIS

Finally, the concrete deck is poured on top of the steel superstructure, and five placement stages are considered in order to minimize cracking in the negative moment regions. Parameters that are often overlooked by the engineer are the bending and torsion-induced lateral truss forces during placement. The distribution of these forces at each stage along the placement sequence is shown in Figures 6.71-6.80. One can observe that overall, the maximum and minimum axial forces are equal to 30.1 kips and 28.8 kips, respectively. For placement stages number 3 and 5, it can also be observed that the distribution of those brace forces is not perfectly symmetric. This is due to the differential hardening of the deck sections already cast that provide composite action with the steel superstructure underneath it.

The evaluation of those brace forces, and especially, of the maximum compressive force that is encountered throughout the placement sequence, is critical to prevent braces from buckling. Once the concrete deck is fully cast and stiffens, it provides all the required lateral bracing to the bridge. The single diagonal lateral bracing system is therefore no longer critical for controlling the bridge deformations and ensuring bridge stability.

This chapter presented two plate girder and two tub girder examples subjected to a variety of loads and analyses. A summary of the work undertaken in this research is provided in the next chapter. Additional examples consisting of actual curved plate girder bridges are described in the appendices.

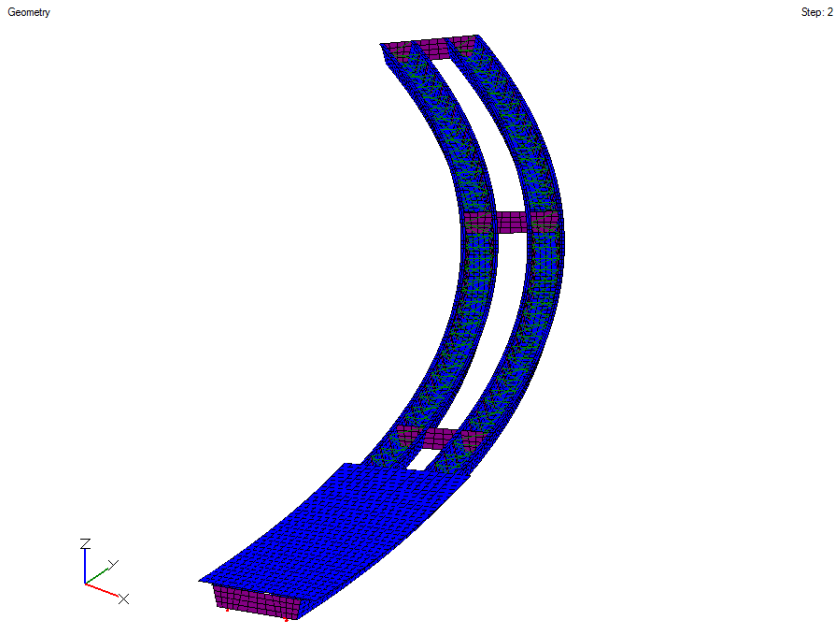

Figure 6.71: Bridge model (placement stage 1)

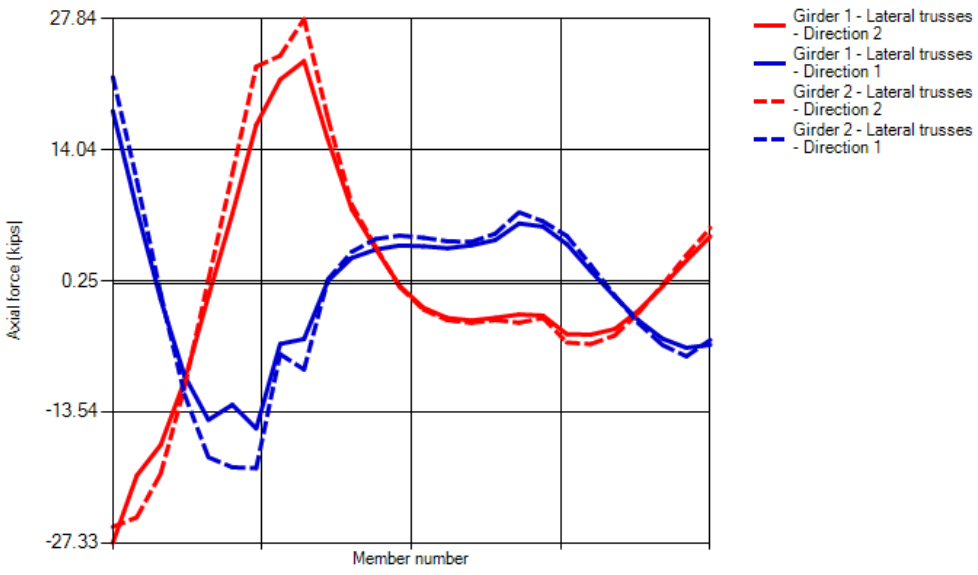

Figure 6.72: Lateral truss forces (placement stage 1)

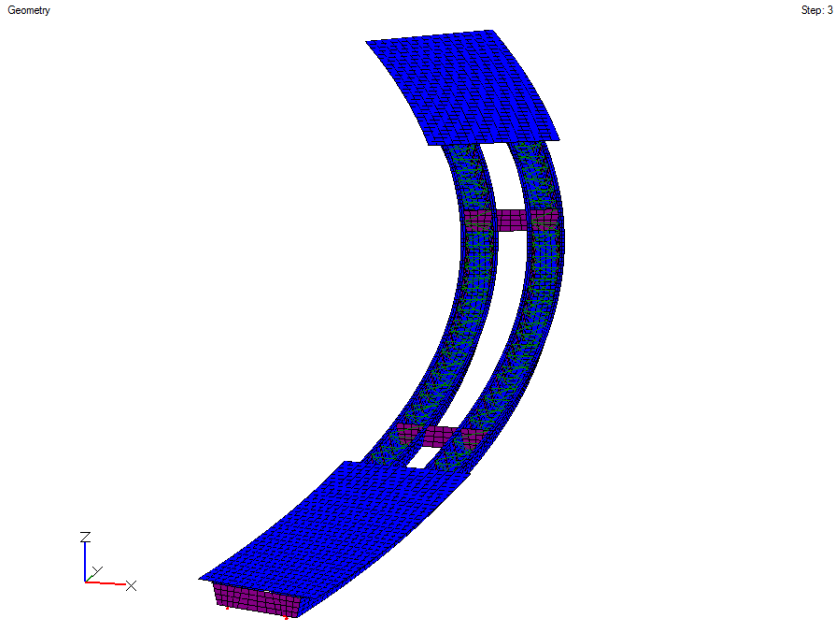

Figure 6.73: Bridge model (placement stage 2)

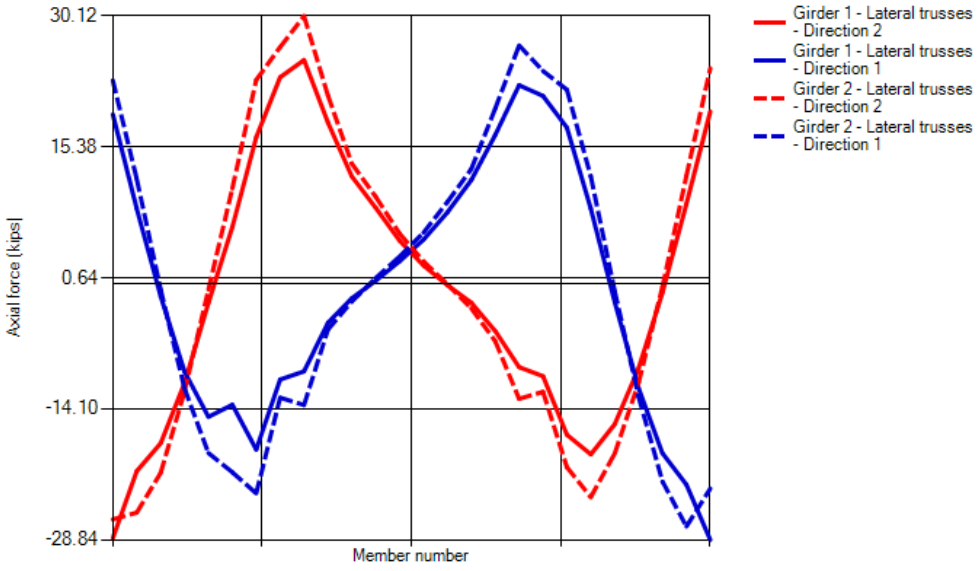

Figure 6.74: Lateral truss forces (placement stage 2)

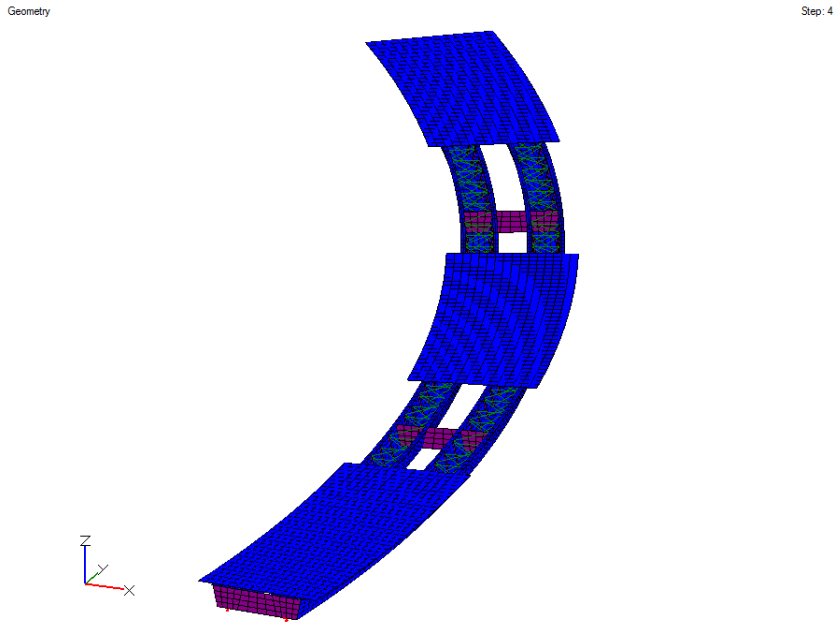

Figure 6.75: Bridge model (placement stage 3)

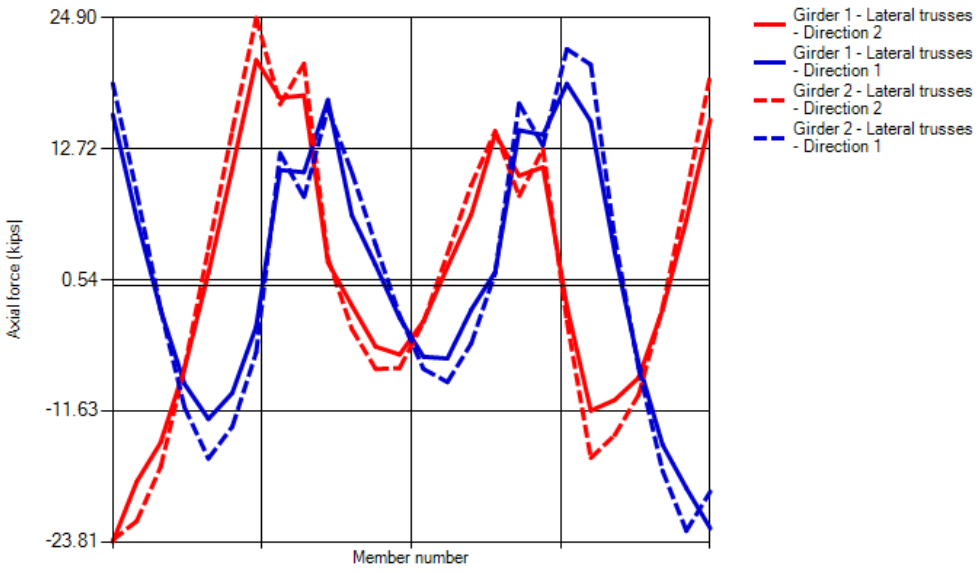

Figure 6.76: Lateral truss forces (placement stage 3)

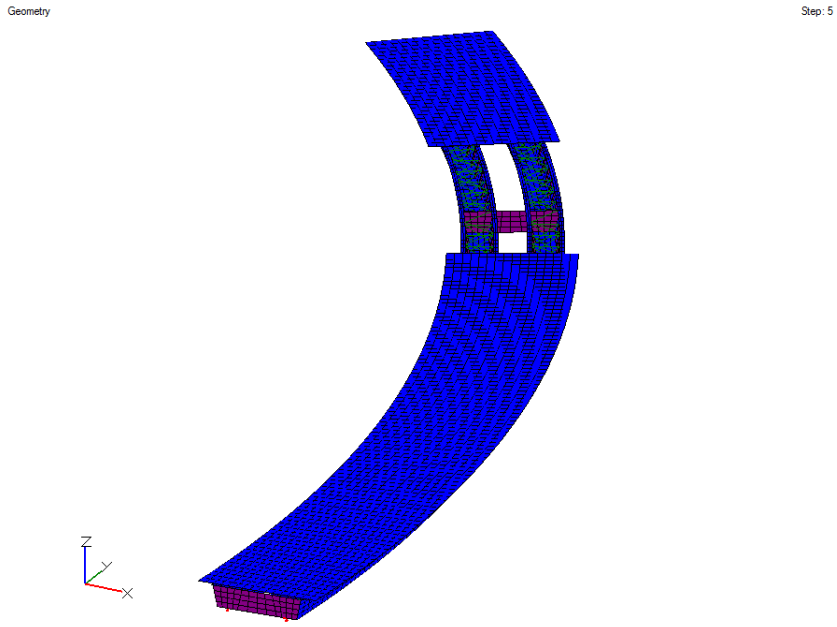

Figure 6.77: Bridge model (placement stage 4)

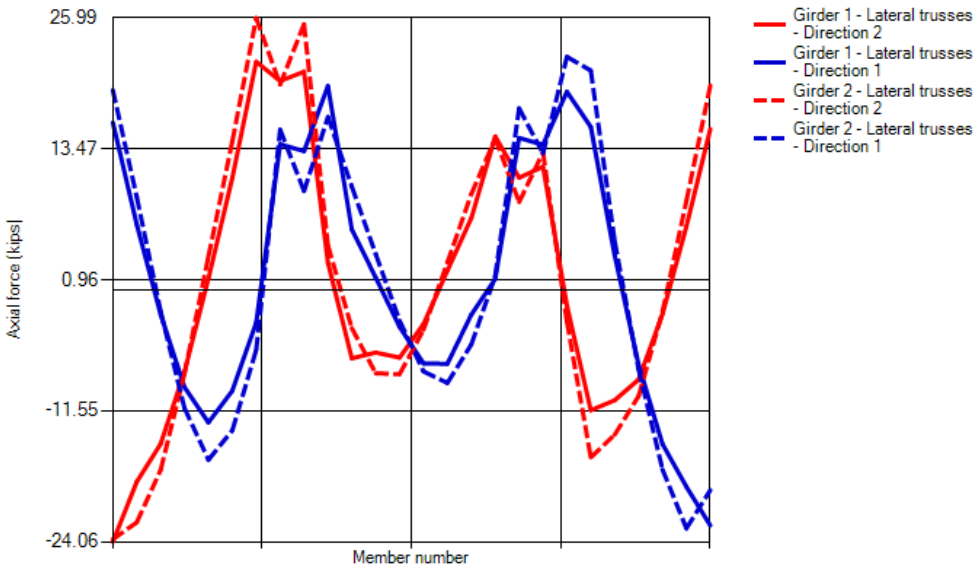

Figure 6.78: Lateral truss forces (placement stage 4)

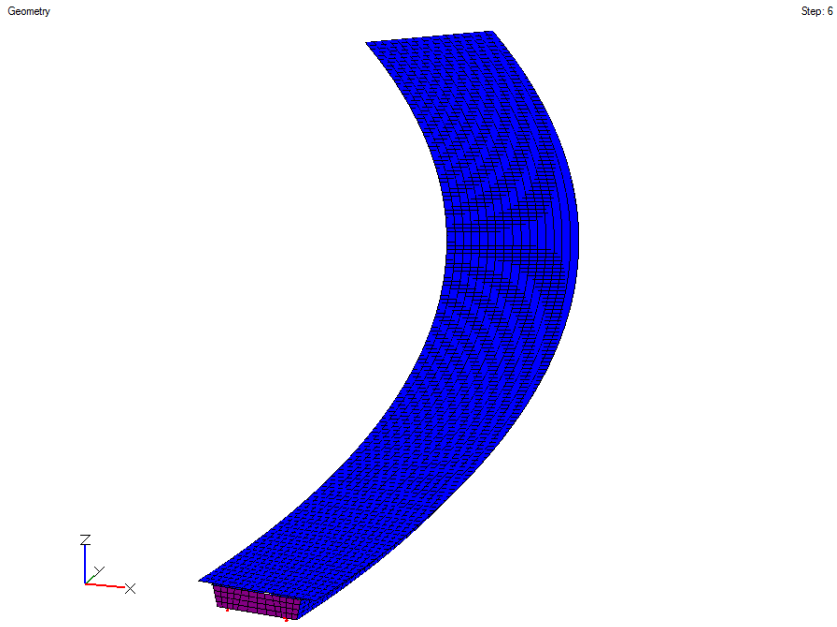

Figure 6.79: Bridge model (placement stage 5)

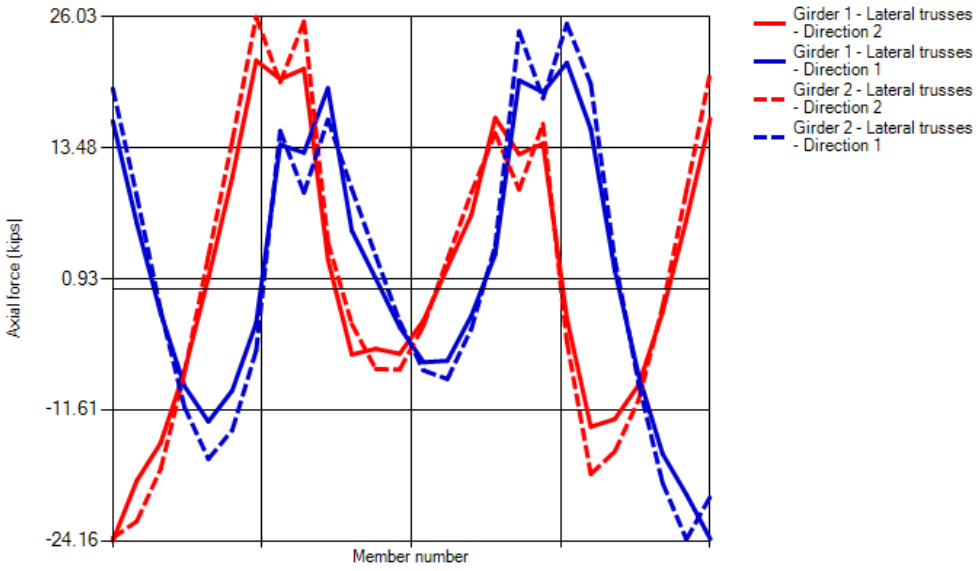

Figure 6.80: Lateral truss forces (placement stage 5)

Chapter 7: Conclusions

UT Bridge V2.2 is a finite element program that can generate a three-dimensional shell model of curved plate girder and tub girder bridges. It can conduct different types of analyses: linear elastic, linearized buckling, modal dynamic, and geometrically nonlinear. A variety of bracing options are offered to the analyst, including X-frames, K-frames, lateral trusses, struts and diaphragms. The program also allows for different loading options, including self-weight, point loads, uniform loads, wind loads, and temperature loads.

The implementation of an isoparametric, quadratic, eight-noded general shell element, considering both bending and membrane forces, leads to accurate results, generally within a few percent of well-known solutions or values obtained from commercial programs such as ABAQUS. As the program targets specific types of structural systems, its architecture is designed to provide a user-friendly experience. A multitude of time-consuming tasks encountered with commercial programs can be conducted efficiently with UT Bridge V2.2. These tasks include, for example, the definition of any erection or deck placement scenario.

UT Bridge V2.2 aims to fill the gap between state-of-the-art computational methods and routine engineering practice. The program has already been used by several design firms across the United States, which shows how effective it can be as a replacement to traditional one-dimensional line-analysis and two-dimensional grid methods.

The beginning of the dissertation introduced the details of horizontally curved plate girder and tub girder bridge systems, which must resist both bending and torsion. In particular during the erection and construction phases, these structures are prone to lateral-torsional buckling or global buckling, which can in severe cases lead to tragic failures.

Next, the dissertation provided an overview of the different programs available on the market today to analyze curved structures, and it also described the latest research projects undertaken to understand their behavior. The architecture of UT Bridge V2.2 and its main three components was then described, using flowcharts whenever possible to visually show the main algorithms implemented in the code.

Illustrating all of the program capabilities would result in an excessively lengthy dissertation. Instead, four representative examples were selected. These example include two plate girder structures and two tub girder structures. In the first example, well-known stability concepts—such as lateral-torsional, lateral or torsional buckling, load height effects, and ideal stiffness—were revisited. This first example also served as a validation study. A parametric study was further conducted to evaluate the influence of support skew angle on twin-girder structures subjected to a uniform moment distribution.

In the second example, a severely curved, three-girder bridge subjected to self-weight and freshly cast concrete was analyzed. Shear, moment, torsion, and bi-moment diagrams were presented. A parametric study relating the effect of curvature on the ratio of flange warping stresses to bending stresses was conducted. A geometrically nonlinear analysis was also performed, showing how a linear elastic analysis can be inappropriate for evaluating the deformations, cross-frame forces, and stability of curved systems having a low first buckling eigenvalue. The study also indicated that cross-frame forces increase linearly with curvature and that only a geometrically nonlinear analysis produces a symmetrical distribution of the cross-frame forces.

In the third example, the Marcy Bridge was modeled. This bridge was a straight tub girder that collapsed during deck placement in the early 2000s. Affordable bracing solutions that would have prevented its failure were presented. A parametric study showed

how lateral trusses are most efficient at restraining warping deformations at the ends of simply-supported tub girders.

Finally, the fourth example described a multi-stage erection and placement analysis on a large curved, twin tub girder bridge. The erection procedure selected included the use of a drop-in segment. Lateral truss forces were evaluated at each stage of the erection and construction. In addition, the influence of the external diaphragms in controlling differential deflections between adjacent tubs was studied. Finally, temperature loads were also modeled to evaluate the bridge response under a variety of guided bearing orientations.

Two examples of actual plate girder bridges, analyzed with UT Bridge V2.2, are presented in the appendices. The first one is a curved, skewed, simply-supported bridge. It is a fully erected structure having a large first buckling eigenvalue. For this case, it is shown that a geometrically nonlinear analysis does not bring significant additional accuracy to the estimation of bridge displacements and cross-frame forces. The second bridge, in contrast, is first partially erected before the remainder of the superstructure is assembled and the deck cast. A study shows how the bridge gains stability throughout the erection sequence. It also shows how torsional deformations can be quickly estimated by the program.

UT Bridge V2.2 is a new program that targets the same structures as UT Bridge V1.0 (Stith 2010), UTrAp (Topkaya 2002) and BASP (Akay, Johnson and Will 1977). It combines the capabilities of all three programs into one, with extended options. All of these programs have been developed at the University of Texas at Austin. Like all computer programs, there is room for improvement. For UT Bridge V2.2, these improvements may include:

- Modeling the K-frame chords with beam elements instead of truss elements to eliminate the current use of a kinematic constraint that is acceptable for girder

behavior but leads to an inaccurate estimation of the axial forces within the K-frames.

- Modeling initial imperfections on straight systems to evaluate their influence on bridge stability using a geometrically nonlinear analysis.
- Modeling detailing methods other than the no-load detailing method, which is the one recommended for curved structures but not necessarily for straight, skewed systems.
- Modeling material nonlinearity to evaluate the plastic and potentially the ultimate behavior of plate girder and tub girder bridges.
- Modeling moving loads to produce influence surfaces and to evaluate the bridge behavior in its finished state.
- Modeling abutments and piers for greater accuracy in predicting bridge dynamic behavior.

Lastly, key subroutines describing the assembly of the isoparametric, quadratic, eight-noded general shell element stiffness, geometric stiffness, and mass matrices are schematically described in the appendices. The subroutine for the stress recovery procedure is also included. Providing these subroutines is meant to reduce an existing gap between the presented shell theory and its implementation into finite element programs. These subroutines are applicable to all shell structures, not only to the bridge systems addressed in the present dissertation.

All in all, UT Bridge V2.2 is meant to be a useful contribution to the bridge industry. Bridge engineers and erectors can use to program to efficiently conduct detailed analyses that provide much more accurate assessments of behavior without requiring

detailed FEA knowledge. The time to produce such a solution is equivalent if not less than the amount of time needed for the software commonly used in practice. The program therefore provides a way of conducting more accurate analyses with essentially no increased demands on time or knowledge.

Appendices

Appendix A: Real bridges – Case studies

In November 2016, a prior version of the program (UT Bridge V2.1) was released to a group of about forty bridge engineers around the country. The group primarily included senior, experienced engineers, working either for private consulting firms or for State Departments of Transportations. The group also included recent graduates of the Structural Engineering program at the University of Texas at Austin. The feedback provided was generally positive. In some cases, problems were nevertheless encountered and technical support was provided. The following plate girder bridges were two of them. As the version that was released at the time handled plate girders only, tub girder bridges are not included. In general, the issues were quickly resolved, and the present version of the program (UT Bridge V2.2) is able to handle most of the configurations encountered by bridge engineers.

A.1 Analysis of a curved, skewed, simply-supported five-girder bridge

The following bridge model (Bridge A) is a simply-supported, curved, skewed plate girder bridge, consisting of five girders spaced at 9.667 ft on center. The overall length of the girders are respectively equal to 152.16 ft, 149.50 ft, 146.99 ft, 144.60 and 142.30 ft. The radius of curvature of the interior girder is equal to 290.67 ft. A radial bracing layout consisting of cross-frames (X-frames) is provided. The cross-sectional area for the cross-frames is taken equal to 4.75 in^2. The cross-frames are mounted on 8”×0.625” connecting plates. The bridge is subjected to its self-weight only.

A top view of the bridge model is shown in Figure A.1. As the steel superstructure is fully erected and braced, it is quite stable under its own self-weight. A linearized buckling analysis shows indeed that the first non-local buckling mode, which is the 88th

overall buckling mode encountered by the eigensolver, is a global lateral buckling mode and is reached for an eigenvalue equal to 17.8 (Figure A.2). As this is a large eigenvalue, a linear elastic analysis should be sufficient to provide an accurate enough description of the bridge behavior. A geometrically nonlinear analysis is nevertheless conducted to assess the validity of the previous statement. The deflected shape based on the linear elastic and on the geometrically nonlinear analyses are displayed in Figure A.3 and A.4 respectively. The overall maximum deflection is equal for both analyses, noting that a coarser mesh is used for the geometrically nonlinear analysis to accelerate convergence of the modified Newton-Raphson procedure. Based on the stresses calculated from a linear elastic analysis, the moment and shear diagrams are then displayed in Figures A.5 and A.6. Although the deflected shapes for both analyses are generally very comparable, there are nevertheless minor differences that result in a redistribution of the cross-frame forces (Figures A.7 and A.8). As explained in §6.2, cross-frame forces based on the geometrically nonlinear analysis are nearly symmetrical: both diagonal chords show opposite axial forces, which also applies to the top and bottom chords. Although minor in this particular case, second-order effects can be further observed in Figure A.9, which shows the load versus displacement curve for two degrees of freedom: the displacement in the x-direction at mid-span of the exterior girder for the top flange node (DOF 1) and the bottom flange node (DOF 2). Similarly to what was shown in §6.2, the bottom flange node initially deflects inward, before moving in the reverse direction. In this case though, the bridge is quite stiff, so the overall lateral movement is limited. Finally, Figure A.10 shows the first dynamic mode of the structure, which is a lateral bending mode having a natural frequency equal to 0.51 Hz.

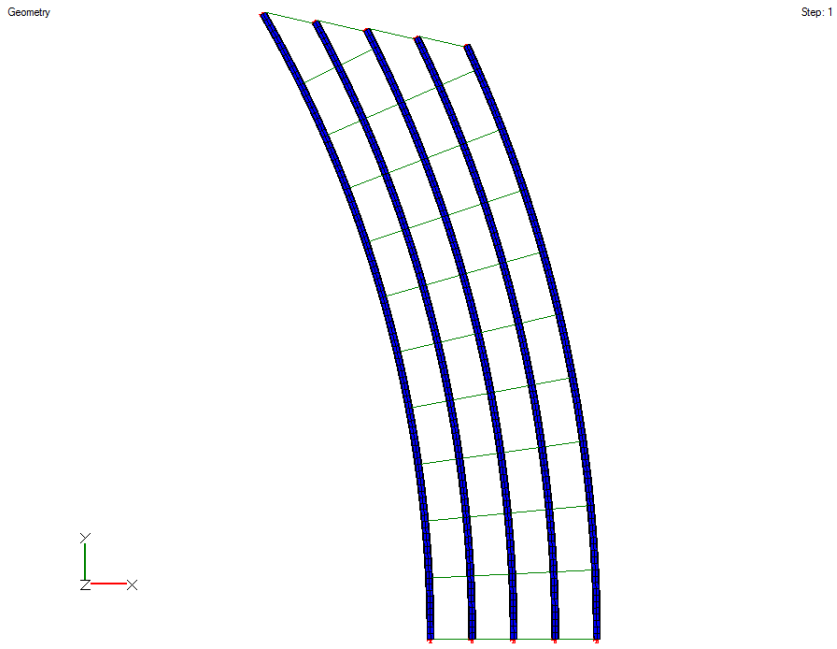

Figure A.1: Bridge A model (top view)

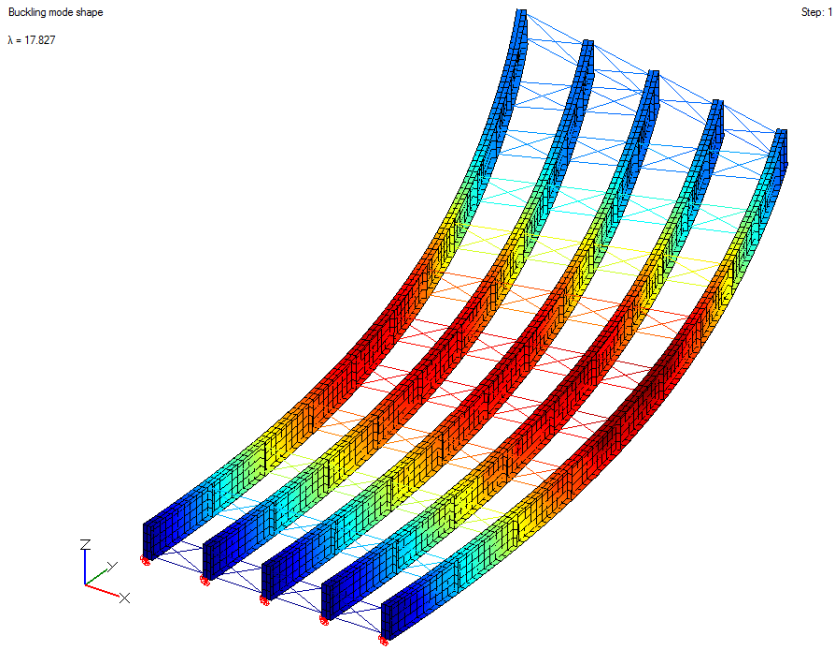

Figure A.2: Bridge A global lateral buckling mode (88th overall buckling mode, λ = 17.827)

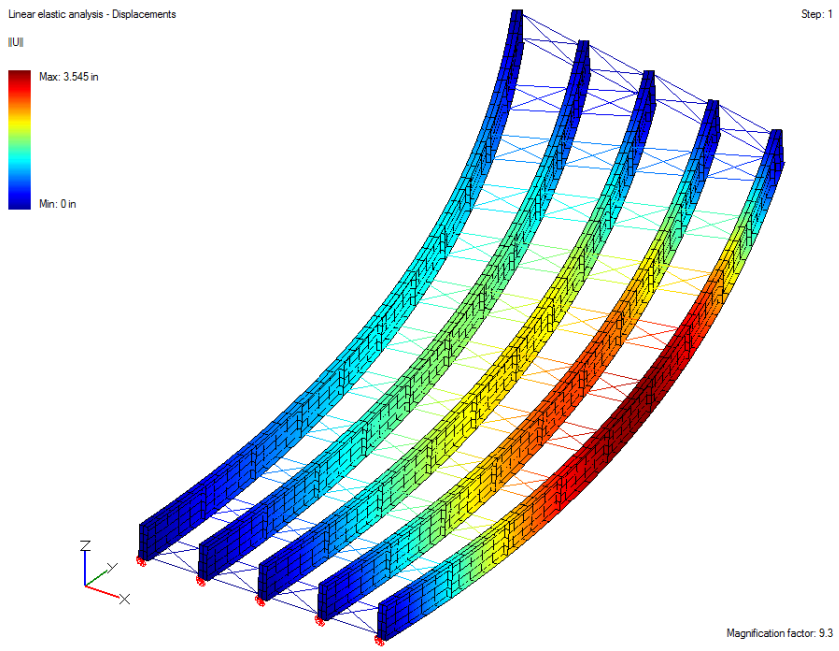

Figure A.3: Bridge A deflected shape (linear elastic analysis)

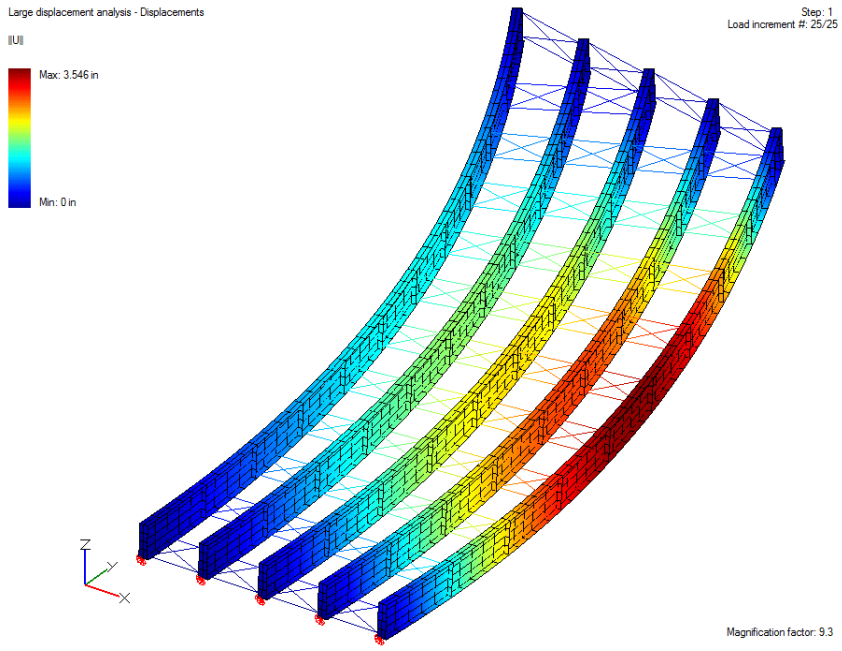

Figure A.4: Bridge A deflected shape (geometrically nonlinear analysis)

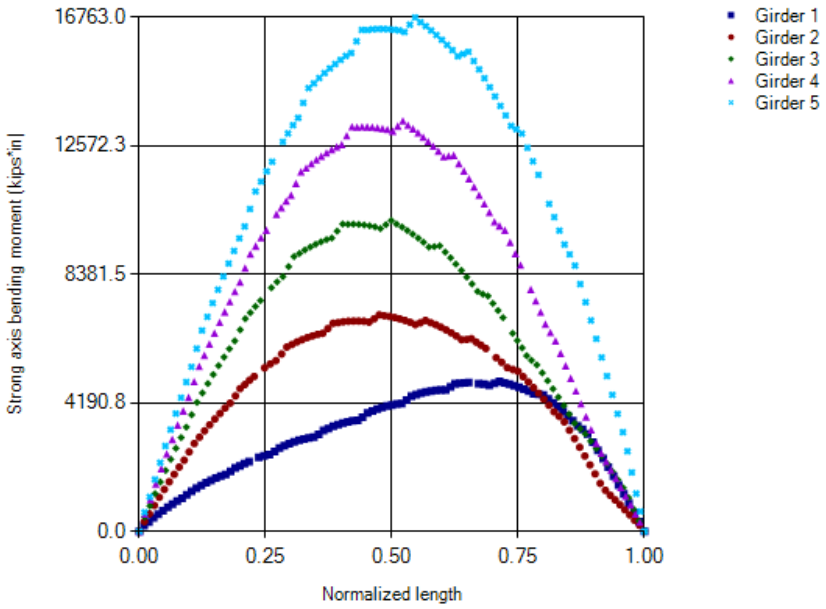

Figure A.5: Bridge A moment diagram

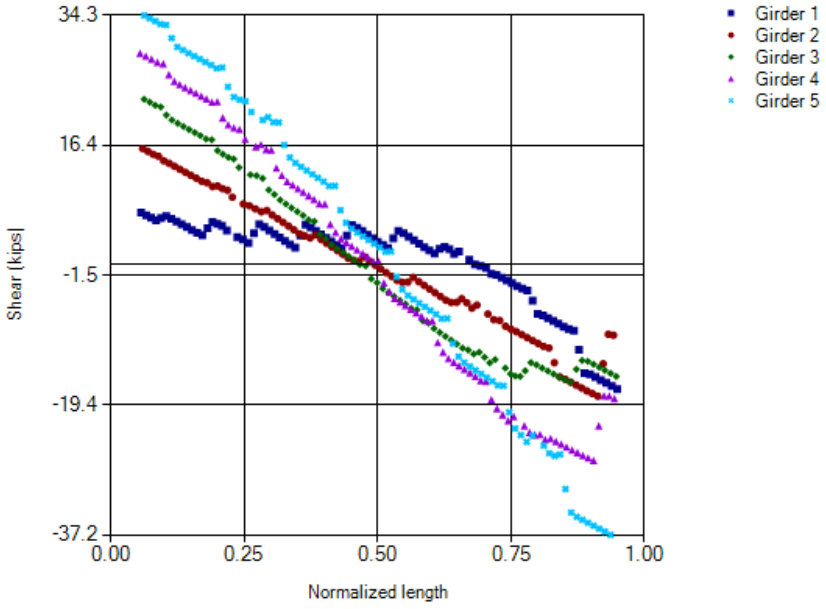

Figure A.6: Bridge A shear diagram

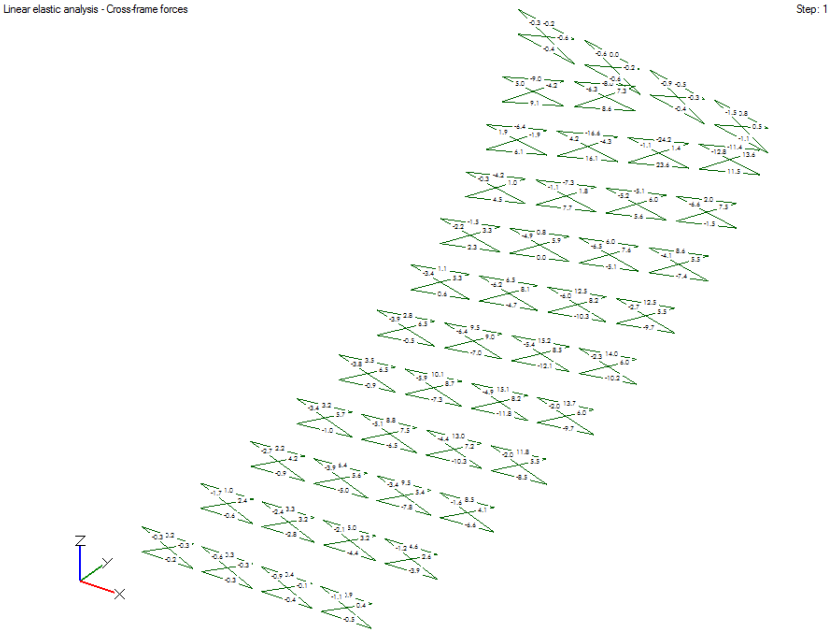

Figure A.7: Bridge A cross-frame forces (linear elastic analysis)

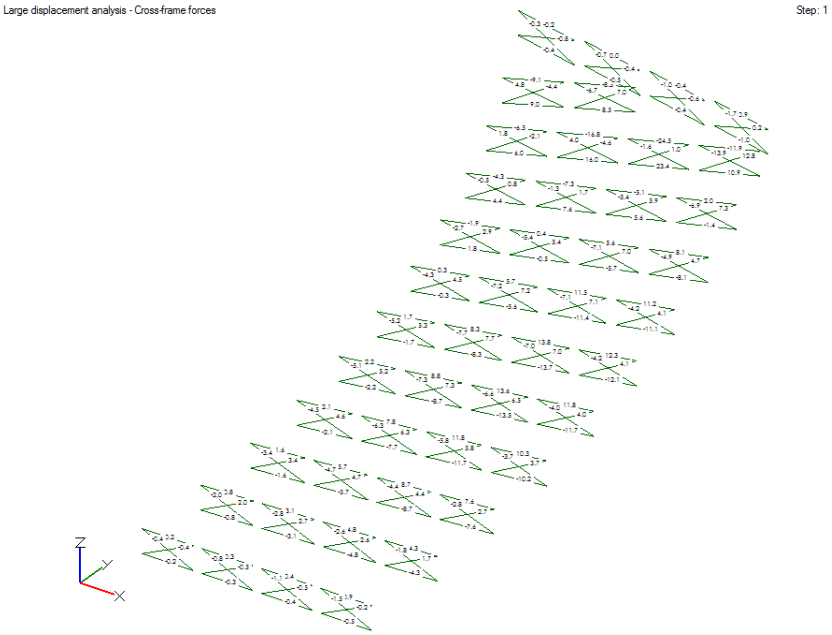

Figure A.8: Bridge A cross-frame forces (geometrically nonlinear analysis)

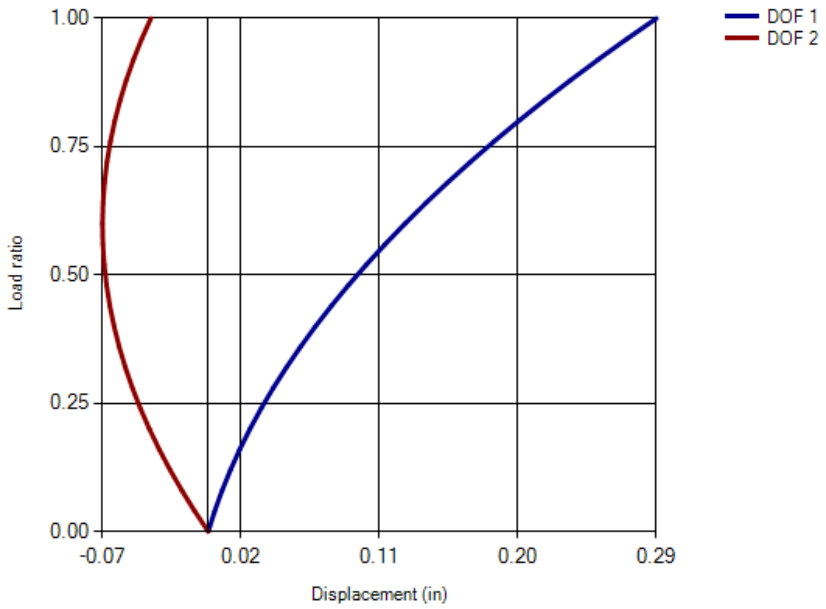

Figure A.9: Bridge A load vs. displacement curve (geometrically nonlinear analysis)

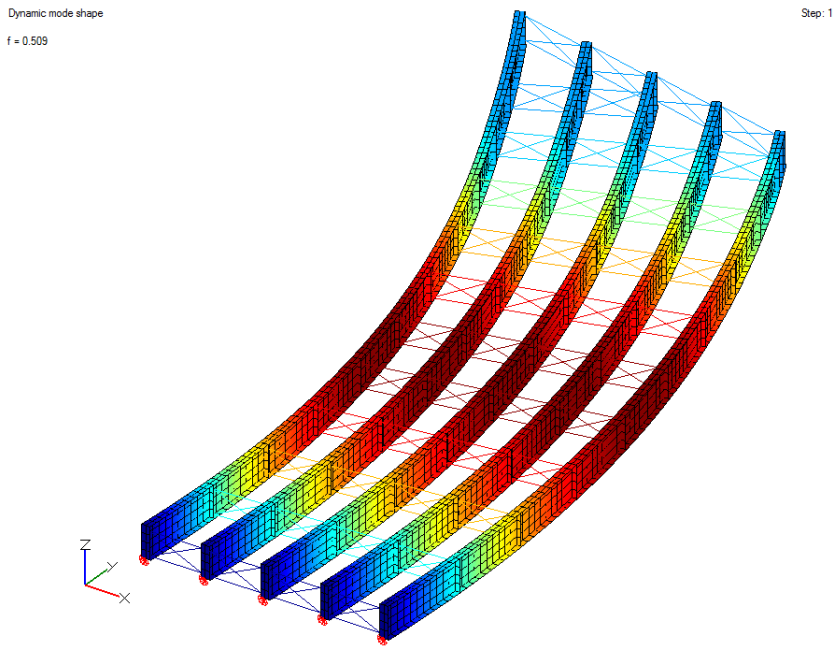

Figure A.10: Bridge A first dynamic mode (f = 0.509 Hz)

A.2 ANALYSIS OF A CURVED, CONTINUOUS, FOUR-GIRDER BRIDGE WITH MULTIPLE ERECTION STAGES

The second bridge model (Bridge B) is a continuous, curved plate girder bridge, consisting of four girders spaced at 7 ft on center. Contrary to all the bridge models previously presented, it has a right curvature orientation. The overall lengths of the girders are respectively equal to 413.22 ft, 407.39 ft, 401.55 ft and 395.72 ft. The radius of curvature of the interior girder is equal to 477 ft. A radial cross-frame layout is provided, consisting of K-frames having a cross-sectional area equal to 7.13 in^2. The cross-frames are mounted on 8-in. × 0.5-in. connecting plates. The bridge is subjected to its self-weight only. Three stages are analyzed along the erection sequence. A first analysis is conducted when the left two girders are partially erected (stage 1). A second analysis is performed when all four girders are partially erected (stage 2). Finally, the fully erected steel superstructure is analyzed (stage 3). In addition, a placement analysis is conducted, with the concrete deck fully cast. 4-ft. wide overhangs are assumed. The concrete strength is taken equal to 5 ksi. Three shear studs per row are assumed, with a shear stud nominal diameter equal to 0.75-in. and a shear stud spacing of 1 ft.

The deflected shape for erection stage 1 is shown in Figure A.11. The bridge layover, meaning the relative lateral displacement between the top flange and the bottom flange, is shown in Figure A.12. Calculating the layover along the girders is a meaningful way to estimate the torsional behavior of the bridge. The first buckling mode is a global buckling mode and is reached for an eigenvalue equal to 10.5 (Figure A.13). The first dynamic mode has a natural frequency equal to 0.52 Hz (Figure A.14). For stage 2, the deflected shape and layover diagram are shown in Figures A.15 and A.16 respectively. The global lateral buckling mode is reached for an eigenvalue equal to 21.1 (Figure A.17), which is twice the buckling eigenvalue corresponding to stage 1. Erecting the right two

girders clearly stabilizes the structure. The first dynamic mode for stage 2 is similar to the one obtained for stage 1, with a natural frequency equal to 0.52 Hz (Figure A.18). For stage 3, the deflected shape is shown in Figure A.19. The maximal Von Mises stress is calculated equal to 5.9 ksi (Figure A.20). Figure A.21 and A.22 show the moment and shear diagrams. As expected, the exterior girder is subjected to higher moment and shear. Finally, the bridge model with the concrete deck fully placed is shown in Figure A.23. It can be observed that most shells modeling the deck are quads. A few triangles can also be identified. As explained in Chapter 4, those triangular elements are required for a continuous, compatible mesh. For this final stage, with the deck fully placed, the maximum vertical displacement is calculated equal to 2.4 in (Figure A.24). Figure A.25 and A.26 show the moment and shear diagrams respectively. No uplift at the supports is observed.

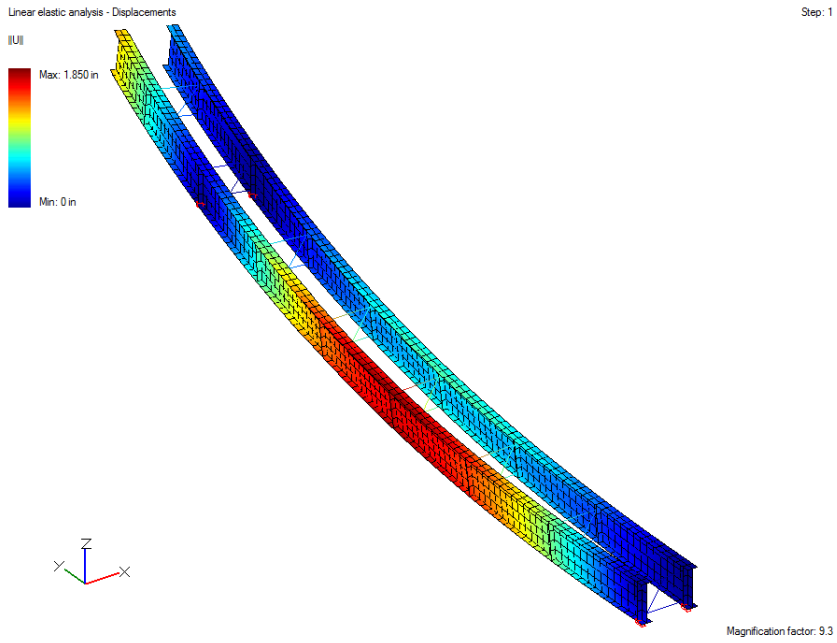

Figure A.11: Bridge B deflected shape – Erection stage 1 (linear elastic analysis)

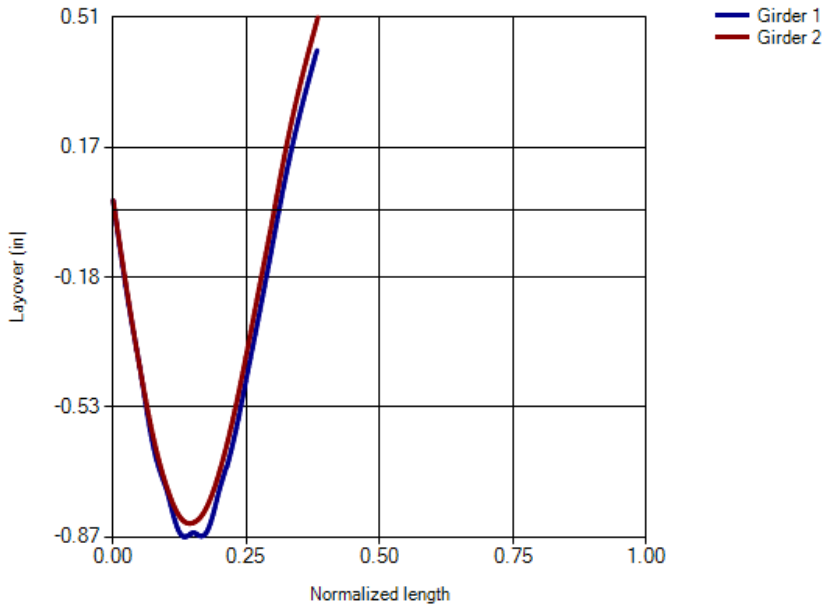

Figure A.12: Bridge B layover diagram – Erection stage 1 (linear elastic analysis)

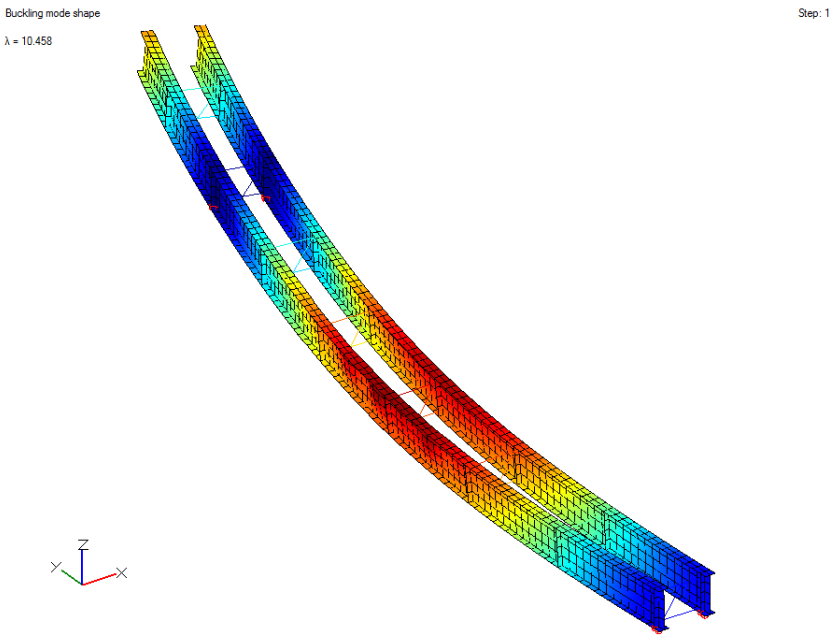

Figure A.13: Bridge B global lateral buckling mode – Erection stage 1 (4th overall buckling mode, λ = 10.458)

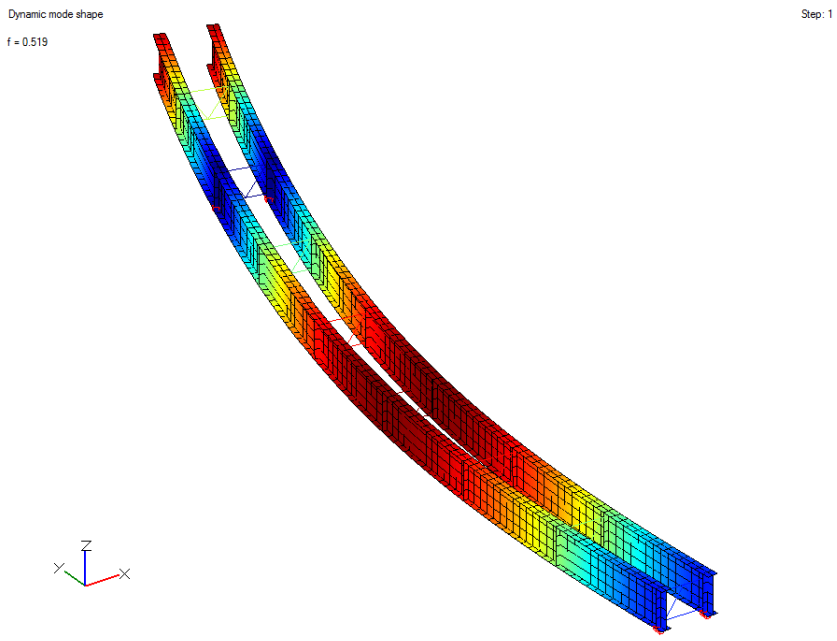

Figure A.14: Bridge B first dynamic mode – Erection stage 1 (f = 0.519 Hz)

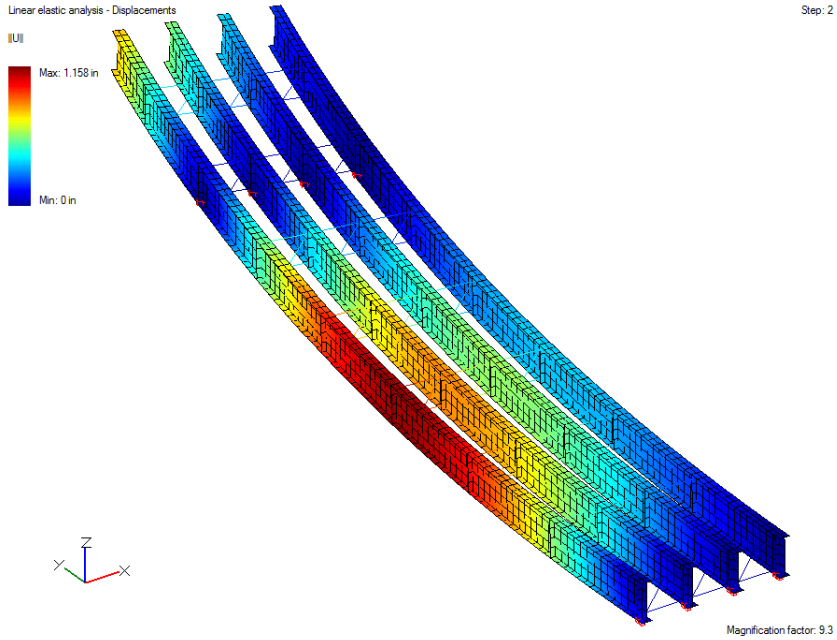

Figure A.15: Bridge B deflected shape – Erection stage 2 (linear elastic analysis)

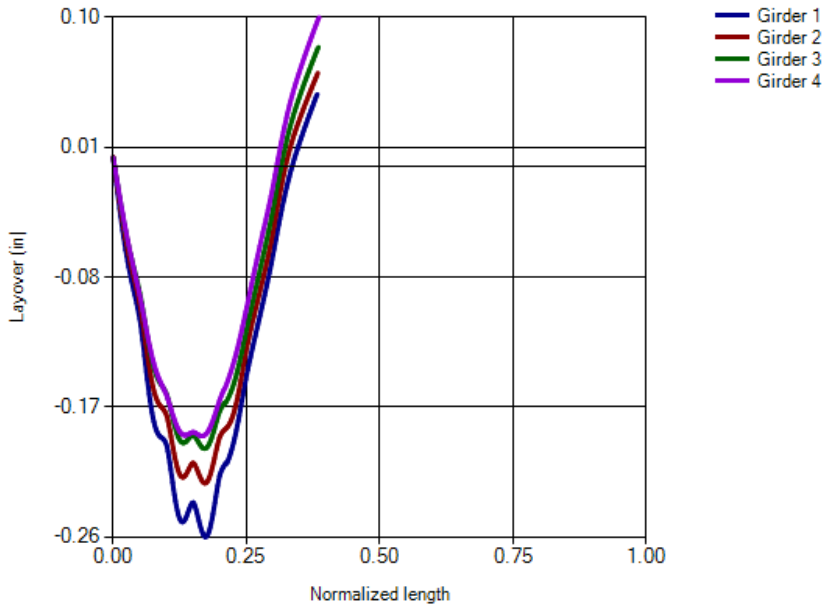

Figure A.16: Bridge B layover diagram – Erection stage 2 (linear elastic analysis)

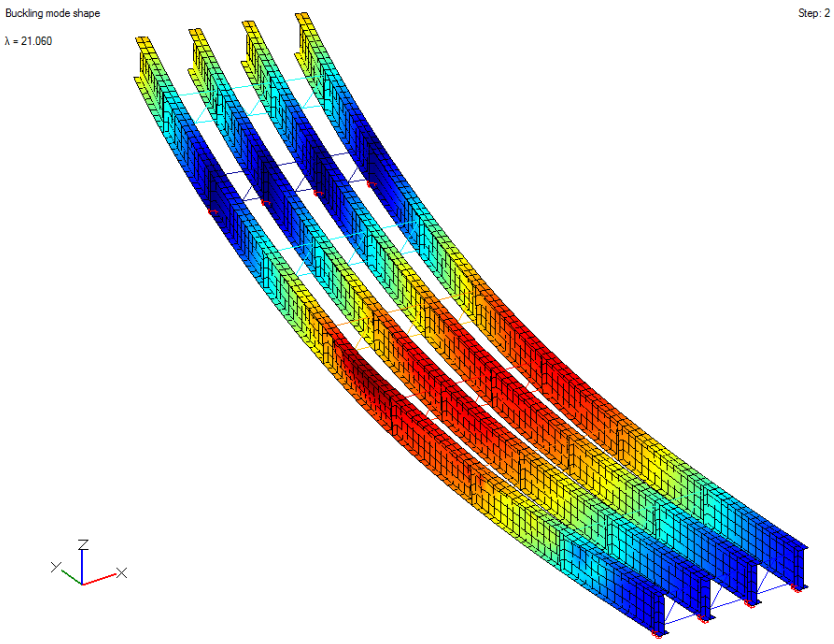

Figure A.17: Bridge B global lateral buckling mode – Erection stage 2 (46^{th} overall buckling mode, $\lambda = 21.060$)

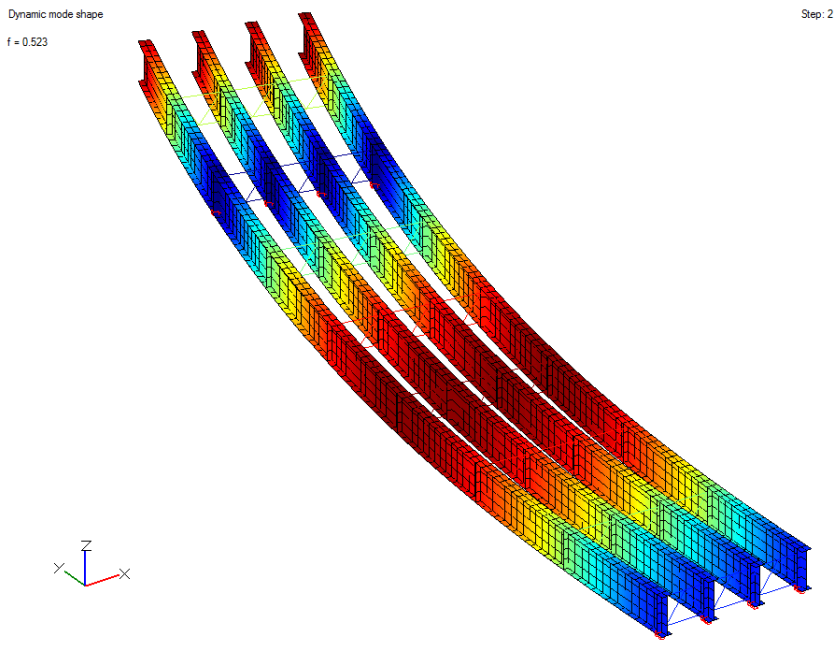

Figure A.18: Bridge B first dynamic mode – Erection stage 2 (f = 0.523 Hz)

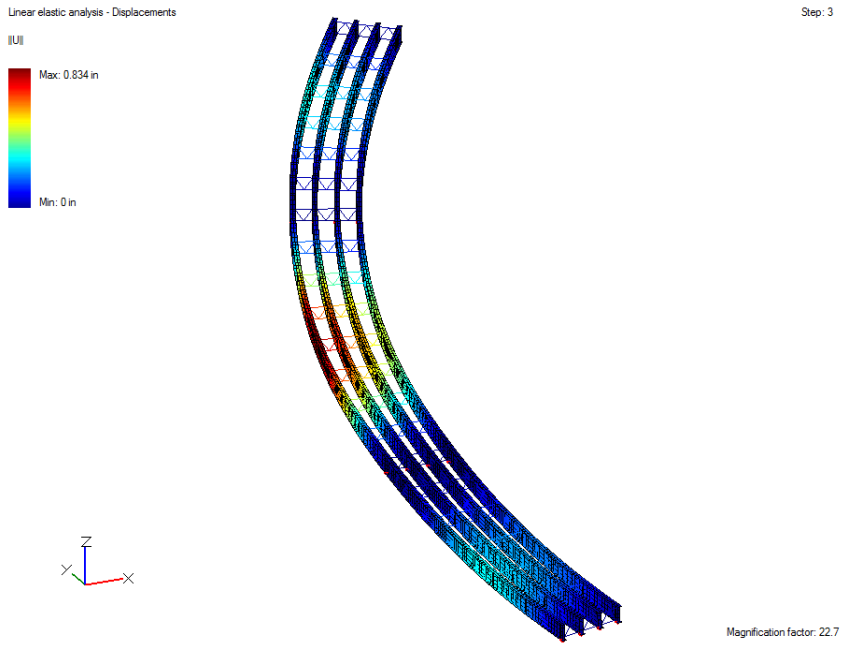

Figure A.19: Bridge B deflected shape – Erection stage 3 (linear elastic analysis)

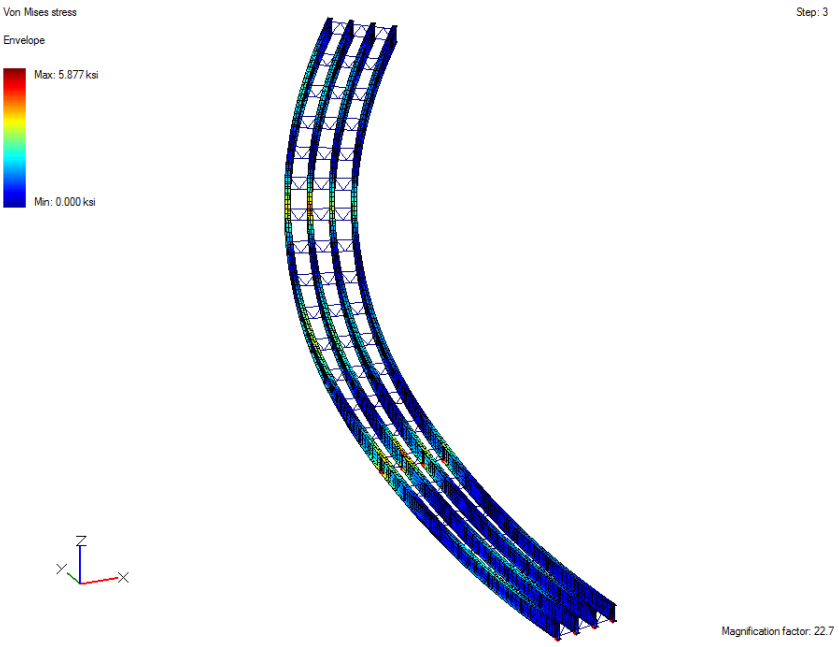

Figure A.20: Bridge B Von Mises stress distribution – Erection stage 3 (linear elastic analysis)

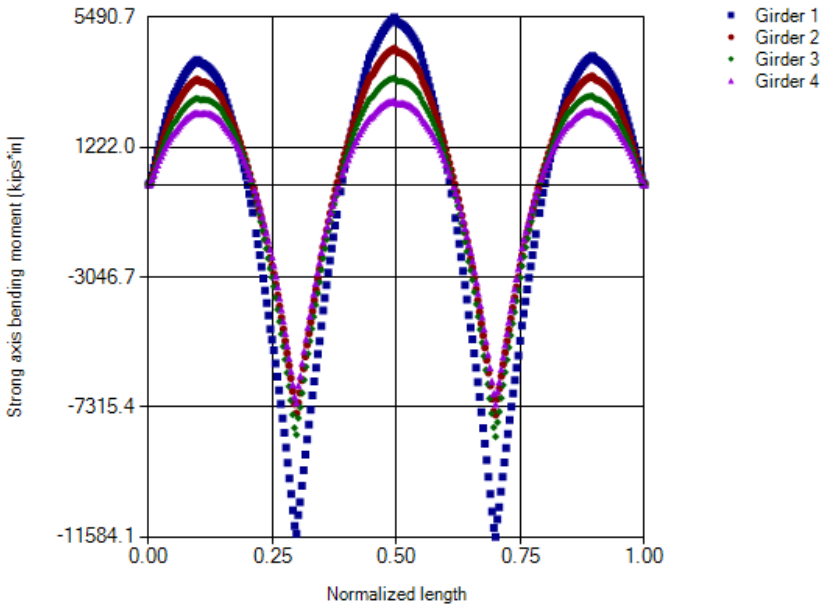

Figure A.21: Bridge B moment diagram – Erection stage 3

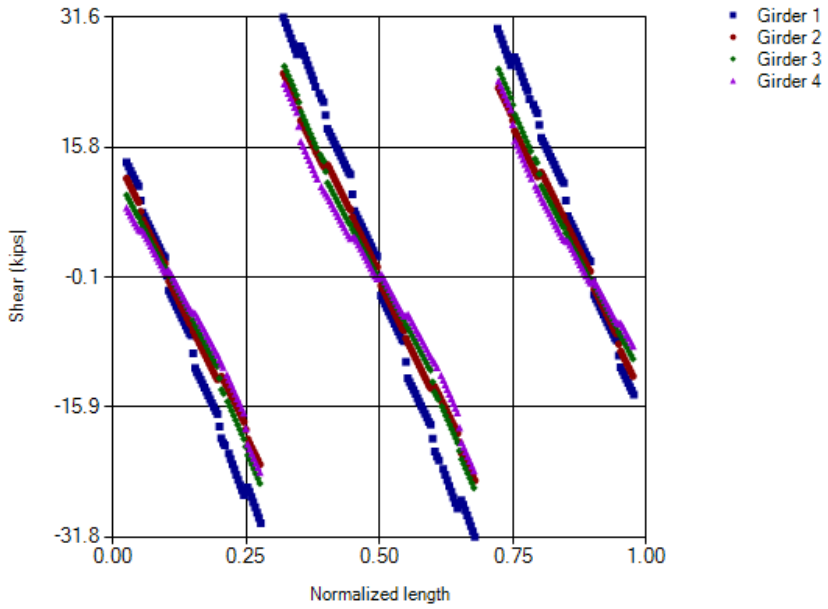

Figure A.22: Bridge B shear diagram – Erection stage 3

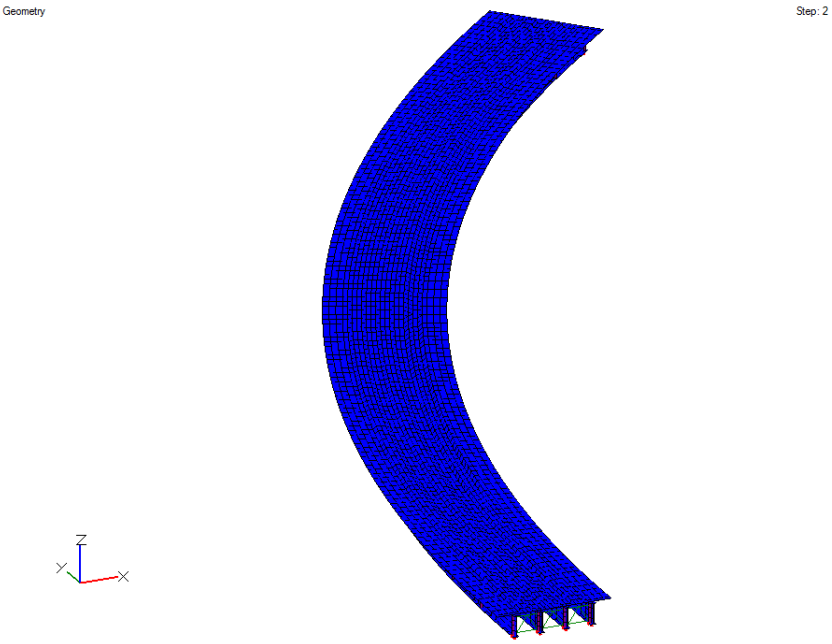

Figure A.23: Bridge B model – Placement analysis

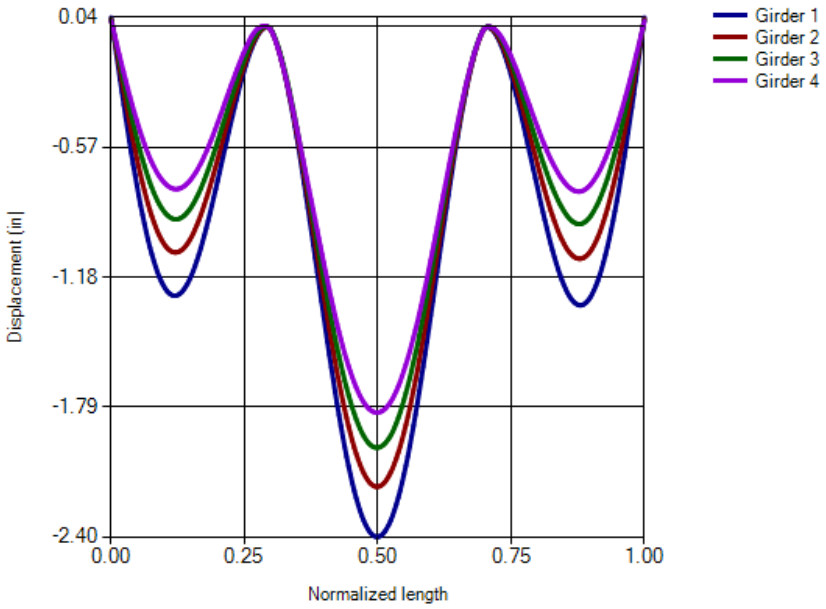

Figure A.24: Bridge B vertical displacement chart – Placement analysis (linear elastic analysis)

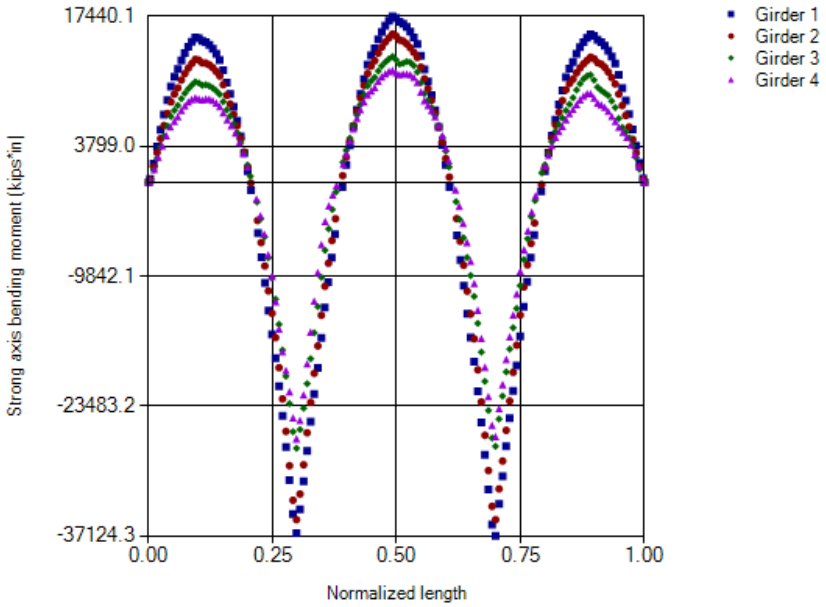

Figure A.25: Bridge B moment diagram – Placement analysis

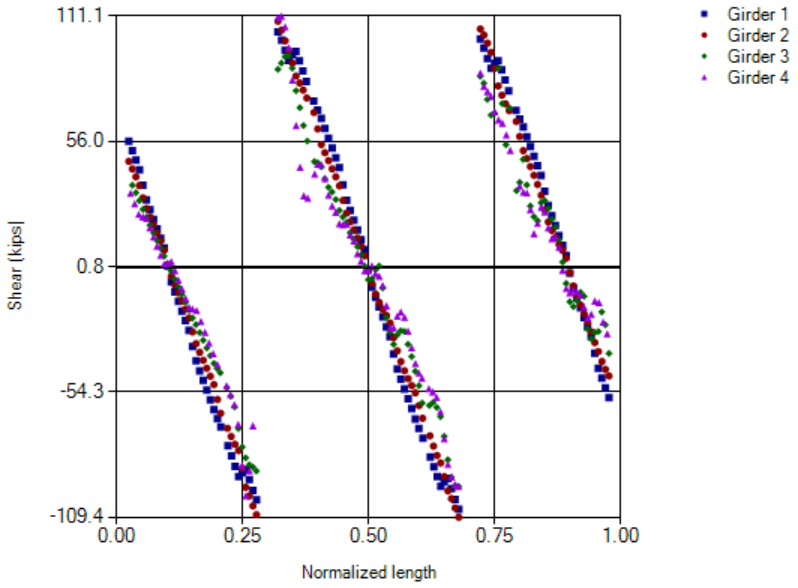

Figure A.26: Bridge B shear diagram – Placement analysis

Appendix B: Derivation of the general shell stiffness matrix

Notations:

(r, s) : integration point coordinates evaluated in the shell natural coordinate system

$h_k(r, s)$: k-th shape function evaluated at point (r, s)

$t(i), i = 1{,}2$: location of the two integration layers through the shell depth

$\omega(j), j = 1{,}4$: weight coefficient for the four integration points per layer

$C_{ij}, i = 1{,}6, j = 1{,}6$: steel constitutive law matrix

$X_{kp}, k = 1{,}3, p = 1{,}8$: p-th coordinate of nodal point k in the global Cartesian coordinate system

$a_k, k = 1{,}8$: shell thickness evaluated at nodal point k

$J_{ij}, i = 1{,}3, j = 1{,}3$: Jacobian matrix

$\sigma_{Gauss,(i-1)\cdot 4+j,p}, i = 1{,}2, j = 1{,}4, p = 1{,}6$: p-th stress vector component at the j-th integration point on the i-th integration layer

$x\big(shell(i)\big), i = 1{,}4$: x-coordinate of the shell i-th exterior node

$y\big(shell(i)\big), i = 1{,}4$: y-coordinate of the shell i-th exterior node

$z\big(shell(i)\big), i = 1{,}4$: z-coordinate of the shell i-th exterior node

All other notations were previously defined in Chapter 4 and Chapter 5.

! Define the interpolation functions

$$h_5(r, s) = \frac{1}{2} \cdot (1 - r^2) \cdot (1 - s)$$

$$h_6(r, s) = \frac{1}{2} \cdot (1 + r) \cdot (1 - s^2)$$

$$h_7(r, s) = \frac{1}{2} \cdot (1 - r^2) \cdot (1 + s)$$

$$h_8(r,s) = \frac{1}{2} \cdot (1-r) \cdot (1-s^2)$$
$$h_1(r,s) = \frac{1}{4} \cdot (1-r) \cdot (1-s) - \frac{1}{2} \cdot (h_8(r,s) + h_5(r,s))$$
$$h_2(r,s) = \frac{1}{4} \cdot (1+r) \cdot (1-s) - \frac{1}{2} \cdot \left(h_5(r,s) + h_6(r,s)\right)$$
$$h_3(r,s) = \frac{1}{4} \cdot (1+r) \cdot (1+s) - \frac{1}{2} \cdot \left(h_6(r,s) + h_7(r,s)\right)$$
$$h_4(r,s) = \frac{1}{4} \cdot (1-r) \cdot (1+s) - \frac{1}{2} \cdot (h_7(r,s) + h_8(r,s))$$

! Define the integration points

$$(r,s)_1 = \left(-1/\sqrt{3}, -1/\sqrt{3}\right)$$
$$(r,s)_2 = \left(-1/\sqrt{3}, +1/\sqrt{3}\right)$$
$$(r,s)_3 = \left(+1/\sqrt{3}, -1/\sqrt{3}\right)$$
$$(r,s)_4 = \left(+1/\sqrt{3}, +1/\sqrt{3}\right)$$

! Define the location of the integration layers through the shell depth

$$t(1) = -\frac{1}{\sqrt{3}}$$
$$t(2) = +\frac{1}{\sqrt{3}}$$

! Define the weight coefficient of each integration point

For j = 1,4

$$\omega(j) = 1$$

Loop

! Define the stress-strain material law

$$C_{11} = \frac{E}{1-\nu^2}$$
$$C_{12} = \frac{E \cdot \nu}{1-\nu^2}$$
$$C_{21} = \frac{E \cdot \nu}{1-\nu^2}$$
$$C_{22} = \frac{E}{1-\nu^2}$$

$$C_{44} = \frac{E}{2 \cdot (1+\nu)}$$
$$C_{55} = 0.8 \cdot \frac{E}{2 \cdot (1+\nu)}$$
$$C_{66} = 0.8 \cdot \frac{E}{2 \cdot (1+\nu)}$$

! Perform the numerical integration

For i=1,2 ! For both integration layers through the shell thickness

For j = 1,4 ! For all integration points on that layer

! Initialize the Jacobian matrix

For p = 1,3 ! For all three rows of the Jacobian matrix

For q = 1,3 ! For all three columns of the Jacobian matrix

$$J_{pq} = 0$$

Loop

Loop

! Assemble the Jacobian matrix

For p = 1,3 ! For all three columns of the Jacobian matrix

For k = 1,8 ! For all the shell nodal points

$$J_{1p} = J_{1p} + \frac{\partial h_k}{\partial r}(j) \cdot \left(X_{kp} + t(i) \cdot \frac{a_k}{2} \cdot \ {}^0V_{Np}^k(j) \right)$$
$$J_{2p} = J_{2p} + \frac{\partial h_k}{\partial s}(j) \cdot \left(X_{kp} + t(i) \cdot \frac{a_k}{2} \cdot \ {}^0V_{Np}^k(j) \right)$$
$$J_{3p} = J_{3p} + \frac{a_k}{2} \cdot \ {}^0V_{Np}^k(j) \cdot h_k(j)$$

Loop

Loop

! Calculate the determinant of the Jacobian matrix

$$\det(J) = J_{11}J_{22}J_{33} - J_{11}J_{23}J_{32} - J_{21}J_{12}J_{33} + J_{21}J_{13}J_{32} + J_{31}J_{12}J_{23} - J_{31}J_{13}J_{22}$$

! Invert the Jacobian matrix

$$J_{11}^{-1} = \frac{J_{22}J_{33} - J_{23}J_{32}}{\det(J)}$$
$$J_{12}^{-1} = \frac{-J_{12}J_{33} + J_{13}J_{32}}{\det(J)}$$
$$J_{13}^{-1} = \frac{J_{12}J_{23} - J_{13}J_{22}}{\det(J)}$$
$$J_{21}^{-1} = \frac{-J_{21}J_{33} + J_{23}J_{31}}{\det(J)}$$
$$J_{22}^{-1} = \frac{J_{11}J_{33} - J_{13}J_{31}}{\det(J)}$$
$$J_{23}^{-1} = \frac{-J_{11}J_{23} + J_{13}J_{21}}{\det(J)}$$
$$J_{31}^{-1} = \frac{J_{21}J_{32} - J_{22}J_{31}}{\det(J)}$$
$$J_{32}^{-1} = \frac{-J_{11}J_{32} + J_{12}J_{31}}{\det(J)}$$
$$J_{33}^{-1} = \frac{J_{11}J_{22} - J_{12}J_{21}}{\det(J)}$$

! Compute the shape function derivatives in the global coordinate system

For k = 1,8

$$\frac{\partial h_k}{\partial x} = \frac{\partial h_k}{\partial r} \cdot J_{11}^{-1} + \frac{\partial h_k}{\partial s} \cdot J_{12}^{-1}$$
$$\frac{\partial h_k}{\partial y} = \frac{\partial h_k}{\partial r} \cdot J_{21}^{-1} + \frac{\partial h_k}{\partial s} \cdot J_{22}^{-1}$$
$$\frac{\partial h_k}{\partial z} = \frac{\partial h_k}{\partial r} \cdot J_{31}^{-1} + \frac{\partial h_k}{\partial s} \cdot J_{32}^{-1}$$

Loop

! Compute intermediate expressions required for the strain-displacement matrix

For k = 1,8

$$g_{1x}^k = -\frac{a_k}{2} \cdot {}^0V_{21}^k(j)$$
$$g_{1y}^k = -\frac{a_k}{2} \cdot {}^0V_{22}^k(j)$$
$$g_{1z}^k = -\frac{a_k}{2} \cdot {}^0V_{23}^k(j)$$

$$g_{1x}^{k} = +\frac{a_k}{2} \cdot \ {}^{0}V_{11}^{k}(j)$$
$$g_{1y}^{k} = +\frac{a_k}{2} \cdot \ {}^{0}V_{12}^{k}(j)$$
$$g_{1z}^{k} = +\frac{a_k}{2} \cdot \ {}^{0}V_{13}^{k}(j)$$
$$G_x^k = t \cdot \frac{\partial h_k}{\partial x} + J_{13}^{-1} \cdot h_k$$
$$G_y^k = t \cdot \frac{\partial h_k}{\partial y} + J_{23}^{-1} \cdot h_k$$
$$G_z^k = t \cdot \frac{\partial h_k}{\partial z} + J_{33}^{-1} \cdot h_k$$

Loop

! Assemble the strain-displacement matrix

For k = 1,8

! First column

$$B_{1,1+5\cdot(k-1)} = \frac{\partial h_k}{\partial x}$$
$$B_{2,1+5\cdot(k-1)} = 0$$
$$B_{3,1+5\cdot(k-1)} = 0$$
$$B_{4,1+5\cdot(k-1)} = \frac{\partial h_k}{\partial y}$$
$$B_{5,1+5\cdot(k-1)} = \frac{\partial h_k}{\partial z}$$
$$B_{6,1+5\cdot(k-1)} = 0$$

! Second column

$$B_{1,2+5\cdot(k-1)} = 0$$
$$B_{2,2+5\cdot(k-1)} = \frac{\partial h_k}{\partial y}$$
$$B_{3,2+5\cdot(k-1)} = 0$$
$$B_{4,2+5\cdot(k-1)} = \frac{\partial h_k}{\partial x}$$
$$B_{5,2+5\cdot(k-1)} = 0$$
$$B_{6,2+5\cdot(k-1)} = \frac{\partial h_k}{\partial z}$$

! Third column

$$B_{1,3+5\cdot(k-1)} = 0$$

$$B_{2,3+5\cdot(k-1)} = 0$$

$$B_{3,3+5\cdot(k-1)} = \frac{\partial h_k}{\partial z}$$

$$B_{4,3+5\cdot(k-1)} = 0$$

$$B_{5,3+5\cdot(k-1)} = \frac{\partial h_k}{\partial x}$$

$$B_{6,3+5\cdot(k-1)} = \frac{\partial h_k}{\partial y}$$

! Fourth column

$$B_{1,4+5\cdot(k-1)} = g_{1x}^k \cdot G_x^k$$

$$B_{2,4+5\cdot(k-1)} = g_{1y}^k \cdot G_y^k$$

$$B_{3,4+5\cdot(k-1)} = g_{1z}^k \cdot G_z^k$$

$$B_{4,4+5\cdot(k-1)} = g_{1x}^k \cdot G_y^k + g_{1y}^k \cdot G_x^k$$

$$B_{5,4+5\cdot(k-1)} = g_{1x}^k \cdot G_z^k + g_{1z}^k \cdot G_x^k$$

$$B_{6,4+5\cdot(k-1)} = g_{1y}^k \cdot G_z^k + g_{1z}^k \cdot G_y^k$$

! Fifth column

$$B_{1,5+5\cdot(k-1)} = g_{2x}^k \cdot G_x^k$$

$$B_{2,5+5\cdot(k-1)} = g_{2y}^k \cdot G_y^k$$

$$B_{3,5+5\cdot(k-1)} = g_{2z}^k \cdot G_z^k$$

$$B_{4,5+5\cdot(k-1)} = g_{2x}^k \cdot G_y^k + g_{2y}^k \cdot G_x^k$$

$$B_{5,5+5\cdot(k-1)} = g_{2x}^k \cdot G_z^k + g_{2z}^k \cdot G_x^k$$

$$B_{6,5+5\cdot(k-1)} = g_{2y}^k \cdot G_z^k + g_{2z}^k \cdot G_y^k$$

Loop

! Calculate the weight coefficient

$$\alpha_{ij} = \omega(j) \cdot \det(J)$$

! Multiply the stress-strain matrix by the weight coefficient

For p = 1,6

For q = 1,6

$$C_{pq} = \alpha_{ij} \cdot C_{pq}$$

Loop

Loop

! Get the orthonormal base at the integration point

For p = 1,3

$$T_{1p} = J_{1p}$$

$$T_{2p} = J_{2p}$$

Loop

! Get the third unit vector by doing the cross-product of the first two unit vectors

$$T_{31} = T_{12} \cdot T_{23} - T_{13} \cdot T_{22}$$

$$T_{32} = T_{13} \cdot T_{21} - T_{11} \cdot T_{23}$$

$$T_{33} = T_{11} \cdot T_{22} - T_{12} \cdot T_{21}$$

! Normalize the vectors

$$\|T_1\| = \sqrt{{T_{11}}^2 + {T_{12}}^2 + {T_{13}}^2}$$

$$\|T_3\| = \sqrt{{T_{31}}^2 + {T_{32}}^2 + {T_{33}}^2}$$

For p = 1,3

$$T_{1p} = \frac{T_{1p}}{\|T_1\|}$$

$$T_{3p} = \frac{T_{3p}}{\|T_3\|}$$

Loop

! Recalculate the third unit vector

$T_{21} = T_{32} \cdot T_{13} - T_{33} \cdot T_{12}$

$T_{22} = T_{33} \cdot T_{11} - T_{31} \cdot T_{13}$

$T_{23} = T_{31} \cdot T_{12} - T_{32} \cdot T_{11}$

! Assemble the rotation matrix from the shell natural coordinate system to the global coordinate system

! First row

$R_{11} = T_{11} \cdot T_{11}$

$R_{12} = T_{12} \cdot T_{12}$

$R_{13} = T_{13} \cdot T_{13}$

$R_{14} = T_{11} \cdot T_{12}$

$R_{15} = T_{13} \cdot T_{11}$

$R_{16} = T_{12} \cdot T_{13}$

! Second row

$R_{21} = T_{21} \cdot T_{21}$

$R_{22} = T_{22} \cdot T_{22}$

$R_{23} = T_{23} \cdot T_{23}$

$R_{24} = T_{21} \cdot T_{22}$

$R_{25} = T_{23} \cdot T_{21}$

$R_{26} = T_{22} \cdot T_{23}$

! Third row

$R_{31} = T_{31} \cdot T_{11}$

$R_{32} = T_{32} \cdot T_{32}$

$R_{33} = T_{33} \cdot T_{33}$

$R_{34} = T_{31} \cdot T_{32}$

$R_{35} = T_{33} \cdot T_{31}$

$R_{36} = T_{32} \cdot T_{33}$

! Compute the matrix product CR

For p = 1,6

For q = 1,6

For r=1,6

$CR_{pq} = CR_{pq} + C_{pr} \cdot R_{rq}$

Loop

Loop

Loop

! Compute the stress-strain matrix in the global coordinate system:

D=R^TCR

For p = 1,6

For q = 1,6

For r = 1,6

$D_{pq} = D_{pq} + R_{rp} \cdot CR_{rq}$

Loop

Loop

Loop

! Compute the matrix product DB

For p = 1,6

For q = 1,40

For r = 1,6

$DB_{pq} = DB_{pq} + D_{pr} \cdot B_{rq}$

Loop

Loop

Loop

! Compute the shell stiffness matrix: K=K+B^TDB

For p = 1,6

For q = 1,40

For r = 1,6

$$K_{pq} = K_{pq} + B_{rp} \cdot DB_{rq}$$

Loop

Loop

Loop

Loop

Loop

Appendix C: Derivation of the shell stresses

! Perform the numerical integration

For i=1,2 ! For both integration layers through the shell thickness

For j = 1,4 ! For all integration points on that layer

! Initialize the Jacobian matrix

! Assemble the Jacobian matrix

! Calculate the determinant of the Jacobian matrix

! Invert the Jacobian matrix

! Compute the shape function derivatives in the global coordinate system

! Compute intermediate expressions required for the strain-displacement matrix

! Assemble the strain-displacement matrix

! Calculate the weight coefficient

! Multiply the stress-strain matrix by the weight coefficient

! Get the orthonormal base at the integration point

! Get the third unit vector by doing the cross-product of the first two unit vectors

! Normalize the vectors

! Recalculate the third unit vector

! Assemble the rotation matrix from the shell natural coordinate system to the global coordinate system

! Compute the matrix product CR

! Compute the stress-strain matrix D in the global coordinate system

! Compute the matrix product DB

! Compute the shell stresses: S=S+DB·U

For $p = 1,6$

For $q = 1,40$

$$\sigma_{Gauss,(i-1)\cdot 4+j,p} = \sigma_{Gauss,(i-1)\cdot 4+j,p} + DB_{pq} \cdot U_q$$

Loop

Loop

Loop

Loop

Appendix D: Derivation of the general shell geometric stiffness matrix

! Perform the numerical integration

For i=1,2 ! For both integration layers through the shell thickness

For j = 1,4 ! For all integration points on that layer

! Initialize the Jacobian matrix

! Assemble the Jacobian matrix

! Assemble the nonlinear strain-displacement matrix B_{NL}

For k = 1,8

! First column

$$B_{1,1+5\cdot(k-1)} = \frac{\partial h_k}{\partial x}$$

$$B_{2,1+5\cdot(k-1)} = 0$$

$$B_{3,1+5\cdot(k-1)} = 0$$

$$B_{4,1+5\cdot(k-1)} = \frac{\partial h_k}{\partial y}$$

$$B_{5,1+5\cdot(k-1)} = 0$$

$$B_{6,1+5\cdot(k-1)} = 0$$

$$B_{7,1+5\cdot(k-1)} = \frac{\partial h_k}{\partial z}$$

$$B_{8,1+5\cdot(k-1)} = 0$$

$$B_{9,1+5\cdot(k-1)} = 0$$

! Second column

$$B_{1,2+5\cdot(k-1)} = 0$$

$$B_{2,2+5\cdot(k-1)} = \frac{\partial h_k}{\partial x}$$

$$B_{3,2+5\cdot(k-1)} = 0$$

$$B_{4,2+5\cdot(k-1)} = 0$$

$$B_{5,2+5\cdot(k-1)} = \frac{\partial h_k}{\partial y}$$

$$B_{6,2+5\cdot(k-1)} = 0$$

$$B_{7,2+5\cdot(k-1)} = 0$$

$$B_{8,2+5\cdot(k-1)} = \frac{\partial h_k}{\partial z}$$

$$B_{9,2+5\cdot(k-1)} = 0$$

! Third column

$$B_{1,3+5\cdot(k-1)} = 0$$

$$B_{2,3+5\cdot(k-1)} = 0$$

$$B_{3,3+5\cdot(k-1)} = \frac{\partial h_k}{\partial x}$$

$$B_{4,3+5\cdot(k-1)} = 0$$

$$B_{5,3+5\cdot(k-1)} = 0$$

$$B_{6,3+5\cdot(k-1)} = \frac{\partial h_k}{\partial y}$$

$$B_{7,3+5\cdot(k-1)} = 0$$

$$B_{8,3+5\cdot(k-1)} = 0$$

$$B_{9,3+5\cdot(k-1)} = \frac{\partial h_k}{\partial z}$$

! Fourth column

$$B_{1,4+5\cdot(k-1)} = g_{1x}^k \cdot G_x^k$$

$$B_{2,4+5\cdot(k-1)} = g_{1y}^k \cdot G_x^k$$

$$B_{3,4+5\cdot(k-1)} = g_{1z}^k \cdot G_x^k$$

$$B_{4,4+5\cdot(k-1)} = g_{1x}^k \cdot G_y^k$$

$$B_{5,4+5\cdot(k-1)} = g_{1y}^k \cdot G_y^k$$

$$B_{6,4+5\cdot(k-1)} = g_{1z}^k \cdot G_y^k$$

$$B_{7,4+5\cdot(k-1)} = g_{1x}^k \cdot G_z^k$$

$$B_{8,4+5\cdot(k-1)} = g_{1y}^{k} \cdot G_{z}^{k}$$

$$B_{9,4+5\cdot(k-1)} = g_{1z}^{k} \cdot G_{z}^{k}$$

! Fifth column

$$B_{1,5+5\cdot(k-1)} = g_{2x}^{k} \cdot G_{x}^{k}$$

$$B_{2,5+5\cdot(k-1)} = g_{2y}^{k} \cdot G_{x}^{k}$$

$$B_{3,5+5\cdot(k-1)} = g_{2z}^{k} \cdot G_{x}^{k}$$

$$B_{4,5+5\cdot(k-1)} = g_{2x}^{k} \cdot G_{y}^{k}$$

$$B_{5,5+5\cdot(k-1)} = g_{2y}^{k} \cdot G_{y}^{k}$$

$$B_{6,5+5\cdot(k-1)} = g_{2z}^{k} \cdot G_{y}^{k}$$

$$B_{7,5+5\cdot(k-1)} = g_{2x}^{k} \cdot G_{z}^{k}$$

$$B_{8,5+5\cdot(k-1)} = g_{2y}^{k} \cdot G_{z}^{k}$$

$$B_{9,5+5\cdot(k-1)} = g_{2z}^{k} \cdot G_{z}^{k}$$

Loop

! Calculate the weight coefficient

! Derive the stress matrix S

$S = 0$

For p =1,3

$$S_{p,p} = \sigma_{Gauss,(i-1)\cdot 4+j,xx}$$

$$S_{p,p+3} = \sigma_{Gauss,(i-1)\cdot 4+j,xy}$$

$$S_{p,p+6} = \sigma_{Gauss,(i-1)\cdot 4+j,xz}$$

Loop

For p =4,6

$$S_{p,p-3} = \sigma_{Gauss,(i-1)\cdot 4+j,xy}$$

$$S_{p,p} = \sigma_{Gauss,(i-1)\cdot 4+j,yy}$$

$$S_{p,p+3} = \sigma_{Gauss,(i-1)\cdot 4+j,yz}$$

Loop

For p =7,9

$S_{p,p-6} = \sigma_{Gauss,(i-1)\cdot 4+j,xz}$

$S_{p,p-3} = \sigma_{Gauss,(i-1)\cdot 4+j,yz}$

$S_{p,p} = \sigma_{Gauss,(i-1)\cdot 4+j,zz}$

Loop

! Multiply the stress matrix by the weight coefficient

For p = 1,9

For q = 1,9

$S_{p,q} = \alpha_{ij} \cdot S_{p,q}$

Loop

Loop

! Compute the matrix product SB_{NL}

For p = 1,6

For q = 1,6

For r=1,6

$SB_{pq} = SB_{pq} + S_{pr} \cdot B_{rq}$

Loop

Loop

Loop

! Compute the shell geometric stiffness matrix: $K_g = K_g + B_{NL}^T SB_{NL}$

For p = 1,6

For q = 1,40

For r = 1,6

$K_{pq} = K_{pq} + B_{rp} \cdot SB_{rq}$

Loop

Loop

Loop

Loop

Loop

Appendix E: Derivation of the general shell mass matrix

E.1 CONSISTENT MASS MATRIX FORMULATION

! Define the location of the integration layers through the shell depth

! Define the weight coefficient of each integration point

! Define steel mass density

$$\rho = \frac{490}{12^3 \cdot 1000} \cdot \frac{1}{386.2}$$

! Perform the numerical integration

For i=1,2 ! For both integration layers through the shell thickness

For j = 1,4 ! For all integration points on that layer

! Initialize the Jacobian matrix

! Assemble the Jacobian matrix

! Assemble the interpolation matrix N

For k = 1,8

! First column

$N_{1,1+5\cdot(k-1)} = h_k(j)$

$N_{2,1+5\cdot(k-1)} = 0$

$N_{3,1+5\cdot(k-1)} = 0$

! Second column

$N_{1,2+5\cdot(k-1)} = 0$

$N_{2,2+5\cdot(k-1)} = h_k(j)$

$N_{3,2+5\cdot(k-1)} = 0$

! Third column

$N_{1,3+5\cdot(k-1)} = 0$

$N_{2,3+5\cdot(k-1)} = 0$

$N_{3,3+5\cdot(k-1)} = h_k(j)$

! Fourth column

$N_{1,4+5\cdot(k-1)} = g_{1x}^k(j)$

$N_{2,4+5\cdot(k-1)} = g_{1y}^k(j)$

$N_{3,4+5\cdot(k-1)} = g_{1z}^k(j)$

! Fifth column

$N_{1,5+5\cdot(k-1)} = g_{2x}^k(j)$

$N_{2,5+5\cdot(k-1)} = g_{2y}^k(j)$

$N_{3,5+5\cdot(k-1)} = g_{2z}^k(j)$

Loop

! Calculate the weight coefficient

! Compute the matrix product N^TN

For p = 1,40

For q = 1,40

For r=1,40

$N^T N_{pq} = N^T N_{pq} + N_{rp} \cdot N_{rq}$

Loop

Loop

Loop

! Compute the shell consistent mass matrix: $M = M+N^TN$

For p = 1,40

For q = 1,40

$M_{pq} = M_{pq} + N^T N_{pq} \cdot \alpha_{ij} \cdot \rho$

Loop

Loop

Loop

Loop

E.2 LUMPED MASS MATRIX FORMULATION

! Define steel mass density

$$\rho = \frac{490}{12^3 \cdot 1000} \cdot \frac{1}{386.2}$$

! Define the shell diagonal vectors P and Q

$$P_1 = x\big(shell(3)\big) - x\big(shell(1)\big)$$

$$P_2 = y\big(shell(3)\big) - y\big(shell(1)\big)$$

$$P_3 = z\big(shell(3)\big) - z\big(shell(1)\big)$$

$$Q_1 = x\big(shell(4)\big) - x\big(shell(2)\big)$$

$$Q_2 = y\big(shell(4)\big) - y\big(shell(2)\big)$$

$$Q_3 = z\big(shell(4)\big) - z\big(shell(2)\big)$$

! Calculate the cross-product vector PQ

$$PQ_1 = P_2 Q_3 - P_3 Q_2$$

$$PQ_2 = P_1 Q_3 - P_3 Q_1$$

$$PQ_3 = P_1 Q_2 - P_2 Q_1$$

! Calculate the area, volume, and mass of the shell element

$$A = \frac{1}{2} \cdot \sqrt{PQ_1^2 + PQ_2^2 + PQ_3^2}$$

$$V = h \cdot A$$

$$m = \rho \cdot V$$

! Construct the shell lumped mass matrix

For k = 1,8

$$M_{5\cdot(i-1)+1,5\cdot(i-1)+1} = \frac{m}{8}$$
$$M_{5\cdot(i-1)+2,5\cdot(i-1)+2} = \frac{m}{8}$$
$$M_{5\cdot(i-1)+3,5\cdot(i-1)+3} = \frac{m}{8}$$
$$M_{5\cdot(i-1)+4,5\cdot(i-1)+4} = \frac{m}{32}\cdot h^2$$
$$M_{5\cdot(i-1)+5,5\cdot(i-1)+5} = \frac{m}{32}\cdot h^2$$

Loop

References

Abaqus (2017), Dassault Systèmes, Johnston, RI

Ahmad, Irons and Zienkiewicz (1970), "Analysis of Thick and Thin Shell Structures by Curved Finite Elements", International Journal for Numerical Methods in Engineering, Vol. 2, No. 3, July

Akay, H.U., Johnson, C.P. and Will, K.M. (1977), "Lateral and Local Buckling of Beams and Frames", Journal of the Structural Division, ASCE, ST9, September, pp. 1821-1832

American Association of State Highway Transportation Officials (AASHTO) (2014), *Guidelines for Steel Girder Bridge Analysis*, 2nd Edition, Washington, D.C.

American Association of State Highway Transportation Officials (AASHTO) (2017), *LRFD Bridge Design Specifications*, 8th Edition, Washington, D.C.

American Institute of Steel Construction, Inc. (AISC) (2017), 15th Edition Steel Construction Manual, Chicago, IL

Arbocz, J. and Babcock, Jr., C.D. (1980), "The Buckling Analysis of Imperfection Sensitive Shell structures", NASA CR 3310

Armijos, S., Wang, Y., Helwig, T., Engelhardt, M., Clayton, P., Williamson, E. (2017), "Experimental Study of Steel Tub Girders with Partial Top Lateral Bracing", Structural Stability Research Council Proceedings, Annual Stability Conference, San Antonio, TX, March 21-24, 2017

Ball, A.W. (2005). *Modal Analysis of a Multi-Span Reverse Curve Steel Girder Bridge Using Computer Modeling*, Master's Thesis, Utah State University, Logan, UT

Bathe, K.-J. (1982). Finite Element Procedures in Engineering Analysis, Prentice Hall, Upper Saddle River, NJ

Battistini, A.D., Wang, W., Helwig, T.A. and Engelhardt, M.D. (2016). "Stiffness Behavior of Cross Frames in Steel Bridge Systems", Journal of Bridge Engineering, Vol. 21, No. 6, June

Bell, B.J. and Linzell, D.G. (2007). "Erection Procedure Effects on Deformations and Stresses in a Large-Radius, Horizontally Curved, I-Girder Bridge", Journal of Bridge Engineering, Vol. 12, No. 4, July

Bolourchi, S. (1979). *On Finite Element Nonlinear Analysis of General Shell Structures*, Ph.D. Dissertation, Massachusetts Institute of Technology, Cambridge, MA

Chang, C.-J. (2006). *Construction Simulation of Curved Steel I-Girder Bridges*, Ph.D. Dissertation, Georgia Institute of Technology, Atlanta, GA

Chavel, B.W. and Earls, C.J. (2005). "Inconsistent Detailing of Cross-frame Members in Horizontally Curved Steel I-Girder Bridges", Structures Congress 2005, New York, NY, April 20-24, 2005

Chavel, B., Sanchez, A., White, D., Coletti, D., Ozgur, C. and Jimenez, J. (2012). "Erection Engineering Analysis for Curved and Skewed Bridges", Structures Congress 2012, Chicago, IL, March 29-31, 2012

Chen, Q. (2008). *Effects of Thermal Loads on Texas Steel Bridges*, Ph.D. Dissertation, The University of Texas at Austin, Austin, TX

Cook, R.D. et al. (2001). Concepts and Applications of Finite Element Analysis, 4th Edition, John Wiley & Sons, Hoboken, NJ

Corr, D.J., McCann, D.M., and McDonald, B.M. (2009). "Lessons Learned from Marcy Bridge Collapse", Fifth Forensic Engineering Congress, Washington, DC, November 11-14, 2009

Cottrell, J.A., Hughes, T.J.R., and Bazilevs, Y. (2009). Isogeometric Analysis: Toward Integration of CAD and FEA, Wiley, Chichester, West Sussex, UK

CSi Bridge (2017), Computers & Structures, Inc., Walnut Creek, CA

Davidson, J.S. and Yoo, C.H. (1996). "Local Buckling of Curved I-Girder Flanges", Journal of Structural Engineering, Vol. 122, No. 8, August

DESCUS I and DESCUS II (2008), Bridge Engineering Software & Technology Center, University of Maryland, College Park, MD

Dvorkin, E.N. (1984). *On Nonlinear Finite Element Analysis of Shell Structures*, Ph.D. Dissertation, Massachusetts Institute of Technology, Cambridge, MA

Egilmez, O.O., Helwig, T.A. and Herman, R. (2016). "Using Metal Deck Forms for Construction Bracing in Steel Bridges", Journal of Bridge Engineering, Vol. 21, No. 5, May

Fan, Z. and Helwig, T.A. (1999). "Behavior of Steel Box Girders with Top Flange Bracing", Journal of Structural Engineering, Vol. 125, No. 8, August

Fan, Z. and Helwig, T.A. (2002). "Distortional Loads and Brace Forces in Steel Box Girders", Journal of Structural Engineering, Vol. 128, No. 6, June

Fasl, J.D., Stith, J.C., Helwig, T.A. and Schuh, A. (2015). "Instrumentation of a Horizontally Curved Steel I-Girder Bridge During Construction", Journal of Structural Engineering, Vol. 141, No. 1, January

Fiechtl, A.L., Fenves, G.L., and Frank, K.H. (1987). "Approximate Analysis of Horizontally Curved Bridges", *Final Report No FHWA/TX-91+360-2F*, Center for Transportation Research, The University of Texas at Austin, Austin, TX

Hahn, K.H. and Johnson, C.P. (1991). “Computer Program for the Analysis of Curved Steel Bridges”, *Final Report No FHWA/rx-92+360-l*, Center for Transportation Research, The University of Texas at Austin, Austin, TX

Helwig, T.A. (1994). *Lateral Bracing of Bridge Girders by Metal Deck Forms*, Ph.D. Dissertation, The University of Texas at Austin, Austin, TX

Helwig, T.A., Frank, K.H. and Yura, J.A. (1997). “Lateral-Torsional Buckling of Singly-Symmetric I-Beams”, Journal of Structural Engineering, Vol. 3, No. 9, September

Helwig, T.A., Yura, J., Herman, R., Williamson, E. and Li, D. (2007). “Design Guidelines for Steel Trapezoidal Box Girder Systems”, *Final Report No FHWA/TX-07/0-4307-1*, Center for Transportation Research, The University of Texas at Austin, Austin, TX

Herman, R.S., Helwig, T.A. and Zhou, C. (2007). “Use of Lean-On Cross-frame Bracing in Steel Girder Bridges”, New Horizons and Better Practices, Structures Congress, Long Beach, CA, May 16-19, 2007

Jimenez Chong, J.M. (2012). *Construction Engineering of Steel Tub-Girder Bridge Systems for Skew Effects*, Ph.D. Dissertation, Georgia Institute of Technology, Atlanta, GA

Kim, K. (2004). *Research on Horizontally Curved Steel Box Girders*, Ph.D. Dissertation, Auburn University, Auburn, AL

LARSA 4D (2016), LARSA, Inc., Melville, NY

Linzell, D.G. (1999). *Studies of Full-Scale Horizontally Curved Steel I-Girder Bridge System Under Self-Weight*, Ph.D. Dissertation, Georgia Institute of Technology, Atlanta, GA

LUSAS Bridge (2015), LUSAS, Kingston upon Thames, UK

MDX Version 6 (2009) Curved & Straight Steel Bridge Design & Rating, MDX Software, Inc.

National Cooperative Highway Research Program (NCHRP) Report No 725 (2012). *Guidelines for Analysis Methods and Construction Engineering of Curved and Skewed Steel Girder Bridges*, Transportation Research Board, Washington, D.C.

Nickas, W. and Dick, J. (2015). “Working Together to Create the Future”, ASPIRE – The Concrete Bridge Magazine, Summer 2015, pp. 24-27

Ozgur, C. (2011). *Influence of Cross-Frame Detailing on Curved and Skewed Steel I-Girder Bridges*, Ph.D. Dissertation, Georgia Institute of Technology, Atlanta, GA

Polizzi, E. (2009). “Density-Matrix-Based Algorithm for Solving Eigenvalue Problems”, Physical Review B, Vol. 79, No. 11, March

Popp, D.R. (2004). *UTrAp 2.0: Linearized Buckling Analysis of Steel Trapezoidal Girders*, Master’s Thesis, The University of Texas at Austin, Austin, TX

Quadrato, C.E. (2010). *Stability of Skewed I-Shape Girders Using Bent Plate Connections*, Ph.D. Dissertation, The University of Texas at Austin, Austin, TX

Robalino, A.F. and Sanchez, T.A. (2017). "Global Lateral-Torsional Buckling of I-Girder Systems in Cantilever", Structural Stability Research Council Proceedings, Annual Stability Conference, San Antonio, TX, March 21-24, 2017

Sanchez, T.A. (2011). *Influence of Bracing Systems on the Behavior of Curved and Skewed Steel I-Girder Bridges During Construction*, Ph.D. Dissertation, Georgia Institute of Technology, Atlanta, GA

Sanchez, T.A. and White, D.W. (2017). "Improved 2D-Grid Construction Analysis of Curved and Skewed Steel I-Girder Bridges", Journal of Bridge Engineering, Vol. 22, No. 9, September

Sharafbayani, M. and Linzell, D.G. (2012). "Effect of Temporary Shoring Location on Horizontally Curved Steel I-Girder Bridges During Construction", Journal of Bridge Engineering, Vol. 17, No. 3, May

Sharafbayani, M. and Linzell, D.G. (2014). "Optimizing Horizontally Curved, Steel Bridge, Cross-Frame Arrangements to Enhance Construction Performance", Journal of Bridge Engineering, Vol. 19, No. 7, July

Shenk, O. (2000). *Scalable Parallel Sparse LU Factorization Methods on Shared Memory Multiprocessors*, Ph.D. Dissertation, ETH, Zurich, Switzerland

Stith, J.C. (2010). *Predicting the Behavior of Horizontally Curved I-Girders During Construction*, Ph.D. Dissertation, The University of Texas at Austin, Austin, TX

Stith, J.C., Helwig, T.A., Williamson, E.B. and Frank, K.H. (2012). "Comparison of the Computed and Measured Behavior of Curved Steel I-Girders During Lifting", Journal of Structural Engineering, Vol. 138, No. 1, January

Stith, J.C., Helwig, T.A., Williamson, E.B. and Frank, K.H. (2013). "Behavior of Horizontally Curved I-Girders During Lifting", Journal of Structural Engineering, Vol. 139, No. 4, April

Timoshenko, S.P. and Gere, J.M. (1963). Theory of Elastic Stability, McGraw-Hill Book Company, New York, NY

Topkaya, C. (2002). *Behavior of Curved Steel Trapezoidal Box Girders During Construction*, Ph.D. Dissertation, The University of Texas at Austin, Austin, TX

Topkaya, C. and Williamson, E.B. (2003). "Development of Computational Software for Analysis of Curved Girders Under Construction Loads", Computers & Structures, Vol. 81, No. 21, September, pp. 2087-2098

Topkaya, C., Williamson, E.B. and Frank, K.H. (2004). "Behavior of Curved Steel Trapezoidal Box-Girders During Construction", Engineering Structures, Vol. 26, No. 6, May, pp. 721-733

Topkaya, C., Yura, J.A. and Williamson, E.B. (2004). “Composite Shear Stud Strength at Early Concrete Ages”, Engineering Structures, Vol. 130, No. 6, June

Tung, D. and Fountain, R. (1970). “Approximate Torsional Analysis of Curved Box Girders by the M/R-Method”, AISC Engineering Journal, July 1970, AISC, pp. 65-74

Yoo, C.H., Kim, K., and Choi, B.H. (2005). *Research on Horizontally Curved Steel Box Girders*, Highway Research Center, Auburn University, Auburn, Alabama

Yura, J.A. (2001). “Fundamentals of Beam Bracing”, Engineering Journal, American Institute of Steel Construction, Vol. 38, No. 1

Yura, J.A., Helwig, T.A., Herman, R. and Zhou, C. (2008). “Global Lateral Buckling of I-Shaped Girder Systems”, Journal of Structural Engineering, Vol. 134, No. 9, September

Yura, J.A. and Widianto (2005). “Lateral Buckling and Bracing of Beams – A Re-evaluation After the Marcy Bridge Collapse”, Structural Stability Research Council Proceedings, Annual Stability Conference, Montreal, QC, Canada, April 6-9, 2005

Zureick, A. and Naqib, R. (1999). “Horizontally Curved Steel I-Girders State-of-the-Art Analysis Methods”, Journal of Bridge Engineering, Vol. 4, No. 1, February